Large Eddy Simulation of Turbulent Flows in Wind Energy

Sarlak Chivaee, Hamid; Sørensen, Jens Nørkær; Mikkelsen, Robert Flemming; Shen, Wen Zhong

Publication date:
2014

Document Version
Publisher's PDF, also known as Version of record

Large Eddy Simulation of Turbulent Flows in Wind Energy

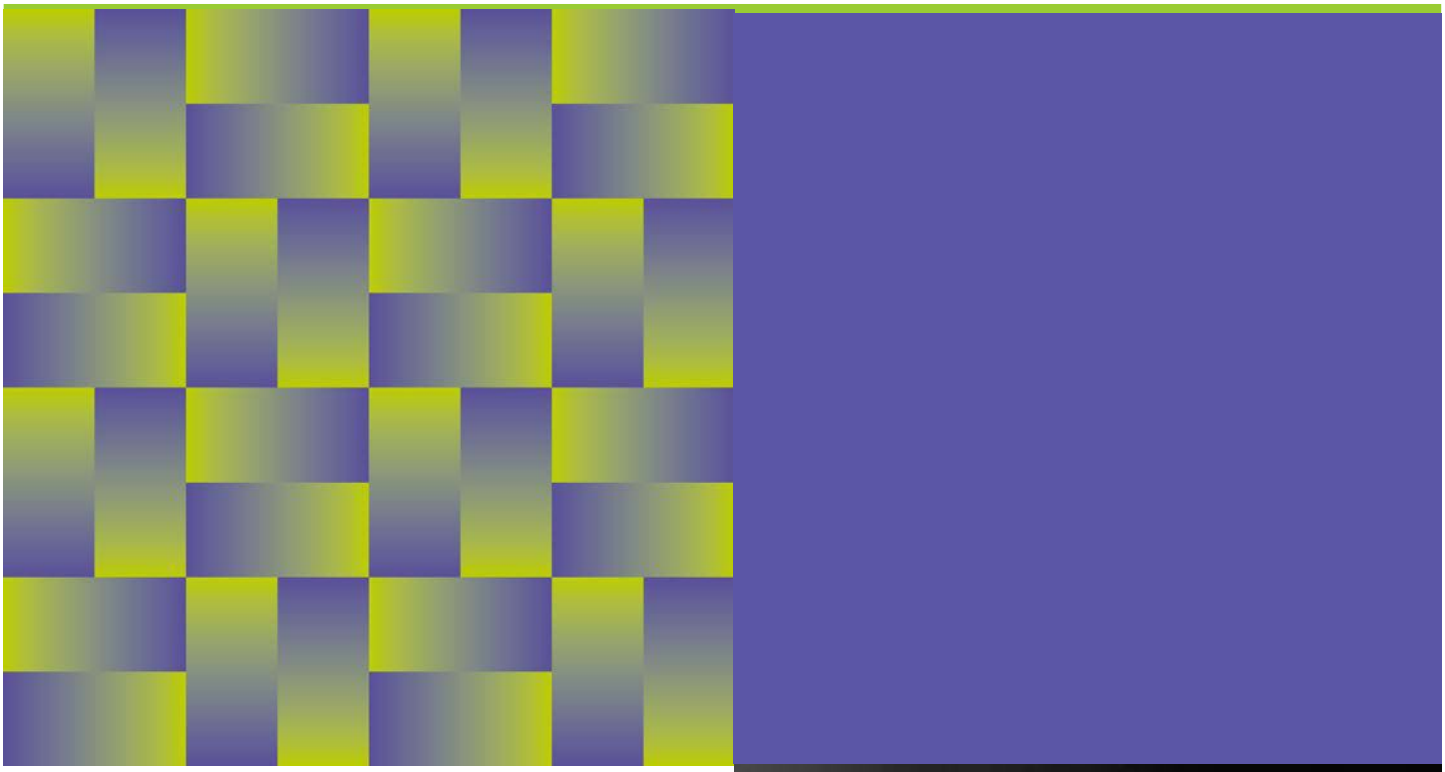

Hamid Sarlak Chivaee

DTU Wind Energy PhD-0037 (EN)
ISBN: 978-87-92896-82-7

January 2014

DTU Vindenergi
Institut for Vindenergi

Title: Large Eddy Simulation of Turbulent Flows in Wind Energy

Keywords:

Large Eddy Simulation, Sub-grid Scale modeling, Atmospheric Boundary Layer, Airfoil Aerodynamics, Wind Turbine Wakes

Abstract:

This research is devoted to the Large Eddy Simulation (LES), and to lesser extent, wind tunnel measurements of turbulent flows in wind energy. It starts with an introduction to the LES technique associated with the solution of the incompressible Navier-Stokes equations, discretized using a finite volume method. The study is followed by a detailed investigation of the Sub-Grid Scale (SGS) modeling. New SGS models are implemented into the computing code, and the effect of SGS models are examined for different applications. Fully developed boundary layer flows are investigated at low and high Reynolds numbers, and thereafter, the fully-developed infinite wind farm boundary later simulations are performed. Sources of inaccuracy in the simulations are investigated and it is found that high Reynolds number flows are more sensitive to the choice of the SGS model than their low Reynolds number counterparts. Wind tunnel measurements of an airfoil at Reynolds numbers ranging from 40,000 to 400,000 are carried out. The measurements include detailed surface pressure as well as force balance measurements for obtaining the lift, drag and pressure distribution over the airfoil. Measurements are performed in the upstroke and downstroke pitching for angles of attack between -10° and $+25^{\circ}$ and the static stall hysteresis phenomenon is investigated experimentally. Following the wind tunnel measurements, LES of the airfoil is performed using a numerical wind tunnel for Re=40,000 and Re=100,000 at a range of angles of attack. Laminar-turbulent transition, generation of laminar boundary layer separation, and formation of stall cells are investigated. The simulated airfoil characteristics are validated against measurements. It is concluded that the LES computations and wind tunnel measurements are in good agreement, should the mesh resolution, numerical discretization scheme, time averaging period, and domain size be chosen wisely.

A thorough investigation of the wind turbine wake interactions is also conducted and the simulations are validated against available experimental data from external sources. The effect of several parameters on the wake structures and blade loadings are investigated. In particular, the role of SGS modeling on the flow structures and wind turbine loadings is quantified in great detail. It is found that, for the studied cases (using body-force to represent wind turbines), when a fine mesh is used to capture the tip vortices somewhat accurately, the particular choice of the SGS model is not a determining factor in simulation accuracy. To increase the role of SGS models therefore, one needs to coarsen the computational mesh, which, in return, results in poor wake predictions.

Printed in Denmark

DTU Wind Energy PhD-0037 (EN)

ISBN: 978-87-92896-82-7

January 2014

Projektperiode:

2011-14

Uddannelse:

Doctor of Philosophy

Område:

Fluid Mechanics/ Wind Energy

Vejledere:

Jens N. Sørensen

Robert F. Mikkelsen

Bemærkninger:

Kontakt nr.:

Projektnr.:

Sponsorship:

Statkraft

COMWIND, DTU

Forside:

Total pages: 185

Figures: 87

Tables: 17

References:

Danmarks Tekniske Universitet
Institut for Vindenergi
Nils Koppels Allé
Bygning 403
2800 Kgs. Lyngby
Telefon 45254340

mahj@dtu.dk

www.vindenergi.dtu.dk

Large Eddy Simulation of Turbulent Flows in Wind Energy

by

Hamid Sarlak Chivaee

Submitted to the Department of Wind Energy in partial fulfilment of the requirements for the degree of

Doctor of Philosophy

at

The Technical University of Denmark

Jens N. Sørensen, Robert F. Mikkelsen, Advisers.

2014

"Sistan [of Iran] is the land of winds and sand. There are winds [which] drive mills and raise water from the streams, whereby gardens are irrigated. There is in the World, and God alone knows it, no place where more frequent use is made of the winds."

Egyptian Historian and Geographer, Al-Mas'udi (947 AD.).

Preface

niversity of Denmark (DTU). This research was conducted during the period from January 2011 to January 2014 at the Section of Fluid Mechanics. The funding for this project was provided by the DTU Center for Computational Wind Turbine Aerodynamics and Atmospheric Turbulence (COMWIND) as well as Statkraft through the Statkraft Ocean Energy Research Program (SOERP). I appreciate the financial support from Otto Mønsteds Fond for partial sponsorship during conferences and my stay abroad.

I am grateful to my supervisor, Jens N. Sørensen, who has been always there to listen and give advice to me, and also for offering me flexibility to choose the path of my research. Many thanks to my co-supervisor, Robert Mikkelsen. Robert has greatly helped me during both experimental and numerical parts of the research. Thanks to Charles Meneveau for his help and support during my summer visit to the Johns Hopkins University (JHU) in the United States. I shall also thank my colleagues who have helped me every now and then during this research, including but not limited to WZ. Shen, NN. Sørensen and P. Sagaut and the fellows at JHU for the fruitful talks we have had. Thanks to my friends N.R. Garcia, S. Sarmast and R. Read for proofreading this thesis.

Finally, my family, to whom this thesis is dedicated, have inspired me to pursue my education throughout these years. I am thoroughly grateful for all their generous support and unconditional love.

Hamid Sarlak Chivaee
Spring 2014, Copenhagen.

Abstract

This research is devoted to the Large Eddy Simulation (LES), and to lesser extent, wind tunnel measurements of turbulent flows in wind energy. It starts with an introduction to the LES technique associated with the solution of the incompressible Navier-Stokes equations, discretized using a finite volume method. The study is followed by a detailed investigation of the Sub-Grid Scale (SGS) modeling. New SGS models are implemented into the computing code, and the effect of SGS models are examined for different applications. Fully developed boundary layer flows are investigated at low and high Reynolds numbers, and thereafter, the fully-developed infinite wind farm boundary later simulations are performed. Sources of inaccuracy in the simulations are investigated and it is found that high Reynolds number flows are more sensitive to the choice of the SGS model than their low Reynolds number counterparts.

Wind tunnel measurements of an airfoil at Reynolds numbers ranging from 40,000 to 400,000 are carried out. The measurements include detailed surface pressure as well as force balance measurements for obtaining the lift, drag and pressure distribution over the airfoil. Measurements are performed in the upstroke and downstroke pitching for angles of attack between -10° and $+25^\circ$ and the static stall hysteresis phenomenon is investigated experimentally [1]. Following the wind tunnel measurements, LES of the airfoil is performed using a numerical wind tunnel for Re=40,000 and Re=100,000 at a range of angles of attack. Laminar-turbulent transition, generation of laminar boundary layer separation, and formation of stall cells are investigated. The simulated airfoil characteristics are validated against measurements. It is concluded that the LES computations and wind tunnel measurements are in good agreement, should the mesh resolution, numerical discretization scheme, time averaging period, and domain size be chosen wisely.

[1] Benchmark results for the airfoil aerodynamic data are appended to the report.

A thorough investigation of the wind turbine wake interactions is also conducted and the simulations are validated against available experimental data from external sources. The effect of several parameters on the wake structures and blade loadings are investigated. In particular, the role of SGS modeling on the flow structures and wind turbine loadings is quantified in great detail. It is found that, for the studied cases (using body-force to represent wind turbines), when a fine mesh is used to capture the tip vortices somewhat accurately, the particular choice of the SGS model is not a determining factor in simulation accuracy. To increase the role of SGS models therefore, one needs to coarsen the computational mesh, which, in return, results in poor wake predictions.

Contents

Chapter 1

Introduction

1.1 Wind Power: from past to future

Wind energy is perhaps the oldest discovered source of renewable energy with roots going back to 3000BC when Egyptians started utilizing it in their sailing boats[1]. Persian *Panemone*s, as the first recorded examples of windmills, were in use as early as 3000 years ago (Sørensen, 2011). As shown in figure 1.1, they had long vertical drive shafts with six to twelve blade rotors (sails) covered in cloth and were used for grinding grain and pumping water. The first detailed drawings of such windmills were made around 1300 AD. (Forbes, 1964; Shepherd, 1990).

The desire to harness wind energy spread throughout the world and in 14th century, several windmill and wind turbines were designed, including the Dutch horizontal-axis windmill which became a platform for future developments in the wind turbine technology (Sørensen, 2011). Due to its high winds, Denmark became one of the pioneers in wind energy industry, too, and by the beginning of 20th century, there were about 2,500 windmills in Denmark. During 1887-1908, Charles F. Brush (USA) and Poul la Cour (Denmark) constructed the first electricity producing wind turbine prototypes, independently (Sørensen, 2011). Today, Denmark has kept its position as a leading country in wind energy research and development. The small wind turbines are now gradually replaced by the higher capacity on-shore and off-shore machines. The largest wind turbine installed for testing at the Danish national wind turbine test centre at Osterild is an 8 MW Vestas machine [2]. Figures 1.2 (left) and 1.2 (right) show la Cour's turbine as well as a modern offshore wind turbine.

[1] Encyclopedia Of International Sports Studies. Page 31

[2] http://www.windpowermonthly.com/article/1211056/close—vestas-v164-80-nacelle-hub

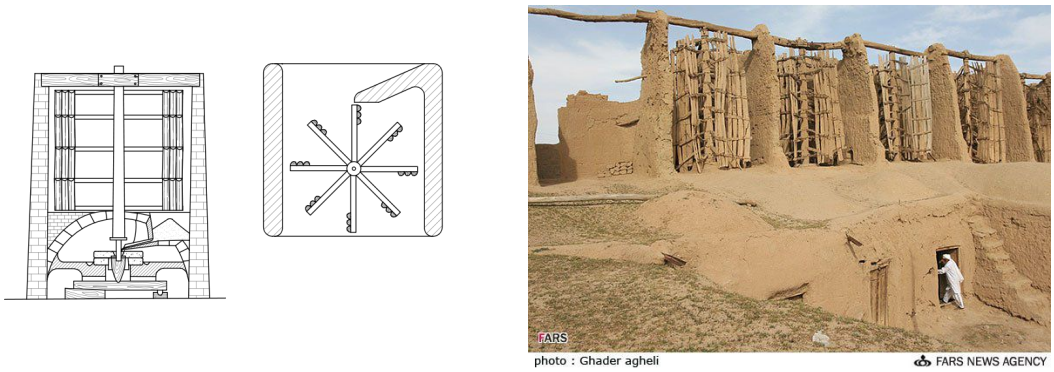

Figure 1.1: Sketch and ruins of the drag-based Persian windmill, Panemone, still in use in some villages in Sistan region (south-east Iran). Ref.: Forbes (1964). (left figure); Fars News Agency (right figure).

Figure 1.2: Danish wind turbine (1891) (left) and a modern 10MW offshore wind turbine (right). Ref.: www.Google.com/imghp.

	1982 (MW)	1987 (MW)	1992 (MW)	1997 (MW)	2002 (MW)	2007 (MW)	2012 (MW)
Net Annual Addition‡	65	180	340	1,500	7,200	19,633	44,395
Cum. Installed Capacity	90	1,450	2,510	7,600	31,100	93,639	282,430

† 1980-1995 data from Janet L. Sawin, "Wind Power Still Soaring," in Worldwatch Institute, 2007; and 1996-2012 data from Global Wind Energy Council, Global Wind Statistics 2012.

‡ Net annual addition equals new installations minus retirements.

Table 1.1: Development in wind power generation †.

During the past three decades, the wind power industry has experienced a tremendous growth. Table 1.1 shows the capacity increase of the wind turbines during the past 30 years. The growth has been made by employing and erecting larger wind turbines and wind farms, which in return, brings on new design and construction challenges. Larger turbines are subject to higher wind shear and turbulence loads from the atmospheric boundary layer (ABL) causing them severe external loads. In recent years, numerical simulations have become important tools for design and optimization of wind turbines and wind farms.

1.2 Literature review

Wind turbines operate in the wind shear layer and often gusts and therefore face significant interactions with the ABL in all ranges of scales in a complicated process: the small-scale shear-generated turbulent structures formed on the blade surface are responsible for the break-down of the tip and root vortices and the wake development downstream of the rotor and must be considered in the design process. Meanwhile, operation of the very large wind farms, as a whole, can be so intense that they impact the local climate directly. Table 1.2 shows the various turbulence length, velocity, and time scales involved in the wind turbine wake studies. As can be seen, the largest scales of motion are about 7 orders of magnitude larger than the smallest ones.

Depending on the scales of motion, Large Eddy Simulation (LES) studies relevant to wind energy are divided into three categories in this thesis: LES of the ABL, LES of the wind turbine wakes, and LES of the flow over airfoils. In the following section, previous works in each of the above-mentioned fields are reviewed.

	Length scale [m]	Velocity scale [m/s]	Time Scale [s]
Airfoil boundary layer	$\mathcal{O}(10^{-3})$	$\mathcal{O}(10^{2})$	$\mathcal{O}(10^{-5})$
Airfoil	$\mathcal{O}(1)$	$\mathcal{O}(10^{2})$	$\mathcal{O}(10^{-2})$
Wind turbine rotor	$\mathcal{O}(10^{2})$	$\mathcal{O}(10)$	$\mathcal{O}(10)$
Cluster of turbines	$\mathcal{O}(10^{3})$	$\mathcal{O}(10)$	$\mathcal{O}(10^{2})$
Wind farm	$\mathcal{O}(10^{4})$	$\mathcal{O}(10)$	$\mathcal{O}(10^{3})$
ABL	$\mathcal{O}(10^{2-3})$ ‡	$\mathcal{O}(10)$	$\mathcal{O}(10^{1-2})$
‡ Varying diurnally due to the thermal stability of the ABL.			

Table 1.2: Turbulence scales in the wind turbine aerodynamics.

1.2.1 Large Eddy Simulation (LES) of the ABL

Along with the satisfaction as a result of technological achievements, the growing number and increasing size of wind turbines installed both off-shore and on-shore has risen common concerns for both wind engineers and meteorologists. Today, wind turbines reach the surface layer (the layer, typically around 10% of the ABL height, in which the winds, temperature and humidity vary rapidly with altitude and and the characteristics of turbulence are affected by the surface [1]), and experience severe loads from the boundary layer. Figure 1.3 shows a schematic diagram of the wind turbine wake interactions with the ABL. As can be seen, several processes is involved in turbine wake interactions with the ABL, the most important of which is the mixing between the wake and the ABL causing downward momentum flux into the wake region, thereby wake recovery at a certain distance behind the turbines. This increased mixing is clearly a good feature of turbulence. In order to know the interactions if the wind turbines and the ABL, it is useful to first study the ABL without the turbines present.

While the Smagorinsky SGS model had already been developed by (Smagorinsky, 1963), the first LES study of the ABL reported was the high Reynolds number channel flow simulated by Deardorff (1970). Not surprisingly, Deardroff's numerical model was based on the Smagorinsky's previous SGS model. Later, he continued his work by simulating the neutral and convective (obtained by surface heating) ABL flows (Deardorff, 1972). LES of the ABL flows with different stability conditions was later performed by Deardorff (1980); Moeng (1984); Moeng and Sullivan (1994); Sullivan et al. (1994) using SGS models based on a time-evolving turbulent kinetic energy equation. Simulations of the stably stratified ABL (SABL), obtained by surface cooling during the night for example, are considered more complicated than the neutral and the convective

[1] http://www.met.rdg.ac.uk/~swrhgnrj/teaching/MT36E/MT36E_BL_lecture_notes.pdf

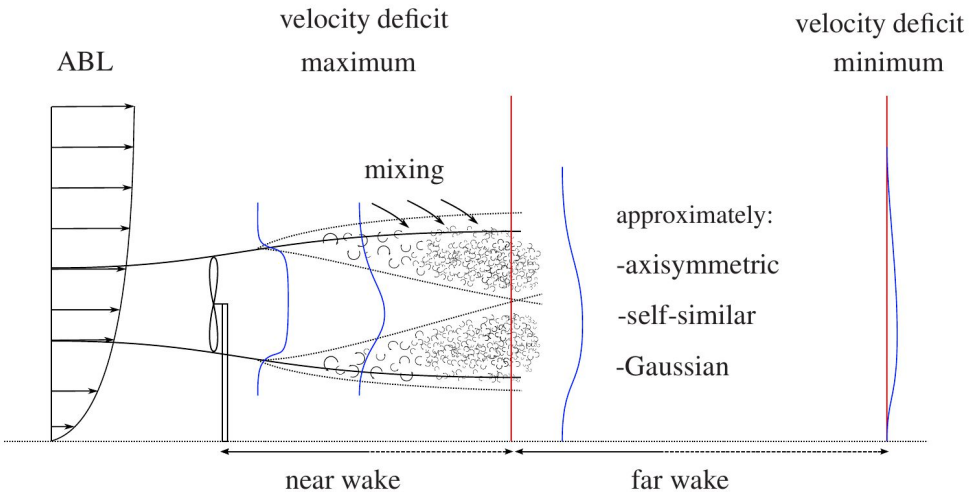

Figure 1.3: Wind turbine wakes in the ABL. Mixing of the ABL and turbine wakes from above the turbine region causes the wake recovery further downstream. Figure reproduced from Sanderse (2009).

boundary layers due to the inability of the flow solvers to capture the right flow relaminarization. Derbyshire (1990) performed the first LES of the SABL using a standard Smagorinsky model. Their results were in agreement with the previous findings about the SABL, however, they observed a non-physical temperature decline in the computational domain over time. The issue with the temperature decline has been tackled by other researchers, such as Sescu and Meneveau (2014).

Talking about the turbine wake-ABL interactions, a number of researchers have focused mostly on the ABL part by neglecting the complicated instabilities in the tip vortices and development of the wake from turbine and instead have used simplified parametrizations to represent the turbines, as it requires vast computational resources otherwise. Others have focused more on the wake and turbine parametrizations and have used simplified ABL models, as briefly discussed in the following.

1.2.2 LES of wind turbine wakes

Wind turbine wakes and aerodynamics have historically been studied using either analytically derived empirical models based on experiments (Frandsen et al., 2006), or experimental wind tunnel measurements (Bartl et al., 2012). Wind tunnel measurements suffer from low Reynolds number and scaling issues and analytical models are usually based on questionable or simplified assumptions. With the increase in the computational power and due to the recent wind turbine modeling developments such as

introduction of the actuator line modeling technique(Sørensen and Shen, 2002), however, numerical studies have also been recently applied to the simulation of wind turbine wakes and their interactions with the atmospheric boundary layers. LES, in particular, has shown capability of resolving the unsteady nature of the wake flows without the previous concerns (Sørensen, 2011; Vermeer et al., 2003).

Mikkelsen (2003); Mikkelsen et al. (2007) coupled the actuator line and actuator disc models with the CFD solver, EllipSys3D. He performed a comprehensive study on the *Tjæreborg* wind turbine and *LM* blade and confirmed the applicability of the LES for wake studies. Jimenez et al. (2007) developed an LES code using dynamic Smagorinsky model and performed wind turbine simulations in the ABL. They used actuator disc representation of the wind turbine using a constant forcing and by comparing with the *Sexbierum* wind farm field data, showed that LES is capable of investigating the detailed wake flows. Ivanell et al. (2009) performed actuator disc simulations of the *Horns Rev* wind farm using a prescribed neutral ABL. They used the rotating AD model implemented by Mikkelsen (2003) and investigated the effect of the yaw angle on the wake deficits. This research concluded that a better agreement holds between the measurements and the LES computations when the wind direction is not completely aligned with the wind turbines. For the cases with zero yaw degree, however, the wake effects were over-predicted and the downstream turbine power production was correspondingly under-predicted, as compared with the 10-min averaged measurements. Troldborg et al. (2007) conducted a detailed study on the actuator line models in sheared and uniform free-stream and documented the effects of the free stream turbulence as well as other numerical parameters on the wake profiles. Simulations performed by Ivanell et al. (2009); Mikkelsen et al. (2007); Troldborg et al. (2007) were all obtained using a mixed scale SGS model originally proposed by Sagaut (1995) and Ta Phuoc (1994).

Calaf et al. (2010) compared two SGS models on two different CFD codes. The codes used the standard Smagorinsky model and the scale dependent Lagrangian dynamic Smagorinsky model Bou-Zeid et al. (2005). They simulated a fully developed infinite wind farm and studied the interactions of the wind turbines with the neutrally stratified ABL. The vertical transport of the momentum accross the ABL was investigated using a combination of different rotor arrangements, domain sizes, thrust coefficients and the surface roughness heights and a model for an effective roughness height -representing the turbine effects- were proposed. Porté-Agel et al. (2011) performed LES of the wind turbine wakes using both AD and AL approaches. They compared their simulations with the wind tunnel measurements and found that to have the most accurate wake predictions in the region of up to 5 rotors downstream, the rotational effects needs to

be included in the wind turbine parametrizations. One problem with the mentioned verifications was, however, that the experimental set-up (and consequently the numerical computations) was made using small fans as opposed to real wind turbine models, therefore, the complexity of wind turbine blade profiles were not taken adequately into account. The wind turbine simulations in the ABL have been mostly performed on the neutral atmospheric stratification. Recently, Porté-Agel et al. (2011) performed LES computations of the wind farms in stably stratified flows using a variant of the dynamic Lagrangian SGS model. [1]

1.2.3 LES of flow around Airfoils

Compared to the simpler approaches like viscous-inviscid solvers and RANS, LES can provide a deeper insight into various scales of motion and therefore is more suitable for the cases with unsteadiness such as dynamic stall (cf. Fairman (2002)). LES of the flow over airfoils has got less attention, as compared with the ABL and wind turbine wake studies, due to the presence of solid walls and rather complex geometries which demands excessive computational power. Yet in the past few years, the studies have proved the capability of LES for airfoil simulations (cf. Mellen et al. (2003)). Recently, a study was performed with the aim of investigating potential of LES in predicting the airfoil characteristics at high Reynolds numbers Davidson (2003). The study included simulations of a $Re = 2 \times 10^6$ flow around an Aerospatiale A-airfoil at an angle of attack $\alpha = 13.3^o$. Different aspects of the simulations were investigated such as the effects of the mesh resolution, size of the computational domain, SGS modeling, near-wall treatment, and transition prediction and it was concluded that the mesh resolution and the span length have a significant impact on predicting an accurate flow. For the similar case, Mary and Sagaut (2002) implemented a local mesh-refinement strategy to save computational time, and used the selective mixed-SGS model of Lenormand et al. (2000) for the computations. They performed simulations using a high resolution mesh which limited them to simulate only a very narrow span width of $s/c = 0.023$ (with s and c being span and chord, respectively). Therefore, they were not able to predict the 3D effects of the flow over the airfoil. Eisenbach and Friedrich (2008) conducted LES of a NACA 4415 profile placed between two flat plates at $\alpha = 18^o$ using the dynamic Smagorinsky model and an immersed boundary method for treatment of the wall. Uranga et al. (2009) performed LES of the flow over a Selig-Donovan SD7003 airfoil for a range of Reynolds numbers between 10,000 and 60,000 at $\alpha = 4^o$, resulting

[1] The SGS models are described in more detail in chapter 2.

in generation of laminar and fullt turbulent flows over the airfoil, respectively. For the computations, they used a high-order discontinuous Galerkin method employing an implicit LES approach, in which effect of the SGS model is applied through the numerical dissipation of the discretization schemes. Their simulations were able to capture an attached flow at low Reynolds numbers and a transient regime, caused by the Tollmien-Schlichting (T-S) waves, followed by the separation at higher Reynolds numbers and close to the trailing edge. Likewise, Zhou and Wang (2010) used an implicit model to simulate the flow over the same airfoil (SD7003) using a high-order spectral difference method. The SD7003 airfoil was chosen in all cases because of the availability of the experimental data (Selig, 2003).

Recent investigations of the airfoil flow is reported by Venugopal et al. (2012) who performed an LES of a DU96 airfoil at the near-stall angle of attack at $Re = 1.5 \times 10^6$. Using a case with low mesh resolution and another set of high mesh resolution cases, they found improvements in the flow predictions by increasing the spanwise resolution.

1.3 Numerical modeling

1.3.1 Parametrizing wind turbines

Direct simulation of turbine blades using LES requires very fine computational cells close to the solid boundaries (Rethore et al., 2008). To save computational power and still have acceptable accuracy, the wind turbines can be represented by body forces following two common models referred to as the *Actuator Line* (AL) and the *Actuator Disc* (AD). In the AL model (Sørensen and Shen, 2002), the flow is simulated by solving the discretized Navier-Stokes equations and instead of modeling the full rotor geometry, the turbine blades are represented by body forces. The body forced are distributed radially along the rotating lines, that act upon the incoming flow. The forces are obtained using

$$\mathbf{f} = (f_L, f_D) = 0.5\rho V_{rel}^2 c(C_L \mathbf{e}_L + C_D \mathbf{e}_D), \tag{1.1}$$

where V_{rel} is the relative velocity, C_L and C_D are lift and drag coefficients, $\mathbf{e}_L$ and $\mathbf{e_D}$ are unit vectors pointing towards direction of the (local) lift (f_L) and drag (f_D) forces and c is the airfoil sections chord length. The forces are commonly smeared out by Gaussian regularization function to avoid numerical oscillations (see figure 1.4 (left)). This is done by taking the convolution of the computed load $\mathbf{f}$ and the regularization

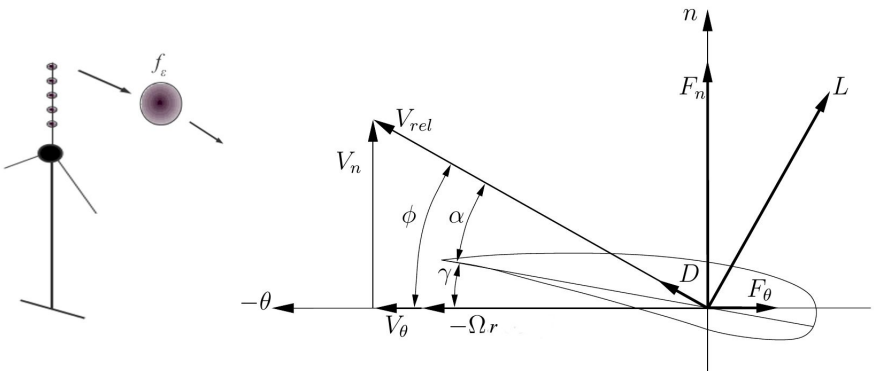

Figure 1.4: Actuator line (AL) concept and velocity triangle used to compute the angle of attack. The circles in the left figure show how the force is smeared out around the center point and applied to the flow field.

kernel η_ϵ,

$$\mathbf{f}_\epsilon = \mathbf{f} \otimes \eta\,, \qquad \eta_\epsilon(d) = \epsilon^{-3}\pi^{-3/2} \exp\left[- \left(\frac{d}{\epsilon}\right)^2 \right], \tag{1.2}$$

where d is the distance between cell centred grid points and points of the actuator line. Here, ϵ is the smearing parameter that serves to adjust the distribution width of the regularized load. The smeared forces are then sampled into the CFD mesh points, as shown in figure 1.5.

The actuator line technique is an appropriate method to obtain the fully resolved wake compared to a full CFD simulation as there is no need for simulating the actual geometry of the blades. However, the accuracy of the numerical computations depends on the quality of the tabulated airfoil data. For simulations where a large number of turbines are being simulated or where a simpler representation of the rotor loading is sufficient, the AD representation of the turbines is used. The AD concept was first combined with the Navier-Stokes equations and used in a CFD model by Sørensen and Myken (1992). The concept of the AD technique is similar to that of the AL yet the lift and drag forces are integrated over a circular rotor disk as opposed to rotating lines.

1.3.2 Applying a Prescribed Mean Shear (PMS) to the flow field

Simulation of the ABL in a complex terrain or in a wind farm, usually requires a precursor simulation to generate a realistic turbulent flow and a successor simulation which reads the input unsteady velocity from the pre-generated turbulent flow and includes the desired geometry such as wind turbines or any terrain complexities. The precursor

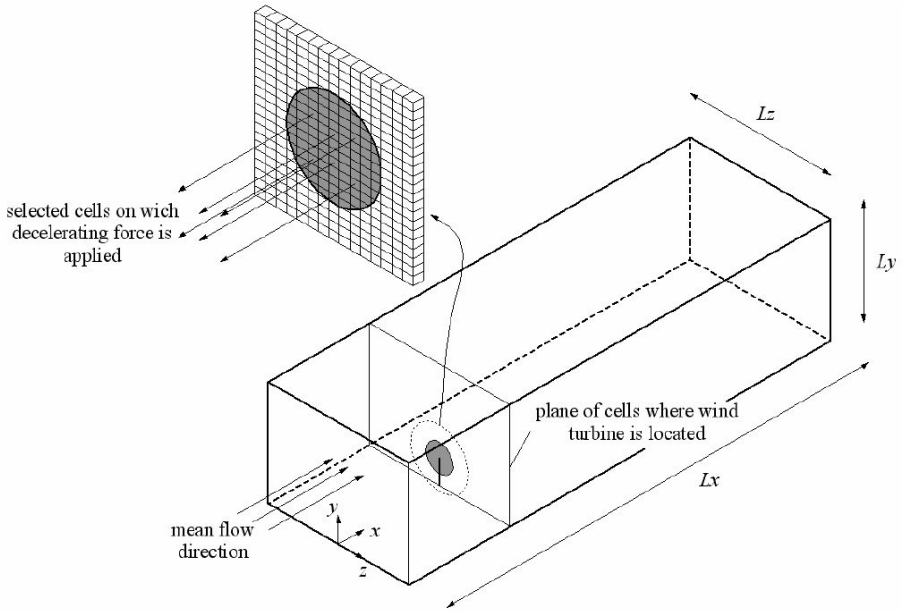

Figure 1.5: Implementation of actuator forces into the computational domain. Reproduced from Jimenez et al. (2007).

simulation is computationally demanding. Several wind turbine wake studies in the wind farm have been performed using the precursor/successor approach (Calaf et al., 2010; Lu and Porté-Agel, 2011). As opposed to the precursor-successor simulations and in order to save computational time and mesh points in the boundary layer, a method has been practised here that enforces a prescribed boundary layer profile into the computational domain using body forces similar to an immersed boundary method. The body forces are obtained initially and stored and later applied to the computational domain throughout the whole simulation domain at each time step. The body forces calculated from the PMS approach are usually of 1-2 orders of magnitude smaller than the physical forces appearing in the simulations such as the turbine forces and buoyancy effects (Sarlak et al., 2012; Troldborg et al., 2007), allowing the boundary layer yet to be modified due to the interaction of the turbine wakes and buoyancy contributions. The procedure for applying any desired body force to the flow field is as follows:

The discretized Navier-Stokes equation on the particular node, P, reads

$$A_p V_p^{t+\Delta t} + \sum_i A_i V_i^{t+\Delta t} = S_p + f_{PMS}, \tag{1.3}$$

where the summation is performed over the neighbouring nodes to P, denoted by i. V is velocity vector, S_p is the body force applied as a source term and $f_{PMS} = f(x, y, x)$ is an external body force which sets a desired velocity field U_d in the computational cell P through the following equation,

$$f_{PMS} = A_p U_d^{t+\Delta t} + \sum_i A_i V_i^{t+\Delta t} - S_p. \tag{1.4}$$

1.3.3 Adding resolved atmospheric turbulence

Operating wind turbines are exposed to the ABL, turbulence and perhaps the influence of wakes from upstream turbines. When simulating wind turbines using actuator techniques, on the other hand, the body forces are directly excreted on the flow domain without resolving the blades boundary layer. As a result, no shear generated instability (hence transition and turbulence) occurs and the tip vortices can be convected far downstream without breaking down. To avoid this non-physical behaviour, some perturbations are needed to trigger instabilities for the tip vortices Troldborg et al. (2007).

Resolved turbulence may be added to the CFD flow field using additional forces scaled in order to archive a desired level of turbulence. In this approach, a given synthetically generated, three-dimensional, frozen turbulence is first generated, and later, sequentially superimposed to the flow field by introducing equivalent body forces, similar to an actuator disk and the previously mentioned PMS approach.

In this thesis, where needed, a box *turbulent box* is first generated by the method of Mann (1998). When used to generate isotropic turbulence fields, the Mann's turbulent box gives divergence free velocity fields with auto-correlation and cross-correlation matching the theoretical correlation functions by Von Karman Von Karman (1948) as shown by Gilling (2009). The velocities are then extracted at different sections of the box assuming Taylor's frozen hypothesis and the corresponding body forces are applied, unsteadily, to the domain in a similar manner as the PMS method. Figure 1.6 shows a sample introduction of a plane of turbulence for the wind turbine wake simulations.

1.3.4 CFD solver

For all of the cases discussed in this thesis, the block structured, general purpose flow solver, EllipSys3D, (Michelsen, 1992; Sørensen, 1995) is used as the base and a number of modifications have been made depending on the desired needs. In EllipSys3D, the in-

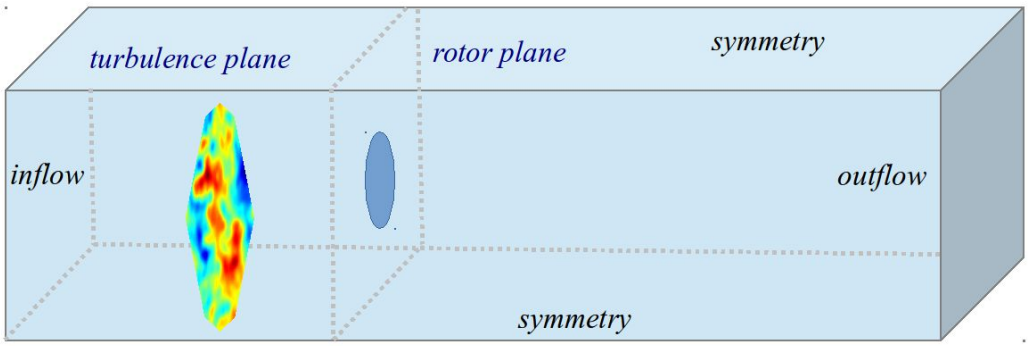

Figure 1.6: Introduction of synthetic turbulence upstream a rotor plane in a typical numerical set up.

compressible NS equations are discretized using the conservative Finite Volume Method (FVM) for the primitive variables (velocity and pressure). Discretization of diffusive terms is handled by 2^{nd} order central difference schemes (CD) and for the convective terms, a blend of CD (2^{nd} or 4^{th} order) and an upwind scheme, such as QUICK, is used for the purpose of numerical stability and accuracy, where most of the weight (usually $\geq 90\%$) is put on the CD. Time is discretized using a second order backward Euler scheme and the solution is marched in time implicitely using inner time stepping where the number of each pseudo time step can be either specified or remain as a function of the residuals. Pressure checkerboarding is prevented by using Rhie and Chow (1983) interpolation on a collocated grid arrangement and the pressure correction equation is solved using the PISO algorithm. Using the coordinate directions (x_i, x_j, x_k), the following set of convective Navier-Stokes and energy equations can be introduced in the most general form as:

$$\begin{aligned}
\frac{\partial \bar{u}_i}{\partial x_i} &= 0, \\
\frac{\partial \bar{u}_i}{\partial t} + \bar{u}_j \frac{\partial \bar{u}_i}{\partial x_j} &= -\frac{1}{\rho}\frac{\partial \bar{p}^*}{\partial x_i} - \frac{\partial \tau_{ij}}{\partial x_j} + \nu \frac{\partial^2 \bar{u}_i}{\partial x_j^2}, \\
&\quad + \delta_{i3} g \frac{\bar{\theta} - \langle \bar{\theta} \rangle}{\theta_0} + f_c \epsilon_{ij3} \bar{u}_i - \frac{f_i}{\rho} + F_i, \\
\frac{\partial \bar{\theta}}{\partial t} + \bar{u}_j \frac{\partial \bar{\theta}}{\partial x_j} &= -\frac{\partial q_j}{\partial x_j} + \alpha \frac{\partial^2 \bar{\theta}}{\partial x_j^2},
\end{aligned}$$

where the filtering operator, denoted by an over-bar, and the variables τ and q imply the LES nature of the equations. $\bar{u}_i$ is the velocity vector, ρ is the density of air, ν is the kinematic viscosity, $\bar{p}^* = \bar{p} + \rho \bar{u}_i \bar{u}_i / 2$ is the modified pressure, $\tau_{ij} = \overline{u_i u_j} - \bar{u}_i \bar{u}_j$ and

$q_j = \overline{u_j\theta} - \bar{u_j}\bar{\theta}$ are the SGS stress tensor and SGS heat flux respectively, and f_c, f_i, F_i are the Coriolis parameter, wind turbine loading, and external forcing such as wind force, respectively. Boussinesq approximation is used for the velocity-temperature coupling, implying that density difference throughout the computational domain is sufficiently small to be neglected, except in the terms multiplied by the gravitational acceleration. $\bar{\theta}$ is the potential temperature (the temperature that the parcel of fluid at pressure p would acquire if adiabatically brought to a standard reference pressure of usually 1 bar.) and α is the air thermal diffusivity. Different methods can be used to evaluate the above SGS terms as discussed in more detail in chapter 2.

1.4 Thesis overview

The objective of this thesis is to extend the previous knowledge in the large eddy simulation of turbulent flows in the wind turbine aerodynamics and the atmospheric boundary layer with the goal of providing better understanding of the role of the SGS modeling in different wind energy applications. The LES technique and its capabilities and limitations are discussed in chapter 2, while the next chapters cover the diverse applications of the LES methodology: Chapter 3 investigates the fully developed boundary layer flows. Simulations of wall-resolved channel flows with and without heat transfer from the walls are carried out with the aim of code validation and also to provide a basis for discussion about the SGS models. Simulation of the fully developed neutral ABL is also examined in chapter 3. Furthermore, the commonly used wall-modeled LES and the PMS methods are compared for the LES of an infinite wind farm using actuator disc parametrization. Chapter 4 presents measurements of the 2D NREL S826 airfoil at DTU's low speed wind tunnel. The study is followed by LES computations of the same airfoil using a numerical wind tunnel and comparison of pressure distributions as well as lift and drag coefficients with the measurements. The obtained airfoil data are corrected for the tunnel effects and used in chapter 5, where the actuator line modeling of wind turbines is performed for a two-rotor arrangement to investigate the wake-interactions. A detailed study is performed in this chapter in order to examine numerical parameters (with an emphasis on quantification of SGS modeling effects) as well as turbine operational conditions (different turbine configurations and tip speed ratios) affecting the wake structures and wind turbine loadings.

The benchmark data from airfoil measurement campaign are provided as an Appendix.

Chapter 2

Large eddy simulation (LES)

Turbulent flows are highly irregular, diffusive, and rotational. They contain a continuous range of scales, called eddies. Eddies can be defined as coherent patterns of velocity, vorticity and pressure fields. For a numerical simulation to be of highest accuracy, all scales of motion should be resolved accurately meaning that the flow domain should be large enough to allow large motions and at the same time, the computational grid needs to be small enough to capture the small dissipative scales of motion. Computations that comply with such restrictions are known as a Direct Numerical Simulation (DNS). The total number of grid points N required to perform a DNS scales with $N^3 = \mathcal{O}(\mathrm{Re}^{9/4})$ and the number of floating-point operations required to solve the flow grows as Re^3 cf. Piomelli et al. (2003). While DNS is the most accurate simulation method for the turbulent flows, it is impossible to apply to many industrial flows because of the data storage and computational resource limitations. For example, for the wind turbines in the atmospheric boundary layer, the largest scales of motion are of the order of a several hundred meters while the boundary layer formed around the blades is of the order of milimeters. Typically, atmospheric boundary layer flows have a characteristic Reynolds number of $\mathcal{O}(10^{8-9})$, requiring about 10^{18} mesh points to perform a total floating point operations of $\mathcal{O}(10^{24-27})$. DNS is therefore mostly used for validation purposes and for flows at low Reynolds numbers.

One of the most practical ways of solving a turbulent flow field with high Reynolds number and complex geometry is called Reynolds-Averaged Navier-Stokes (RANS) method. The RANS simulations can be performed in a short time as they are obtained from time-averaging of the Navier-Stokes equations. Although RANS models offer certain advantages such as (almost) Reynolds number independence to the used computational grid, they are not accurate for the cases with strong unsteadiness (as

it opposes the concept of RANS being derived from the *time-averaged* equations), nor are they ideal where high resolution of the flow (that is, representation of small scales) is needed [1]. Particularly, RANS models are too diffusive for wind energy applications (Sanderse, 2009).

As a compromise between the quality of a DNS and the computational flexibility of RANS, Large Eddy Simulation (LES) seems to be a reliable CFD tool for the future, although it is still in its early stages of development, particularly for industrial flows. LES equations are derived by decomposing the flow field to large *resolvable* scales and the smaller, dissipative *sub-grid* scales (SGS). The small scales which are more universal are modeled using a SGS model. [2] This chapter presents the LES methodology in connection with the computing incompressible Navier-Stokes solver and investigates their evaluation criteria.

2.1 Introduction

A common way to study turbulence is by looking at the energy (or power) content of a range of motion scales as a function of size (wave length) or spinning frequency of the so called *eddies*. The larger structures contain considerably higher energy than the small structures, therefore, to be able to see the energy at all of the scales in one plot, the *energy spectrum* is commonly plotted in Logarithmic scale. Figure 2.1 shows the typical the energy spectrum in frequency domain. As can be seen, DNS (URANS[3]) tends to simulate (model) all ranges of (all except very large) scales while in the LES technique, only a small fraction of scales are modeled and the rest of dynamically important and energetic scales are naturally resolved.

[1] The unsteady version of RANS (URANS) can also be used by including the time derivative in the governing equations, but even URANS suffers from low temporal resolution.

[2] In this case, since the integral scales scale smoothly with the Reynolds number, the computational cost can be kept nearly independent of the Reynolds number and the total cost of simulation can be scaled down to as low as $\mathcal{O}(Re^{0.6})$.

[3] The unsteady version of RANS which is derived by including the time derivative in the governing equations.

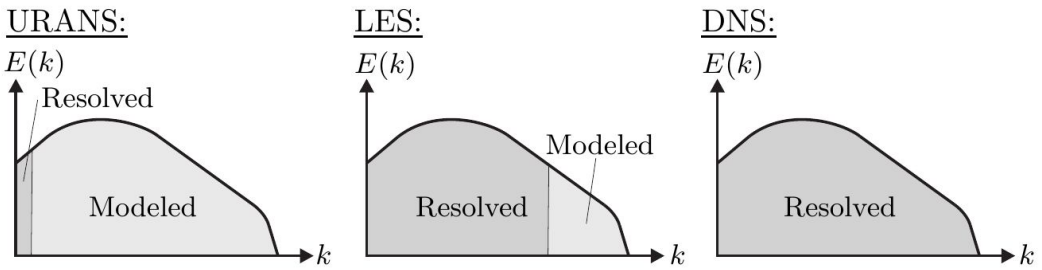

Figure 2.1: A general picture of turbulent energy spectrum. Sketch taken from Gilling (2009).

2.2 Filtered Navier-Stokes Equations

Modeling the *sub-filter* (SFS) or *sub-grid* scales (SGS)[1] of motion requires decomposing the small scales from the bulk flow using the low pass filters

$$u_i = \bar{u}_i + u_i', \tag{2.1}$$

where $\bar{u}_i$ is the resolvable part and u_i' is the sub-filter part. Considering the incompressible Navier-Stokes equations and decomposing each variable to its filtered and sub-filter components results in

$$\frac{\partial \bar{u}_i}{\partial t} + \bar{u}_j \frac{\partial \bar{u}_i}{\partial x_j} = -\frac{1}{\rho}\frac{\partial \bar{p}}{\partial x_i} + \frac{\partial}{\partial x_j}\left(\nu \frac{\partial \bar{u}_i}{\partial x_j}\right) + \frac{1}{\rho}\frac{\partial \tau_{ij}}{\partial x_j}, \tag{2.2}$$

where $\tau_{ij} = \overline{u_i u_j} - \bar{u}_i \bar{u}_j$ is the sub-grid scale stress tensor.

Analytical explicit filtering can be performed by taking convolution[2] of a function with a filtering kernel G:

$$\bar{\Phi}_i(\vec{x}) = \int G(\vec{x} - \vec{\tau})\Phi(\vec{\tau})d\vec{\tau}, \tag{2.3}$$

The effect of convolution filtering can be visually seen in figure 2.2. The horizontal axis can be defined as either time or space. Considering it as the time, the convolution formula acts as a weighted average of the function $\Phi(\tau)$ at the moment t where the weighting kernel, shifted by amount t,is given by $G(t-\tau)$. As t changes, the weighting function emphasizes different parts of the input function, which results in the filtered

[1] SFS refer to the scales that are filtered out using an explicit (formal) filter. However, both *sub-grid* and *sub-filter* terms can be used interchangeably when the grid is used as an implicit low-pass filter.

[2] Convolution is defined as the integral of the product of the two functions after one is reversed and shifted.

variable shown in the upper left green boxes in the figures.

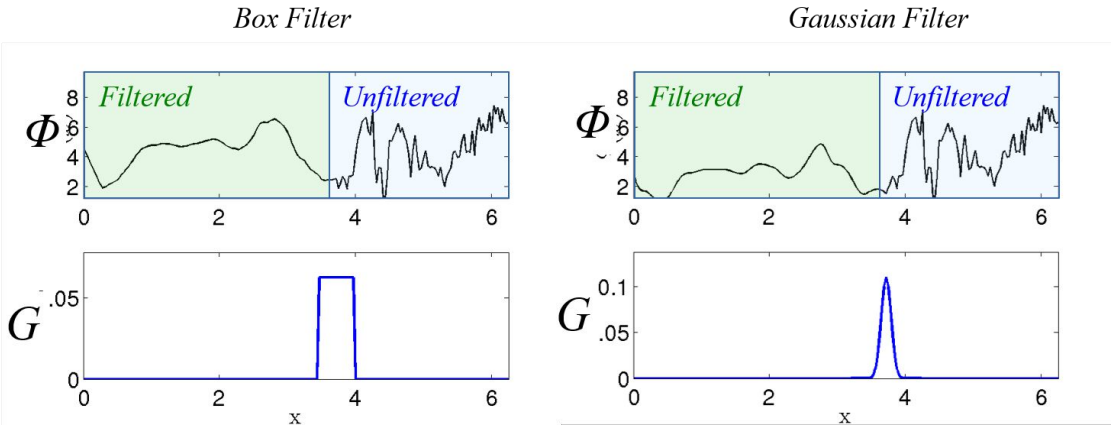

Figure 2.2: The visual effects of two common filtering processes on the original signal. The filtered values of the signal Φ are obtained by the convolution of the filtering kernels G (bottom) and the variable itself.

In general an LES filter is required to have the following features:

- Linearity $\overline{\phi + \psi} = \bar{\phi} + \bar{\psi}$.
- Ability to keep a constant unchanged $\overline{a\phi} = a\bar{\phi}$.
- Commutation between filtering and differentiation $\frac{\overline{\partial \phi}}{\partial x} = \frac{\partial \bar{\phi}}{\partial x}$ to ensure that the filtered Navier-Stokes equations have the same structure as the unfiltered equations. The difference $\frac{\overline{\partial \phi}}{\partial x} - \frac{\partial \bar{\phi}}{\partial x}$ is termed "commutation error". [1]
- Being positive definite (in real space) to ensure that quantities like the SGS kinetic energy $k = 0.5(\overline{u_i u_i} - \bar{u}_i \bar{u}_i)$ and the SGS heat flux remain positive after filtering (Benhamadouche, 2006).

[1] It is shown that the commutation error is a function of the filter width and that if non-uniform grids is being used, the filter width will also change and there will always be commutation error. However, a set of rules for minimizing the commutation error by modifying the weighting functions of the filtering operators was proposed by Vasilyev et al. (1998). An example of such filtering function for an arbitrary variable ϕ with a 5-stencil cell reads:

$$\bar{\phi} = -\frac{1}{32}\phi_{i-3} + \frac{9}{32}\phi_{i-1} + \frac{1}{2}\phi_i + \frac{9}{32}\phi_{i+1} - \frac{1}{32}\phi_{i+3}. \tag{2.4}$$

- Being easy to implement. For example, the spectral cut-off filter is very easy to implement in a spectral code as one just needs to remove all the frequencies higher than a threshold.
- Similarity between the LES filter and the test filter, when dynamic mixed models are used.

Three common filter kernels frequently used in LES are the box, Gaussian and the sharp spectral cut-off filters. The filter shapes are shown in figure 2.3 and definitions of the filters are explained below (for more details, see Pope (2000)).

- **Top hat (Box) filter:**

  The top hat filter is commonly used in finite difference and implicit finite volume methods (where grid length equals filter width). The filter kernel in physical space and its transfer function in Fourier space are given respectively by:

  $$G(\boldsymbol{x}-\boldsymbol{r}) = \begin{cases} \frac{1}{\Delta}, & \text{if } |\boldsymbol{x}-\boldsymbol{r}| \leq \frac{\Delta}{2}, \\ 0, & \text{otherwise.} \end{cases}$$

  and

  $\hat{G}(\boldsymbol{k}) = \frac{\sin\left(\frac{1}{2}k\Delta\right)}{\frac{1}{2}k\Delta}$.

- **Gaussian filter:**

  Gaussian filters are very common in LES. The Gaussian filter kernel in physical and Fourier spaces are given by:

  $G(\boldsymbol{x}-\boldsymbol{r}) = \left(\frac{6}{\pi\Delta^2}\right)^{\frac{1}{2}} \exp\left(-\frac{6(\boldsymbol{x}-\boldsymbol{r})^2}{\Delta^2}\right)$,

  and

  $\hat{G}(\boldsymbol{k}) = \exp\left(-\frac{\boldsymbol{k}^2\Delta^2}{24}\right)$.

- **Sharp spectral filter:**
  Sharp spectral filter is defined in physical and Fourier spaces as :

  $G(\boldsymbol{x}-\boldsymbol{r}) = \frac{\sin\left(\pi(\boldsymbol{x}-\boldsymbol{r})/\Delta\right)}{\pi(\boldsymbol{x}-\boldsymbol{r})}$,

  and

  $\hat{G}(\boldsymbol{k}) = H\left(k-k_c\right), \qquad k_c = \frac{\pi}{\Delta}$.

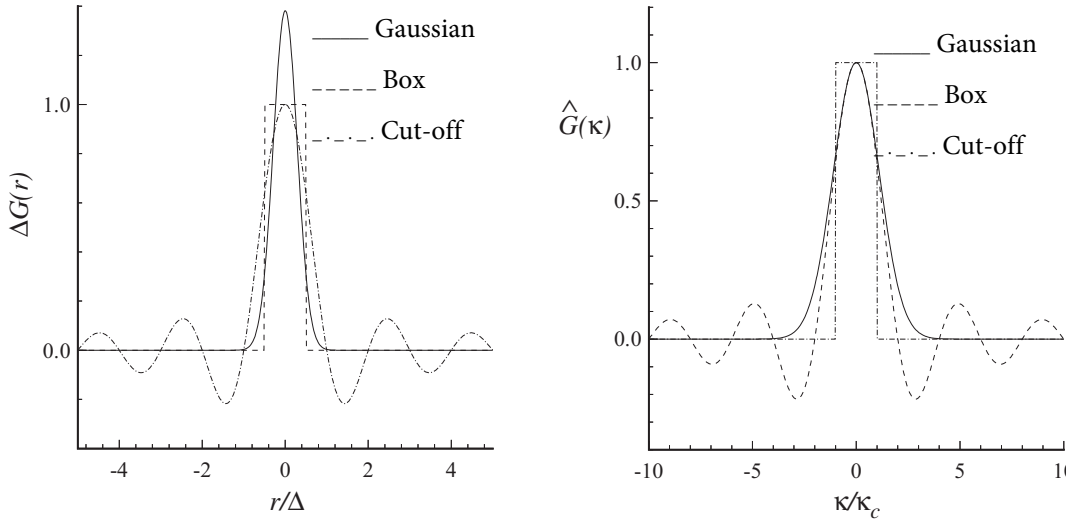

Figure 2.3: Filter shapes in physical space (left) and their transfer function (Fourier spaces) (right). The abscissa shows the filter width. Reproduced from Pope (2000).

When applied to a fluctuating field such as velocity, each filter represents a different behaviour. Figure 2.4 shows the effects of the cut-off, box and Gaussian filters using two different filter widths $K1$ and $K2$ on data obtained from a DNS of rotating turbulence by Lu et al. (2007) where $K1$ and $K2$ refer to filtering by using stencils of 16 and 32 points (of the DNS data), respectively. The area, in the right side of the figure, between the DNS spectrum and the filtered spectra shows the amount of attenuated sub-filter scale (SFS) energy. As can be seen, the sharp cut-off filter removes all of the scales smaller than the filter cut-off width, thus termed an "ideal filter" as noted by JL. (1958), and the obtained spectrum for lower wave numbers is identical to the DNS spectrum down to the cut-off level. Therefore, no SFS energy will be captured if sharp cut-off filter is applied. The box and Gaussian filters on the other hand, remove the energy from a wide range of wave numbers centered around the cutt-off value, therefore, even at the wave numbers higher than the filter width, some energy remains in the flow (also, note the energy build-up at frequencies higher than the cut-off length, obtained by a box filter).

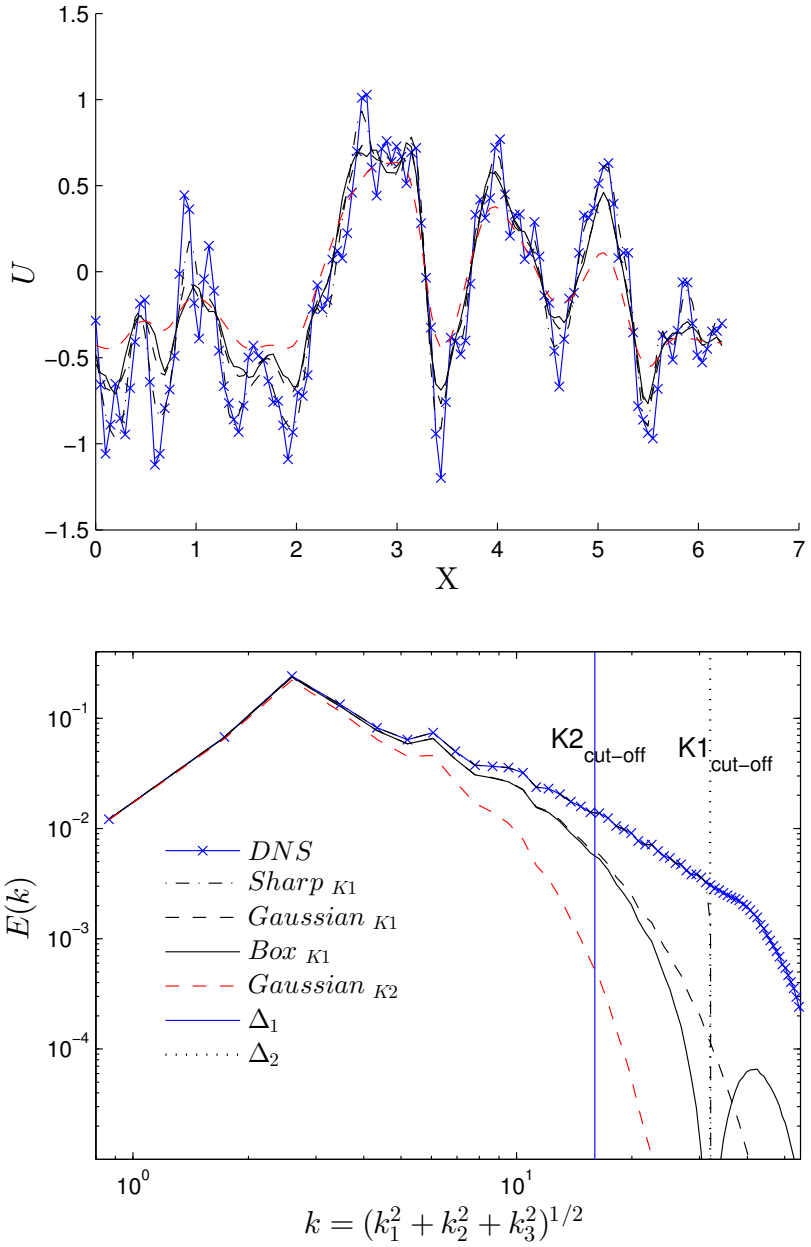

Figure 2.4: Effect of filtering in a fluctuating signal (top) and its energy spectrum (bottom) using sharp cut-off, Gaussian, and box filters. Original DNS data taken from Lu et al. (2007).

2.3 Sub-Grid Scale (SGS) modeling

In order to solve equation 2.2, the term τ_{ij} must be known a-priori. Different methods are used in the literature for calculating the τ_{ij} term. A common approach is to use the eddy viscosity assumption, which postulates a linear relation between the SGS shear stress and the strain rate tensor for the resolved scales. This sections presents different methodologies for solving for τ_{ij} (or equivalently the eddy viscosity ν_{SGS}).

$$\tau_{ij} - \frac{1}{3}\tau_{kk}\delta_{ij} = -2\mu_t \bar{S}_{ij} \text{ with } \bar{S}_{ij} = \frac{1}{2}\left(\frac{\partial \bar{u}_i}{\partial x_j} + \frac{\partial \bar{u}_j}{\partial x_i}\right), \tag{2.5}$$

where $\bar{S}_{ij}$ is the rate-of-strain tensor for the resolved scales.

2.3.1 Smagorinsky model

The oldest yet the most common SGS models is the Smagorinsky model, named after Smagorinsky (1963). This eddy viscosity model is based on the assumption of equilibrium between energy production and dissipation at the small scales and reads

$$\nu_{SGS} = (C_s\Delta)^2\sqrt{2\bar{S}_{ij}\bar{S}_{ij}} = (C_s\Delta)^2\,|S|\,, \tag{2.6}$$

where Δ is the grid size and C_s is the Smagorinsky constant. The constant needs to be adjusted for different flows but in many cases it takes a value between 0.1-0.2. The Smagorinsky model was first used in Deardorff (1970) for turbulent channel flow simulation. The classical Smagorinsky model has some major drawback. In wall-bounded flows, the eddy viscosity should drop asymptotically to zero because of viscous flow domination close to the wall hence laminarization of the flow. The Smagorinsky model on the other hand, always results in a positive eddy viscosity due to a non-zero coefficient and presence of the velocity gradients. This non-physical value makes Smagorinsky model over-dissipative in these cases. Inability to accommodate the physical phenomena known as *backscatter*[1] is another issue as the eddy viscosity cannot take a negative value in Smagorinsky model. Moreover, experiments have shown that the Smagorinsky coefficient is not always constant and changes for different flow applications.

[1] Regeneration of larger scales due to the interaction of subgrid scales which, in mathematical sense, requires a negative eddy viscosity to happen.

2.3.2 Family of dynamic Smagorinsky models

To cope with the shortcomings associated with the standard Smagorinsky model, Germano et al. (1991) proposed a significant modification by calculating the C_s in a dynamic manner. Utilizing the computational grid as the original implicit filter and an extra *test filter*, larger than the original filter, they defined the Germano identity as,

$$\mathcal{L}_{ij} = T^r_{ij} - \widetilde{\tau}^r_{ij} = \widetilde{\overline{u_i}\overline{u_j}} - \widetilde{\overline{u}}_i\widetilde{\overline{u}}_j. \tag{2.7}$$

In the above equation, $T^r_{ij} = \widetilde{\overline{u_i u_j}} - \widetilde{\overline{u}}_i\widetilde{\overline{u}}_j$ is the residual stress tensor for the test filter scale, and $\widetilde{\tau}^r_{ij} = \widetilde{\overline{u_i u_j}} - \widetilde{\overline{u}_i\overline{u}_j}$ is the test-filtered residual stress tensor for the grid filter. The resolved turbulent stress tensor $\mathcal{L}_{ij}$ represents the contribution to the SGS stresses by length scales smaller than the test filter width $\tilde{\Delta}$ and larger than the grid filter width $\overline{\Delta}$. As can be noticed, using the Germano identity lifts the dependency of the residual stresses to the unknown SGS terms, $\overline{u_i u_j}$, hence $\mathcal{L}_{ij}$ becomes only a function of resolved velocities. Figure 2.5 shows the T_{ij}, τ_{ij}, $\mathcal{L}_{ij}$ and the filters used for the derivation of the dynamic Smagorinsky model. The above equation may be re-arranged to

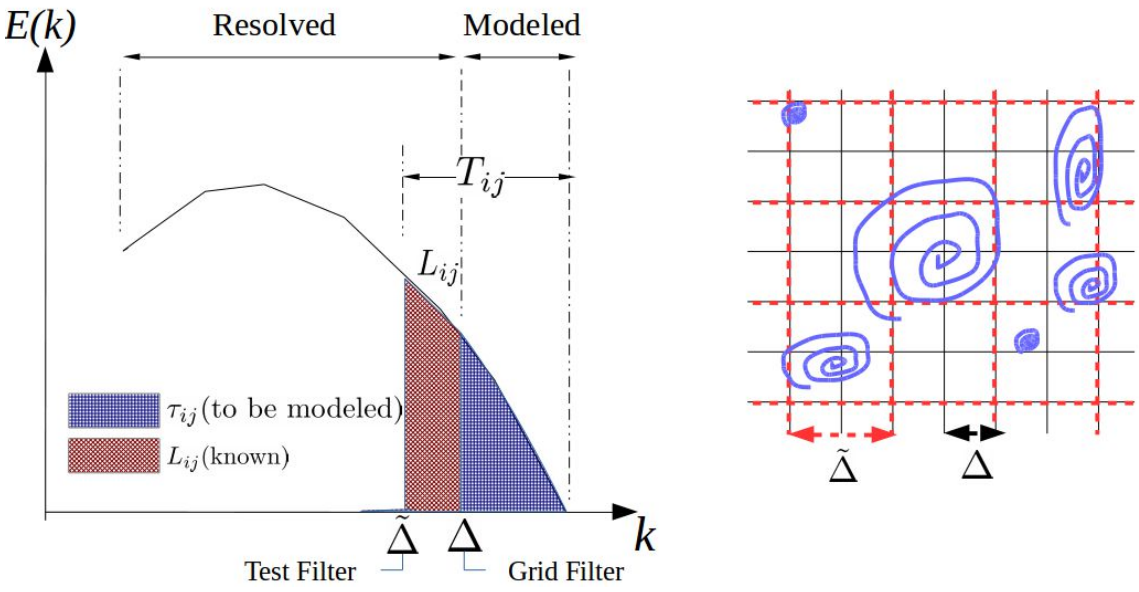

Figure 2.5: Representation of the eddies as well as grid filter (Δ) and test-filter ($\widetilde{\Delta}$) (right). Extent of different terms appearing in the Germano identity derivation (left).

$$\mathcal{L}_{ij} = C_s^2 \mathcal{M}_{ij}, \tag{2.8}$$

where

$$\mathcal{M}_{ij} = 2\overline{\Delta}^2 \left(\widetilde{|\bar{S}|\,\bar{S}_{ij}} - \beta^2 \left|\widetilde{\bar{S}}\right| \widetilde{\bar{S}}_{ij} \right), \quad \beta = \widetilde{\Delta}/\overline{\Delta}, \tag{2.9}$$

and the goal is to find the coefficient that satisfies the Germano identity locally at each time step,

$$C_s^2 = \frac{\mathcal{L}_{ij}\mathcal{M}_{ij}}{\mathcal{M}_{ij}\mathcal{M}_{ij}}. \tag{2.10}$$

This procedure can be numerically unstable if the numerator becomes negative and in this case, large fluctuations in C_s will appear. Hence, an additional averaging of the error in the minimization may be employed to make the dynamic model more stable and robust Lilly (1992):

$$C_s^2 = \frac{\langle \mathcal{L}_{ij}\mathcal{M}_{ij} \rangle}{\langle \mathcal{M}_{ij}\mathcal{M}_{ij} \rangle}. \tag{2.11}$$

The averaging should in principle be done along the directions of statistical homogeneity (for example, volume for homogeneous turbulence and horizontal planes for channel flow). There are however many applications for which no direction of homogeneity is preferred. To circumvent this constraint, a new model was proposed which takes the averaging in time following fluid path lines in a Lagrangian manner Meneveau et al. (1996). A further study by Meneveau and Katz (2000) revealed that the coefficient C_s is proportional the grid size (i.e., the C_s is not the same for the original domain and its filtered domain), contrary to the Germano's original assumptions. This was a foundation for a new family of *scale dependent* SGS models, where a *second* test filter is utilized to establish the scale similarity factor. Further information can be found in Bou-Zeid et al. (2005) and Porté-Agel (2000).

2.3.3 Scale-similarity models

The scale-similarity models were first developed by Bardina et al. (1980). They rely on the assumption that the energy transfer from unresolved scales is dominated by the largest SGS motions and is *similar* to the energy transfer from the *smallest resolved* scale to the next smaller resolved scale. Based on this idea, the SGS shear stress can be found by applying a test filter and deriving the following expression

$$\tau_{ij}^{sim} = C_{sim}\mathcal{L}_{ij}, \tag{2.12}$$

where $\mathcal{L}_{ij}$ is similarly defined as the equation 2.7 in the dynamic Smagorinsky model and C_{sim} is a model constant to be adjusted.

2.3.4 Mixed-scale models

Despite their physical foundation, the scale similarity models failed to estimate the correct turbulent dissipation (too small eddy viscosity) in many situations especially when it was used in non-dissipative numerical schemes. To cope with this limitation, Zang et al. (1993) added an eddy-viscosity term and derived the following so called mixed-scale model

$$\tau_{ij}^{mix} = \overline{\overline{u}_i\overline{u}_j} - \overline{\overline{u}}_i\overline{\overline{u}}_i \quad - \quad 2(C_s\Delta)^2|\overline{S}|\overline{S}_{ij}. \tag{2.13}$$

where the eddy viscosity terms are added to provide the model with an extra dissipation. Another type of mixed models was developed by Sagaut (1995) and Ta Phuoc (1994) in which the localized eddy viscosity can be expressed in its most general form as

$$\nu_{SGS}(\alpha, x, y, z, t) = c_m\Delta^{1+\alpha}k_{SGS}^{\frac{1-\alpha}{2}}(x, y, z, t)|\Gamma(\bar{u}(x, y, z, t))|^{\alpha}. \tag{2.14}$$

where $k_{SGS} = \mathcal{L}_{ii} = (\tilde{u}_i - u_i)^2$ is the scale similarity term, and $C_m = C_q^{1-\alpha}C_s^{2\alpha}$ with $C_q = 0.2$ and $C_q = 0.6$ have been used for the vorticity based and for the shear strain tensor based formulations, respectively (see e.g. Cavar (2006)). The model can be adjusted to take either the strain rate tensor or the vorticity $\Gamma(\bar{u}(x, y, z, t)) = \bar{S}_{ij}(x, y, z, t)$ or $\nabla \times \bar{u}(x, y, z, t)$ and $\alpha \in [0, 1]$ is the weighting average function. This model is based on *weighted geometric average* of the Smagorinsky model (using the resolved scales) and the turbulent kinetic energy model based on the sub-grid scales (scale similarity). As can be seen, the model transforms to the Smagorinsky model in case an $\alpha = 1$ is chosen. Similar to the other scale-similarity models, the ν_{SGS} does not require additional damping functions as it vanishes in fully resolved regions of the flow and at solid boundaries. Note that although categorised as a mixed-scale model, the model defined by equation 2.14 is still an eddy viscosity model, *scaled* up or down by a similarity term, k_{SGS}. Therefore, the model does not fundamentally follow the general definition of the mixed-scale models, in which an eddy viscosity term is *added* to the scale similarity model. Nevertheless, it is still called a mixed model in this thesis, due to its similarities to the common mixed scale models.

2.3.5 A new dynamic mixed SGS eddy viscosity model

Due to its simplicity and performance, the SGS model introduced in equation 2.14 had been implemented and used in the EllipSys3D code in recent years. One limitation of the model is dependence on the model constants for different applications. To eliminate the need for specifying the constant C_m, an attempt was made in this research to have a model that dynamically estimates the coefficient by applying the Germano identity. Introducing a second (test) filter (denoted by $\widehat{u}$ for the variable u for example), the following expression for the residual stress tensor for the test filter scale T_{ij} is obtained

$$T_{ij} = -2c_m|\widetilde{\overline{S}}|^{\alpha}\mathcal{L}_{ii}^{\frac{1-\alpha}{2}}\widetilde{\Delta}^{1+\alpha}\widetilde{\overline{S_{ij}}}, \tag{2.15}$$

where

$$\mathcal{L}_{ii} = K_{SFS} = (\widetilde{\overline{u_i}} - \widehat{\widetilde{\overline{u_i}}})(\widetilde{\overline{u_i}} - \widehat{\widetilde{\overline{u_i}}}) = \widehat{\widetilde{\overline{u_i}}\widetilde{\overline{u_i}}} - \widehat{\widetilde{\overline{u_i}}}\widehat{\widetilde{\overline{u_i}}}, \tag{2.16}$$

is the sub-filter scale turbulent kinetic energy calculated for the scales between the test and the grid filters. The 27-point stencil for the explicit filtering of variable ϕ on both the grid filter and the test filter have the same structure and reads

$$\begin{aligned}
\phi^{avg}_{i,j,k} = &\frac{1}{8}\phi_{i,j,k} + \frac{1}{16}\left(\phi_{i+1,j,k} + \phi_{i-1,j,k} + \phi_{i,j+1,k} + \phi_{i,j-1,k} + \phi_{i,j,k+1} + \phi_{i,j,k-1}\right) \\
&+\frac{1}{32}(\phi_{i-1,j-1,k} + \phi_{i-1,j+1,k} + \phi_{i+1,j-1,k} + \phi_{i+1,j+1,k} + \phi_{i-1,j,k-1} + \phi_{i-1,j,k+1} \\
&\quad + \phi_{i+1,j,k-1} + \phi_{i+1,j,k+1} + \phi_{i,j-1,k-1} + \phi_{i,j-1,k+1} + \phi_{i,j+1,k-1} + \phi_{i,j+1,k+1}) \\
&+\frac{1}{64}(\phi_{i-1,j-1,k-1} + \phi_{i-1,j-1,k+1} + \phi_{i-1,j+1,k-1} + \phi_{i+1,j-1,k-1} + \phi_{i-1,j+1,k+1} \\
&\quad + \phi_{i+1,j-1,k+1} + \phi_{i+1,j+1,k-1} + \phi_{i+1,j+1,k+1}).
\end{aligned} \tag{2.17}$$

Introducing the new (deviatoric) residual stress tensors into the Germano identity yields to,

$$\begin{aligned}
\mathcal{L}_{ij} &= T_{ij} - \widetilde{\tau_{ij}} \\
&= -2c_m\left[|\widetilde{\overline{S}}|^{\alpha}\mathcal{L}_{ii}^{\frac{1-\alpha}{2}}\widetilde{\Delta}^{1+\alpha}\widetilde{\overline{S_{ij}}} - |\overline{S}|^{\alpha}\mathcal{L}_{ii}^{\frac{1-\alpha}{2}}\Delta^{1+\alpha}\overline{S}_{ij}\right] \\
&= c_m\mathcal{M}^n_{ij},
\end{aligned} \tag{2.18}$$

where the terms in the square brackets are defined as the new tensor $\mathcal{M}^n_{ij}$. From this point, calculation of the dynamic coefficient is analogous to the standard dynamic

procedure:

$$C_m^2 = c_m = \frac{\left\langle \mathcal{L}_{ij}\mathcal{M}_{ij}^n \right\rangle}{\left\langle \mathcal{M}_{ij}^n\mathcal{M}_{ij}^n \right\rangle}. \tag{2.19}$$

The implementation of the new model is in practice very straightforward: The equation 2.9 in the standard dynamic Smagorinsky formulation should be replaced by,

$$\mathcal{M}_{ij}^n = 2\Delta^{1+\alpha}\left[\left(\widetilde{\mathcal{L}_{ii}^{\frac{1-\alpha}{2}}|\overline{S}|^\alpha \overline{S_{ij}}}\right) - \left(\beta^{1+\alpha}\mathcal{L}_{ii}^{\frac{1-\alpha}{2}}\widetilde{|\overline{S}|^\alpha}\,\widetilde{\overline{S_{ij}}}\right)\right]. \tag{2.20}$$

Evaluation of the Germano identity error

Traditionally a value of $\alpha = \frac{1}{2}$ has been employed as the scale similarity weighting function in equation 2.14 (see e.g. Cavar (2006); Mikkelsen et al. (2007)). Here, an analysis has been performed to investigate the effects of α on the Germano identity error with the aim of further optimizing the dynamic procedure. Plugging equations 2.14 and 2.15 in the identity $\mathcal{L}_{ij} = T_{ij} - \widetilde{\tau_{ij}}$, results in a *contraction* error of the form $e_{ij} = L_{ij}^D - (T_{ij}^D - \bar{\tau}_{ij}) = L_{ij}^D - c_m\mathcal{M}_{ij}$, where the superscript n is droped from the term $\mathcal{M}$ and the superscript D denotes the deviatoric parts of the stress tensors[1]. Substituting C_m from equation 2.19 and performing further mathematical work leads to

$$\begin{aligned}
\langle e_{ij}e_{ij}\rangle &= \langle(\mathcal{L}_{ij} - C_m^2\mathcal{M}_{ij})^2\rangle && (2.21)\\
&= \langle\mathcal{L}_{ij}^2\rangle - 2C_m^2\langle\mathcal{L}_{ij}\mathcal{M}_{ij}\rangle + (C_m^2)^2\langle\mathcal{M}_{ij}^2\rangle && (2.22)\\
&= \langle\mathcal{L}_{ij}^2\rangle - 2\left(\frac{\langle\mathcal{L}_{ij}\mathcal{M}_{ij}\rangle}{\langle\mathcal{M}_{ij}\mathcal{M}_{ij}\rangle}\right)\langle\mathcal{L}_{ij}\mathcal{M}_{ij}\rangle + \left(\frac{\langle\mathcal{L}_{ij}\mathcal{M}_{ij}\rangle}{\langle\mathcal{M}_{ij}\mathcal{M}_{ij}\rangle}\right)^2\mathcal{M}_{ij}^2; && (2.23)
\end{aligned}$$

which finally reduces to

$$\langle e_{ij}e_{ij}\rangle = \langle\mathcal{L}_{ij}^2\rangle - \frac{\langle\mathcal{L}_{ij}\mathcal{M}_{ij}(\alpha)\rangle^2}{\langle\mathcal{M}_{ij}(\alpha)^2\rangle}, \tag{2.24}$$

where $\mathcal{M}_{ij}$ is proportional to the parameter α, that is $\mathcal{M}_{ij} = \mathcal{M}_{ij}(\alpha)$. The contraction error can be minimized by analytically solving for $\frac{d\langle e_{ij}e_{ij}\rangle}{d\alpha} = 0$ and deriving an

[1]The stress tensor is usually decomposed into an *isotropic* or *hydrostatic* part and a *deviatoric* part. The deviatoric part of the resolved and SGS stresses are modeled and the isotropic parts (u_ju_j and τ_{kk}) are merged into the pressure term, making the *modified* pressure, $p^* = p + (1/3)\tau_{kk} + (1/2)u_ju_j$.

expression for α:

$$\begin{aligned}\frac{\partial\langle e_{ij}e_{ij}\rangle}{\partial\alpha} =& 2\left(\Delta^{\alpha+1}\,\mathcal{L}_{ii}^{\frac{1}{2}-\frac{\alpha}{2}}\,\bar{S}\,\bar{S}^{\alpha}-\widetilde{\Delta}^{\alpha+1}\,\mathcal{L}_{ii2d}^{\frac{1}{2}-\frac{\alpha}{2}}\,\widetilde{S}\widetilde{S}^{\alpha}\right)\\ &[\Delta^{\alpha+1}\,\mathcal{L}_{ii}^{\frac{1}{2}-\frac{\alpha}{2}}\,\bar{S}\,\bar{S}^{\alpha}\,\ln(\Delta)-\widetilde{\Delta}^{\alpha+1}\,\mathcal{L}_{ii2d}^{\frac{1}{2}-\frac{\alpha}{2}}\,\widetilde{S}\,\widetilde{S}^{\alpha}\,\ln\left(\widetilde{\Delta}\right)\\ &-\frac{\Delta^{\alpha+1}\,\mathcal{L}_{ii}^{\frac{1}{2}-\frac{\alpha}{2}}\,\bar{S}\,\bar{S}^{\alpha}\,\ln(\mathcal{L}_{\mathrm{ii}})}{2}+\frac{\widetilde{\Delta}^{\alpha+1}\,\mathcal{L}_{ii2d}^{\frac{1}{2}-\frac{\alpha}{2}}\,\widetilde{S}\,\widetilde{S}^{\alpha}\,\ln\mathcal{L}_{ii}^{2d}}{2}\\ &+\Delta^{\alpha+1}\,\mathcal{L}_{ii}^{\frac{1}{2}-\frac{\alpha}{2}}\,\bar{S}\,\bar{S}^{\alpha}\,\ln\left(\bar{S}\right)-\widetilde{\Delta}^{\alpha+1}\,\mathcal{L}_{ii2d}^{\frac{1}{2}-\frac{\alpha}{2}}\,\widetilde{S}\,\widetilde{S}^{\alpha}\,\ln\left(\widetilde{S}\right)].\end{aligned} \tag{2.25}$$

The above equation can be burdensome to solve and implement in a numerical procedure. Instead, a simpler two-step approach has been implemented in the current work: In the first step, an arbitrary value for α is chosen first and based on which, the optimal value for c_m is obtained by forming the Germano identity. In the second step, the calculated c_m value from the last time step is used and the optimal value for the coefficient α is calculated for the next iteration and this procedure continues. The second step uses different values of α between 0 and 1 (in ascending order) and chooses the one corresponding to the minimal error. This procedure has been applied to a fully developed channel flow case with periodic walls and plots of the contraction error as a function of α for different distances from the bottom wall are illustrated in figure 2.6. The channel has a length of π, a width of 2π and a height of 1 and is run at $Re_\tau = 395$ (see chapter 3 for the definition of the channel flow and details of the simulation set-up). As can be seen, the minimal errors are found by an α around 0.5 very close to the wall, but by increasing the height, the smaller α values lead to a minimal error. It is also clear that the error has a peak value at $y/H = 0.06$ which is reduced towards zero with increasing height. It should be noted that this procedure only investigates the Germano's contraction error behaviour as a function of α and cannot indicate the effect of α value on the quality of the SGS modeling.

2.3.6 SGS eddy diffusivity models

In combination with the heat equations, the SGS eddy dissusivity models are added to the flow solver to make more accurate predictions of temperature field and heat fluxes. As mentioned in section 1.3.4, filtering the energy equation results in the extra SGS

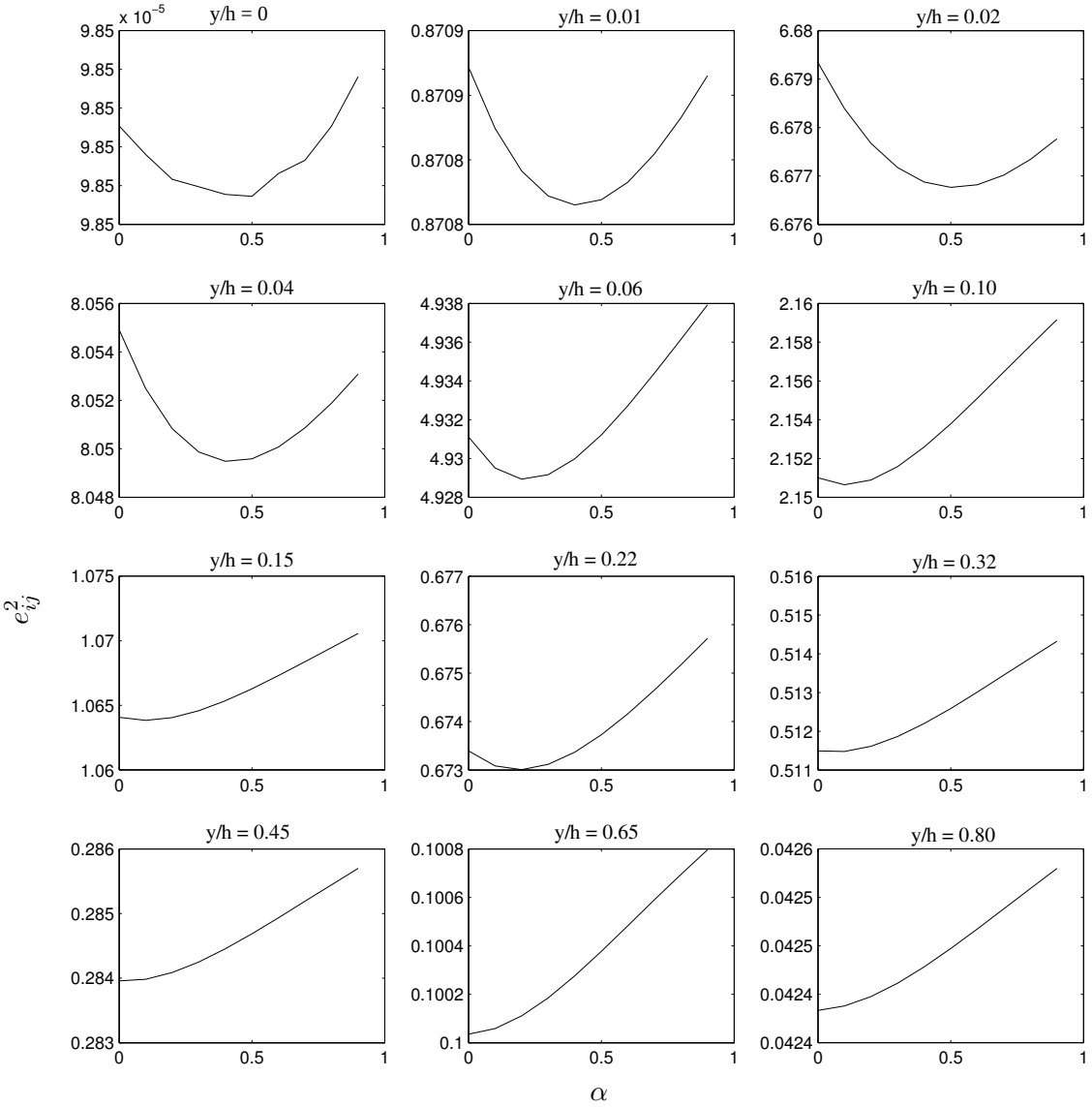

Figure 2.6: SGS modeling contraction error as a function of α for the dynamic mixed model LES of channel flow at different distances from the bottom wall.

heat diffusivity term q_j in

$$\frac{\partial \bar{\theta}}{\partial t} + \bar{u}_j \frac{\partial \bar{\theta}}{\partial x_j} = -\frac{\partial q_j}{\partial x_j} + \alpha \frac{\partial^2 \bar{\theta}}{\partial x_j^2}. \tag{2.26}$$

With analogy to the eddy viscosity concept, q_j can be defined as a function of the large-scale temperature gradient,

$$q_j = \overline{u_j \theta} - \bar{u}_j \bar{\theta} = -\alpha_{SGS} \frac{\partial \bar{\theta}}{\partial x_j}. \tag{2.27}$$

where θ is the temperature field defined at the cell center and $\alpha_{SGS} = \frac{\nu SGS}{Pr_{SGS}}$ is the SGS diffusivity and Pr_{SGS} is the SGS Prandtl number. Prandtl number controls the relative thickness of the thermal boundary layer to the momentum boundary layer. A small Pr indicates a much quicker heat diffusion in relation to the momentum diffusion and vice versa. The values of the Prandtl number have been established for isotropic homogeneous turbulence. However, it is shown by Basu et al. (2005) and Porté-Agel et al. (2011) that the Prandtl number changes rather significantly in stable, neutral and convective flow conditions. [1] Therefore, it is required to use SGS diffusivity models for finding the turbulent Prandtl number. By employing similar ideas to the eddy viscosity, several models have been derived and implemented to calculate the Pr_{SGS} (see Kleissl et al. (2006); Lu and Porté-Agel (2011)). The simplest model for Pr_{SGS} is obtained by Reynolds analogy which assumes a constant Prandtl number (usually $Pr_{SGS} = 1$) and calculates the SGS diffusivity $\alpha_{SGS} = \frac{\nu SGS}{Pr_{SGS}}$ which assumes that the subgrid scales of temperature depend only on the resolved velocity scales. This assumption does not hold for the convective flows, for example, where the flow is dominated by the large buoyant forces. Besides, the static procedures similar to the standard Smagorinsky need a prescribed thermal stability and shear damping function.

The procedure to find dynamic coefficient was implemented for the energy equation by Moin et al. (1991). The procedure is very similar to the original dynamic procedure of Germano et al. (1991) and leads to calculation of the so called lumped coefficient, $C_s^2 Pr_{SGS}$, via:

$$C_s^2 Pr_{SGS}^{-1} = \frac{\langle \mathcal{K}_i \mathcal{X}_i \rangle}{\langle \mathcal{X}_i \mathcal{X}_i \rangle}, \tag{2.28}$$

[1] Pr has a value of 0.7 for a neutral case, 0.3-0.4 in the convective case where the thermal diffusivity grows, and up to 1 under very stable conditions where momentum diffusivity dominates over the thermal diffusivity (Porté-Agel et al., 2011).

where

$$\mathcal{X}_i = \widetilde{\Delta}^2 \left(\widetilde{|\overline{S}| \frac{\partial \overline{\theta}}{\partial x_i}} - \beta_\theta^2 \left|\widetilde{\overline{S}}\right| \frac{\partial \widetilde{\overline{\theta}}}{\partial x_i} \right) \text{ and } \mathcal{K}_i = \widetilde{\overline{u}\overline{\theta}} - \widetilde{\overline{u}}\widetilde{\overline{\theta}}. \tag{2.29}$$

The averaging procedure to find the lumped coefficient can be performed by analogy to the eddy viscosity models, that is, over any homogeneous direction. The variants of the Lagrangian dynamic model, more localized horizontal averaging methods over a stencil of a few grid points, and even simple clipping of negative values of coefficients can be used as well (see Ghosal et al. (1995) and Basu (2004)).

Another SGS model can be derived by analogy to the equation 2.14 which directly computes the eddy diffusivity, α_{SGS}. The model was originally proposed by Sergent et al. (2000) and assumes similar mechanisms of energy exchange between the resolved and the sub-grid scales for the SGS turbulent kinetic energy k_{SGS} and SGS heat flux Φ_{SGS}.

$$\alpha_{SGS}(\beta, x, y, z, t) = C_a \frac{\Delta^{1+2\beta}}{\Delta\theta} \overline{T}^{2\,\frac{\beta}{2}}(x, y, z, t) |\Phi^2|^{\frac{1-\beta}{2}}. \tag{2.30}$$

Here, β can take values between 0 and 1, $\Delta\theta$ is the reference temperature difference and Φ_c is the SGS heat flux at the smallest resolved scales. $|\overline{T}| = \sqrt{T_{ij}T_{ij}}$ where $T_{ij} = \left|\bar{S}\right| \frac{\partial \bar{\theta}}{\partial x_i}$. The constant $C_a = 0.5$ offers the closest comparison to the DNS data Sergent et al. (2000). In this thesis, the SGS eddy diffusivity models defined by equations 2.28 and 2.30, along with the simple $Pr_{SGS} = 1$ model are implemented in the CFD code.

2.4 Evaluation of LES

Since the evolution of large eddy simulation technique in the 1970s, several studies has been conducted to evaluate the accuracy and reliability of the LES. The important factors affecting the quality of SGS modeling are briefly discussed here.

2.4.1 Effects of the filtering and grid resolution

Since information from the smallest resolved scales with low energy content is used for SGS modeling, it is very crucial that accurate numerical schemes with low numerical error are used to ensure that numerical errors do not devastate the SGS contributions. For this purpose, the high order and non-dissipative methods are ideal. In the finite volume methods, it is difficult to have high order numerical schemes and when low-

order discretization schemes are applied in LES, the magnitude of numerical errors can become even larger than the contributions from the SGS modeling. In such cases, explicit filtering together with using a fine mesh can reduce numerical errors Bose et al. (2010); Brandt (2004); Gullbrand (2002); Lund (1997). For example, to have numerical errors smaller than the contribution from the SGS modeling, a combination of either a fourth-order scheme with a filter width of at least twice the cell size, or a second-order scheme with filter width of at least four times the cell size has been recommended to minimize the numerical errors (Chow and Moin, 2003).

The choice of the computational grid size has also sensible impact on the quality of the LES computations. In wall bounded flows, the flow structures scale with the distance from the wall. In the buffer layer and the viscous sub-layer, flow is dominated by the streamwise streaks that contain most of the energy. Therefore, the grid can be stretched in the streamwise direction. Away from the walls, the grid should be as cubic as possible since isotropy in the sub-grid scales is presumed. In all cases, the LES grid should be fine enough to capture most of the turbulent kinetic energy (TKE) of the flow even without a SGS model. In particular, in the wall-resolved LES, the first cell needs to be located at $y^+ \leq 1-2$ and the grid spacing in the streamwise and lateral directions should be of the order $\Delta x^+ \sim 50-130$ and $\Delta z^+ \sim 15-40$, respectively, to resolve the structures in the near-wall region accurately (see Piomelli (2008)). A common way to investigate the resolution of an LES simulation is to obtain the ratio between the total kinetic energy and the modeled kinetic energy to ensure that the most part of the flow is simulated and only a small portion is modeled (Pope, 2004). The energy spectra is also a useful measure for evaluation of the LES results. Brandt et al. (2004) argued that if the energy spectra for a certain streamwise or spanwise resolution does not decline fast enough, the resolution is not sufficient. For flows with periodic boundaries, Davidson (2009) found that the two-point correlation function is an appropriate measure of resolution. For example, he recommended that a minimum of eight cells could be enough to resolve the large scales of motion. Further discussion about evaluation of LES may be found in Chow (2004); Lundquist (2010).

2.4.2 Effects of temporal and spatial discretization

LES is known to be more sensitive to the numerical errors than RANS and DNS (Amiri et al., 2005; Park, 2006). LES solvers have been commonly coded using finite difference, finite volume, finite element and spectral methods. The finite difference methods allow for high order approximations, but they are difficult to apply to domains with a

complicated geometry or complicated boundary conditions. Spectral methods are very accurate with minimized dissipation error and no conservation issues, however, they suffer from hard implementation for complex geometries and boundary conditions. Finite element methods work very well on domains with complex geometry, but they need more calculations for the same accuracy, as compared with other methods (Petrila and Trif, 2005). This leaves the finite volume methods particularly interesting for the fluid simulations as they combine the simplicity of the finite differences methods with the local accuracy of the finite element method by automatically conserving the mass on each cell.

Due to the nature of LES (that is, importance of the smallest resolved scales and the universality of the SGS terms) it is ideal to have non-dissipative schemes for both spatial and temporal discretizations as much as possible. In the case of high Reynolds number flows, however, the use of non-dissipative central differencing produces spurious waves in the flow. A solution is to use a scheme consisting of a central scheme for preserving accuracy combined with an upwind scheme for stabilizing the flow, although this makes a small dissipation due to the upwind schemes. This method is practised in the current thesis for the numerical simulations.

One way to investigate the numerical errors existing in the simulations, is to look at the energy spectra. An increase in the slope of the spectra at high frequency end indicates the contamination of the flow at high wave numbers with numerical errors (noise).

2.4.3 Effect of grid arrangement

CFD codes are in general mass and momentum conservative. For an LES code to be accurate, however, the kinetic energy needs to be conserving as well. A kinetic energy conserved method is guaranteed to be stable and will improve the accuracy of the LES cf. Larsson and Iaccarino (2010). Besides sources of error associated with, grid resolution, discretization schemes and the filtering operation, there are numerical errors associated with the choice of variable storing strategy, that is, grid arrangement (staggered or collocated), which come from conservation point of view [1]. Staggered grids exhibit good performance in delivering conservative flow, their use is however limited to simpler geometries. On the other hand, collocated grids are generally easier

[1] It is worth mentioning that finite difference methods do not exhibit conservation issues because the differential incompressible Navier-Stokes equations are fully conservative (all of the terms in the kinetic energy transport equation can be re-arranged in a convergence-free form or yield continuity equation (Ham and Iaccarino, 2004).

to implement and modify and, for example, multi-blocking and adaptive meshes, take less time and memory. They also give superior results for the complicated geometries as compared with the staggered grid arrangement (Melaaen, 1992a,b). In the standard implementation of the collocated grids, however, the conservation of kinetic energy is not guaranteed Benhamadouche (2006); Felten and Lund (2006); Larsson and Iaccarino (2010); Mahesh et al. (2004). The reason is that the Rhie-Chow interpolation which is needed to fix the pressure checker-boarding, results in a spurious term in the pressure equation that causes dissipation of kinetic energy (Ham and Iaccarino, 2004). Conservation of kinetic energy can be measured in a numerical simulation with periodic domain by monitoring the temporal evolution of the kinetic energy (since the walls are periodic, the corresponding terms in the Navier-Stokes equation vanish and $\frac{\partial E}{\partial t} = 0$ should be maintained with a certain accuracy).

2.5 Summary

The concepts of LES technique and filtering were investigated in this chapter and the role of the grid spacing, discretization techniques, filtering and the collocated grid arrangement were discussed with respect to the finite volume CFD solvers. The SGS models were briefly introduced and a new dynamic mixed SGS eddy viscosity as well as two SGS eddy diffusivity models were introduced and implemented in the computing code, EllipSys3D. The SGS models introduced in this chapter are applied to different flows and discussed furthermore in the proceeding chapters.

Chapter 3

LES of the fully-developed boundary layers and infinite wind farms

Fully-developed boundary layer flows are of special interest and importance in wind energy and atmospheric sciences. A boundary layer over large wind farms where the length of the farm is over an order of magnitude larger than the height of the ABL, can be considered fully-developed (Calaf et al., 2010; Frandsen et al., 2006). The ABL flows are associated with high Reynolds numbers and for such flows, a very fine near-wall mesh is required to simulate the flow accurately. Accurate simulation of such high Reynolds number flows is beyond today's computational power. To circumvent the use of a very fine mesh close to the solid boundaries, the so called wall-modeled LES can be employed in which a coarse grid is used so that the flow structures in the viscous sub-layer and the buffer layer are modeled, and the first mesh point in the wall region is placed in the logarithmic layer. The informations from these grid points is then used for imposing a wall shear stress (instead of a usual no-slip wall). This chapter starts with an investigation of low Reynolds number wall-resolved LES of fully-developed channel flow with and without heat transfer from the walls. The study of the wall-resolved LES cases will be used to evaluate the SGS models and to examine the grid resolution criteria for the airfoil simulations presented later in this report. Simulations are then continued with simulation of high Reynolds number wall-modeled ABL and a comparison is made between the flow structures obtained at different Reynolds numbers. The chapter concludes towards a more wind-energy specific cases, where simulations of the infinite wind farm in the neutral ABL using a wall-modeled LES and a simplified

prescribed ABL approach, are investigated.

3.1 Introduction

In the fully-developed channel flow or ABL simulation, the flow is driven by a pressure drop in the streamwise direction while the pressure gradient in the spanwise and vertical directions is zero. The imposed streamwise pressure gradient is counteracted by the shear stress at the walls so that the mean streamwise velocity does not accelerate. The streamwise momentum equation then reduces to (Pope, 2000),

$$\begin{aligned} 0 &= \nu\frac{d^2\langle U\rangle}{dy^2} - \frac{d}{dy}\langle uv\rangle - \frac{1}{\rho}\frac{\partial\langle p\rangle}{\partial x} \\ &= \frac{d}{dy}\left(\rho\nu\frac{d\langle U\rangle}{dy} - \rho\frac{d}{dy}\langle uv\rangle\right) - \frac{dp_w(x)}{dx}; \quad \text{since} \quad \frac{\partial\langle p\rangle}{\partial x} = \frac{dp_w(x)}{dx}. \end{aligned} \tag{3.1}$$

Defining $\tau(y) = \rho\nu\frac{d\langle U\rangle}{dy} - \rho\frac{d}{dy}\langle uv\rangle$- consisting of the Reynolds shear stress and the mean viscous shear stress- as the total shear stress, leads to,

$$-\frac{dp_x}{dx} = \frac{d\tau}{dy}. \tag{3.2}$$

Equation 3.2 introduces a balance between the streamwise normal stress gradient, $-\frac{dp_x}{dx}$, being only a function of x, and the vertical shear stress gradient, $\frac{d\tau}{dy}$, being only a function of y. Therefore, both terms are constant. Furthermore, the shear stress tensor is anti-symmetric about the mid-plane ($\tau_0 = -\tau_{2h}$) so $\tau_h = 0$. So the solution to the previous equation reduces to,

$$-\frac{dP}{dx} = \frac{\tau_w}{h}, \tag{3.3}$$

and

$$\tau(y) = \tau_w\left(1 - \frac{y}{h}\right). \tag{3.4}$$

This linear shear stress profile is independent of the fluid properties and its state of motion, and has to be retained for any channel flow simulation provided that the flow is statistically stationary. The wall shear stress can also be expressed in the normalized form, called skin friction, $C_f \equiv \frac{\tau_w}{\frac{1}{2}\rho U^2}$, where U is a reference velocity (usually the free-stream velocity or mean bulk flow velocity). Fully-developed channel flows can be

established either by applying a known pressure gradient and solving for the unknown mean velocity, or equivalently, by imposing a mean velocity while the pressure gradient is unknown. When choosing the pressure gradient approach, the imposed shear stress is known according to equation 3.3 and the simulation is continued until the simulated shear stress matches the desired value defined by equation 3.4, and then averaging is performed to obtain the converged statistics.

3.1.1 Flow initialization and the numerical set up

A fully-developed turbulent boundary layer can be generated in a numerical solver by using any arbitrary initial velocity profile, provided that the Reynolds number is *at* or *above* the transition regime. The reason is that, at such Reynolds numbers, the truncation and round-off errors can act as sustainable perturbations and, due to instabilities, transit the flow to turbulence. The transition process, however, can take a long simulation time in practice, since the infinitesimally unstable modes grow at a very slow rate (Drazin and Reid, 2004).

To accelerate the transition to turbulence, 3D random noise can be superimposed to the initial velocity field. In many cases, however, this is not a very effective tool, for the random velocity components do not contain any turbulence structures and the resulting velocity field will not be divergence free. Therefore, the fluctuations get damped out and the flow relaminarizes rapidly. Other improved methods include initial perturbations that contain turbulent structures. One such method was implemented by DeVilliers (2006), who used a laminar parabolic profile superimposed with artificially generated near-wall vortical structures to mimic the real wall bounded flow simulation.

In this thesis, two approaches have been used to trigger the transition to turbulence. In the first method, thanks to the presence of the multi-grid solver, random perturbations were introduced on a coarser grid than the desired to increase the probability of generation of large scale fluctuations and accelerate the flow development. After convergence was achieved, the data was interpolated to the fine grid. This method was used for the wall-modeled ABL cases. For the wall-resolved channel flows, the approach was to run a steady-state flow for a few iterations until the mean shear profile is established, after which random noise was added for a few time steps. In both cases, the random perturbations are of the order of 10-30% of the mean velocity. These were the most effective methods for generating a fully-developed flow in the shortest time.

For the numerical simulations performed in this chapter, the pressure correction equation is solved using the PISO algorithm and pressure decoupling is avoided using

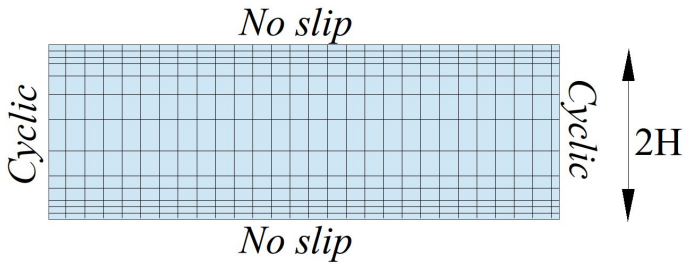

Figure 3.1: Schematic of a turbulent channel flow numerical set up and its boundary conditions, where the flow moves from left to right. Mesh points are distributed uniformly in the horizontal plane while the grid is stretched in the vertical direction.

the Rhie-Chow interpolation technique. The convective terms are discretized using a hybrid scheme combining the third order accurate QUICK scheme (10%) to stabilize the numerical oscillations and the fourth order CDS (90%) scheme to maintain the numerical accuracy.

3.2 Fully-developed channel flow at low Reynolds numbers

In this section, the fully developed flow between two parallel walls, a sketch of which depicted in figure 3.1, is simulated using different SGS models. The computational grid is uniform in the horizontal directions and stretched out in the wall normal plane using

$$y_j = -\frac{\tanh(1 - \frac{2j}{N_y})}{\tanh(\gamma)} \quad j = 0, ..., N_y \tag{3.5}$$

function with $\gamma = 2.75$. This type of grid stretching has also been commonly practised for wall-resolved channel flows (cf. Gullbrand (2002) and Cavar (2006)), due to the nature of the boundary layer[1]. The flow field is assumed to be horizontally homogeneous so periodic boundary conditions are employed in the streamwise and spanwise directions. For all the cases, $\Delta_{i,j,k} = (dx \times dy \times dz)^{\frac{1}{3}}$ is used as the implicit (grid) filter. The top and bottom walls have no-slip noundary conditions. Table 3.1 shows different simulations performed for the wall-resolved LES of the fully developed flow in the channel of length L, height H, and width W. The non-dimensional units z^+ and x^+ represent the grid size in the spanwise and the streamwise directions, and y_w^+ and y_c^+ show the minimum and maximum cell heights near the wall and at the core of the channel. The flows are simulated at two friction Reynolds numbers $Re_\tau = \frac{u_\tau H}{\nu} = 180$ and 395, where u_τ is the friction velocity and H is the channel half-height. In the table, $Re_{\tau,n.}$ refers to the nominal friction Reynolds number according to the input

[1]The solution to the boundary layer equations can be expressed in hyperbolic tangent form

SGS	$Re_{\tau,n.}$	*Grid Res.*	$L \times H \times W$	$Re_{\tau,act.}$	z^+	$y_w^+ - y_c^+$	x^+
NO	180	$48 \times 48 \times 48$	$4\pi \times 2 \times \frac{4\pi}{3}$	212.99	13.9	1.4-18.1	27.9
MO	180	$48 \times 48 \times 48$	$4\pi \times 2 \times \frac{4\pi}{3}$	192.98	12.6	1.2-16.4	25.2
SM	180	$48 \times 48 \times 48$	$4\pi \times 2 \times \frac{4\pi}{3}$	199.10	13.0	1.3-16.9	26.0
DMo	180	$48 \times 48 \times 48$	$4\pi \times 2 \times \frac{4\pi}{3}$	178.55	16.1	1.2-15.7	48.3
MO	180	$64 \times 64 \times 64$	$4\pi \times 2 \times \frac{4\pi}{3}$	208.07	13.6	1.0-13.4	40.8
MO	395	$32 \times 32 \times 32$	$2\pi \times 2 \times \pi$	391.00	13.4	1.3-63.3	76.8
MO	395	$48 \times 48 \times 48$	$4\pi \times 2 \times \frac{4\pi}{3}$	367.71	32.1	2.4-31.2	96.3
MO	395	$64 \times 64 \times 64$	$2\pi \times 2 \times \pi$	395.74	19.4	0.6-33.7	38.9
DNS†	180	$128 \times 129 \times 128$	$4\pi \times 2 \times \frac{4\pi}{3}$	178.13	5.9	N/A-4.4	17.7
DNS†	395	$256 \times 193 \times 192$	$2\pi \times 2 \times \pi$	392.24	6.5	N/A-6.5	10.0

† DNS data are taken from Moser et al. (1999)

Table 3.1: Test cases for wall-resolved the channel flow simulations

driving pressure gradient, and $Re_{\tau,act.}$ is the actual Reynolds number obtained from the simulations. Different SGS models mentioned in the table can be summarised as follows:

- *NO*: No explicit treatment for the SGS scales $\nu_{sgs} = 0$.
- *SM*: Standard Smagorinsky model (eq. 2.6) with $C_s = 0.1$
- *DS*: Dynamic Smagorinsky model with C_s found from eq. 2.11
- *MO*: Mixed model (eq. 2.14) using vorticity formulation, $c_m = 0.01$ and $\alpha = 0.5$
- *DMo*: Dynamic Mixed model using vorticity formulation with c_m found from eq. 2.19 and $\alpha = 0.5$

The eddy viscosity predicted by the standard Smagorinsky (SM) model is non-zero at viscosity-dominated solid boundaries, which is contrary to the notion of zero eddy viscosity in the laminar parts of the flow. Therefore, a function (van Driest, 1956) is applied to the Smagorinsky constant to account for an exponential decay of the eddy viscosity to zero close to the wall

$$C_s(y) = \left(C_s[1 - \exp(-y^+/A^+)]\right)^2 \text{ where } A^+ = 25. \tag{3.6}$$

where the modified coefficient, $C_s(y)$, is replaced by the C_s constant introduced in equation 2.6. Figure 3.2 shows the initialization of the flow at the coarse grid level, as explained previously, and the final fully developed flow in the finest grid for $Re_\tau = 395$. The mean streamwise velocity normalized by the maximum velocity is plotted in figure 3.3(a) for $Re_\tau = 180$ and $Re_\tau = 395$. The mean velocity and other statistics for the

two Reynolds numbers have very similar magnitudes. Therefore, to distinguish between the two cases, the values for the higher Reynolds number case are plotted in red and shifted slightly. For more clarity, the statistics obtained from the wall resolved cases are only shown for half-channel height, that is, $\leq 0y/H \leq 1$. In both cases, the thick blue line represents the DNS data. It can be seen from the figure that using a mesh of 64^3 grid points gives the most accurate flow prediction among all cases for both Reynolds numbers, when compared with the DNS results of Moser et al. (1999). For the lower Reynolds number, the DMo model under-estimates the velocity below $y/H \sim 0.2$ and the other models over-estimate the velocity very slightly. In the channel flow studies, it is often useful to plot the velocities in a semi-logarithmic scale to be able to compare the differences in the profiles for the whole range and investigate the effects of the Reynolds stress at the wall. Such a plot is shown in figure 3.3(b) where the velocity is normalized by the skin friction velocity and the abscissa shows the height in wall units. Different red curves show the effect of mesh refinement on the accuracy of the simulation for $Re_\tau = 395$. The curves in black show convergence of the results for the $Re_\tau = 180$ case and as can be seen, different models give very similar velocity profiles.

The over-estimation of u^+ as shown in figure 3.3(b) is related to the over-dissipation of the resolved turbulent kinetic energy which results in lower surface shear stress and thus acceleration of the flow towards the core of the channel (cf. Bou-Zeid et al. (2005)). In contrast, the under-dissipation of the NO model for $Re_\tau = 180$ indicates that this model is not dissipative enough, which results in over-prediction of the velocity close to the wall and subsequent acceleration of the velocity towards the core of the channel.

Figure 3.4 shows the turbulence intensity and turbulent kinetic energy plots for the different cases. It can be seen that the coarser grids at $Re_\tau = 395$, lead to an over-estimation of the streamwise turbulence intensity as well as TKE and under-estimation of two other components. The TKE profiles are very similar for all cases. They are close to the DNS results for the $Re_\tau = 180$ case but are over-predicted for the higher Reynolds number, especially coarse grid cases.

Figure 3.5 compares the eddy viscosities normalized with the molecular viscosity. In general, the eddy viscosities are zero in the viscous sub-layer, where the flow is laminar and governed by the molecular viscosity, followed by the maximum values at $y/H \sim 0.05$ where the most turbulence production happens and the values decrease towards the core of the channel, implying a turbulence decline upwards. Also, as can be seen from the $Re_\tau = 395$ cases (plotted in red), refining the grid makes the magnitude of the eddy viscosity smaller. In other words, the dependence on SGS modeling is reduced with a finer mesh and if the grid is refined towards a DNS grid, there will

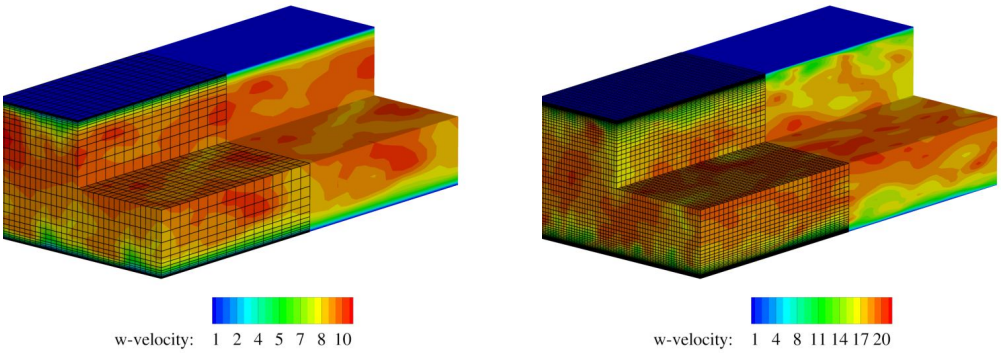

(a) (b)

Figure 3.2: Slices of the instantaneous velocity field through the computational domain for the channel flow at $Re_\tau = 395$. (a) Initial flow started on the coarse grid level with 32^3 mesh points, (b) flow in the fully developed conditions as interpolated from the coarse grid to the finest grid level of 64^3 mesh points.

be no eddy viscosity in the flow field. It is also clear from the comparison of the two Reynolds numbers that the lower Reynolds number presents a lower eddy viscosity, as expected.

3.2.1 Thermally stratified boundary layer simulations

In order to perform simulations in the non-neutral atmospheric boundary layers, the energy equations and SGS diffusivity models, as described in chapter 2, are added to the present CFD solver, and the turbulent channel flow with heated walls is considered for the validations. Since the code is incompressible, the Boussinesq approximation is used to couple the momentum and energy equations by assuming $\Delta\rho/\rho \ll 1$. The problem of heat transfer in a turbulent channel flow is similar to the momentum transfer in many ways. The domain consists of a diffusive sub-layer similar to the viscous sub-layer in the usual channel flow and a buffer layer followed by a logarithmic layer for the temperature field. The Prandtl number $Pr = \frac{\nu}{\alpha}$, is used together with the viscosity to characterize the flow regime and the state of the flow can be defined according to the Richardson number as well as the Reynolds number. The Richardson number indicates the level of stratification in the flow and is defined similar to the friction Reynolds

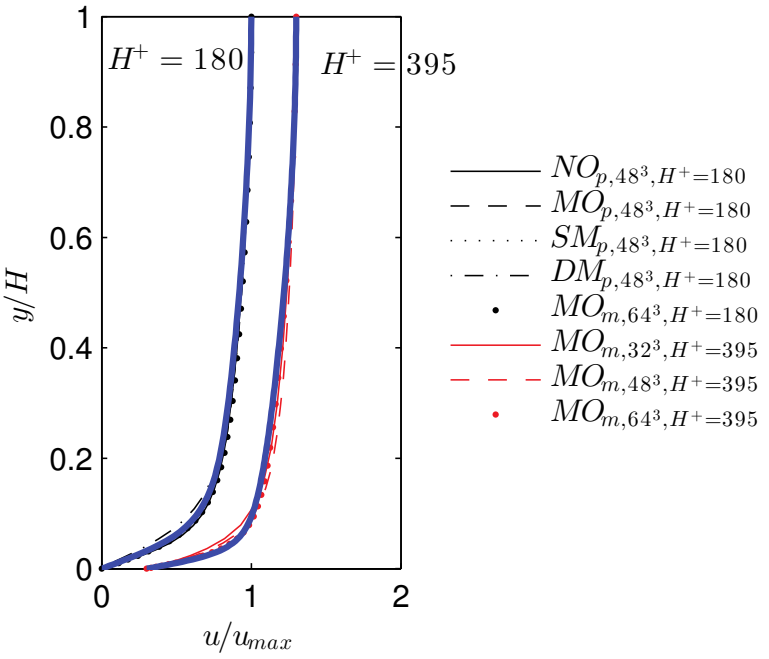

(a)

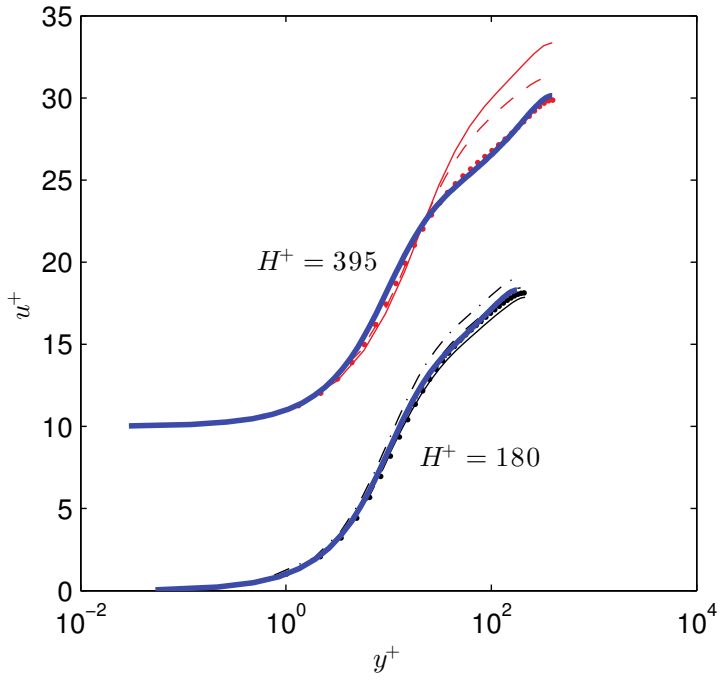

(b)

Figure 3.3: (a) Mean normalized streamwise velocity using different SGS models and flow resolutions. (b) Mean streamwise velocity in wall units. The solid blue lines represent the standard logarithmic profiles. Also the $Re_\tau = 395$ cases is separated from the $Re_\tau = 180$ cases by a 0.3 unit shift in horizontal direction and by a vertical shift of 10 units in the vertical direction for in (a) and (b), respectively. Solid blue lines represent DNS results of Moser et al. (1999).

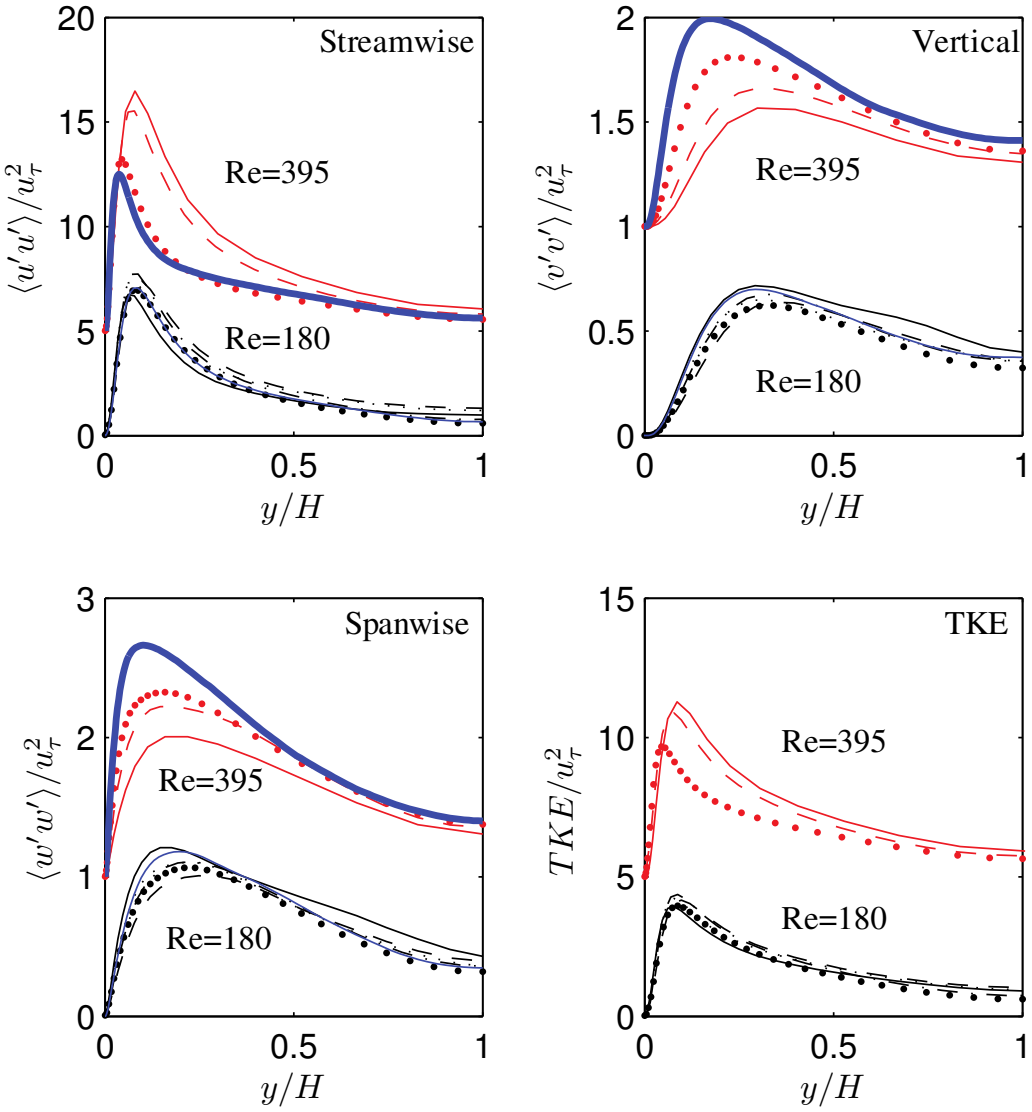

Figure 3.4: Turbulence intensity components and the turbulent kinetic energy plots for two cases. Computations at $Re_\tau = 395$ are shifted up by 5, 1, 1, and 5 units for the different sub-figures top left to the bottom right, respectively (all the values close to the wall reach zero originally). Solid blue lines represent DNS results of Moser et al. (1999) and the symbols are the same as figure 3.3.

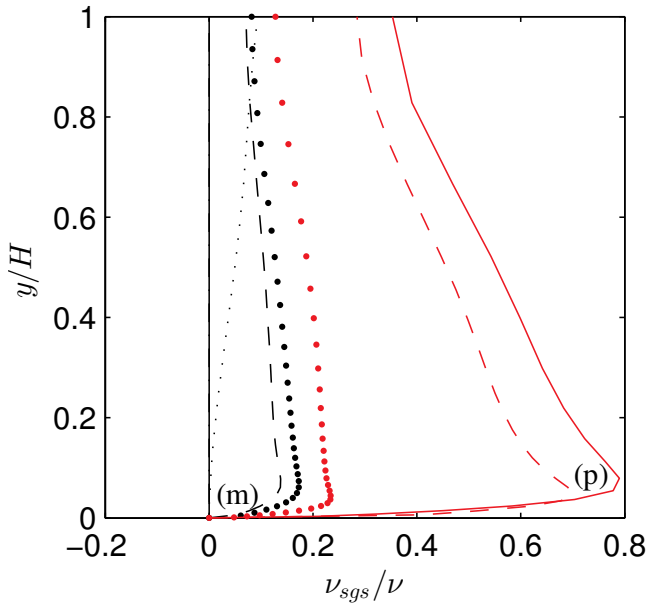

Figure 3.5: Non-dimentional eddy viscosity profile. The laminar flow regime where the molecular viscosity dominates and the part of the flow with highest SGS production are shown on the figure by (m) and (p), respectively. (legends are similar to the figure 3.3).

number, $Re_\tau = \frac{hu_\tau}{\nu}$, as

$$\mathrm{Ri}_\tau = \frac{\alpha g \Delta T h}{u_\tau^2}, \tag{3.7}$$

following the definitions proposed by Armenio and Sarkar (2002) and Dong and Lu (2005), where h is the channel height, $u_\tau = \sqrt{\tau_w/\rho}$ is the friction velocity, α is the thermal expansion coefficient, g is the gravitational acceleration, pointing downwards, and ΔT is measured with some reference temperature setting. Stable and unstable stratifications can be defined on the grounds of the Richardson number. In the stably stratified channel flow, the temperature at the top wall is higher than at the bottom wall and in the unstably stratified case, it is the opposite. It is very challenging to perform a DNS of the channel flow at high Reynolds and Prandtl numbers, as the total required grid points scale with $Pr^3 Re^{9/4}$, while LES seems to be a reliable choice for such problems Wang and Lu (2005).

3.2.2 Description of the problem

The simulated flow field is a fully developed two-dimensional turbulent flow between two parallel walls. The flow field is homogeneous both in the streamwise and spanwise directions and the statistics are dependent only upon the distance from the wall. The data presented here are non-dimensionalized by the wall variables, that is, u_τ and ν.

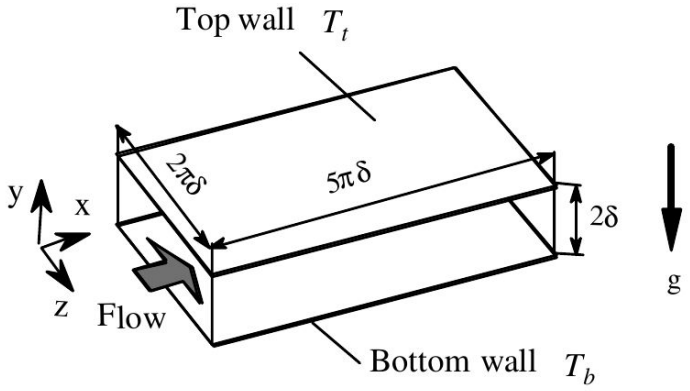

Figure 3.6: Schematic diagram of the fully developed turbulent channel flow with iso-thermal walls. Sketch reproduced from Kasagi and Iida (1999).

Figure 3.6 shows a sketch of the problem. Top and bottom walls walls are assumed to be kept at different, though uniformly distributed, temperatures without fluctuations where $\Delta T = T_{bottom} - T_{top} = 1$, and the gravitational acceleration is directed towards the bottom. The lateral walls have cyclic boundary conditions. The flow cases are simulated at $Re_\tau = 150$ and $Ri_\tau = 100$, and the simulations are compared with the DNS data of Kasagi and Iida (1999).

The velocity and temperature contours are plotted in figures 3.7 and 3.8, respectively. It can be seen that the structures of the velocity field and the temperature fields are very similar. They both exhibit streamwise streaks close to the wall and a more homogeneous field at higher distances from the wall although the streamwise structures are still visible at higher distances from the wall.

The SGS Prandtl number is obtained from the mixed scale SGS eddy diffusivity model introduced in equation 2.30. Figure 3.9 shows the Pr_{sgs} at different distances from the hot wall. For the simulations, a molecular Prandtl number of 0.7 is used while the Pr_{sgs} ranges between 0 and 10. The figure shows that Pr_{sgs} field is affected by the streamwise streaks close to the wall, and, away from the wall, the distribution is more homogeneous.

Figure 3.10 shows the velocity and the TKE comparisons between the present study and the DNS of Kasagi and Iida (1999). It can be seen from the figure 3.10(left) that the velocity in the core of the channel is under-predicted. This suggest that there is more mixing and turbulence in the present LES computations than in the DNS results, as can also be confirmed from the TKE plots in figure 3.10(right). Figure 3.11 shows the temperature distribution along the walls. As can be seen, the mean temperature is predicted with good accuracy. The temperature profile in the wall units shows that in the core of the channel, a lower normalized temperature is predicted, similar to the velocity profiles. The low grid resolution, the numerical errors associated with the

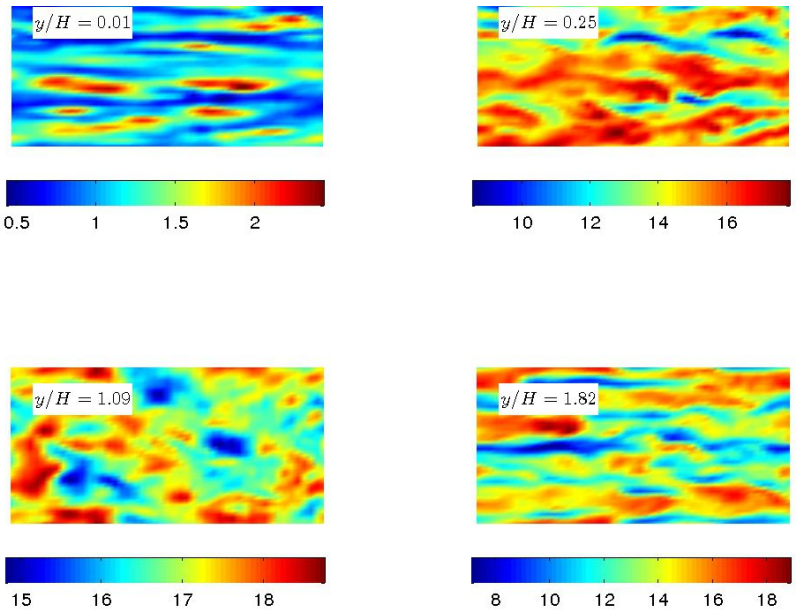

Figure 3.7: Instantaneous streamwise velocity contours for the flow at $Re_\tau = 150$ and $Ri_\tau = 100$, as a function of channel height.

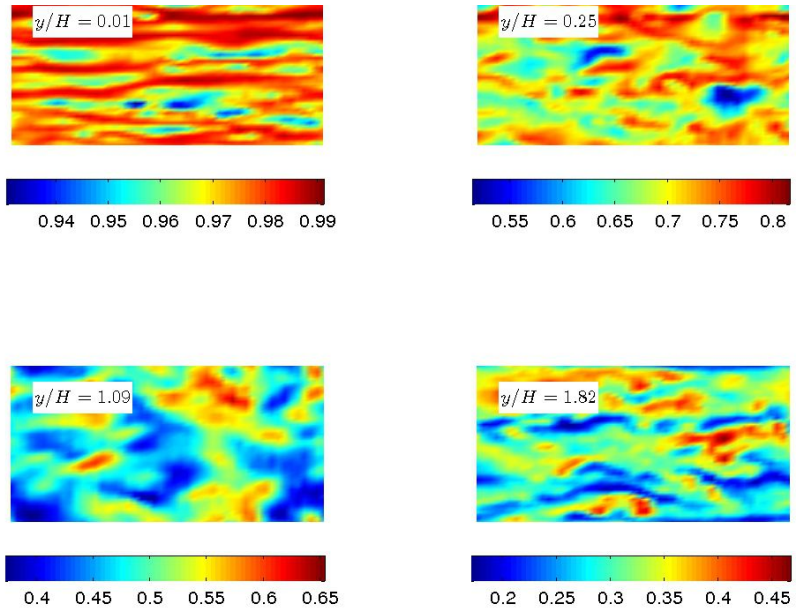

Figure 3.8: Instantaneous temperature contours for the flow at $Re_\tau = 150$ and $Ri_\tau = 100$, as a function of channel height.

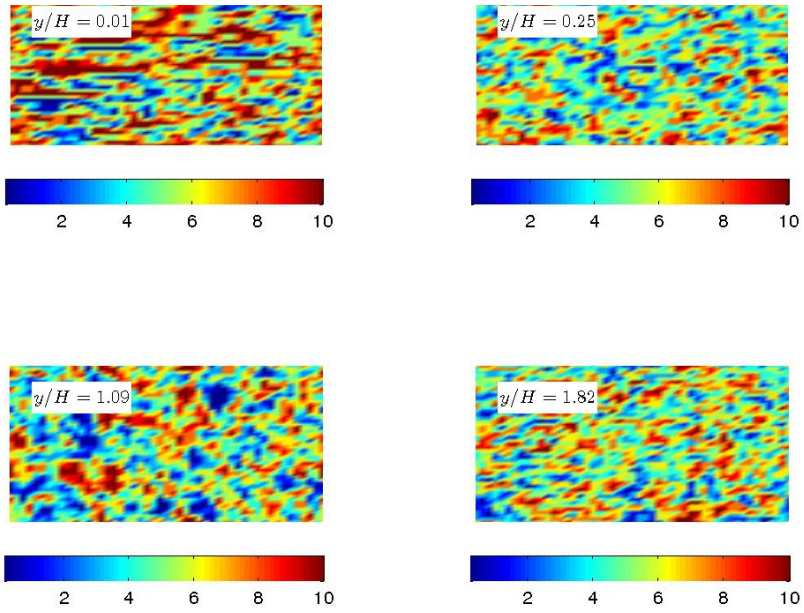

Figure 3.9: The SGS Prandtl number predicted for the flow at $Re_\tau = 150$ and $Ri_\tau = 100$, as a function of channel height.

partial use of the upwind schemes, and the use of low order methods (2^{nd} order CDS for the diffusive terms and a blend of CDS and 3rd order QUICK scheme for the convective terms) can explain the discrepancies.

3.3 Neutrally stratified Atmospheric Boundary Layer (ABL)

For the high Reynolds number ABL flows, the near-wall, dynamically important motions which contain most of the energy become progressively smaller. Therefore, to be able to solve such flows with the current computational power, the inner layer, $y/H \leq 0.1$, has to be somewhat modeled. Wall modeling can be performed by placing the first grid point in the logarithmic layer where the flow is not influenced by the molecular viscosity, and, based on the resolved velocity at that level, calculating a surface shear stress and applying it as a wall boundary condition (instead of the standard no-slip B.C.) (cf.Mellor and Yamada (1974); Piomelli (2008); Porté-Agel et al. (2001); Smits et al. (2011)). Getting the right statistics in wall-modeled LES cases is very difficult and most models have failed to predict the correct wall shear stress, since the wall modeling approach poses an inevitable numerical error due to the under-resolved information that is fed into the wall-model from the first grid height (Kawai and Larsson,

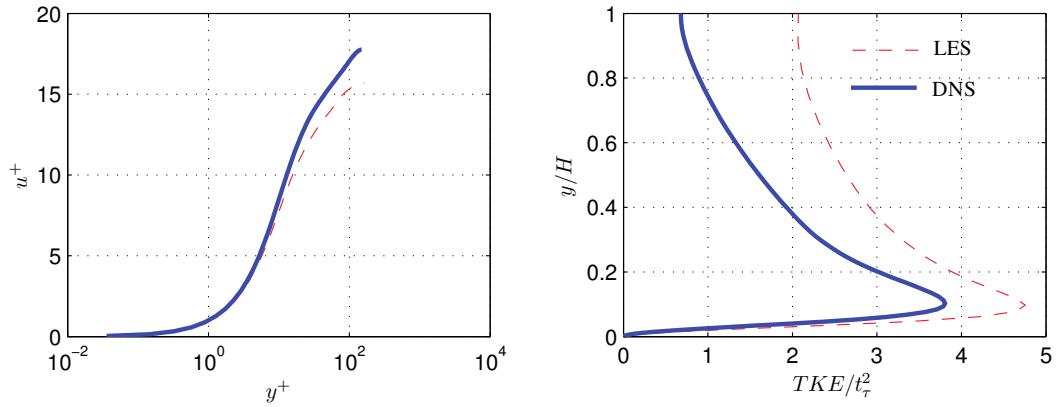

Figure 3.10: Velocity (left) and the TKE (right) profiles in the wall-resolved channel flow at $Re_\tau = 150$ and $Ri_\tau = 100$ using MO SGS stress and MO SGS eddy diffusivity models.

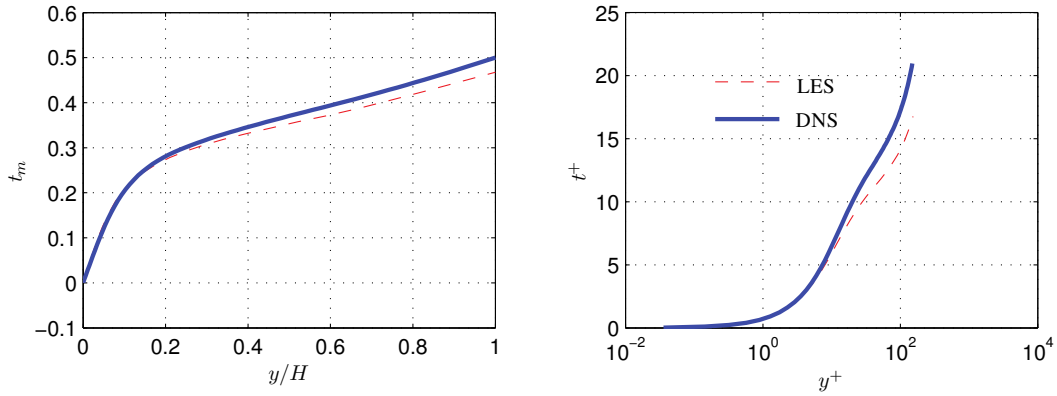

Figure 3.11: Temperature plots in wall-resolved channel flow at $Re_\tau = 150$ and $Ri_\tau = 100$ using MO SGS stress and MO SGS eddy diffusivity models.

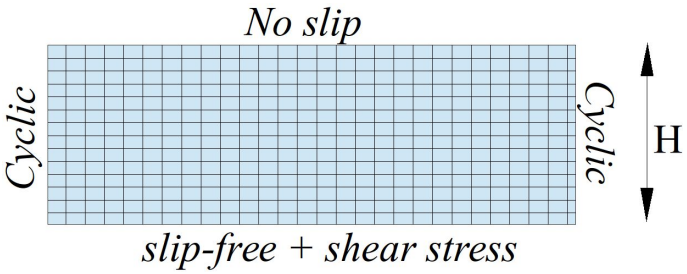

Figure 3.12: Schematic of a wall modeled channel flow -a.k.a fully developed boundary layer- numerical set up and its boundary conditions. The flow advances from left to right and uniform grid spacings is used in all directions.

SGS	$\frac{z_0}{H}$	*Grid Res.*	$L \times H \times W$	Forcing†
NO	0.0001	$64 \times 64 \times 64$	$2\pi \times 1 \times \pi$	$U_b = 21.29$
SM	0.0001	$64 \times 64 \times 64$	$2\pi \times 1 \times \pi$	$U_b = 21.29$
MO	0.0001	$64 \times 64 \times 64$	$2\pi \times 1 \times \pi$	$U_b = 21.29$
DS	0.0001	$64 \times 64 \times 64$	$2\pi \times 1 \times \pi$	$U_b = 21.29$
DS	0.0001	$64 \times 64 \times 64$	$2\pi \times 1 \times \pi$	$\nabla P = \rho u_*^2/H = 1$
NO	0.0015	$64 \times 64 \times 64$	$2\pi \times 1 \times \pi$	$\nabla P = \rho u_*^2/H = 1$
MO	0.0015	$64 \times 64 \times 64$	$2\pi \times 1 \times \pi$	$\nabla P = \rho u_*^2/H = 1$

† Controlled mass flux, U_b, and pressure gradient, ∇P, approaches.

Table 3.2: test cases for the the Atmospheric Boundary Layer (ABL) simulations.

2012).

This section presents the ABL simulations with two different roughness heights. The flow is governed by a pressure gradient in the streamwise direction, while the top wall has a symmetry boundary condition, the bottom wall has a no-slip B.C. and the lateral boundaries are cyclic walls. The simulations are started using random perturbations in the cyclic domain. The numerical set up is sketched in figure 3.12 and the simulation test cases are is defined in table 3.2. ABL simulations are usually defined by the surface roughness. For the neutral case, the mean velocity profiles follow the logarithmic profile defined by the law of the wall. The imposed shear stress due to the wall modeling is calculated locally as

$$\tau_w(x,z,t) = -\left[\frac{\kappa}{\ln(z/z0)}\right](\overline{u(x,2,z,t)}^2 + \overline{v(x,2,z,t)}^2), \tag{3.8}$$

where z is the height and u and v are the horizontal velocities at the first cell center. This equation defines the surface shear stress as a function of the horizontal components of the velocity at the first grid height.

Similar to the damping function introduced for the wall-resolved cases, the Mason & Thomson damping function is used here to account for the decay of the eddy viscosity

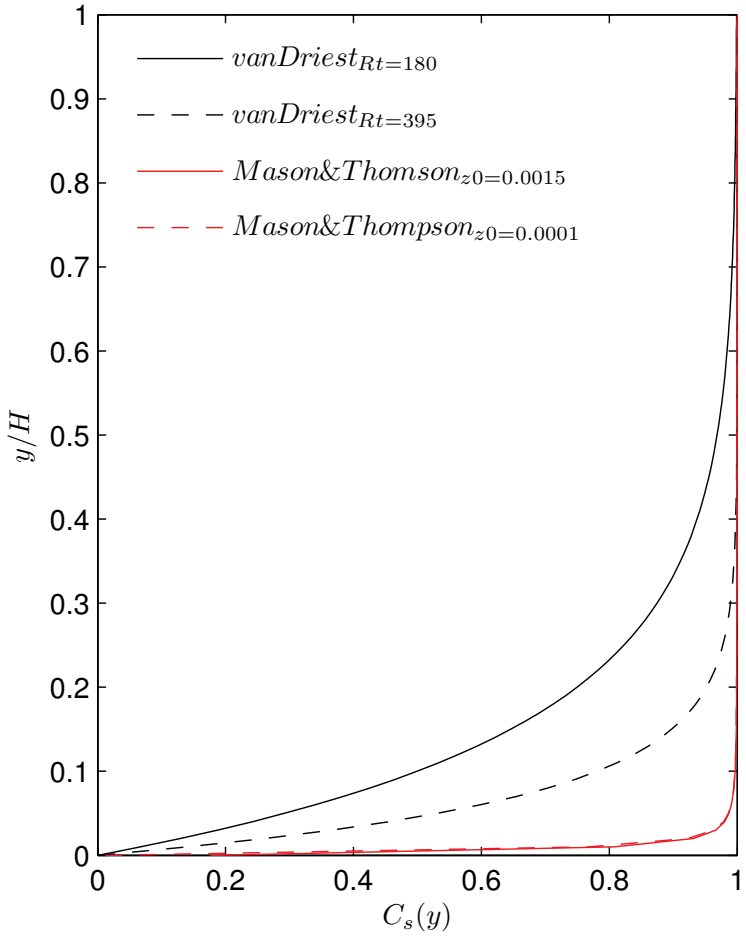

Figure 3.13: Representation of VanDriest (at two Reynolds numbers) and Mason & Thomson (at two roughness heights) damping functions for wall-resolved and wall-modeled Smagorinsky models, respectively.

close to the wall for the standard Smagorinsky (SM) model (Mason and Thomson, 1992)

$$\frac{1}{\lambda^n} = \frac{1}{\lambda_0^n} + \frac{1}{\kappa(z+z_0)^n} \text{ where } \lambda = C_s.\Delta \text{ and n=2.} \tag{3.9}$$

This relation forces the SGS mixing length [1] $\mathcal{L}$ to decrease close to the solid walls and merge with the expected $\mathcal{L} \sim z$ behavior (Bou-Zeid et al., 2005). Note that the damping functions used for the wall-resolved and wall-modeled cases are not identical. Figure 3.13 shows both vanDriest and Mason & Thomson damping functions used for different simulations conducted in this research.

[1] Following Prandtl's definition, (Prandtl, L. (1925). "Z. angew". Math. Mech. **5** (1): 136-139.), a mixing length can be defined as a characteristic distance in which a fluid parcel will conserve its properties before mixing with the surrounding fluid

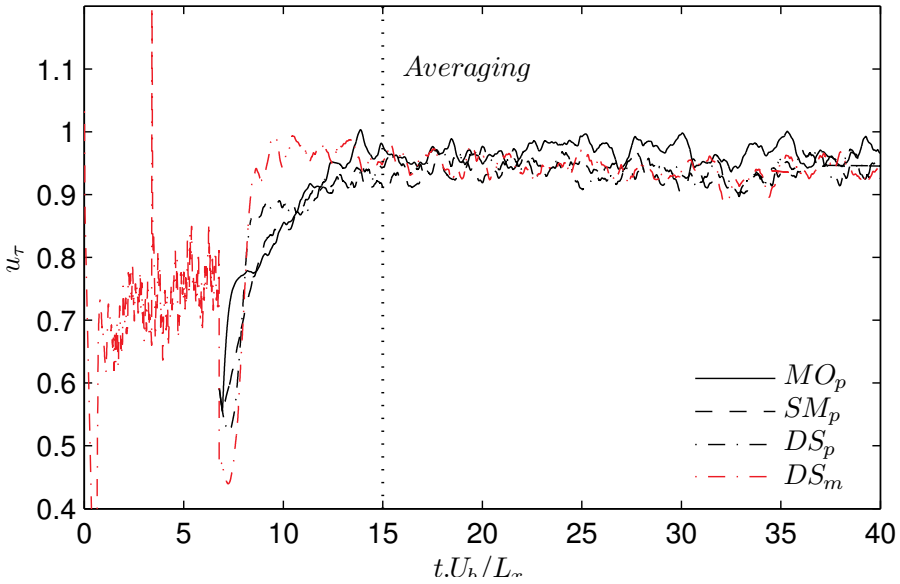

Figure 3.14: Time evolution of the skin friction velocity using different SGS models, used to identify the statistically-stationary state of the flow.

Figure 3.14 shows the temporal evolution of the skin friction velocity for four different test case. For the first five Non-dimentional Time Units (NTU), the solution is accelerated on a twice coarser grid for all of the cases, and then the solution is mapped to the finer mesh. The transition takes place after about 15 NTUs, and the statistics are averaged for around 25 NTUs. Employing the imposed mass flux method using the dynamic Smagorinsky model resulted in achieving the fastest convergence, as compared with the other SGS models and also compared with pressure gradiant approach.

Similar to the wall-resolved cases, figure 3.15 shows the normalized mean streamwise velocity profiles in the standard and Logarithmic axes wall units for different ABL simulations. As shown in the figure, the dynamic Smagorinsky model predicts a closer velocity profile to the logarithmic profile. It can also be seen from the figures that for most of the SGS cases, the velocity at the core is over-predicted. The reason can most likely be explained by the inconsistency between the law-of-the-wall concept and its implementation in LES. The law-of-the-wall was originally derived in an average sense, i.e.,

$$\tau_w|^{log} = -\left[\frac{\kappa}{ln(z/z0)}\right]\overline{\langle u\rangle}^2 \quad \text{and } \overline{\langle v\rangle}^2 = 0, \tag{3.10}$$

as introduced by Von Karman (1930). In LES implementations, however, the mean stress that is imposed (over time) on the flow is

$$\tau_w|^{LES}(x,z,t) = -\left[\frac{\kappa}{ln(z/z0)}\right](\overline{\langle u(x,2,z,t)\rangle}^2 + \overline{\langle v(x,2,z,t)\rangle}^2). \tag{3.11}$$

Due to the presence of velocity fluctuations, $\langle \bar{u}^2 \rangle \geq \langle \bar{u} \rangle^2$. Therefore using local fluctuating velocities instead of the time averaged values leads to an over-predicted imposed wall shear stress which slows down the flow close to the wall compared to the standard Logarithmic profile. The jump shown at the right end of the DS plot in figure 3.15(b) is known as the wake layer and has been observed in experimental data as well (Coles, 1956).

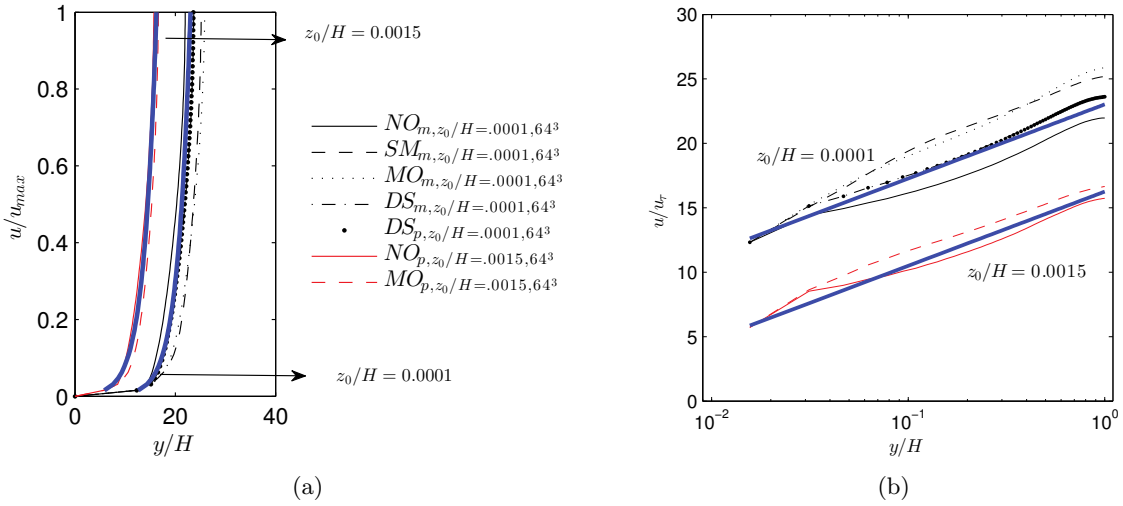

(a) (b)

Figure 3.15: (a) Mean normalized streamwise velocity using different SGS models and flow resolutions and (b) Mean streamwise velocity in wall units. The blue lines are standard logarithmic profile. Note that since the difference in mean velocities using different roughness lengths is significant, the velocity plots are not shifted unlike the wall-resolved cases.

The variances of the resolved velocity components normalized by the friction velocity and the TKE plots are shown in figure 3.16. Results are compared with the scale dependent dynamic Largrangian SGS model simulations of Bou-Zeid et al. (2005) which are made on a 64^3 uniform mesh with the same roughness height of $z0/H_{Bou-zeid} = 0.0001$ and plotted in blue in the figure. It can be appreciated that the NO model results in the highest values due to its non-physically excessive turbulent fluctuations. The values predicted by other SGS models are somewhat lower than the NO model. LES of Bou-Zeid et al. (2005), however, gives a similar value to the NO model for the u and w components in the top of the boundary layer (lower right) and gradually adapts to the other SGS models close to the wall. The standard Smagorinsky model also under-predicts the peak values. The rest of the test cases show a similar behaviour that compares well with Bou-Zeid et al. (2005). However, the difference rises close to

the wall between the different test cases.

Figure 3.17 shows the normalized eddy viscosity comparisons using different test cases. A quick comparison with its wall resolved counterpart (figure 3.5) reveals that the normalized eddy viscosities for ABL cases are much larger than the low Reynolds number cases. That is why the SGS modeling plays a more important role in the accuracy of the simulations. It is seen from the figure that the eddy viscosities predicted by the SM model are much higher than the rest of the SGS models, which is in agreement with the previous studies arguing that the Smagorinsky model is over-dissipative.

The flow structures using different SGS models and roughness heights can be visually compared in figure 3.18. It is seen that the flow predicted by the NO model is contaminated by small structures because of the lack of physically present dissipation. The Smagorinsky model (SM) on the other hand, over-dissipates the energy and results in larger flow structures. The MO model gives a similar flow structure to that of the DS model. The flow structures for the high roughness case are somewhat similar to the low roughness case. Yet the predicted velocities are smaller for the high roughness case which is due to the increased shear stresses imposed at the wall.

Figure 3.19 shows a top-view of the velocity snapshots for the fully-developed boundary layer flows at different Reynolds numbers at different heights from the ground. Note that for the wall-resolved case, the dimensions of the domain are presented using wall units since the flow is characterized by the skin friction velocity and viscous length whereas in the ABL cases, the ABL height is used to normalize the dimensions. The streamwise velocity streaks are significant in the low Reynolds number flow. Their length may extend up to 1000 wall units whereas their width can be of the order of 50 wall units. This can be interpreted as the meshing requirement in the near-wall region since the grid should be able to capture these streamwise streaks accurately. Figures 3.19(b) and 3.19(c) show similar velocity structures with weaker velocity streaks as a result of wall modeling. It can also be seen that, for the low roughness case (3.19(b)) the velocity streaks are less dominant at $y/H \sim 0.02$.

3.4 Wind farm simulations in the neutral ABL

This section discusses the application of the wall-modeled (WM) LES, as discussed in the previous section, and the prescribed Mean Shear (PMS) methods in the LES of an infinite wind farm, that is, fully developed flow simulations in the atmospheric boundary layer at the presence of wind turbines. The wind turbines are modeled using actuator disc turbine parametrization. WM simulations of the fully-developed

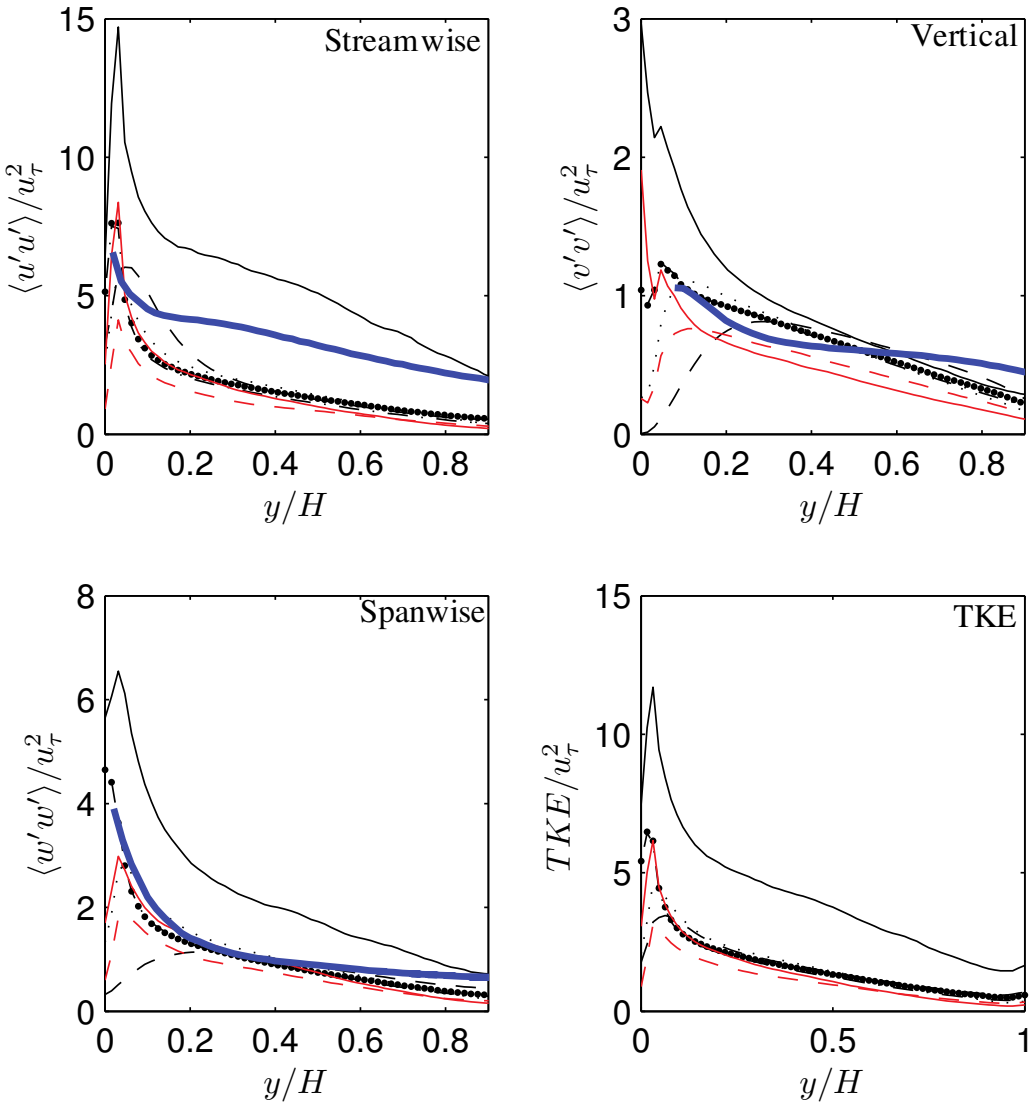

Figure 3.16: Turbulence intensity components and the turbulent kinetic energy. The blue lines are taken from the LES data from Bou-Zeid et al. (2005) using the Scale dependent dynamic Lagrangian SGS model on a 64^3 mesh, and the rest of the legends are similar to 3.15.

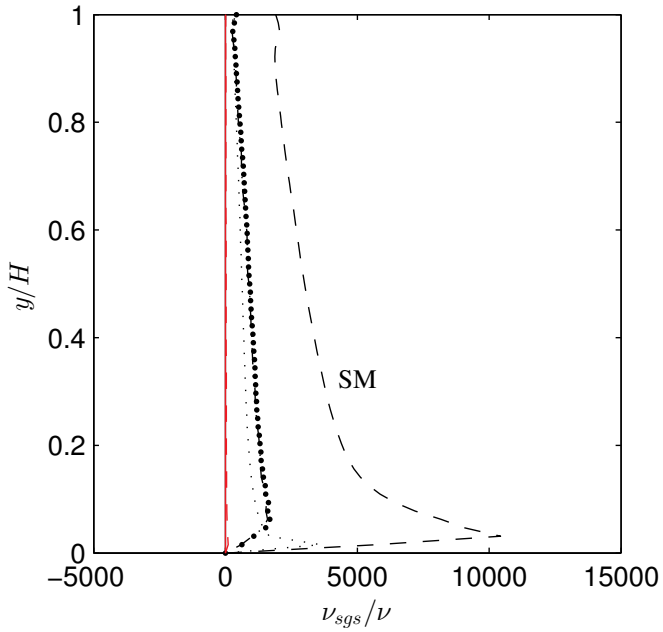

Figure 3.17: Non-dimentional eddy viscosity profile (legends are similar to 3.15).

wind farm boundary layer are performed by including the wind turbines directly in a fully-developed ABL flow with cyclic domain similar to the cases discussed in the previous sections, and running the simulations with the wind turbines present until a new fully-developed regime is established. In the PMS cases, as outlined in chapter 1, the initial boundary layer obtained using a standard logarithmic profile is enforced through the computational domain using body forces. To account for the turbulence, velocity components of a pre-generated turbulent box are extracted and imposed using unsteady body forces at the inlet with the method described in 1.3.3 (see Sarlak and Sørensen (2013); Troldborg et al. (2007) for more details). To compare the same flow field, the parameters for generating the turbulence box were chosen to give the same turbulence intensities as in the WM case. Figure 3.20 shows the domains used for WM and PMS simulations.

For the WM case, a $\frac{z_0}{H} = 0.0001$ roughness height is chosen, and the simulations are run on a domain of $10R\pi \times 10R \times 10R\pi$ in streamwise, vertical, and lateral directions where R is the rotor radius. The grid resolution is 64^3 cells, distributed equidistantly in all directions. The resulting fully developed flow is used as initial flow field and the turbines are placed in order to extract the energy of the ABL.

For the PMS computations, instead of a cyclic domain, a long domain of $87R\pi \times 10R \times 10R\pi$ in streamwise, vertical, and lateral directions is chosen with a total number

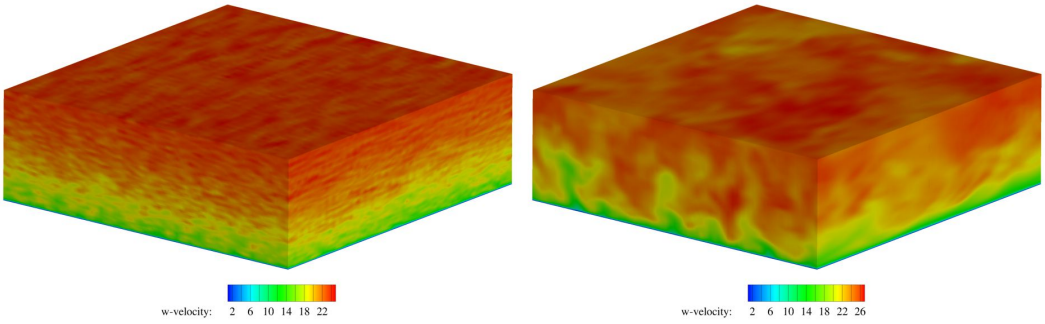

(a) NO, $z_0/H = 0.0015$ (b) SM, $z_0/H = 0.0015$

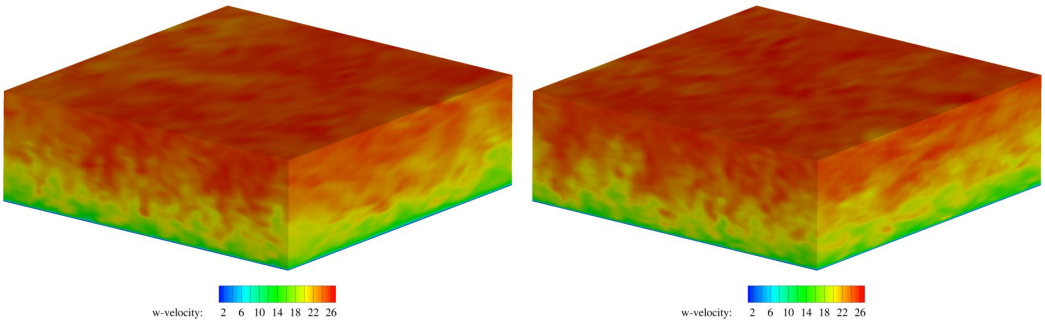

(c) MO, $z_0/H = 0.0015$ (d) DS, $z_0/H = 0.0015$

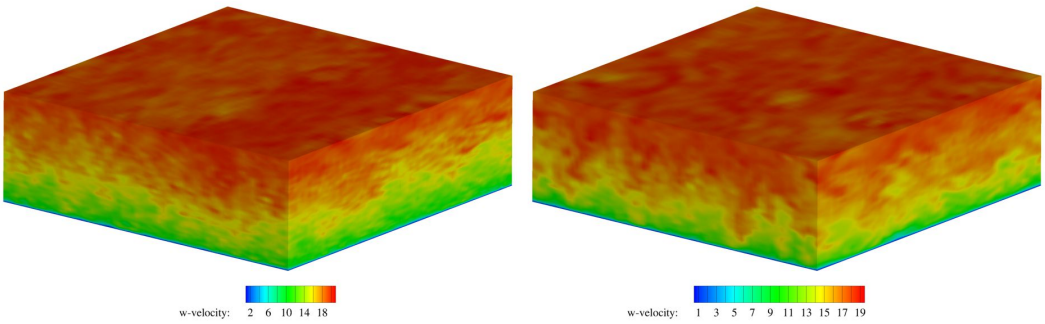

(e) NO, $z_0/H = 0.0001$ (f) MO, $z_0/H = 0.0001$

Figure 3.18: Velocity snapshots using different SGS models using z0/H=0.0015 (a) NO, (b) SM, (c) MO, (d) DS and z0/H=0.0001 (e) NO, (f) MO. Note, for instance, the significant change between sub figures (a) and (b) due to increase of the SGS model's dissipation.

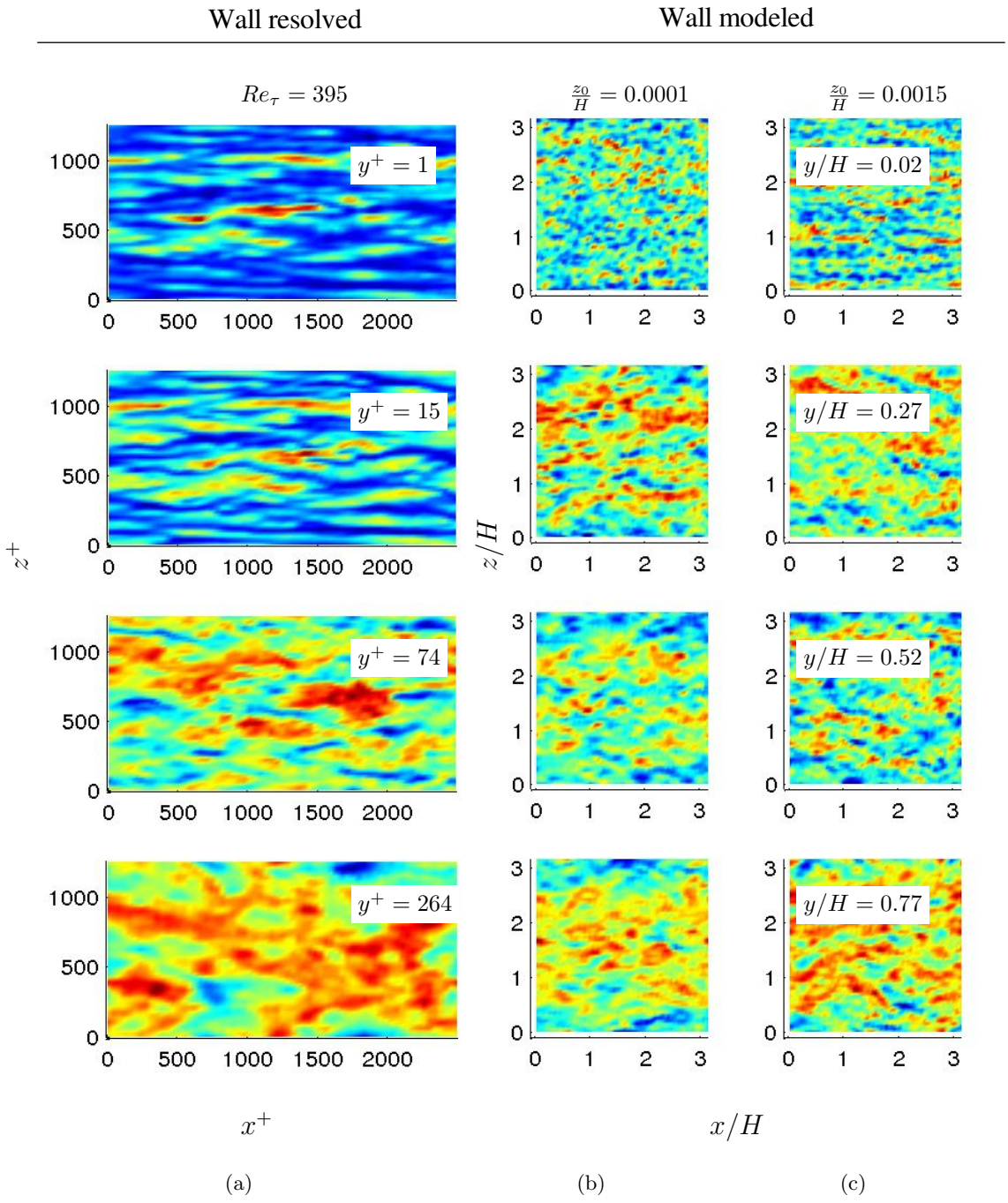

Figure 3.19: Comparison of flow structures in (a) wall-resolved flow at $Re_\tau = 395$ (b) wall-modeled ABL with low roughness $\frac{z_0}{H} = 0.0001$ using Dynamic Smagorinsky model and (c) ABL with high roughness $\frac{z_0}{H} = 0.0015$ using Mix-O model.

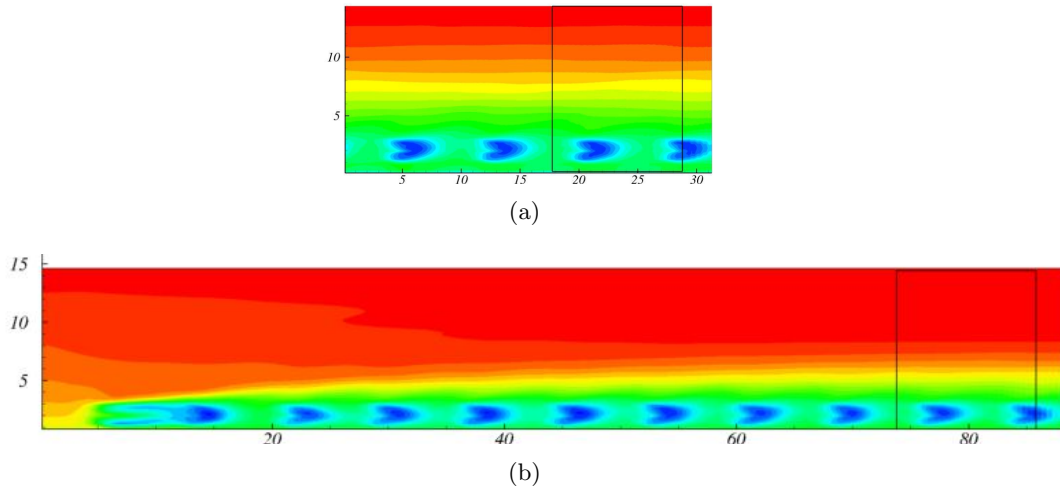

Figure 3.20: Mean streamwise velocity contours obtained by using (a) the WM and (b) the PMS approaches. The solid black lines represent the location where the quantitative comparisons are performed.

of 11 turbines. The turbines are placed equidistantly in a row with the same separation as the WM cases and the statistics are obtained at the location where the flow has become fully developed, that is the black box shown in figure 3.20.

3.4.1 Turbine parametrization

The rotating actuator disc (AD) model (Mikkelsen, 2003; Sørensen and Myken, 1992) is used to simulate the effect of the wind turbines. In the actuator disc model of a turbine of B blades, each rotor is divided into a finite number of sections. For each section, the aerodynamic coefficients, C_L and C_D, are looked up from a table based on the relative velocity, the angle of attack α, and the chord length c. The relative velocity on an airfoil element is determined as $\mathbf{V}_{rel} = (V_n, V_\theta - \Omega r)$ where the sub-scripts n and θ denote the axial and the tangential directions respectively, V_n and V_θ are the axial and tangential velocity components in the inertial frame of reference, obtained from CFD solution, and Ω is the angular velocity of the disc (see figure 3.21). The flow angle between V_{rel} and the rotor plane is then defined as $\phi = tan^{-1}\left(\frac{V_0}{\Omega r - V_\theta}\right)$.
The local angle of attack $\alpha = \phi - \gamma$ (with γ being the pitch angle), is used for the table look-up to find the C_L and C_D values, according to $(f_L, f_D) = 0.5\rho V_{rel}^2 cB(C_L e_L, C_D e_D)$, where B = 3 and e_L and e_D are unit vectors showing the direction of the lift f_L and drag f_D forces. The tangential and normal forces to be exerted on the flow domain are then calculated as

$$F_n = L\,cos(\phi) + D\,sin(\phi) \quad \text{and } F_\theta = L\,sin(\phi) - D\,cos(\phi). \tag{3.12}$$

The obtained forces are finally interpolated from the AD grid to the flow field and applied as body forces using a smoothing function of Gaussian shape.

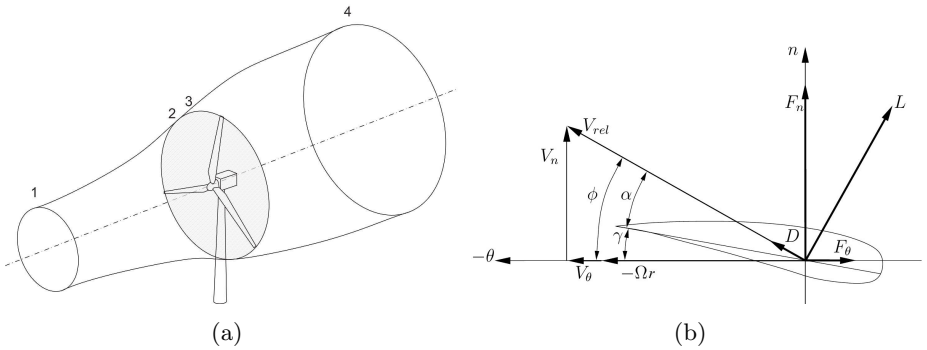

Figure 3.21: (a) The AD and its surrounding volume (b) Airfoil cross sectional element (Mikkelsen, 2003).

For the simulations performed in this chapter, the AD model of the Tjæreborg turbine is used at the fixed tip speed ratio of $\lambda = 8$. The turbine consists of different NACA 44xx airfoils and with a chord varying between 0.9 m at the tip and 3.3 m at hub. The blades are linearly twisted 0.33^o per meter. The rotor has a radius of 30.5m and rotates at $\Omega = 22.1$ rpm. (See Mikkelsen (2003) for more information about the turbine). The airfoil lift and drag polars of the tip and root sections are plotted in figure 3.22. The data are taken from wind tunnel measurements Abbott (1999) with corrections for the three-dimensional effects at high angles of attack (cf.Troldborg (2008)).

3.4.2 Simulation results

Figure 3.23 demonstrates the velocity plots obtained from the WM case at the rotor plane as well as 7 rotor radii downstream the turbine ($x/R = 0, 7$) showing the development of the near wake into the far-wake Gaussian wake profile. Red dots represent the fully-developed boundary layer in absence of the wind turbine models. The mean velocity profile is also obtained by averaging the velocity in the horizontal direction. The mean profiles are plotted with square markers. The thick blue dot-dashed-lines in figure 3.23(b) show the tangents to the mean wake profile. As can be seen, the mean

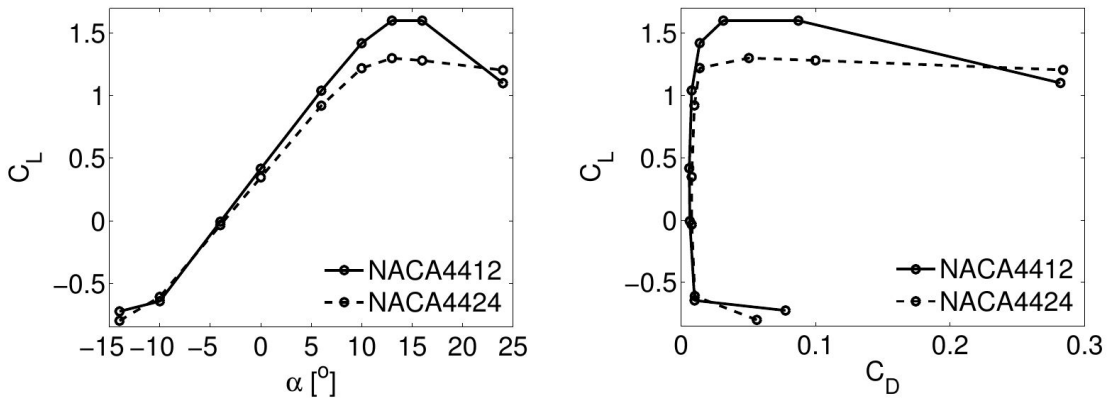

Figure 3.22: (left) lift and (right) lift/drag polars of the NACA 4412 and 4424 airfoils used near the tip and the root, respectively (Troldborg, 2008).

flow can be divided into two regions below and above the rotor plane. As can be appreciated, each region can be represented by its own Logarithmic law corresponding to two roughness heights. It is then possible to improvise an *effective* surface roughness due to the effect of the infinite wind farms. The effective roughness caused by a cluster of obstacles (and in some cases particularly wind turbines) is elaborated further in other empirical Lettau (1969), theoretical Frandsen (1992), and numerical Calaf et al. (2010) studies by assessing the vertical change in the atmospheric boundary layer due to the presence of the wind farms and obstacles in general.

Figure 3.24 shows the comparison of mean streamwise velocity, the Reynolds shear stress, r.m.s. of the streamwise velocity, and the turbulence kinetic energy at different locations using both WM and PMS approaches. As can be appreciated, in the turbine region, the PMS has captured the WM simulations rather closely for all statistics. There are however large differences above the turbine region. The reason for the mismatch between the turbulence stress profiles between the WM and the PMS can be explained by the slightly different velocity profile that is imposed to the PMS case, rather than the naturally developed boundary layer of the WM case. A similar behavior was observed by Tuerke and Jiménez (2013) in artificially generated velocity profiles and it was concluded that even a slightly incorrect imposed velocity profile modifies the Reynolds stresses substantially. The difference in the wall boundary condition implementation, that is, the absence of no-slip wall boundary condition in the PMS approach -since the flow slow-down is imposed by pre-defined body forces- is also responsible for the dissimilarities.

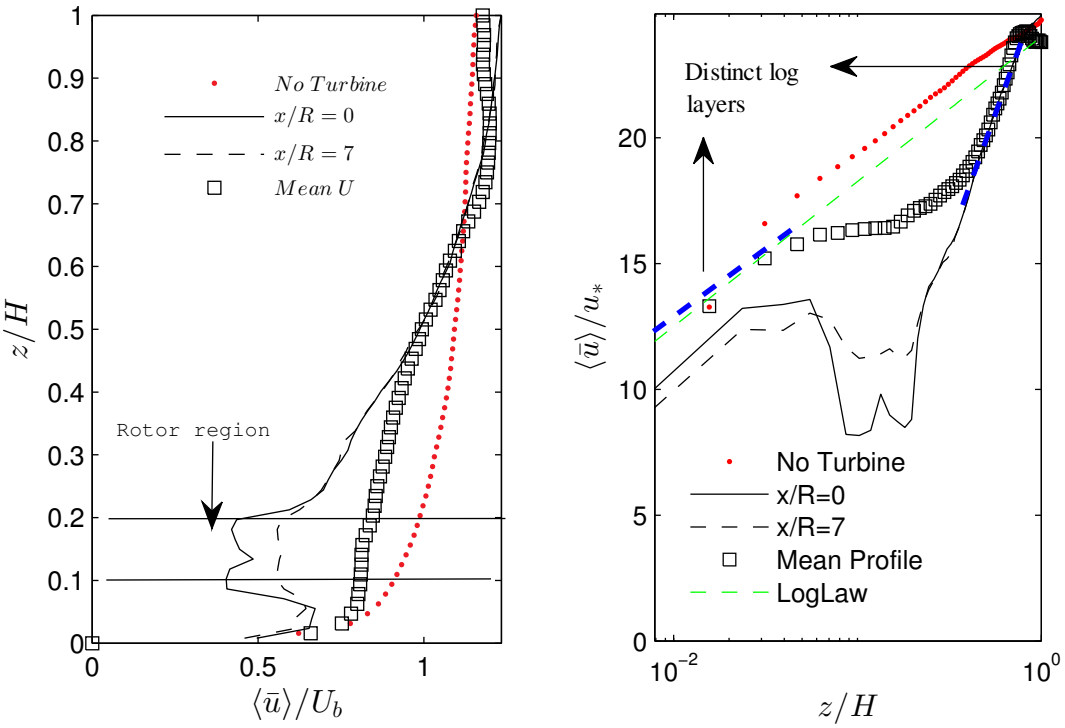

(a) (b)

Figure 3.23: (a) Mean streamwise velocity normalized by the bulk velocity and (b) the Logarithmic plot of the mean streamwise velocity normalized by the friction velocity of the fully developed wind farm boundary layer obtained using Wall-Modeled LES simulations. The red dots refer to the case without wind turbine models, the square markers represents horizontally averaged velocity profile and the solid and dashed lines correspond to 0 and 7 rotor radius downstream of the rotor, respectively.

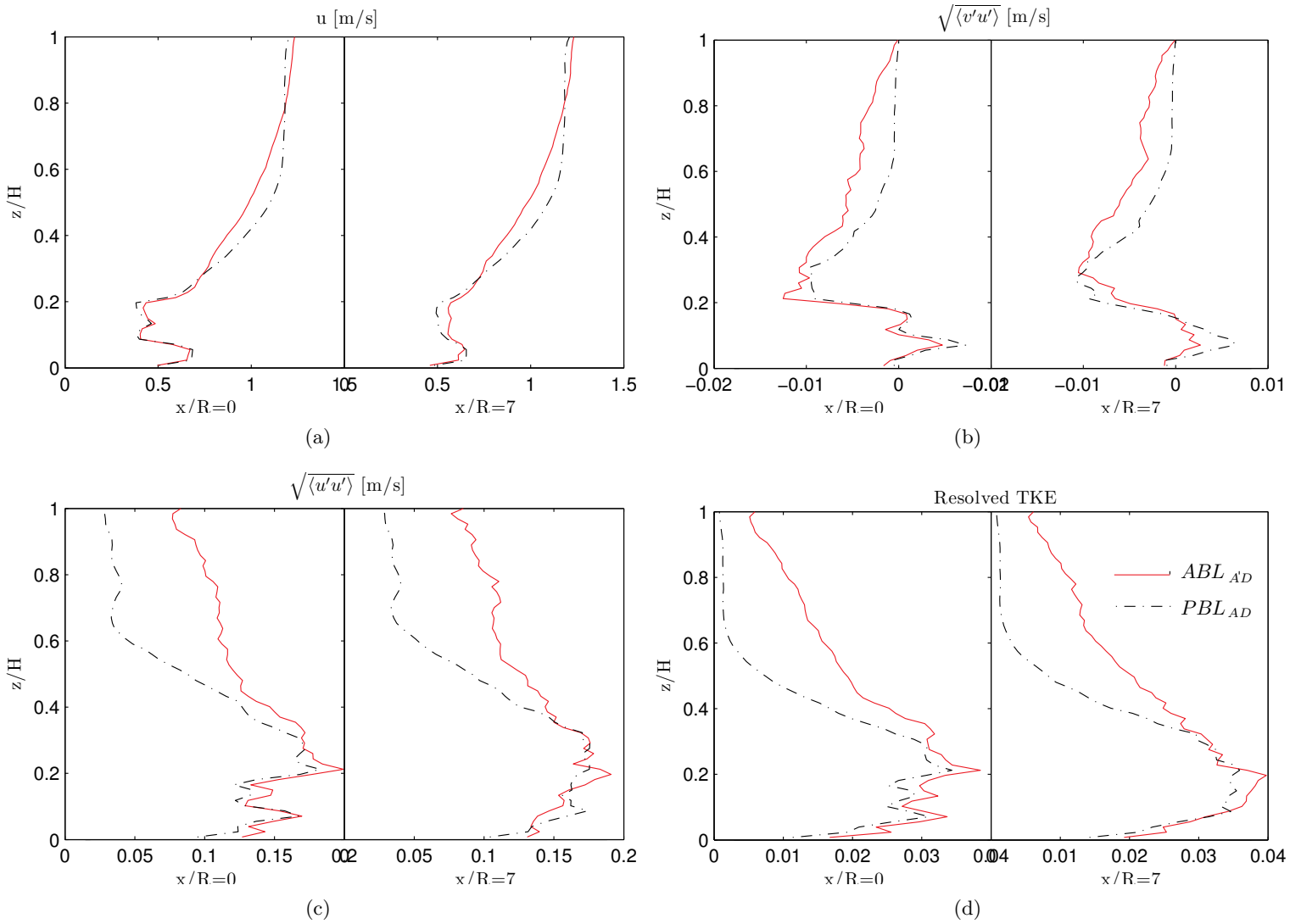

Figure 3.24: Profiles of (a) Mean streamwise velocity, (b) resolved turbulent shear stress, (c) streamwise velocity r.m.s, and (d) TKE, obtained using WM and PMS approach.

Figure 3.25 shows the comparisons of the energy spectra of the streamwise velocity for WM and PMS methods at different heights of the ABL as a function of the distance from the ground. As can be seen there is a very close match between the spectra at the low heights and around the rotor plane, although at the higher distances from the wall, the spectra obtained by the PMS approach start to become smaller than the WM showing a lower energy content. In all cases, the inertial sub-range is captured reasonably accurate.

It is often useful to investigate the velocity autocorrelation (AC) to identify the size of turbulent structures in the flow. AC is defined as the average of the product of the velocity components at two reference times and can indicate the memory of the process, that is, the time over which a coherent structure can be identified in the flow.

$$C(\tau) \equiv \langle u(t)\, u(t+\tau) \rangle , \tag{3.13}$$

where τ is the time lag between the two components. Figure 3.26 shows the autocorrelation function obtained for the WM with and without turbines present as well as for the PMS method. A total of 100 time steps is used as the maximum time lag and the temporal correlation is transformed into the spatial correlation based on the Taylor's frozen turbulence hypothesis to have an indication of the spatial size of the flow structures in the abscissa. The figure shows that the correlation of the WM simulations (without turbine model) is higher than the cases with the turbine model because the flow structures are broken by the wake of the turbine for the latter case. The WM and PMS cases with the turbine model included exhibit a similar behaviour. However, the structures obtained by the WM method are of slightly higher correlation. This could be explained by the different domain and boundary conditions used for WM and PMS methods, although the turbine spacings are the same. The WM case is simulated using a cyclic domain and therefore there might be low-frequency domain-dependent flow structures that affect the correlations, whereas the PMS is simulated using a long domain with inlet and outlet BC. In conclusion, the PMS method is shown to be capable of providing an accurate flow with lower computational cost than a wall-modeled LES as there is no need to run cyclic simulations for a long computational time in order to get the right fully developed velocity field.

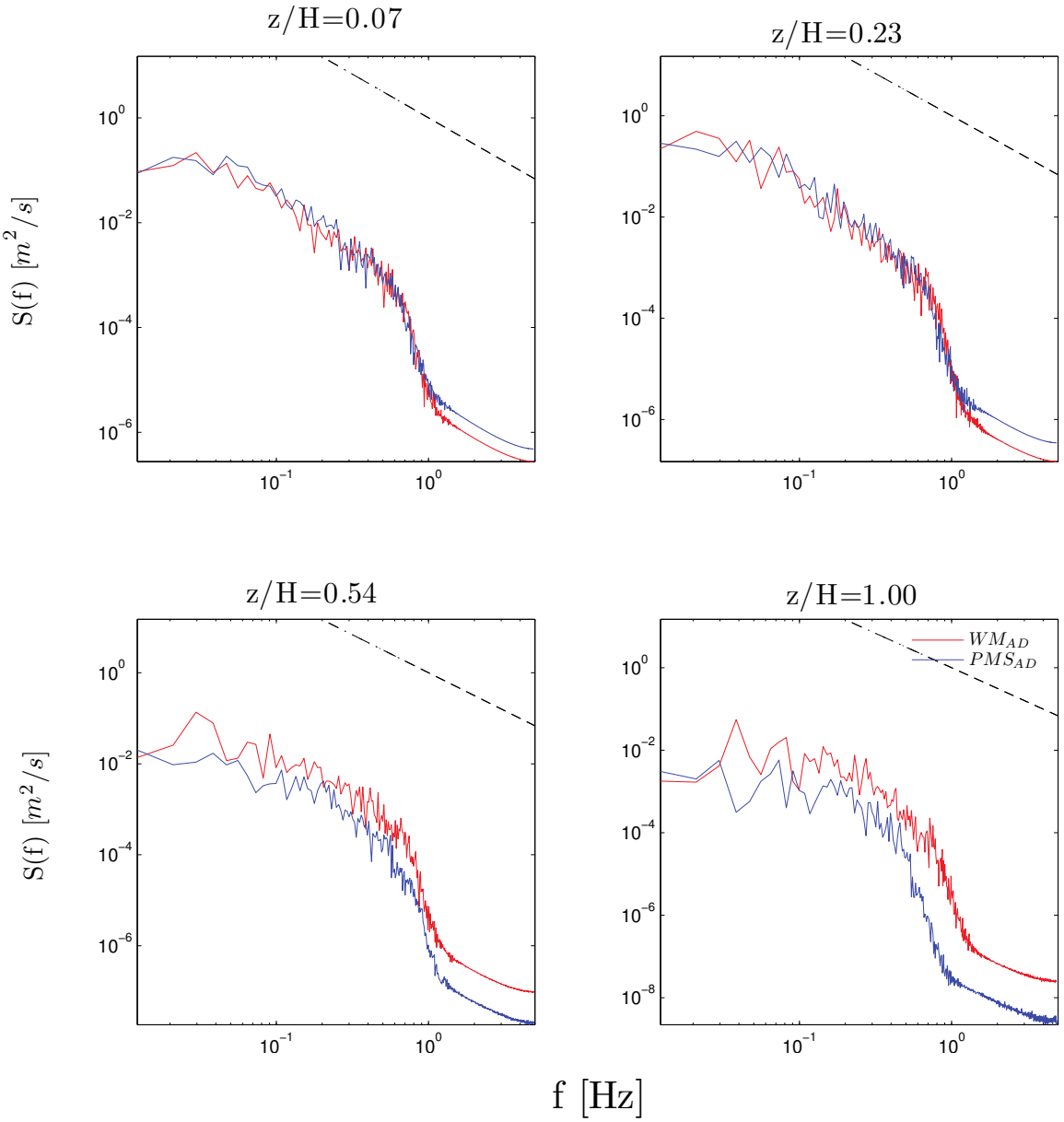

Figure 3.25: Streamwise velocity energy spectra at different heights of the ABL for WM and PMS approaches using AD representation of the wind turbines. Dashed line represents the $\frac{-5}{3}$ law in the inertial range.

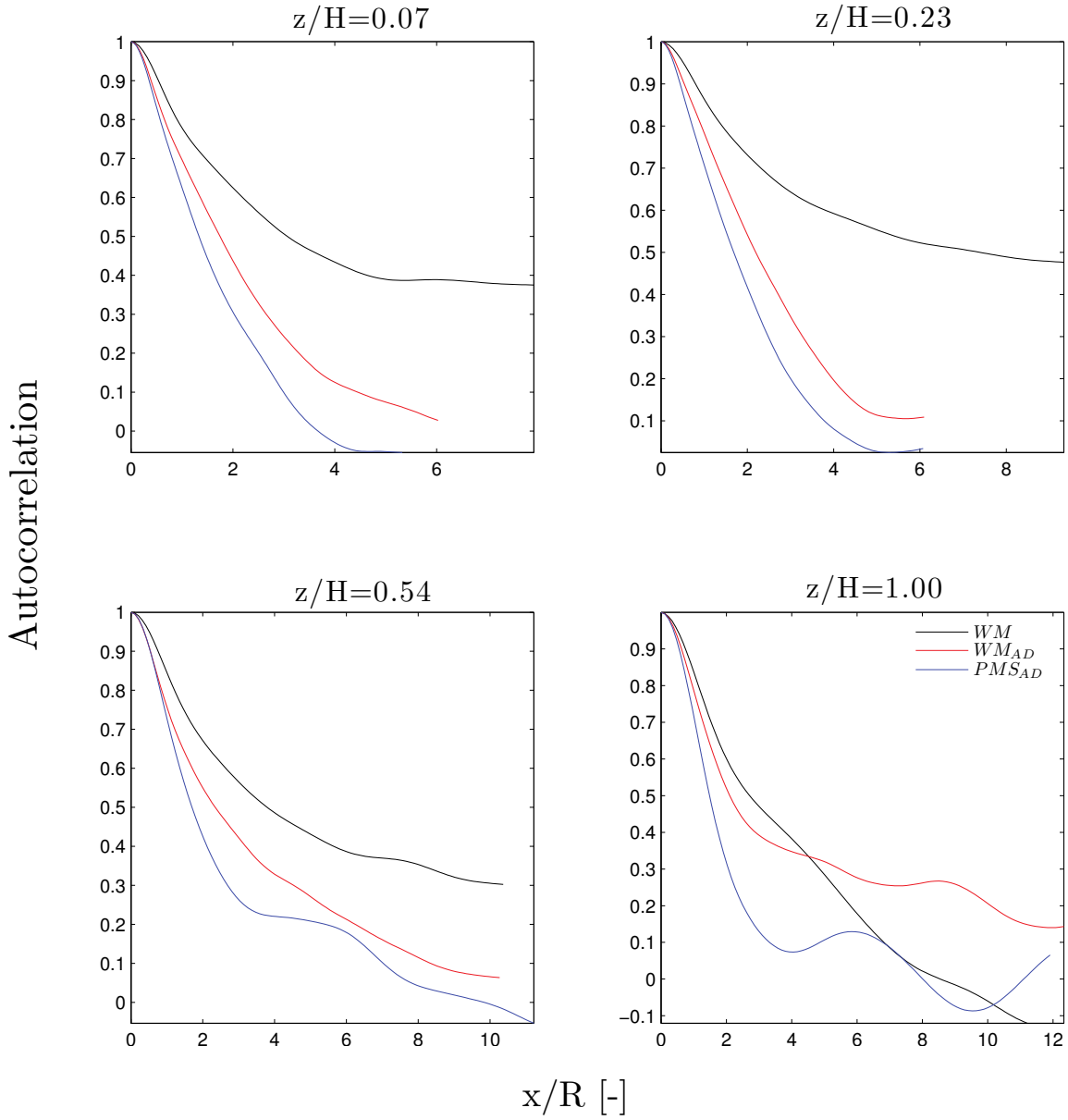

Figure 3.26: Comparison of streamwise velocity autocorrelation at different heights of the ABL for WM and PMS approaches.

3.5 Summary

In this chapter, simulations of the fully developed boundary layer flows with and without heat transfer present from the walls were conducted to examine the role of the grid resolution and SGS modeling on the simulation results. For the low Reynolds number flows, a no-slip boundary condition was implemented at the wall and for the high Reynolds number ABL simulations, the wall functions were introduced to run simulations on rather coarse grids. It was shown that, unlike the low Reynolds number cases, the wall-modeled simulations were more sensitive to the choice of the SGS modeling and the use of the dynamic SGS model was found necessary to predict a more accurate flow statistics. The fully-developed wind farm boundary layer was also studied using the wall-modeled LES and the PMS approach and the results were compared for both approaches. The PMS simulations were able to predict the flow statistics reasonably well around the rotor region. However, some discrepancies were observed between the models, especially above the rotor height, due to the modeling inconsistencies. Particularly, a lower mixing and vertical momentum flux was found using the PMS approach due to the slightly inconsistent implementations of WM LES and PMS methods. There is nonetheless potential for further investigations on the PMS approach in the future, in terms of the thermally stratified flows etc. Next chapter discusses wind tunnel measurements and LES computations of the flow around a 2D airfoil section.

Chapter 4

Flow measurements and LES of airfoils at low and moderate Reynolds numbers

Recently, a series of blind test comparisons on experimental measurements of model scale wind turbines was conducted in a Norwegian low-speed wind tunnel (Krogstad and Lund, 2012), with several researchers invited to perform numerical simulations of rotor performance and wake characteristics. The blades had an NREL S826 airfoil section from root to tip. The design Reynolds number for the rotor airfoil sections was of the order of 100,000 and one of the challenges to perform the right comparison with the experimental results was the lack of accurate airfoil data at the relevant low Reynolds numbers. As a participant in the campaign, the main aim was to establish airfoil polars to be served as input to rotor analysis tools, such as the BEM and actuator line methods. In this chapter, the wind tunnel measurements of the S826 airfoil for selected Reynolds numbers are therefore presented. The results of measurements are then used as a reference and the LES of the NREL S826 airfoil at low Reynolds numbers for the airfoil are performed and validated.

4.1 Introduction

Today's computational power limits the applicability of the wall-resolved LES for the flow over airfoils. Some of the difficulties include capturing separation and prediction of transition to turbulence. The transition location plays a significant role on aerodynamic characteristics of the airfoil. Simulation of transition usually requires low dissipative

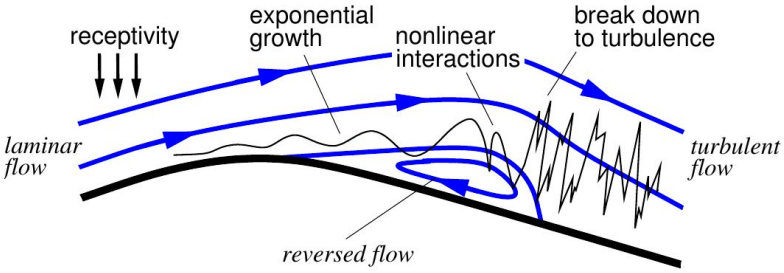

Figure 4.1: Sketch of the laminar separation bubble formed over the airfoil surface. Reproduced from Windte et al. (2004).

and dispersive solvers (Uranga et al., 2009), so the use of high order methods or explicit filtering (as discussed in chapter 2) would be beneficial. Transition of the low Reynolds number flows over aerofoils gives rise to the generation of a *Laminar Separation Bubble* (LSB). The LSB is formed in most cases due to the separation and sudden reattachment of the boundary layer in the presence of an adverse pressure gradient. The separation takes place due to the growth of the small disturbances which can be, for instance, originally caused by small imperfections on the airfoil surface. The momentum flux into the boundary layer then pushes the flow down to reattach to the surface and as a result, a closed bubble (in the time averaged sense) is formed. LSB results in a reduced suction over the forward portion of airfoil and lowers the pressure recovery in the rear parts (Windte et al., 2004) and can lead to excessive drag and low maximum lift.

A schematic diagram of the flow generation phases over the airfoil is shown in figure 4.1. The growth of small perturbations generated by acoustic disturbances etc. leads to the 2D Tollmien-Schlichting (T-S) waves. The growth of the T-S waves generate highly non-linear waves that interact with each other and initiate the flow separation and turbulence further down toward the trailing edge (Windte et al., 2004).

Another feature of the flow over airfoils with a considerable span width, is the formation of stall cells. Stall cells are 3D structures formed on the suction side of the airfoil and are caused by the periodic spanwise breakdown of the separated region at high angles of attack (Rodríguez and Theofilis, 2011). There are empirical models for the time-averaged structure of the stall cells (Winkelman and Barlow, 1980) and they can also be observed using measurement techniques and numerical simulations. The appearance of LSB and stall cell formation are discussed again in section 4.4.

4.2 The experimental set-up

This section discusses the wind tunnel measurements of the NREL S826 airfoil. The 14% thickness airfoil has chord and span lengths of 100mm and 499mm, respectively

and is made of Aluminium using CNC-milling, with surface accuracy of ±0.01mm. Due to the machining limitations, the trailing edge is cut with a finite thickness of 0.5mm. The experiments are performed at the Fluid Mechanics laboratory at the Technical University of Denmark. The red tunnel facility shown in figure 4.2 is a low speed open loop wind tunnel with a cross section of $500 \times 500\ mm^2$, a contraction ratio of 1:12.5, and capable of gaining uniform wind velocities up to $U_\infty = 65$m/s with a maximum turbulent intensity of 0.22%.

Figure 4.2: Wind tunnel facility at the Technical University of Denmark (left) and the test section of the wind-tunnel (right) showing the vertically mounted airfoil, pitot tube, and wake-rake.

Figure 4.3 shows the turbulence intensity (TI) levels as a function of tunnel velocity and the mean pressure drop along the side walls for different inlet velocities. It can be seen that the TI decreases with increase in the velocity and it has a value of 0.22% for $U_\infty = 15$ m/s, which corresponds to the chord Reynolds number of 100,000. The velocity distribution shows a reasonably uniform inflow at different spanwise locations.

The wind tunnel is equipped with the force balance, wake-rake, pressure taps on the test section's side walls and a set of JVL MAC servomotors of 4096 $\frac{pulse}{rev}$ and encoder for pitching the blade with an accuracy of ±0.01°. Pressure distribution over the airfoil and the force gauge measurements are performed to compute the lift, drag and moment coefficient. The bottom of the airfoil is connected to a one component, full bridge force gage through a connection rod where the other end can move freely. Two different gages with ±200N (±0.03N) and ±20N (±0.002N) are used. A total of 30 pressure taps is mounted unevenly on the suction and pressure sides at mid-span and along a 30° chordwise line. Pressure taps are connected to two sets of PSI pressure scanners

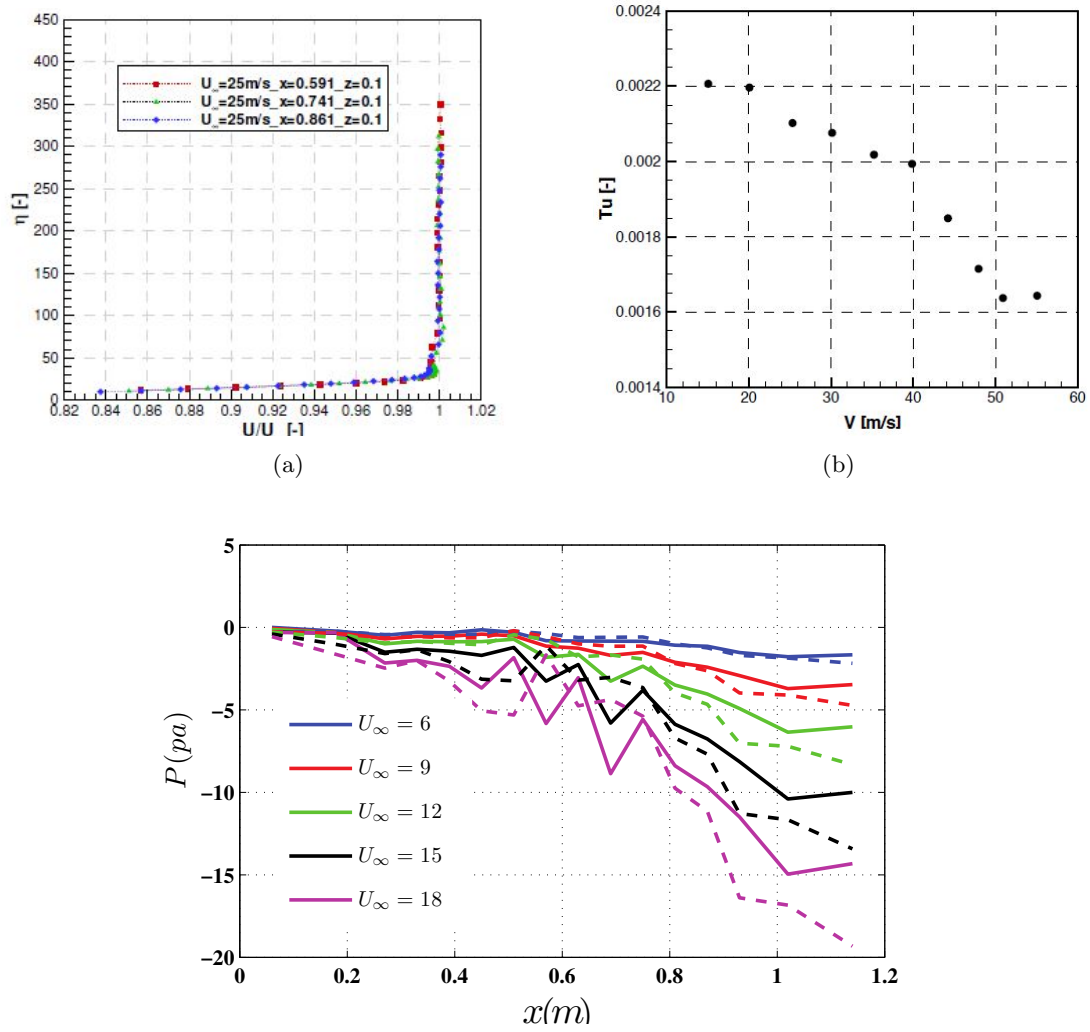

Figure 4.3: (a) Mean velocity profile of the empty tunnel test section at U_∞=25m/s at different spanwise locations. (b) Turbulence intensity of the empty tunnel at different wind velocities. (c) Mean pressure distribution measured at the wind-tunnel side walls. The full and the dashed lines represent the pressure distribution along the right and left walls, respectively.

with a pressure range of ±6895Pa (±1psi) and ±2540Pa ($\pm 10 in H_2O$), respectively. They measure the pressure with an accuracy of ±0.05% of the full scale. The PSI instrument has a maximum scan-rate of 20kHz which, considering a total of 64 taps, amounts for a maximum sampling frequency of 312.5Hz at each pressure tap. Also a set of pressure taps is distributed equidistantly along the test-section side walls. A linear wake-rake is mounted x=1.6c downstream of the airfoil and at a height z=2.1 c (c is the chord length) of the test object (no traverse of the wake-rake). The wake-rake contains 54 uniformly distributed tubes of 1mm diameter, with 3mm spacing between each tube, yet only 32 of the tube mounts are connected to the pressure scanners. The wake-rake and side wall pressure taps are connected to the same pressure sensors as those used for the airfoil. The stagnation pressure is then measured in front of each tube. Figure 4.4 presents the investigated airfoil, showing the location of the pressure taps and the corresponding normal vectors at each location. As shown in the figure, no taps are mounted at the Trailing Edge (TE), the second point from the TE, and on the pressure side near the Leading Edge (LE).

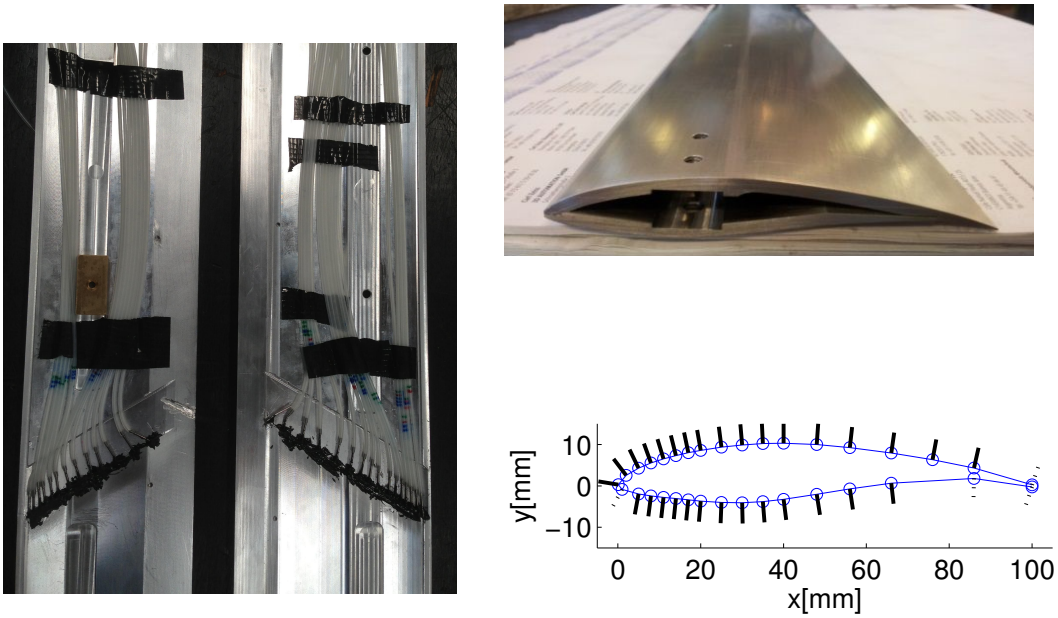

Figure 4.4: The CNC-machined S826 airfoil and the pressure tap locations. The points shown by dash-line are not instrumented and the pressure data is interpolated for these locations based on the neighbouring pressure tap values.

Pressure measurements are performed with a sampling frequency of 125Hz for a duration of 10 sec at each angle of incidence in the upstroke (from -10 to +25) as well

as downstroke (+25 to -10) pitching of the airfoil. The jump from each angle to the next one is performed using a step function and the corresponding recorded data are removed to ensure independence to the transition period.

Figure 4.5 shows the angle of attack settings in time and the corresponding lift coefficient and wind tunnel velocity changes for the Re=100,000 measurements. As can be seen, there is a velocity drop of 0.4m/s ($\sim 2.7\%U_\infty$) (and corresponding dynamic pressure drop) at the highest angle of attack which is caused by the increased drag from the foil (At $\alpha \leq 14°$, the drop is $0.1m/s \sim 0.6\%$). This drop makes the effective Reynolds number slightly lower at the smaller pitch angles. Figure 4.6 shows the airfoil pressure distribution as well as wake deficit measurements for Re=145,000 at angles of attack 0°, 5°, and 15°. The measured lift and drag polars as well as pressure distribution for various Reynolds numbers and angles of attack are benchmarked in the Appendix.

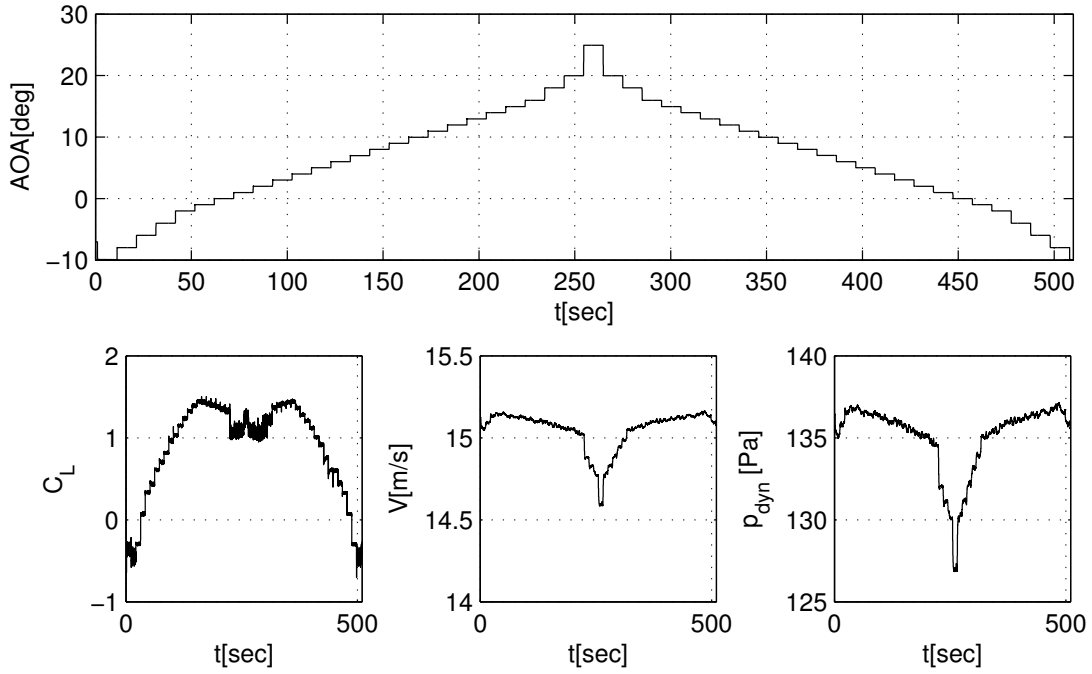

Figure 4.5: Airfoil measurements at Re=100,000. (top) Changes of the angle of attack in time and (bottom, left-to-right) corresponding changes in the force gauge lift coefficient, as well as tunnel velocity and the dynamic pressure.

4.2.1 Investigation of static stall hysteresis

At low Reynolds numbers, the turbulent momentum transport is smaller than the adverse pressure gradient effect so the momentum flux is not able to close the bubble

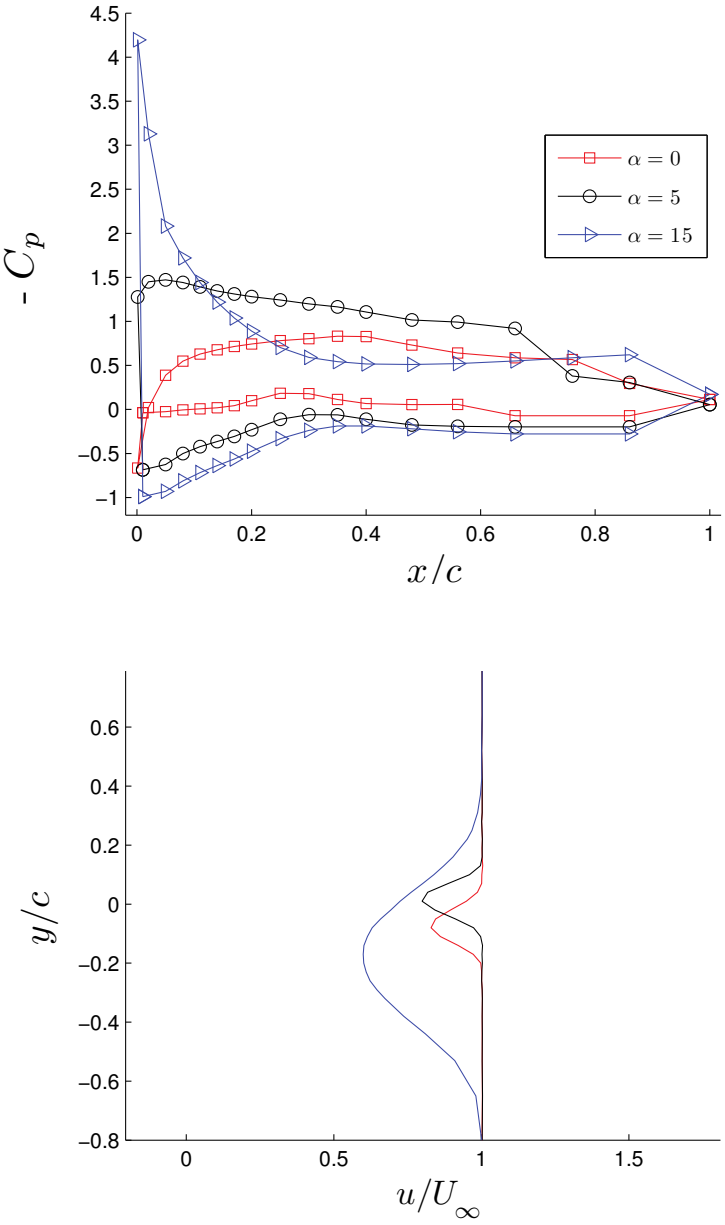

Figure 4.6: Airfoil measurements at Re=145,000. (a) C_p curve (b) Wake deficit.

and a large separation, potentially up to the trailing edge, is formed. This is followed by a further increase in C_D and a loss in C_L and results in a very non-linear behaviour in lift and drag prediction, and a strong hysteresis effect [1] can be observed. Figure

[1]The ability of the flow to remember its past history.

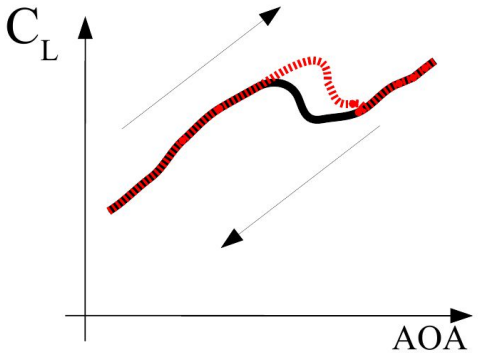

Figure 4.7: A sketch of the observed hysteresis effects: the effect of pitching direction on the predicted lift coefficients, particularlt at low Reynolds number and low free stream turbulence.

4.7 shows a schematic visualization of the effect of hysteresis on lift coefficient when a particular angle of attack is reached from lower or higher angles. The hysteresis effect can be removed by adding artificial turbulence or tripping the boundary layer close to the leading edge of the airfoil. To investigate the sensitivity of the airfoil to the hysteresis behaviour at low Reynolds numbers, an experiment has been performed to place a set of 3 parallel wires with cylindrical cross sections, vertically at a distance of $5.5c$ upstream of the test section to produce a turbulent in-flow with a low intensity. The wires are separated 15mm from each other. To have an accurate measure of the turbulence levels produced by the wires, they are first put in the empty tunnel test section and the turbulence intensity produced by the wires is measured using a single sensor ($5\mu m$ Tungsten wire) *55P11 1D* series hot-wire probe from Dantec Dynamics, mounted on a 1D traversing system. The hot-wire data are acquired using the MiniCTA software.

Figure 4.8(a) shows a sketch of the wire configuration in the tunnel, which is used to generate turbulence and figure 4.8(b) shows the corresponding turbulence intensities at different locations downstream of the test section showing the decay of turbulence alongside the tunnel. The empty tunnel without wires is represented by the markers for $U_\infty = 22.5$ and 30m/s and four wires of 1.3mm, 0.5mm, 0.32mm and 0.15mm thickness are used for the investigations. The turbulence intensities are then measured at different downstream locations where a decay of turbulence can be seen for almost all cases. Clearly, the thicker wires produce higher turbulence. It can also be seen that the turbulence levels are generally higher at lower velocities. For example, the 1.3mm thick wire produces turbulence intensities of 2.28%, 1.93%, and 1.85% with the wind speeds of 6m/s, 12m/s, and 18m/s, respectively, at three chords upstream of the airfoil LE location (x=-300mm). For the thin wires at small inlet velocities, no decay

of turbulence can be seen. This is because the Reynolds number (based on the wire width) for such cases is very small ($Re \approx \mathcal{O}(10-50)$), therefore, introduction of the wire does not make a fully turbulent wake. Nevertheless, it can be assumed that a wire of $D = 0.15mm$ leads to a turbulent flow with $\approx 0.15\%$ intensity at inlet velocities smaller than $\approx$10m/s and $\approx 0.5-0.6\%$ for V=15-30 m/s, respectively, at the location of the leading edge. Similarly, for the wire with D=0.32mm, a turbulence intensity of roughly $0.65-0.85\%$ is achieved at the LE location, as can be seen from the figure.

Figure 4.9 shows the effect of the free-stream turbulence on the aerodynamic performance of the airfoil at Re=40,000 and Re=100,000. At low Reynolds number, using wires results in a higher suction pressure which leads to higher lift coefficient. At $\alpha = 12°$, the two wires of D=0.15mm and D=0.30mm thickness reach an asymptotic behaviour which means no further changes will occur in aerodynamics for higher turbulence levels. In spite of that, a much more similar result can be seen with different turbulence levels for Re=100,000. At $\alpha = 12°$ no change can be observed in the aerodynamic values and for $\alpha = 6°$ adding turbulence results in a slightly smaller separation jump close to the trailing edge. From the lift polars for Re=40,000, mounting a wire of D=0.30mm at the inlet generates turbulence of $I = 0.65\%$ intensity which removes the hysteresis almost completely and results in a rise in the lift curve.

4.2.2 Wind tunnel correction

Presence of the wind-tunnel walls has an impact on the airfoil measurements in the form of an increase in the measured lift, drag, and pitching moments due to the velocity increase around the model. The lateral walls in a 2D airfoil measurement cause solid blockage, wake blockage, and streamline curvature effects, as investigated by Ross and Altman (2011) and Barlow et al. (1999).

Solid blockage happens due to the presence of a model in the test section and results in a decrease in the effective area. The of the solid blockage can be defined by

$$\epsilon_{sb} = \frac{K_1 M_v}{A_{ts}^{1.5}} \tag{4.1}$$

where $K_1 = 0.74$ is a wind tunnel correction constant for solid blockage effects, M_v is the model volume and A_{ts} is the area of the wind tunnel test section, and ϵ_{sb} is the solid blockage correction factor (Barlow et al., 1999).

The wake blockage is due to the displacement effect of the wake. To satisfy the continuity, the velocity outside of the wake (including on the model surface) increases. The effect of wake blockage, ϵ_{wb}, is proportional to the wake size and thus to the

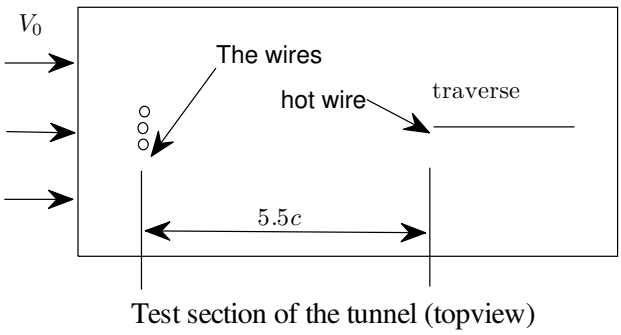

(a)

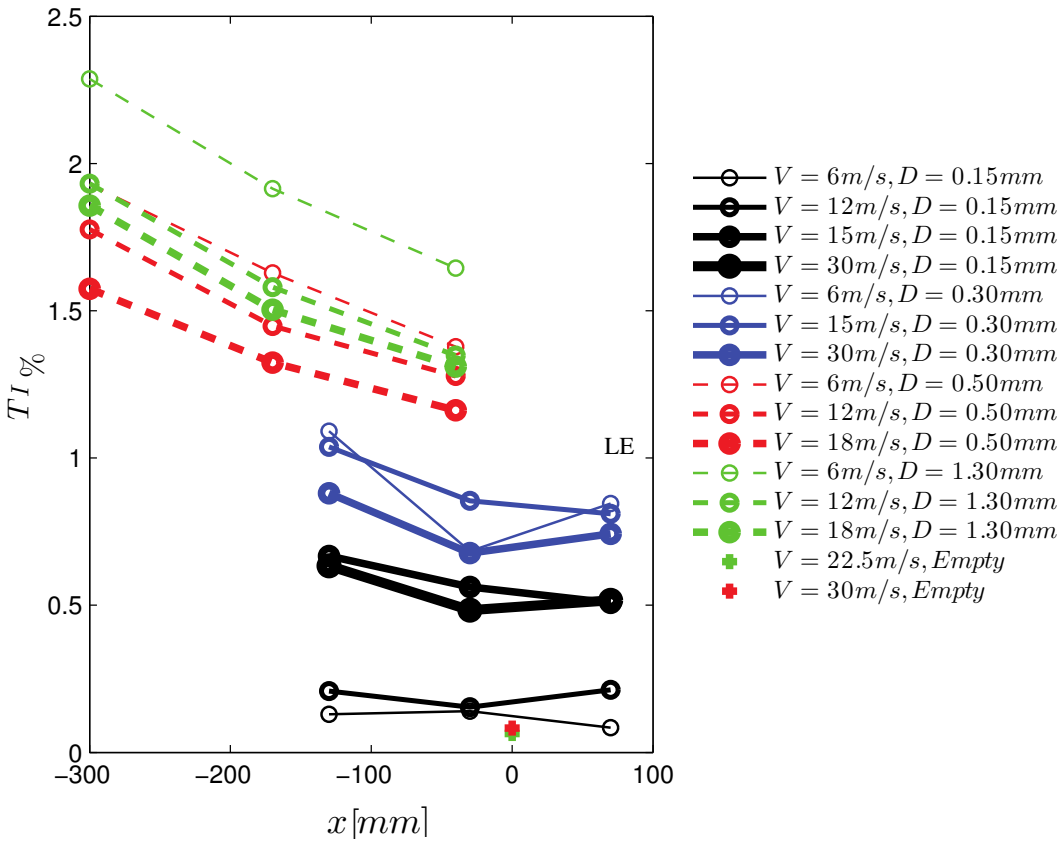

(b)

Figure 4.8: (a) The wire set-up, used to trigger the flow separation over the airfoil. (b) Turbulence intensities alongside the tunnel with wires in place.

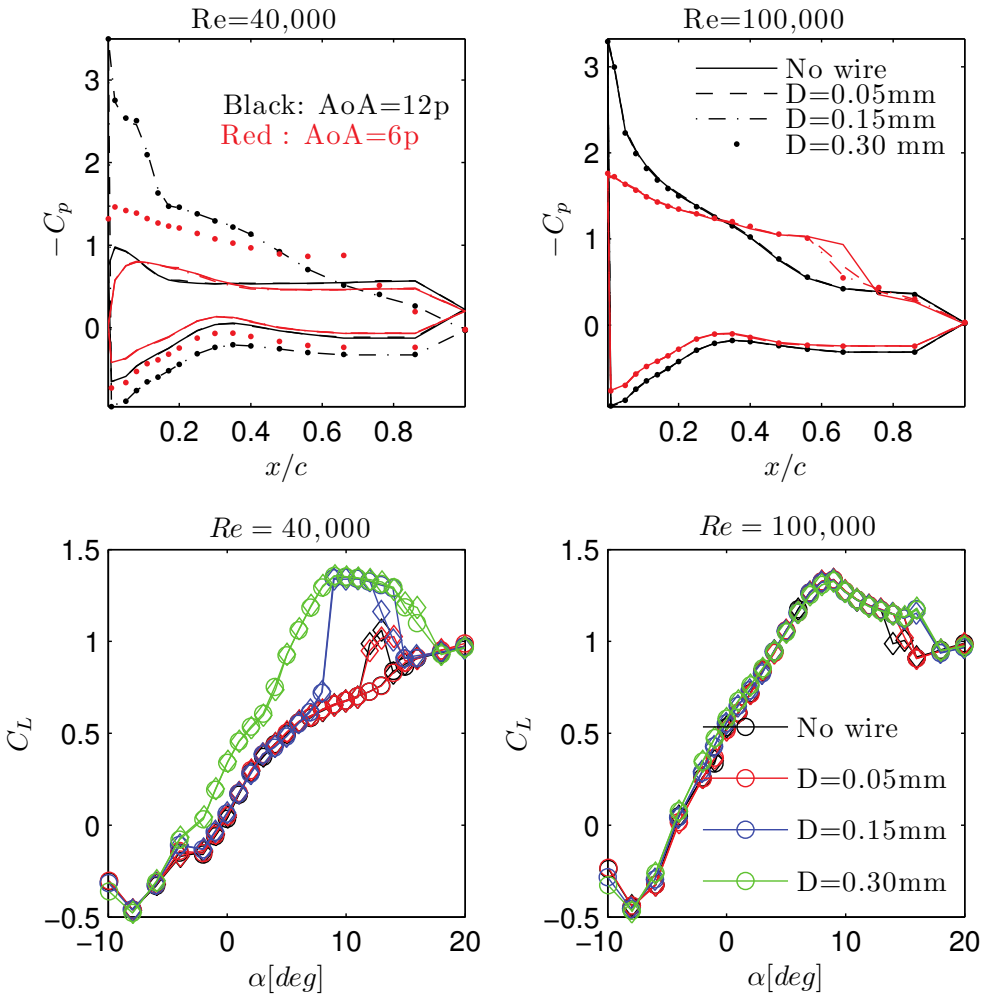

Figure 4.9: Effect of added turbulence in aerodynamic performance of the airfoils at chord Reynolds numbers of Re=40,000 and Re=100,000. The circle and square marks of the same color represent the upstroke and downstroke pitching, respectively. As can be seen, unlike for the Re=40,000 case, the trip wires have neglibible effect on the flow around airfoil at Re=100,000, especially at the high angle of attack of $\alpha = 12°$.

measured drag force on the model.

$$\epsilon_{wb} = (\frac{c}{2h_{ts}})C_{du} \tag{4.2}$$

where h_{ts} represents the height of the test section, C_{du} is the uncorrected drag coefficient.

The last effect stems from the fact that the velocity streamlines as the flow passes over the airfoil in the tunnels test section are constrained by the walls curvature, which is straight. This alteration increases the airfoils effective camber (asymmetry between top and bottom surfaces of the airfoil) as the streamlines are squeezed together and results in an increased lift while the drag is unaffected.

$$\sigma = \frac{\pi^2}{48}(\frac{c}{h_{ts}})^2 \tag{4.3}$$

where σ is the wind-tunnel correction parameter.

The combined effect of the wind tunnel corrections can be expressed as

$$Cl = Cl_u \frac{1-\sigma}{(1+\epsilon_b)^2}, \qquad Cd = Cd_u \frac{1-\epsilon_{sb}}{(1+\epsilon_b)^2}. \tag{4.4}$$

where $\epsilon_b = \epsilon_{wb} + \epsilon_{sb}$. The lift and drag polars are corrected according to equation 4.4 and the lift-drag ratios are plotted in figure 4.10. As can be seen, the effect of tunnel correction is negligible. This is mostly due to the fact that the ratio between the test section-to-airfoil area is rather large so the effect of the blockage and curvature are somewhat minor.

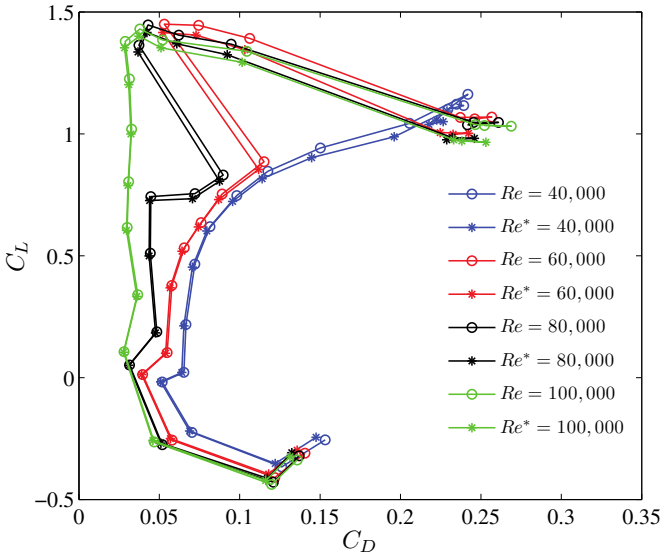

Figure 4.10: Measured lift and drag distributions with the wind tunnel corrections. The circles shows the uncorrected measured data and the curves with star mark show the corrected measurement both obtained at the increasing incidences.

4.3 The numerical simulation set-up

This section presents the numerical set-up for a large eddy simulation study of the flow around airfoils. For the numerical simulations, the same S826 airfoil as in the measurements has been chosen. In the numerical solver, the pressure correction equation is solved using the PISO algorithm and pressure checkerboarding is prevented using the Rhie-Chow interpolation. The convective terms are discretized using a hybrid scheme combining the third order accurate QUICK scheme (10%) to stabilize the numerical oscillations and the second order CDS (90%) scheme to maintain the numerical accuracy. The simulations are performed for Re=40,000 and Re=100,000 for a range of angles of attack and mesh/domain configurations. The filtered Navier-Stokes equation described in chapter 2 reads in its vectorized form as

$$\frac{\partial \mathbf{v}}{\partial t} + \mathbf{v} \cdot \nabla \mathbf{v} \quad = \quad -\frac{\nabla p}{\rho} + \nabla \cdot [(\nu + \nu_{sgs}) \nabla \mathbf{v}] + \frac{\mathbf{f}}{\rho}, \tag{4.5}$$

where ρ and ν are the fluid density and molecular viscosity respectively. $\mathbf{v}$ represents the filtered velocity vector, p is the modified pressure, and $\mathbf{f}$ is the external body force acting on the flow due to the presence of the wind turbine. ν_{sgs} is the eddy viscosity to be specified by the SGS model. The MO model was chosen for all of the test cases. In the MO model, the eddy viscosity is modeled as $\nu_{sgs} = c_{mo}\Delta^{1.5} q_c^{0.25} |\bar{\Omega}|^{0.5}$ using $c_{mo} = 0.01$, where $\Delta(i,j,k) = (dx\ dy\ dz)^{\frac{1}{3}}$ is the implicit filter width, q_c is the SGS kinetic energy obtained with an explicit filtering (defined in chapter 2) and Ω is the vorticity vector magnitude. The simulations have been performed on two types of grid as shown in figure 4.11. For the low angles of attack, a traditional C-mesh was used while for higher angles of attack, a hybrid mesh consisting of O and H-mesh configurations, called the *tunnel* mesh hereafter, were used in a numerical wind tunnel similar to the the experimental wind tunnel's test section (but with a smaller span width).

To have the least dissipation error from the time discretizaton method, a non-dimentional time step of $dt^* = \frac{dtU_0}{c}$ is chosen to ensure that the CFL number is kept below 1 although an implicit time stepping is used. For an estimation of the grid resolution near the airfoil surface, one needs to,

1. Compute the chord Reynolds number Re_x
2. Estimate the skin friction (e.g. from Schlichting (1955)),

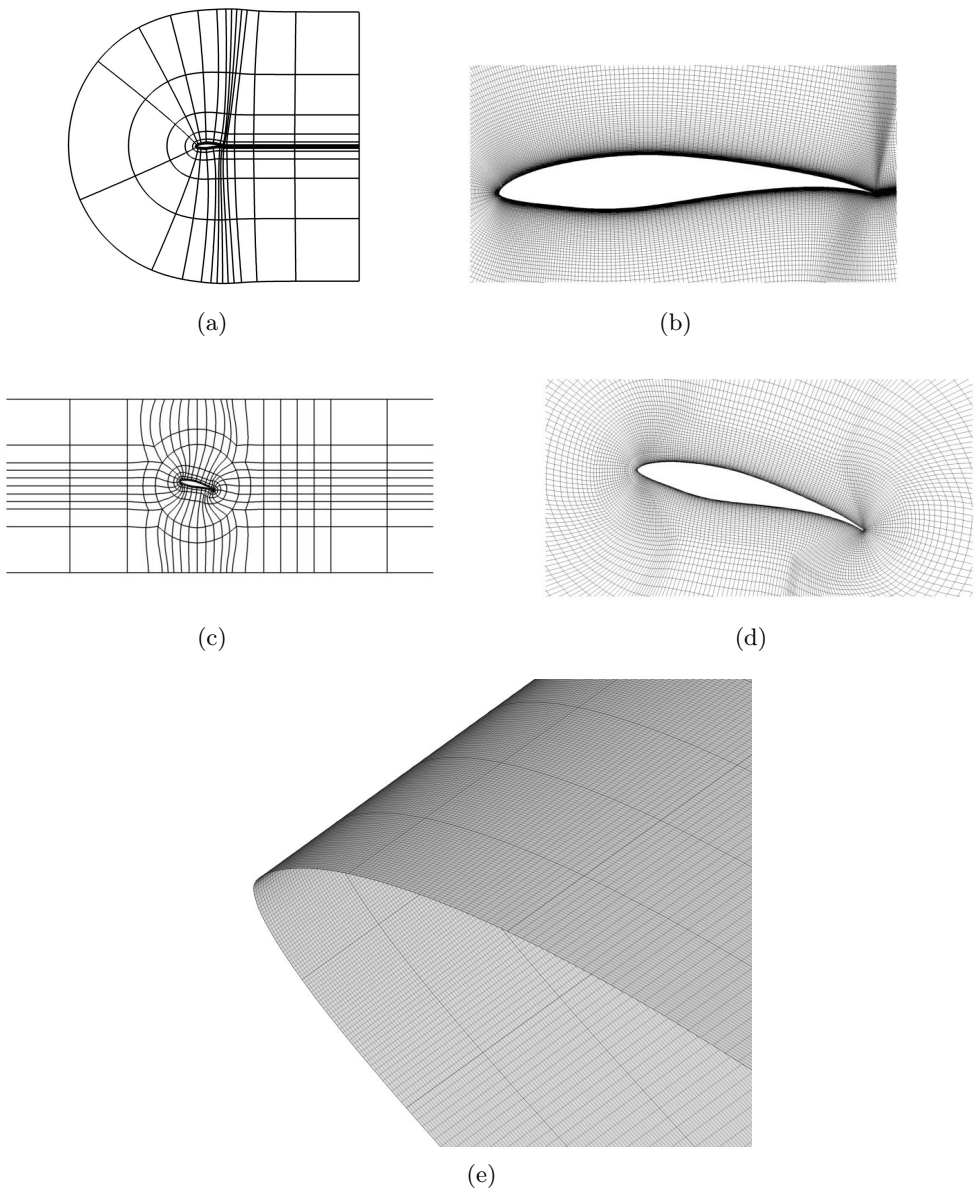

Figure 4.11: Computational domain using (a,b) the C-mesh, and (c,d) the Tunnel mesh, (e) magnified view of the tunnel mesh on the airfoil surface. The bold lines represent edges of each computational block.

$$C_f = [2\,log_{10}(Re_x) - 0.65]^{-2.3} \quad \text{for} \quad Re_x \leq 10^9.$$

3. Compute the wall shear stress, $\tau_w = C_f \cdot \frac{1}{2}\,\rho\,U_\infty^2$.
4. Compute the friction velocity, $u_\tau = \sqrt{\frac{\tau_w}{\rho}}$.
5. Compute the desired grid spacing according to the wall units, $y = \frac{y^+\mu}{\rho\,u_\tau}$.

The grid resolution in wall units is then chosen according to the following wall-resolved criteria (Piomelli and Balaras, 2002) [1]

- Chordwise : $dx^+ = \frac{dx}{y^+} \sim 50 - 130$; where $y^+ = \frac{yu_\tau}{\nu}$ and $u_\tau = \sqrt{\frac{\tau}{\rho}}$,
- Wall-normal : $dy^+ \sim 1 - 2$; ,
- Spanwise : $dz^+ \sim 15 - 40$; .

This range of grid spacing requires a highly-resolved near-wall grid. On the other hand, a large span to chord ratio is needed to resolve the stall cells accurately. Therefore there needs to be a balance between the number of mesh points in the spanwise direction and the span-to-chord ratio. From the previous studies, it has been found that the effect of spanwise resolution is more important than the span width and that a span to chord ratio of at least 0.12 should be used to predict proper 3D flow features (Mellen et al., 2003). In this thesis, the spanwise resolution requirements are preferred to the span width. In two cases, however, highly resolved simulations with aspect ratio of $s/c = 1$ is used.

The simulations are run for a number of NTUs[2] to assure that the mean velocity and turbulence intensities are converged (depending on the Reynolds number and angle of attack) and the flow is averaged for approximately 4 NTUs. Table 4.1 shows a description of different test cases.

4.4 Simulation and measurement results

This section presents a comparison of the pressure distribution as well as lift and drag coefficients obtained from LES computations with the wind tunnel measurements for

[1] Different authors have proposed slightly different values. See for example Davidson (2003); Mary and Sagaut (2002); Mellen et al. (2003)

[2] Non-dimensional Time Unit. (see chapter 3)

Mesh type	α°	*Re*	$N_\zeta \times N_\eta \times N_z^\dagger$	s/c
C	-6 to 4‡	100,000	$960 \times 320 \times 64$	0.5
Tunnel	6 to 20‡	100,000	$1024 \times 256 \times 64 - 320^\star$	[0.12 1]
Tunnel	6 , 12	40,000	$1024 \times 256 \times 64, 320$	0.12, 1

† Chordwise, wall normal, and spanwise resolution, respectively.

‡ A range of AoAs with steps of 2 degrees was performed.

* Different spanwise resolutions corresponding to different span widths are used.

* Unless otherwise stated explicitly, $s/c = 0.12$ and $N_z = 64$ is used for all computations.

Table 4.1: Test cases for LES computations of the flow over airfoil.

a range of angles of attack and Reynolds numbers [1]. Generation of the turbulent boundary layer over the airfoil for Re=40,000 at $\alpha = 12^\circ$ is shown in figure 4.12. In this case, the aspect ratio of the airfoil is $\frac{s}{c} = 1$ and a grid of $1024 \times 256 \times 320$ mesh points in the chordwise, vertical and spanwise directions is used for the simulations.

To compare the effect of both Reynolds number and the flow angle qualitatively, the instantaneous streamwise velocity, resolved turbulent shear stress, and turbulence kinetic energy contours are plotted in figure 4.13 for Re=40,000 and Re=100,000 at $\alpha = 12^\circ$ as well as Re=100,000 at $\alpha = 20^\circ$. For the cases of Re=100,000, grid resolution of $1024 \times 256 \times 64$ with an aspect ratio of 0.12 is employed. The figure shows similar turbulence statistics for $\alpha = 12^\circ$ for both Reynolds numbers. The shear stress has a negative peak at around $\frac{x}{c} = 0.15$ which is due to the flow separation. A pair of peak negative and positive shear stresses is also generated showing the momentum flux into the wake of the airfoil. The shear stress vanishes by the time it reaches $1c$ downstream of the airfoil. Contours of the TKE follow the shear stress contours. They show a peak of turbulence at the separation point which is decreased downstream until the wake recovers. The flow at $\alpha = 20^\circ$ shows a large-scale separation in the suction side starting from the leading edge and radiation of low frequency oscillating flow from the chord.

[1] **A note on the uncertainty assessment:** The measurement uncertainties of lift and pressure distribution are calculated based on the procedure outlined in Barbato et al. (2013) and it is found that the maximum uncertainty of C_L is about 1.4% at $\alpha = 10^\circ$. For the same case, it was also found that the uncertainty in the pressure readings is of the order of 2% with higher values concentrated at the half chord distance to the leading edge on the upper surface of the airfoil. These values of uncertainty were found within the acceptable range of the similar available measurement data (Selig et al., 2011; Smith, 2002)

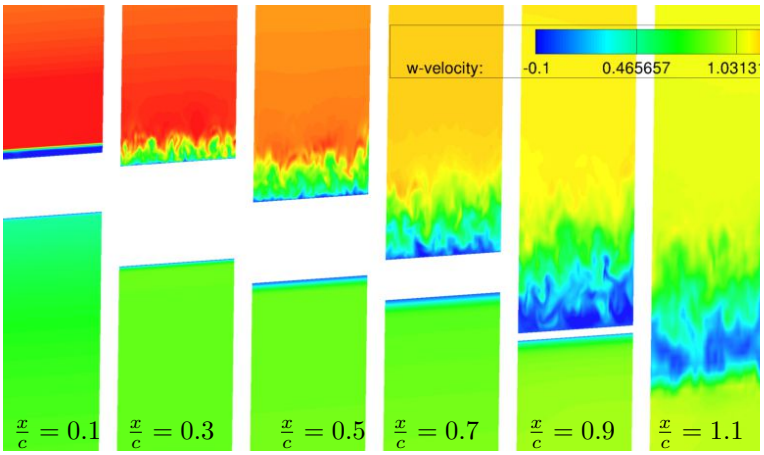

(a)

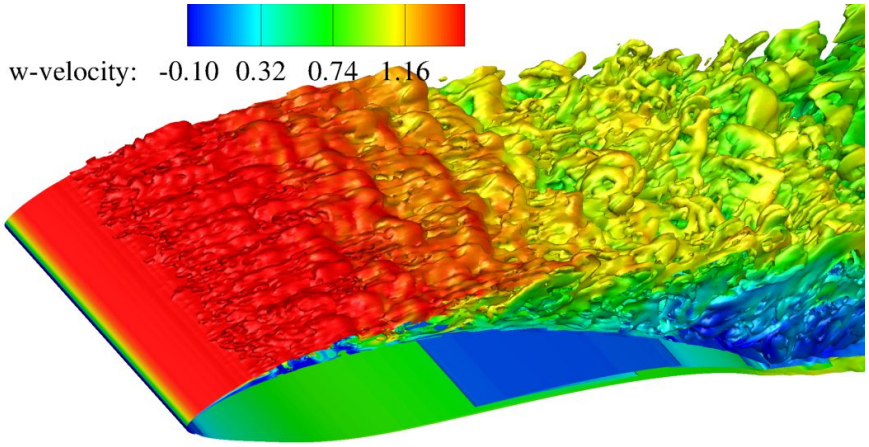

(b)

Figure 4.12: Flow development over the wings showing the growth of the turbulent boundary layer at the suction side for Re=40,000 at $\alpha = 12°$. (a) The flow cross sections at various locations on and downstream of the airfoil and (b) iso-vorticities colored by the streamwise velocity magnitude.

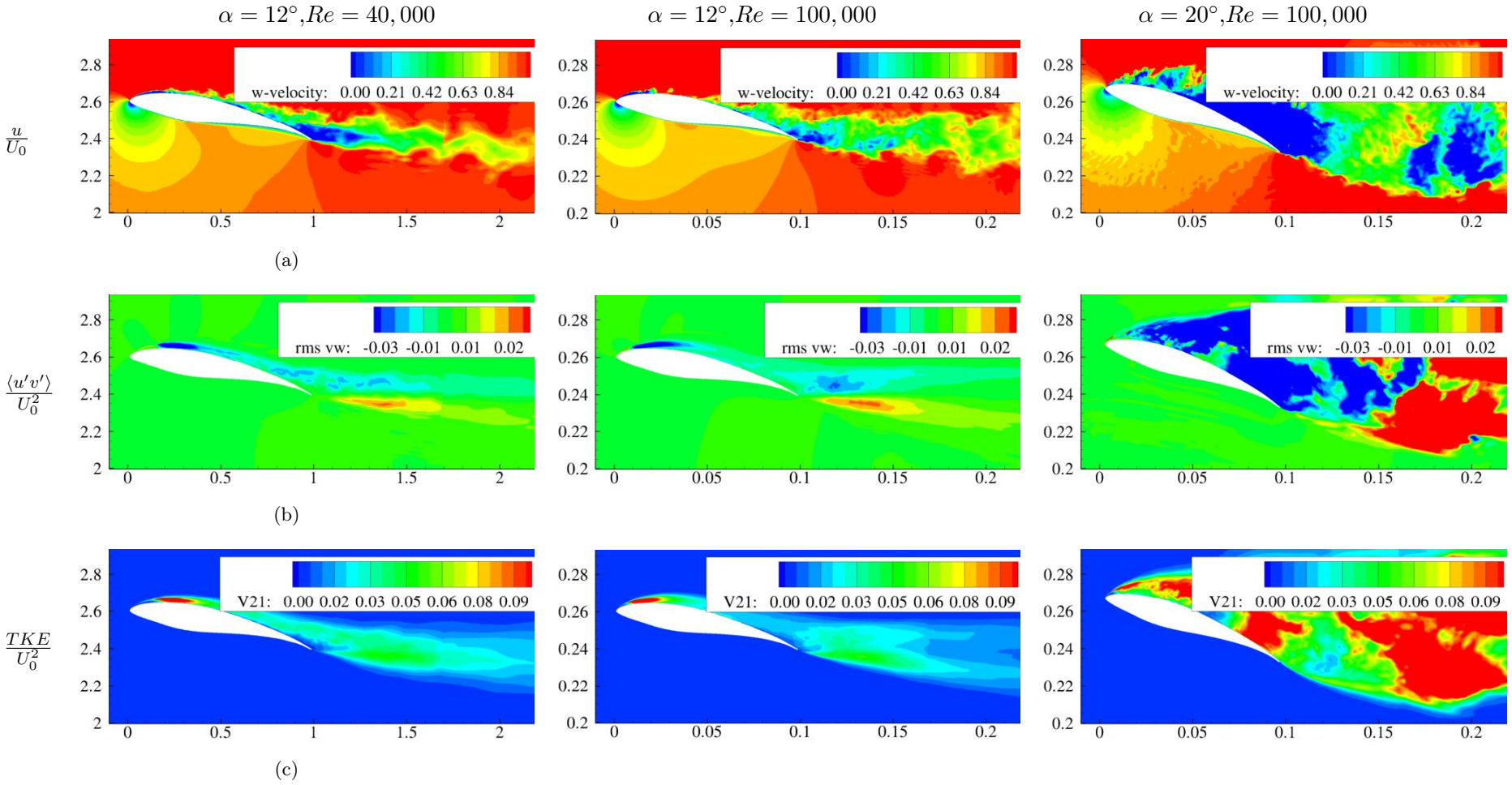

Figure 4.13: Snapshots of (a) instantaneous streamwise velocity, (b) resolved turbulent shear stress, (c) turbulence kinetic energy for Re=40,000 and Re=100,000 at $\alpha = 12°$ as well as for Re=100,000 at $\alpha = 20°$.

The mean streamwise velocities for $\alpha = 12°$ are plotted in figure 4.14. In order to investigate generation of the LSB on the airfoil, the leading edge plots are magnified and shown in separate figures. As can be seen, for Re=40,000, the laminar bubble reattaches at $x/c \approx 0.25$ while for the Re=100,000, the reattachment occurs at $x/c \approx 0.18$. The flow remains attached due to the presence of strong momentum flux until $x/c \approx 0.7$ where turbulent separation begins due to the strong adverse pressure gradient forces.

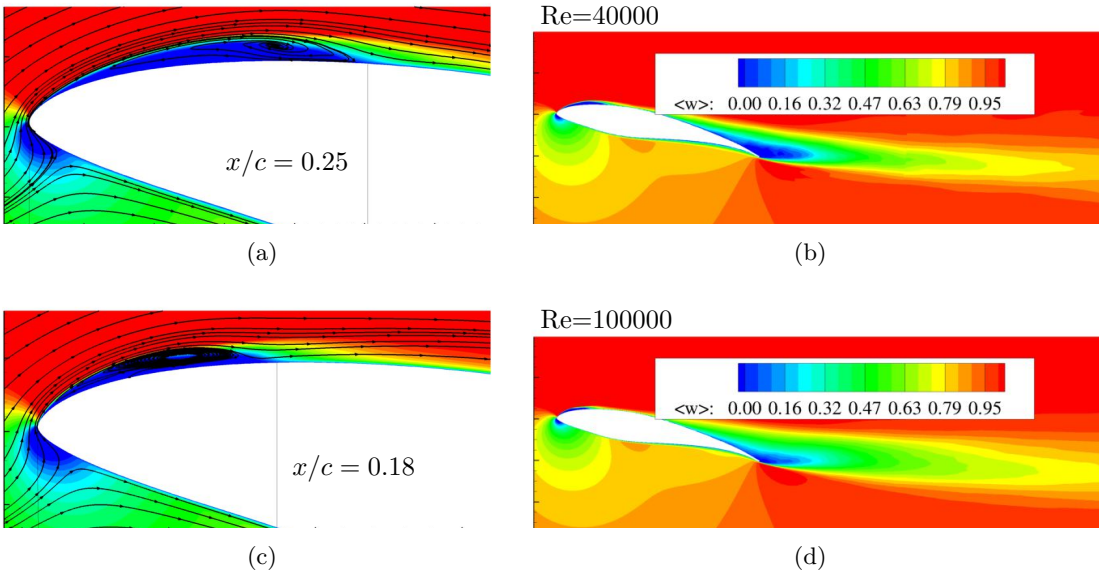

Figure 4.14: Comparison of mean streamwise velocities for Re=40,000 and Re=100,000 at $\alpha = 12°$. (a) Mean streamwise velocity at Re=40,000 showing the extent of laminar and turbulent separation, (b) magnified view of the leading edge showing generation of the LSB, (c, d) corresponding plots for the Re=100,000 case.

Skin friction plots are used to visualize the transition on the airfoil surfaces. Figure 4.15(a) shows the flow patterns on the airfoil surface for Re=40,000 and $\alpha = 12°$. For this case, the T-S waves start to appear very close to the leading edge. A case with Re=100,000 and $\alpha = 8°$ is also shown because of it's clear transition pattern. It can be seen from the figure that the cases with higher angle of attack experience a quicker transition region.

Figure 4.16 shows the formation of stall cells on the suction side of the airfoil at two Reynolds numbers of 1000 and 100,000. The low Reynolds number case was chosen to allow for a coarser mesh and subsequently longer simulation to investigate the effect of longer time averaging on the shape of the SC. The low Reynolds number simulation is performed on a $196 \times 96 \times 64$ grid with an aspect ratio of 1 and the simulations are run for about 50 NTUs for averaging. This could explain why, unlike the high Reynolds

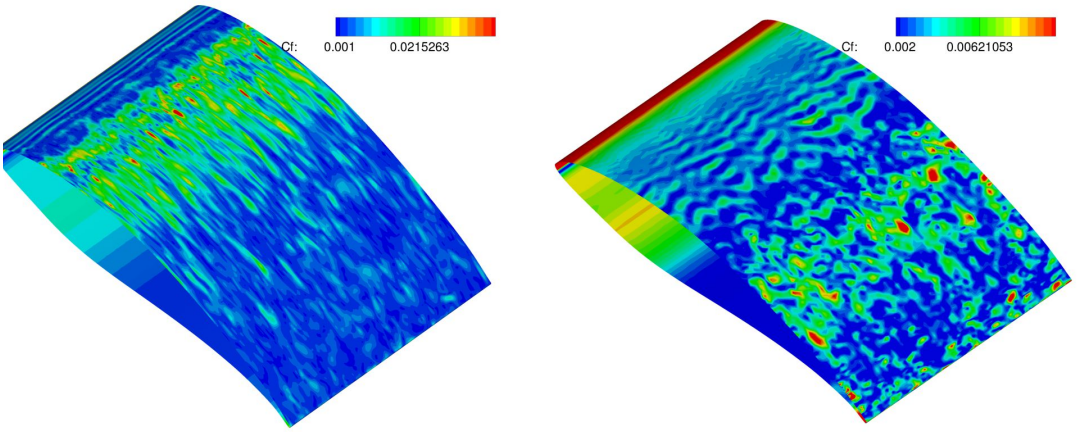

(a) (b)

Figure 4.15: Skin friction contours on the airfoil surface for (a) Re=40,000 and $\alpha = 12°$ and (b) Re=100,000 and $\alpha = 8°$.

number case, a more symmetric stall cell can be observed for the low Reynolds number case. Nonetheless, the spanwise motions are quite clear for both cases.

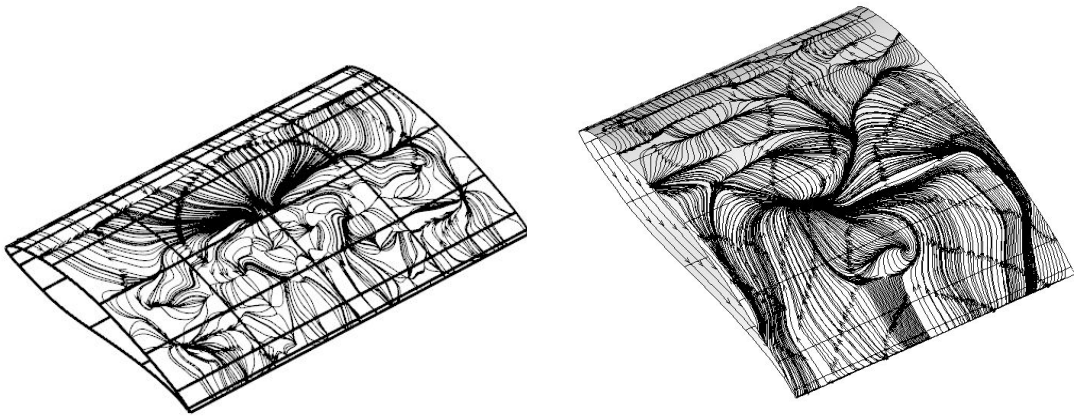

(a) (b)

Figure 4.16: Visualisation of the stall cell at $\alpha = 15°$ on the S826 airfoil using velocity iso-contours for (a) Re=1000 using $s/c = 2$ and (b) Re=100,000 using $s/c = 1$.

4.4.1 Comparison of pressure distribution over the airfoil

Figure 4.17 shows the pressure distribution over the airfoil at Re=40,000 for $\alpha = 6°$ and $\alpha = 12°$. As discussed in the airfoil measurements section, the flow exhibits severe non-linearity and consequently, static stall hysteresis at low Reynolds numbers. Four sets of measurement using different inflow turbulence intensities are used for comparisons. As discussed in the airfoil measurements section, the turbulence is introduced by placing wires upstream of the airfoil in the test section. The legends in figure 4.17 refer to the diameters of the tested wires. The LES case at $\alpha = 6°$, is simulated using laminar inflow with zero turbulence intensity and for $\alpha = 12°$, both laminar and turbulent inflow cases are compared.

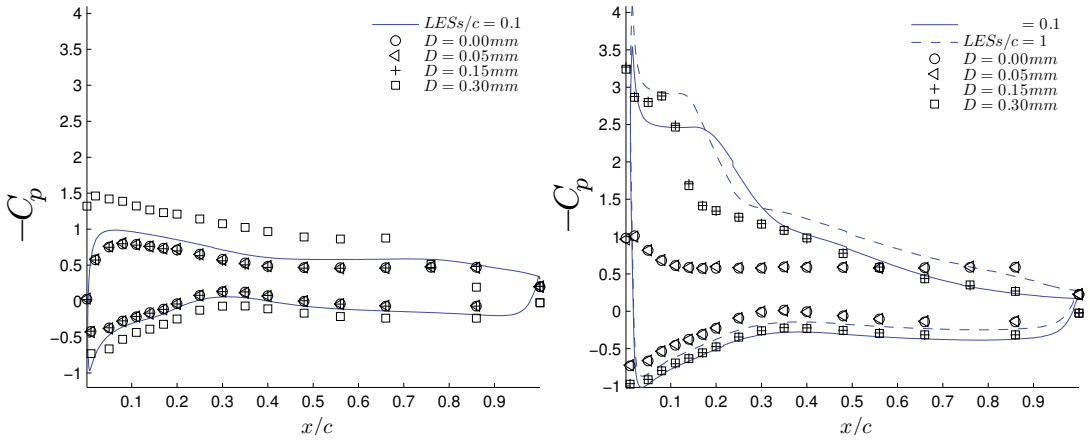

Figure 4.17: Comparison of pressure distributions over the airfoil for Re=40,000 at (a) $\alpha = 6°$ and (b) $\alpha = 12°$. D is the diameter of the wires placed upstream of the airfoil to trigger the separation.

Rest of the figures show the pressure distribution for different angles of attack incremented from $\alpha = -8°$ to $\alpha = 20°$ at Re=100,000. A set of computations using Q^3UIC, a viscous-inviscid interactive solver (Ramos-García et al., 2013) are performed and compared with the LES data. Q^3UIC simulates the flow around airfoils using a potential flow solver. The inviscid flow is coupled with the integral boundary layer equations to account for the viscous effects. Figure 4.18 shows the pressure distributions for $\alpha = -6^o, -4^o, -2^o, 0°$. A reasonably good agreement between LES computations and the measurements can be seen over the entire airfoil surface, especially at $\alpha = -6°$ and $-4°$. It is also seen that Q^3UIC simulations follow the same trend as LES computations for $\alpha = -4^o, -2^o, 0°$.

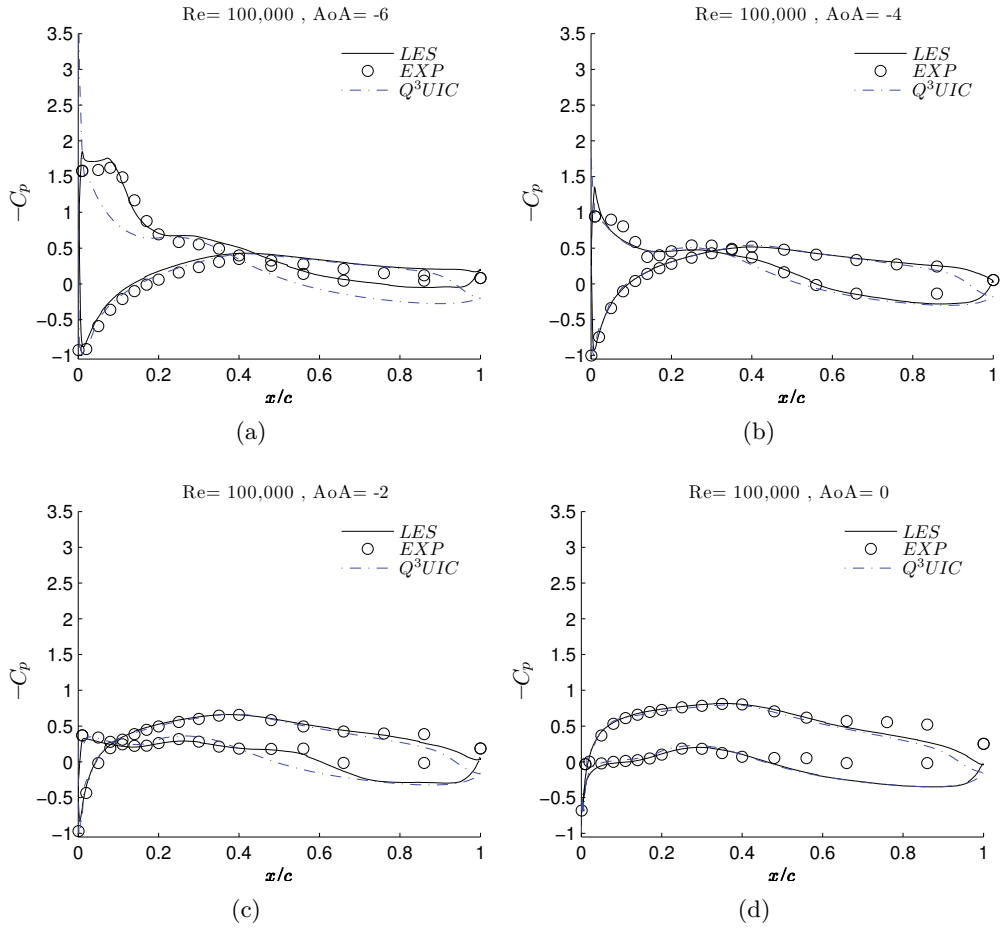

Figure 4.18: Comparison of C_p for Re=100,000 at $\alpha = -6^o, -4^o, -2^o, 0°$.

The C_p distributions for the positive angles of attack of 2°, 4°, 6°, and 8° are plotted in figure 4.19. It can be seen that the transition point has moved forward by increasing the pitch angle. At $\alpha = 4°$, LES computations show a small separation point which is close to the experimental results. Nevertheless, the LES-predicted separation reattaches faster than the experiment. For $\alpha = 2^o, 4^o, 6°$ the LES (and Q^3UIC) data show close similarity in the magnitude of the peak pressure and pressure distribution for up to half a chord length downstream of the leading edge, where the experimental data show separation although a slight separation pattern can be traced in the LES data for $\alpha = 4°$. LES and the experimental results fall nearly one on top of the other for $\alpha = 8°$.

Figure 4.20 shows the pressure distributions for $\alpha = 10°$ and 20°. At $\alpha = 10°$,

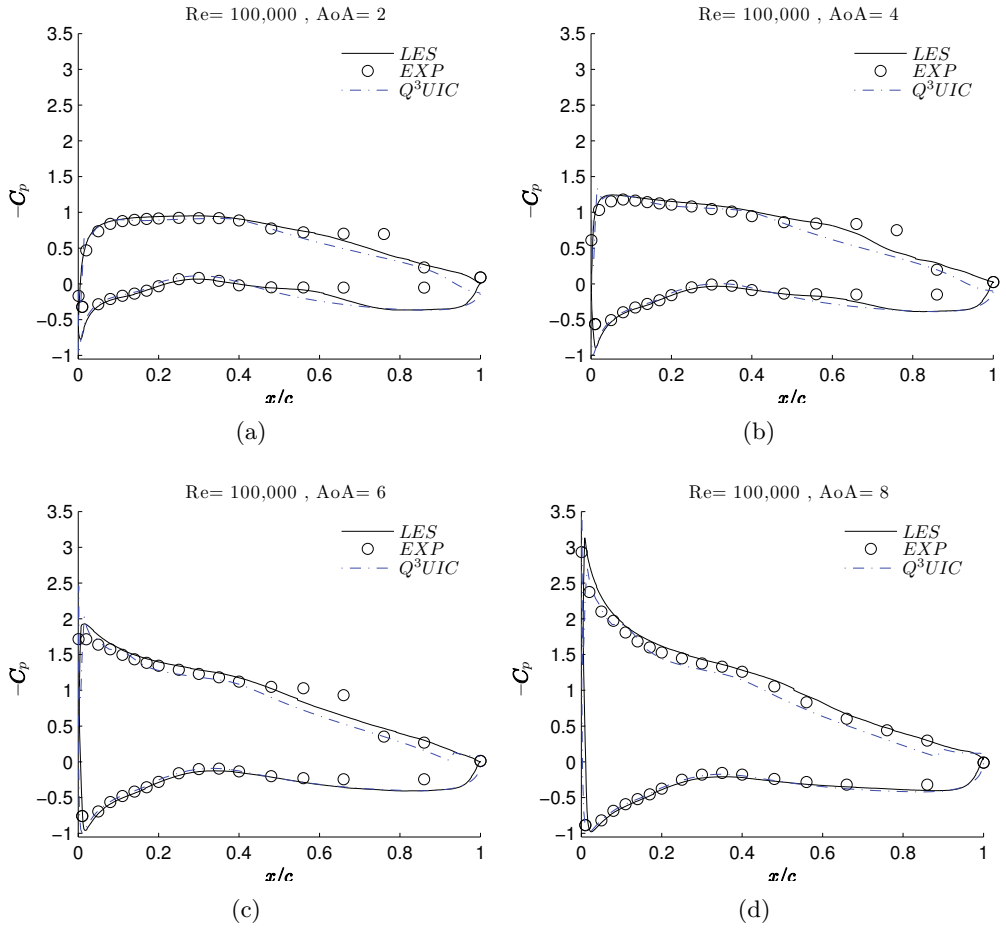

Figure 4.19: Comparison of C_p for Re=100,000 at $\alpha = 2^o, 4^o, 6^o, 8°$.

as shown in figure 4.20(a), LES shows a separation point starting at $x/c = 0.1$ and reattaching at $x/c = 0.4$. Likewise, Q^3UIC computations show a separation point although spanning a smaller area. Finally, figure 4.20(b) shows the pressure distribution at $\alpha = 20°$ where the LES and experimental data are in good agreement, whereas the results of Q^3UIC over-predicts the peak pressure. The reason for inacuracy of Q^3UIC is that it cannot simulate the deep stall conditions where the separation point is located in the leading edge region due to the dominance of the fully separated flow and strong inviscid interactions. This makes application of the panel codes limited to lower angles of attack.

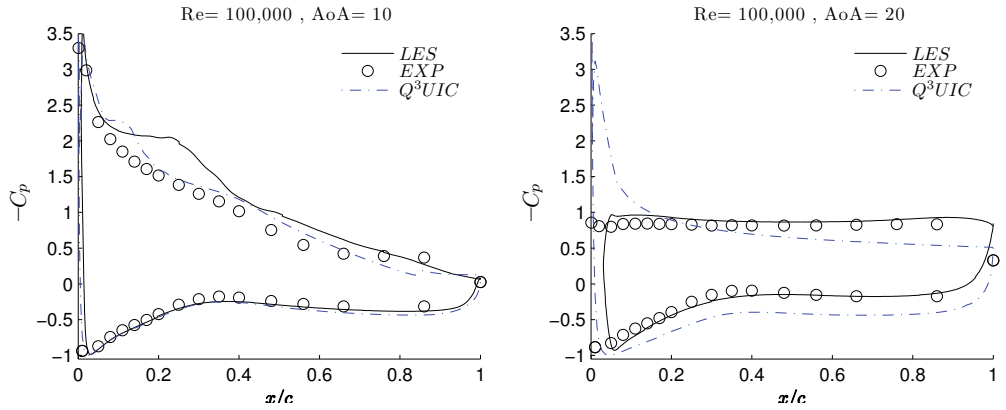

(a) (b)

Figure 4.20: Comparison of C_p for Re=100,000 at $\alpha = 10^o, 20°$.

4.4.2 Comparison of lift and drag polars

The final comparison is obtained between the time-averaged lift and drag polars. The lift coefficient is measured using two methods: pressure integration over the airfoil surface ($C_{L,P}$), and direct force balance measurement (referred to as $C_{L,F}$). The force balance can also be used for drag measurements. However, the drag forces are often 1-2 orders of magnitude smaller than their lift counterparts and therefore, the simultaneous lift and drag measurements using the same force gage results in drag coefficients contaminated with errors. In these measurements, drag force is also calculated using two pressure based alternatives: airfoil surface pressure integration in the streamwise component ($C_{D,P}$), and integration of the momentum loss found by measuring the axial velocity profile in the wake of the airfoil ($C_{D,Wake}$), which requires applying a 2D continuity and momentum balance to a defined control volume, as shown in figure 4.21.

Using the latter method, the drag coefficient, C_D can be defined as

$$C_D = \frac{\theta}{\frac{1}{2}\rho U_\infty^2 c} = 2\int_{cv} \frac{u}{U_\infty}\left(1 - \frac{u}{U_\infty}\right) d\left(\frac{y}{c}\right). \tag{4.6}$$

where,

$$\theta = \int_{cv} \rho u(U_\infty - u)dy \tag{4.7}$$

is the momentum thickness, and assuming Δy_i to be the distance between the measuring

points, it can be presented in the discrete form as,

$$C_D \simeq \sum_{i=1}^{n-1} \left[\frac{u_i}{U_\infty} \left(1 - \frac{u_i}{U_\infty} \right) + \frac{u_{i+1}}{U_\infty} \left(1 - \frac{u_{i+1}}{U_\infty} \right) \right] \frac{\Delta y_i}{c}, \tag{4.8}$$

where the subscript i denotes the position of the pressure tap on the wake rake and the velocities are computed from the measured pressure using the Bernoulli equation,

$$p_i = p_0 + \frac{1}{2}\rho U_\infty^2 \quad \Rightarrow \quad u_i = \sqrt{\frac{p_i - p_0}{\frac{1}{2}\rho}}, \tag{4.9}$$

and p_0 is the reference pressure at the control volume surface. The free stream velocity measurement is obtained from the pitot tube at the upstream of the airfoil.

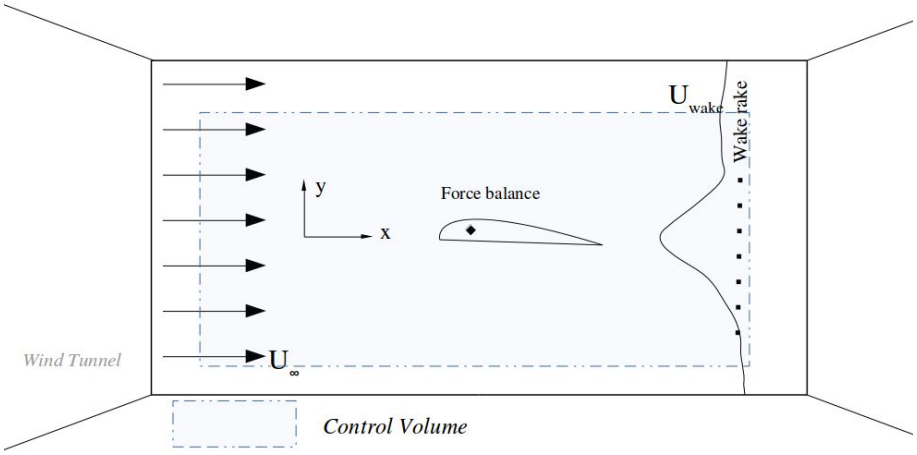

Figure 4.21: Control volume used for calculation of the drag using 2D momentum and continuity balance.

In the LES computations, lift and drag coefficients are calculated by integrating the pressure forces and the skin friction on the airfoil,

$$C_L = \frac{F_{py} + F_{\nu y}}{0.5\rho U_\infty^2 cs}, \tag{4.10}$$

$$C_D = \frac{F_{\nu x} + F_{\nu y}}{0.5\rho U_\infty^2 cs}. \tag{4.11}$$

In the above equations, F_{py} is the pressure force in the vertical direction; $F_{\nu y}$ and $F_{\nu x}$ are viscous forces in vertical and streamwise directions. c and s are the chord and span

lengths, respectively.

Figure 4.22 presents comparisons of the LES and Q^3UIC simulations with the experiments. As for the experiments, the two measured lift coefficients differ in the high angles of attack, where separation starts to play a significant role. This is due to the fact that the number of surface pressure taps used in the $C^{af}_{L,P}$ method is not enough to capture the correct pressure area for integration [1]. From the drag measurements at $\alpha \geq 15°$, the accuracy of the measurements based on the airfoil surface pressure ($C^{af}_{D,P}$) is higher than that of the wake rake measurements, $C_{D,Wake}$. This is because in the latter, at high angles of attack, the wake rake in the current set-up is not wide enough to capture the whole wake profile accurately.

Now looking at the numerical simulations, it is observed from the figure 4.22 that there is a very good agreement between LES (and Q^3UIC) computations with the measurements for pitching angles up to $\alpha = 8°$. The numerical simulations LES and Q^3UIC, while being similar, start to deviate from the measurements at higher angles of attack. The rise in the lift coefficients is associated with the higher pressure values predicted by the numerical methods. Another difference is that the deep stall for both numerical methods occurs at $\alpha \sim 12°$ while the experimental results suggest an earlier stall. The difference between LES results and the measurements can most likely be explained by the inability of the current LES setup to find the exact location of the transition point with the given numerical set-up. Another limitation of the LES is the limited span, which is chosen to be less than one chord length in most of the cases, whereas the measurements are performed using an aspect ratio of $\frac{s}{c} = 5$. Similar to the lift coefficient plots, the LES (and Q^3UIC) and the experimental results exhibit a good agreement between the C_D polars for the low values and the differences appear in higher angles of attack.

4.5 Summary

In this chapter, wind tunnel measurements of the S826 airfoil at low and moderate Reynolds numbers were presented. When operated at chord Reynolds numbers below 80,000, a static stall hysteresis phenomenon was observed, which is caused by the laminar boundary layer separation and transition. The influence of free-stream disturbance on the hysteresis effects on the airfoil was investigated by means of wire-generated turbulence at the inlet of the wind tunnel test section. Based on the trip wire experi-

[1] This is not an issue at low pitching angles, as there are no significant pressure jumps over the airfoil surface that cannot be captured with the current number of pressure tubes

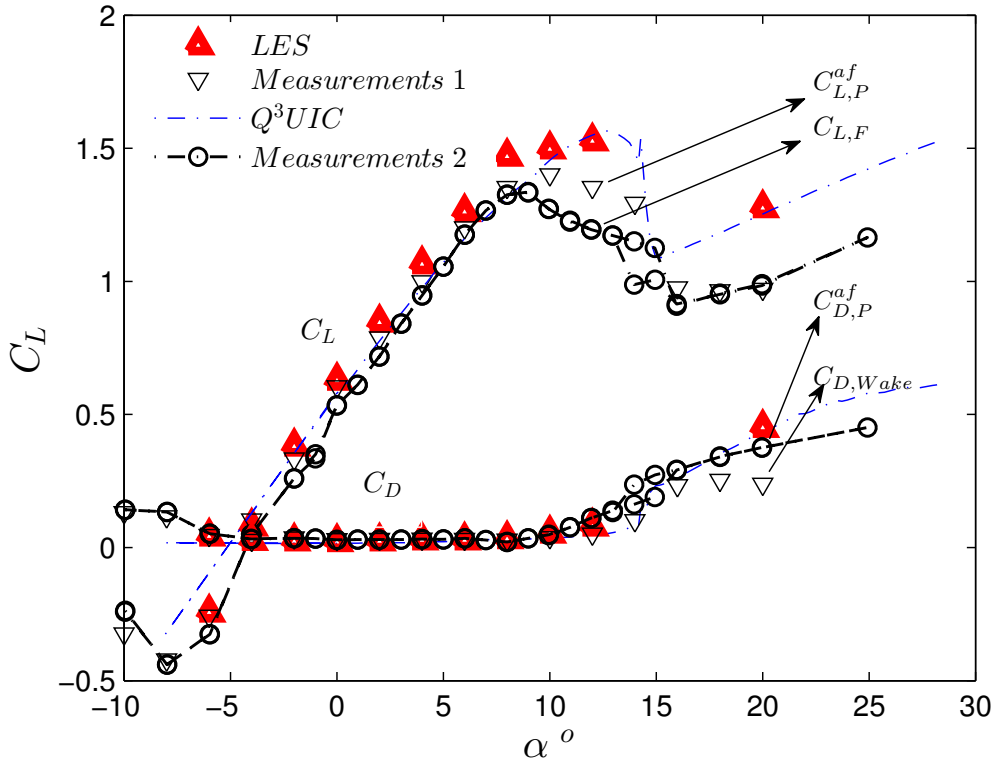

Figure 4.22: Lift and drag polars for the NREL S826 airfoil at Re=100,000.

ments, it could be concluded that introducing a free-stream turbulence of $I = 0.7 - 1\%$ intensity is able to remove the hysteresis effects at Re=40,000. Along with the measurements, wall-resolved LES computations of the airfoil for a wide range of angles of attack and Reynolds number were performed and the pressure distribution as well as lift and drag polars were compared with the wind tunnel measurements. The patterns of transition and Laminar Separation Bubble (LSB) were investigated for Re=40,000 and Re=100,000 and it was shown that the LSB tends to be smaller at higher Reynolds numbers. On the whole, it was shown that LES is capable of producing results with reasonable accuracy. In the next chapter, the airfoil data obtained from the measurements are used to simulate wind turbine wake interactions.

Chapter 5

LES of wind turbine wake interations

The NREL S826 airfoil data which were obtained chapter 4 are used as an input for the actuator line CFD model to investigate the wake interaction between two model scale wind turbines. Two series of simulations are carried out to study the double-wake interactions. In the first series, the two rotors are aligned laterally at the center of the tunnel and the effects of the rotor resolution, actuator line force smearing, and Reynolds number are investigated at fixed tip speed ratios (TSR) and rotor arrangements. Furthermore, an emphasis is placed on investigating the role of the SGS modeling on the flow structures and wind turbine loadings. In the second series, the effects of the different turbine operating conditions on the flow structures and turbine performance are examined. In particular, the effects of low and high free-stream turbulence, different TSRs for the downstream turbine (while the upstream turbine is operating at a fixed rotational velocity), and different lateral turbine placements on wake and streamwise turbulence intensity profiles as well as turbine loadings are investigated. The results are validated against the wind tunnel measurements of Krogstad and Lund (2012) in terms of the wake deficit and turbulence intensity profiles.

5.1 Introduction

As mentioned in chapter 1, LES technique has been recently used to simulate wind turbine wakes (cf. Sørensen (2011)) and while many SGS models have, over the years, been proposed (cf. Sagaut (2000)), the effects of various SGS models in simulations of wind turbine wakes had not been documented in great detail. Recently, Sarlak et al.

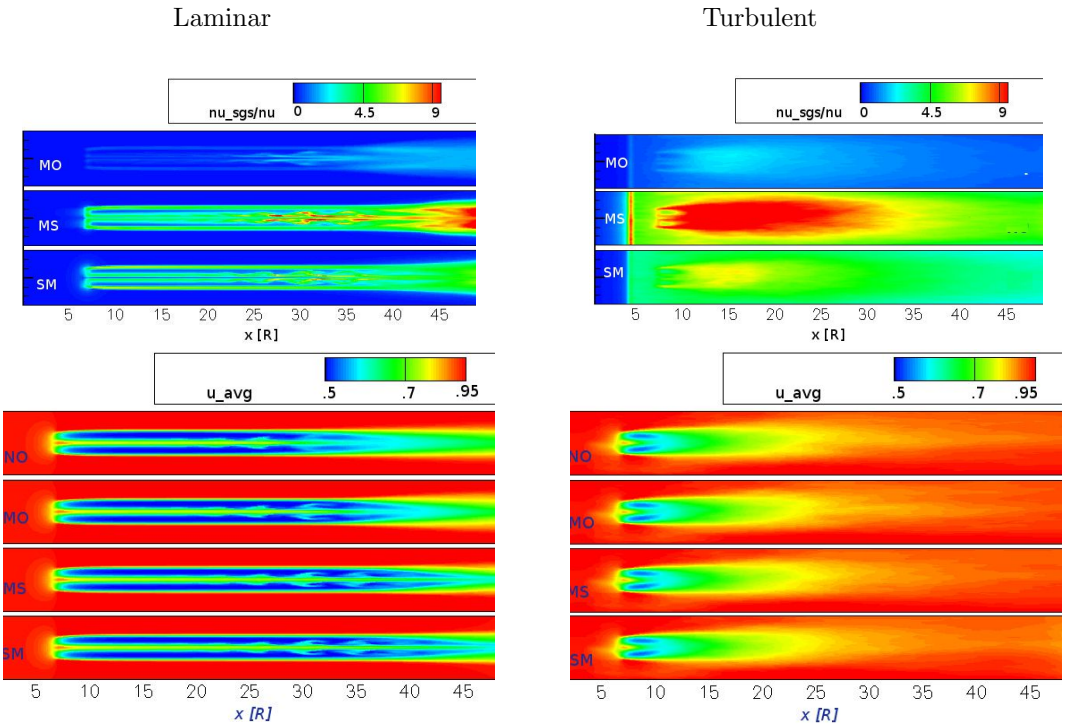

Figure 5.1: Contours of the normalized eddy viscosity (top) and the mean stremwise velocity downstream the rotor (bottom) in laminar and turbulent free-stream for NO, MO, MS, and SM models (Sarlak et al., 2014).

(2014) studied the SGS modeling effects in the wake of a single turbine operating in fully laminar and highly turbulent free-stream velocities. Their results suggest that while the eddy viscosities computed by the various SGS models may be of quite different magnitudes, the mean velocity profiles do not change significantly at least in the near wake region (see figure 5.1).

The Navier-Stokes equation for the problem in the vector form is defined as

$$\frac{\partial \mathbf{v}}{\partial t} + \mathbf{v} \cdot \nabla \mathbf{v} \quad = \quad -\frac{\nabla p}{\rho} + \nabla \cdot [(\nu + \nu_{sgs}) \nabla \mathbf{v}] + \frac{\mathbf{f}}{\rho}, \tag{5.1}$$

where ρ and ν are the fluid density and molecular viscosity, respectively. $\mathbf{v}$ represents the filtered velocity vector, p is the modified pressure, and $\mathbf{f}$ is the external body force acting on the flow due to the presence of the wind turbine. ν_{sgs} is the eddy viscosity to be specified by the SGS model, as defined in chapter 2. During the course of simulations for different cases, several SGS models are used to evaluate ν_{sgs}, as described below:

$\nu_{sgs} = 0,$	No model (NO),
$\nu_{sgs} = c_{SM}\Delta^2\|\bar{S}\|,$	Smagorinsky model(SM),
$\nu_{sgs} = c_{MO}\Delta^{1.5}q_c^{0.25}\|\bar{\Omega}\|^{0.5},$	Mix-ω model(MO),
$\nu_{sgs} = c_{MS}\Delta^{1.5}q_c^{0.25}\|\bar{S}\|^{0.5},$	Mix-S model (MS),
$\nu_{sgs} = c_{DS}\Delta^2\|\bar{S}\|,$	Dynamic Smagorinsky model (DS),
$\nu_{sgs} = c_{DMo}\Delta^{1.5}q_c^{0.25}\|\bar{\Omega}\|^{0.5},$	Dynamic Mix-ω model (DMo),
$\nu_{sgs} = c_{DMs}\Delta^{1.5}q_c^{0.25}\|\bar{S}\|^{0.5}.$	Dynamic Mix-S model (DMs).

where $\Delta = (\delta x \times \delta y \times \delta z)^{1/3}$ is the grid filter width and S is the strain rate tensor. The kinetic energy-scale q_c is defined and computed according to $q_c = (\tilde{u}_i - u_i)^2$, where $\tilde{u}_i$ represents the velocity, explicitly filtered at scale $\tilde{\Delta}$ and can be evaluated using a 3D volume averaging using stencils of size 27 with trapezoidal weights that mimic a box filter, cf. chapter 2.

For the non-dynamic versions of the model, the following values are used in the simulations: $c_{SM} = 0.01$, $c_{MO} = 0.02$, $c_{MS} = 0.06$. For the dynamic version of the models, the coefficients are obtained by implementing test-filtering to apply the Germano identity. To reduce fluctuations, we employ the 3D volume averaging of the numerators and the denominators in the dynamic model using the same averaging technique as the one used for derivation of the q_c term.

For the simulation of wind turbines, the Actuator Line (AL) technique is used. As explained in chapter 1, in the AL approach by Sørensen and Shen (2002), each turbine blade is represented by a line on which the forces are applied according to the velocity field and the angle of attack,

$$\mathbf{f} = (f_L, f_D) = 0.5\rho V_{rel}^2 c(C_L\mathbf{e}_L + C_D\mathbf{e}_D), \tag{5.2}$$

where V_{rel} is the relative velocity, C_L and C_D are lift and drag coefficients, $\mathbf{e}_L$ and $\mathbf{e_D}$ are unit vectors in the direction of the (local) lift (f_L) and drag (f_D) forces and c is the airfoil section chord length. These forces are commonly smeared out by using a Gaussian regularization kernel which is applied to the flow field as shown in figure 5.2 (left).

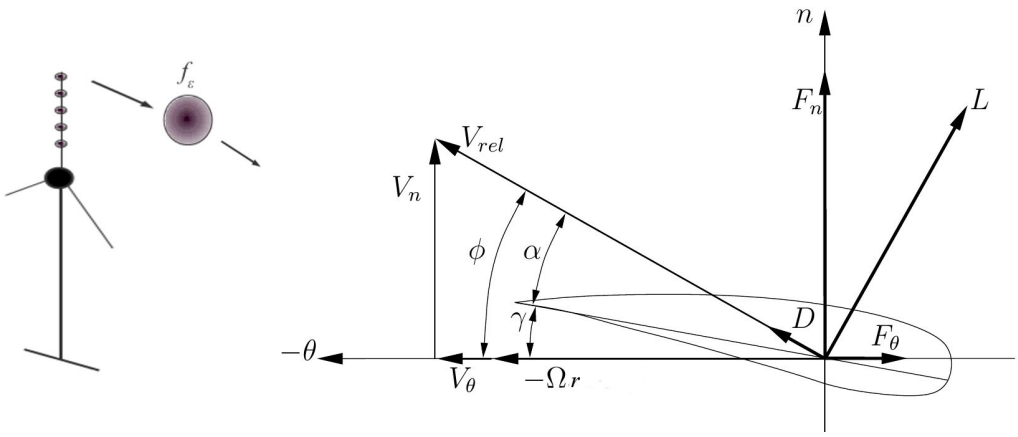

Figure 5.2: Actuator line concept and the airfoil cross-section used to find the angle of attack.

5.2 Description of the experimental and numerical set-up

The rotor experiments used for CFD validations are performed in wind tunnel facility at the Norwegian University of Science and technology. The tunnel test section is $2.71m$ wide, $1.8m$ high and $11.1m$ long. The tunnel roof can be adjusted in order to keep the pressure gradient at zero level (Krogstad and Sætran, 2013). The tunnel height at the outlet is $5cm$ higher than the inlet to account for the boundary-layer growth along the tunnel side-walls. The upstream and downstream turbines have the same type of blades but with diameters of $0.944m$ and $0.894m$, respectively. The turbine models are mounted in the tunnel using two different configurations, as sketched in figure 5.3. An in-line configuration, referred to as BT2, and a laterally separated configuration (with a misalignment of $\Delta y = 0.4m$), referred to as BT3. For both BT2 and BT3 configurations, the streamwise separation between the turbines is three downstream-rotor diameters. The design TSR for both turbines is $\lambda = \Omega R/U_\infty = 6$ which results in a Reynolds number at the design point of $Re_c = \lambda U_\infty c_{tip}/\nu \approx 100,000$, where c_{tip} is the tip chord length and ν is the kinematic viscosity of air.

Measurements are performed at low and high free-stream turbulence. For the low turbulence cases, the flow is uniform across the test section inlet to within $\pm 1\%$, except for the thin wall boundary layer, and the turbulence intensity is $I = 0.24\%$. At the location of the first (upstream) rotor, the velocity is whithin $\pm 0.5\%$ of the full scale with a turbulence intensity of $I = 0.22\%$. For the high turbulence cases, the turbulence is generated using a grid mesh of the size $M = 0.24[m]$, which produces a turbulence intensity of $I = 10 \pm 0.9\%$ at the location of the upstream turbine and a velocity bound

of ±0.65%.

For both rotors, the blade consists of 14% thick NREL S826 airfoil sections. The characteristics of the S826 airfoil was investigated in detail in chapter 4. The airfoil measurements show that the profile is very sensitive to Reynolds number variation and that the blade is subjected to static stall hysteresis at the low Reynolds numbers, as also shown in figure 5.4.

For the numerical simulations, the pressure correction equation is solved using the PISO algorithm and pressure decoupling is avoided using the Rhie-Chow interpolation technique. The convective terms are discretized using a hybrid scheme combining the third order accurate QUICK scheme (10%) to stabilize the numerical oscillations and the fourth order CDS (90%) scheme to maintain the numerical accuracy. A domain similar to the wind tunnel using different grid resolutions, is generated. As shown in figure 5.5, the grid is uniform in the rotor plain as well as the wake region and it is stretched out to the walls, as there is no solid wall boundary layer to resolve. The boundary conditions are constant inflow velocity with free-stream turbulence of $I = 0.24\%$ and $I = 10\%$ for the low and high turbulence cases, respectively. The convective outflow boundary condition is used at the outlet and symmetry boundary conditions is used at the walls to prevent grid clustering near the walls[1]. The growth of the boundary layer is taken into account by having a constant tunnel height with slip walls rather than including the slope from the wind tunnel. Simulations are run for two NTUs [2] until the flow reaches a stationary state. The subsequent averaging takes place for about 3 NTUs to ensure that the high order statistical moments are converged. The mean streamwise velocity and streamwise turbulence intensity profiles are compared with the measurements at three locations downstream the second turbine.

A number of test cases using different grid resolutions are tested as shown in table 5.1. As mentiones earlier, the simulations cover the following SGS models: No model (NO), Smagorinsky (SM), Dynamic Smagorinsky (DS), Mixed-Ω (MO), Mixed-S (MS), Dynamic Mixed-Ω (DMo), and Dynamic Mixed-S (DMs). In addition the following smearing factors were tested: $\epsilon_{AL} = 1.0, 1.5, 2.2$.

5.2.1 Tower modeling

To resemble the experiments, the wind turbine towers are also included in the numerical simulations. The tower is modeled in the same manner as a fixed actuator line, that

[1] No wall boundary layer will be generated as a result.

[2] Non-dimensional Time Unit (NTU) is defined as the time it takes for a particle to pass the entire computational domain

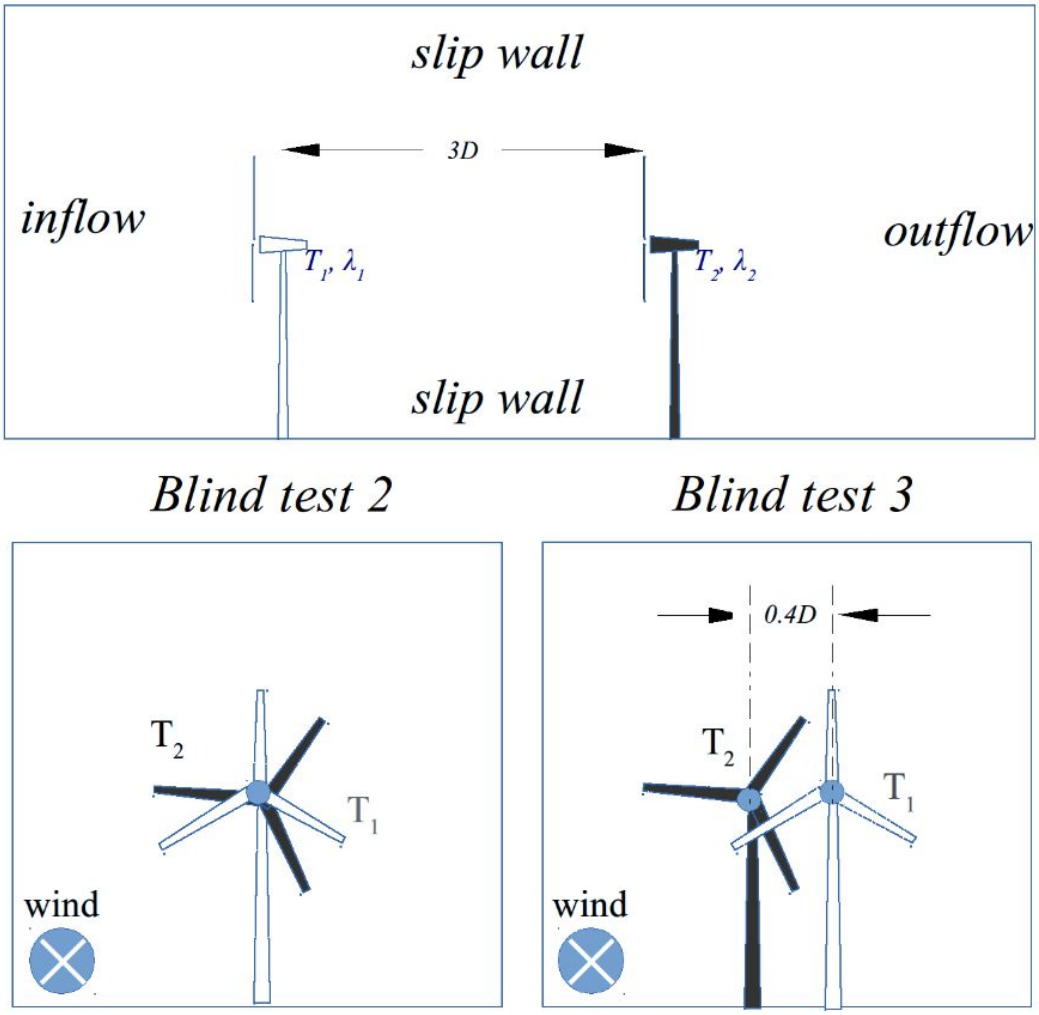

Figure 5.3: A sketch of the two-rotor arrangement in the wind tunnel. Wind direction is from left to right and the two turbines are laterally mounted in the spanwise center of the tunnel in the Blind test 2 (BT2) and laterally shifted in the Blind test 3 (BT3).

Grid Resolution	Rotor resolution (j)
$48 \times 48 \times 240$	13
$72 \times 72 \times 360$	20
$96 \times 96 \times 480$	26
$128 \times 128 \times 640$	35
$192 \times 192 \times 960$	52

Table 5.1: List of grid sizes and corresponding rotor resolutions (j) tested. For each case, the grids and their corresponding rotor resolution are tested using various combinations of subgrid scale models, smearing factors, and inlet turbulence levels.

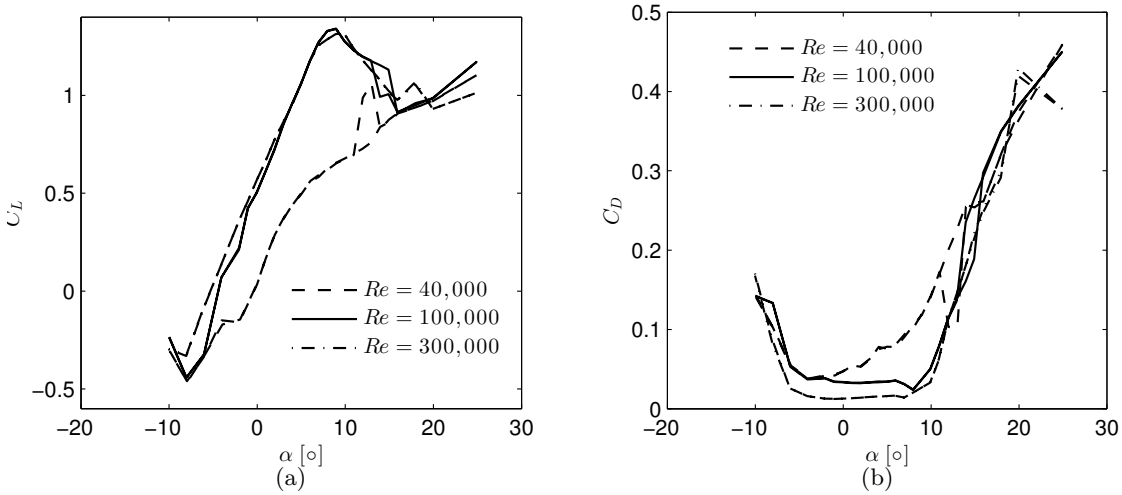

Figure 5.4: (a) Lift and (b) drag coefficient distributions of the NREL S826 airfoil used for the turbine parameterizations.

is, body forces are added to the flow instead of simulating the real geometry of the tower. The forces are superimposed to the flow using the velocity computed from the CFD simulations and lift and drag coefficients defined for the cylinders. The force unsteadiness is included through the oscillating frequency defined by Strouhal number $St = \frac{fD}{u_\infty}$. Figure 5.6 shows the lift, drag and Strouhal numbers for the smooth cylinders subject to laminar inflow. The lift component vanishes for flows and is commonly disregarded in industrial applications at high Reynolds numbers[1], however, the range of Reynolds numbers considered in this research, is associated with a rather strong lift component, as can be seen from the figure.

For the simulations, a Strouhal number of $St = 0.2$ is applied and the following values are used to model the tower:

$$C_D = 1.2, \tag{5.3}$$

$$C_L = A\sin(2\pi ft) + B, \tag{5.4}$$

where $f = 0.2u_\infty/D_{cyl}$ is the shedding frequency, D_{cyl} is the local diameter of the tower, $A = 0.3$ is r.m.s. of the lift coefficient taken from figure 5.6 at $Re \approx 10^5$, and B is a zero-mean uniformly distributed random parameter ($\sigma_B \sim \pm 0.25 C_L$), added to

[1]Flows around offshore mono-piles etc.

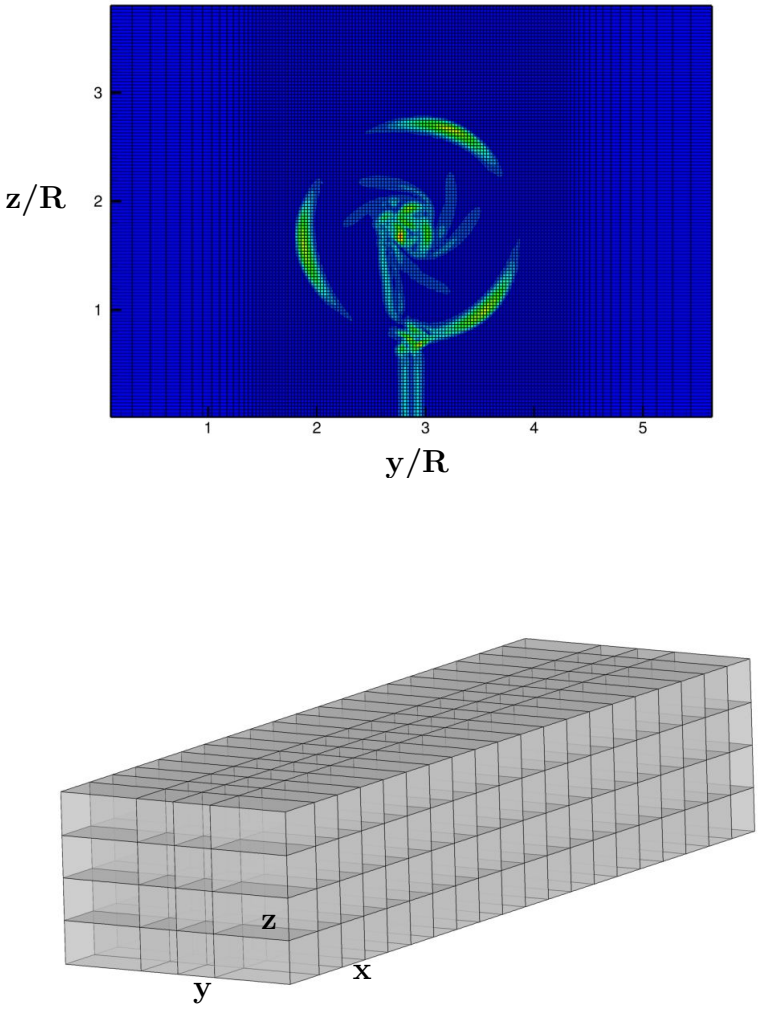

Figure 5.5: The extent of the modeled rotor and its tower inside the numerical tunnel, shown by a 2D snapshot of vorticity downstream the turbine. The 3D computational mesh blocks (320 blocks of 32^3 structured mesh points: $640 \times 128 \times 128$ mesh points in x, y, and z directions). Axially, the rotors are located at $\frac{x}{R} = 4$ and $\frac{x}{R} = 10$ (3 rotor diameters streamwise separation).

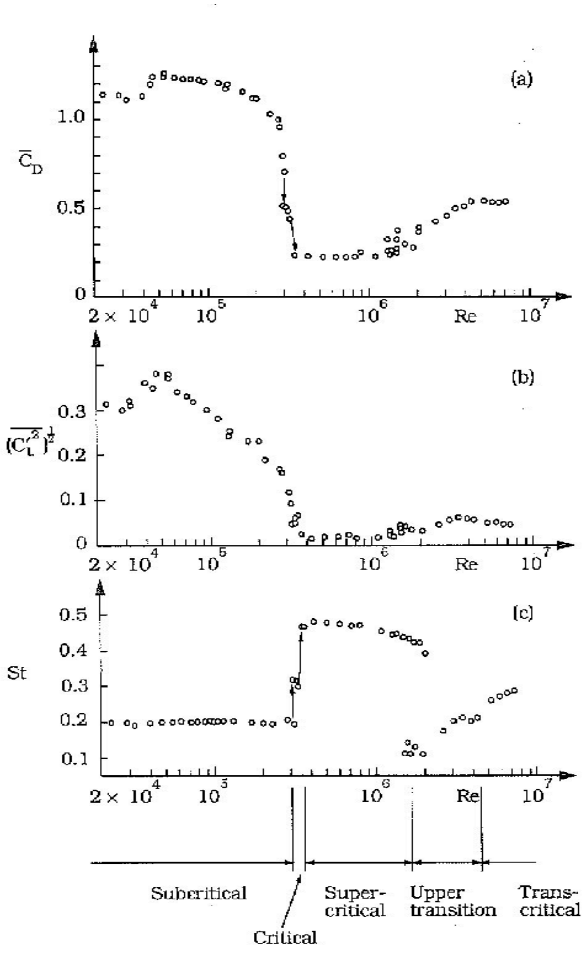

Figure 5.6: (a) Drag, (b) r.m.s. of the lift oscillations, and (c) Strouhal number for smooth cylinders as a function of the Reynolds number (Schewe, 1983).

the lift harmonic in order to induce unsteadiness to the flow.

5.3 Simulation of full wake interactions

This section contains simulation results for the different test cases. The configuration with the in-line turbine arrangement is presented in the present section and the effect of different numerical factors are investigated for this specific simulation. In section 5.4, a configuration with different TSRs and lateral separation of the rotors is chosen and the results of different turbine operating conditions are compared using laminar and turbulent free-stream.

5.3.1 Role of the rotor resolution

Simulations of the in-line rotor configuration are performed with an emphasis on the SGS modeling, upstream turbulent/laminar inflow, the smearing parameter ϵ, Reynolds number, and the rotor resolution. The numerical tunnel is resolved using four different grid resolutions corresponding to a rotor resolution of 13, 20, 35, and 52 points per blade to analyse the effect of resolutions on wake properties and turbine loading. Figure 5.7 demonstrates the resulting mean streamwise velocity, streamwise turbulence intensity, resolved turbulence stress and the resolved TKE at three distances behind the downstream turbine. The results are obtained using the MO model. By convention, the red solid line is used to show the simulations obtained using the NO model at Re=50,000 and rotor resolution of 35 with $\epsilon = 2.2$. It is used in order to establish a clear comparisons between all cases shown in figures 5.7, 5.9, 5.10, 5.15, and 5.16. The legends can be interpreted in all figures in a way that, for example, $MO_{j35}\ Re = 50k\ \epsilon_{2.2}$ refers to a case performed using the Mix-O SGS model, each actuator line (blade) is resolved by $j = 35$ points along the radius, the flow is set at $Re = 50,000$, and the ratio between Gaussian filter width for the actuator line body force smearing to the grid size Δ is $\epsilon = 2.2$.

It can be seen that the resolution of $j = 13$ and $j = 20$ results in an over-prediction of the wake, but for $j = 35$ the results are converged. Investigation of the second moments show a more complicated behaviour. The coarse grids under-predict the turbulence intensity (and hence the TKE) and the resolved shear stress at $x/D = 1$, while, they over-predict the same quantities in the far wake. Taking the finest resolution ($j = 52$) as a reference, the solution seems to be converged for the $j = 35$ grid. For the rest of comparisons, therefore, the grid resolution corresponding to $j = 35$ is used. This amount of rotor resolution corresponds to a grid with a total of $10.5M$ mesh points.

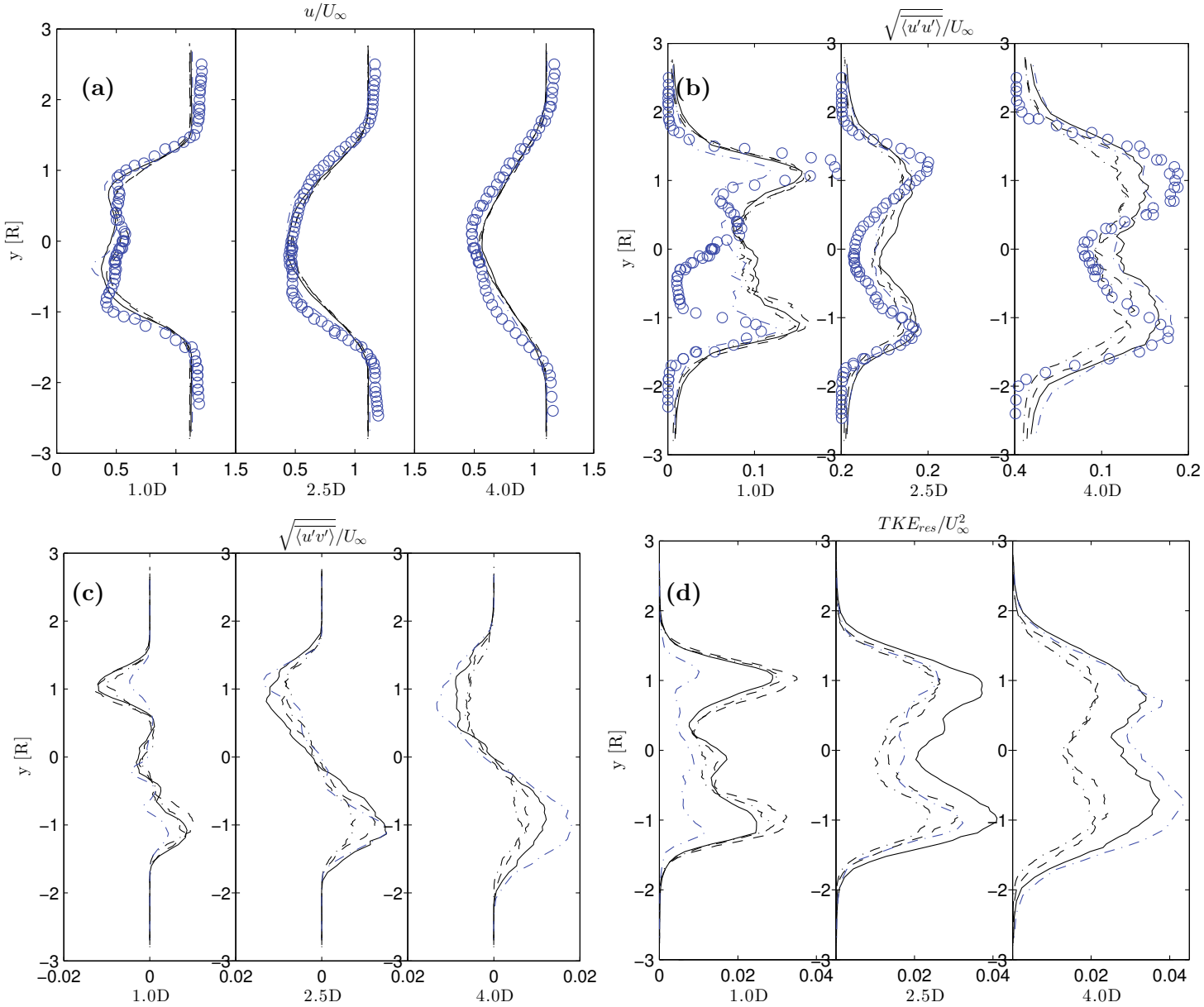

Figure 5.7: Rotor-line grid sensitivity study at Re=50,000. Comparison of (a) mean streamwise velocity (b) turbulence intensity (c) turbulent shear stress and (d) resolved TKE, using different rotor resolutions at $x/D = [1\ 2.5\ 4]$ downstream of the second turbine. [.....] reference case (NO), [- . - . -] $j = 13$, [——] $j = 20$, [- - -] $j = 35$, [- . - . -] $j = 52$. j is the number of grid points per actuator line. All simulations are obtained with $\epsilon = 2.2$, $I = 0.24\%$ and (except the reference case) using the MO model.

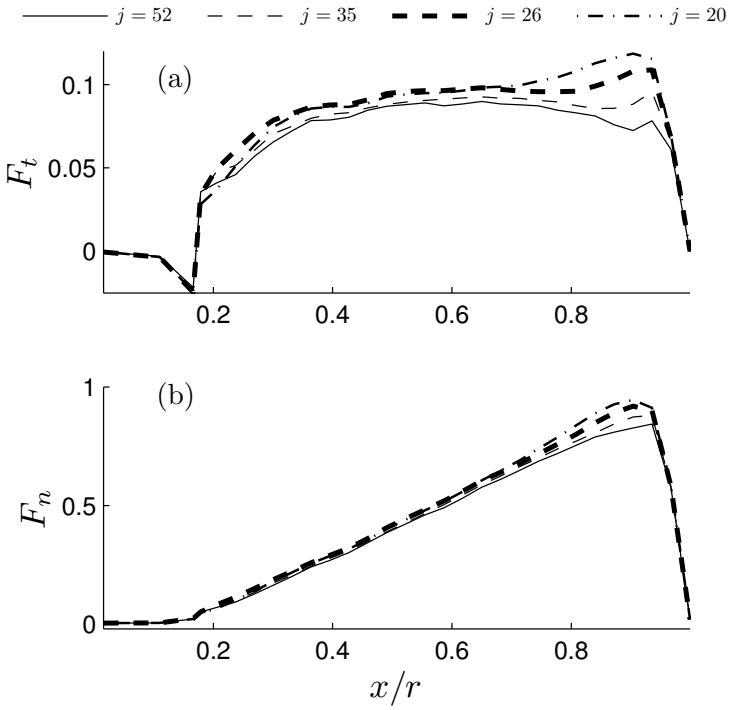

Figure 5.8: (a) Tangential and (b) normal forces acting on the upstream turbine using different rotor resolutions.

Blade loadings are also compared for different mesh resolutions. Figure 5.8 shows the radial distribution of tangential F_t and normal F_n forces, averaged for the three blades. As can be seen, all of the resolutions give similar predictions of the forces, however, increasing the resolution results in lower load predictions on the blades. It is also clear that for both loadings, the differences on the tip part of the blades are more pronounced, especially at the tip.

5.3.2 Effect of the free stream turbulence

To investigate the effects of small perturbations on the flow, two tests have been performed using laminar ($I = 0\%$) and the low-intensity free-stream turbulence ($I = 0.24\%$) where, a homogeneous isotropic turbulence box is generated using the method of Mann (1998) and implemented into the CFD domain as described in section 1.3.3. That is, using the Taylor frozen turbulence hypothesis, the turbulence plains are extracted alongside the turbulence box and inserted at three rotor radii upstream of the first turbine to produce the desired unsteady flow. Figure 5.9 compares the effect of fully laminar and low-intensity turbulent free-stream on the wake structures. As can be acknowledged, using even a small free-stream turbulence can facilitate a more accurate prediction of the flow. The reason is that small fluctuations help to trigger instabili-

ties in the vortices. Without any upcoming turbulent flow, the tip vortices would be preserved through the computational domain without breaking up. In the real case of wind turbines operating in the ABL, the instability-triggering fluctuations originate from the atmospheric turbulence as well as the boundary layer over the blade surface. In the numerical simulations, it should however be mentioned that there will always be a wake recovery due to the numerical errors, however, in the pure laminar inflow, this will happen at a non-physically long distance downstream of the rotor due to the dissipation of the CFD solver, which causes tip vortices to break-up.

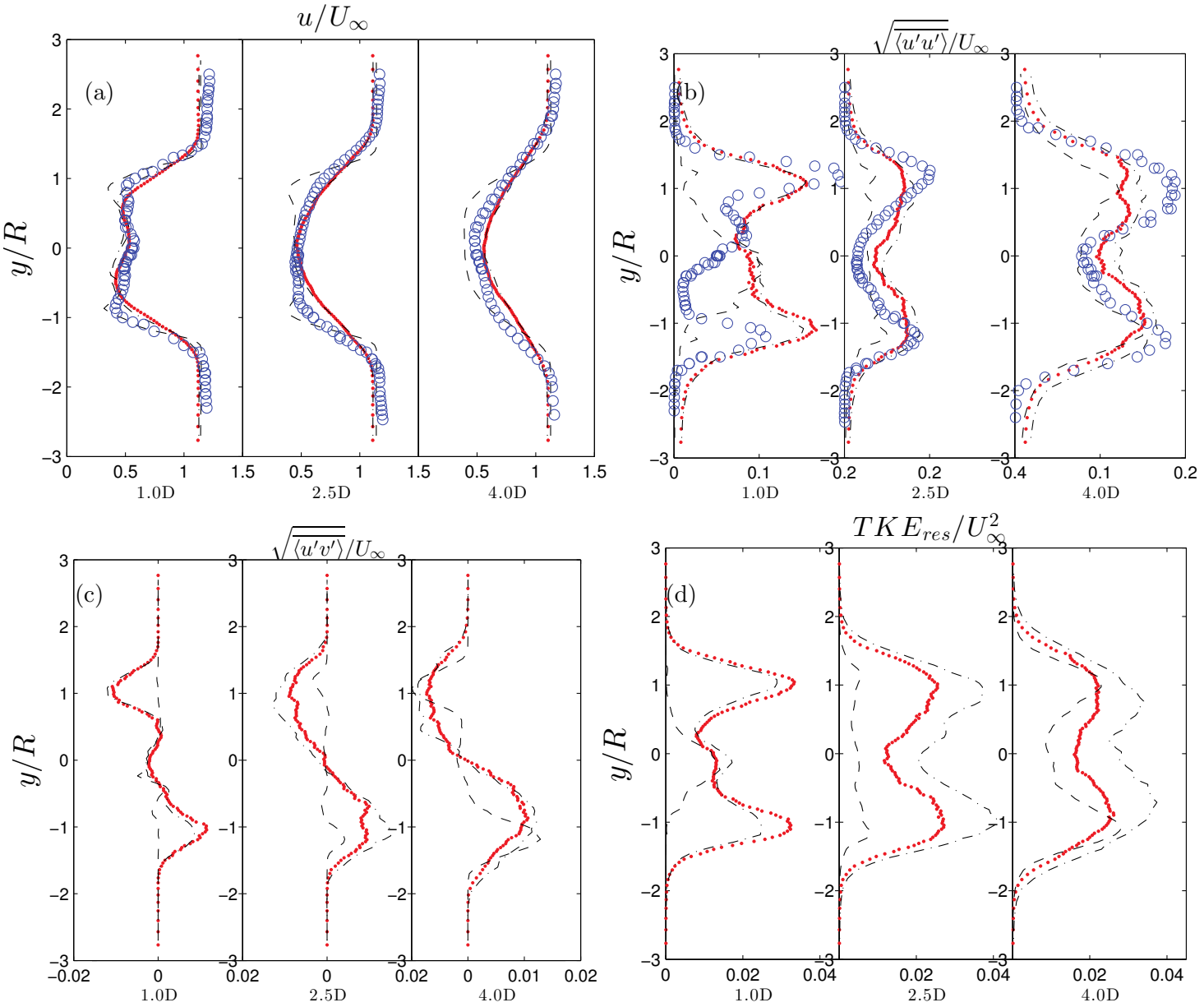

Figure 5.9: Role of free stream turbulence at the Re=50,000. Comparison of (a) mean streamwise velocity, (b) turbulence intensity, (c) turbulent shear stress, and (d) resolved TKE at different free-stream turbulence levels. [.....] reference case (NO), [- - -] laminar free-stream, [- . - .] low free-stream turbulence both obtained using $j = 35$ and MO model, [o o o] experimental data.

5.3.3 Role of the body force smearing parameter

Another test is performed on the sensitivity of the results to the actuator line forcing filter width also known as smearing parameter $\epsilon = \frac{\epsilon_{AL}}{\Delta}$. Three different cases are considered, i.e., $\epsilon = 1$, $\epsilon = 1.5$, and $\epsilon = 2.2$. In theory, the parameter ϵ_{AL} should be as small as possible meaning that the force should be applied on the exact point of interest, but for numerical stability reasons, a value of $\epsilon_{AL} \approx 2 - 4\Delta$ has been recommended cf. Jimenez et al. (2007); Troldborg (2008). It can be seen from figure 5.10(a) that the wake profiles predicted by the smallest ϵ value of 1 at $x/D = 1$ and $x/D = 2.5$ are less accurate compared to the other cases. Subfigures (b,c,d) show that the $\epsilon = 1$ leads to smaller values of turbulence intensity, shear stress and TKE peaks compared to the cases with larger ϵ.

Looking at the blade loadings, figure 5.11, reveals that small values of ϵ lead to wiggled loadings on the blades with smaller force magnitudes. To assure numerical accuracy, therefore, a value of $\epsilon = 2.2$ is chosen for the rest of the simulations.

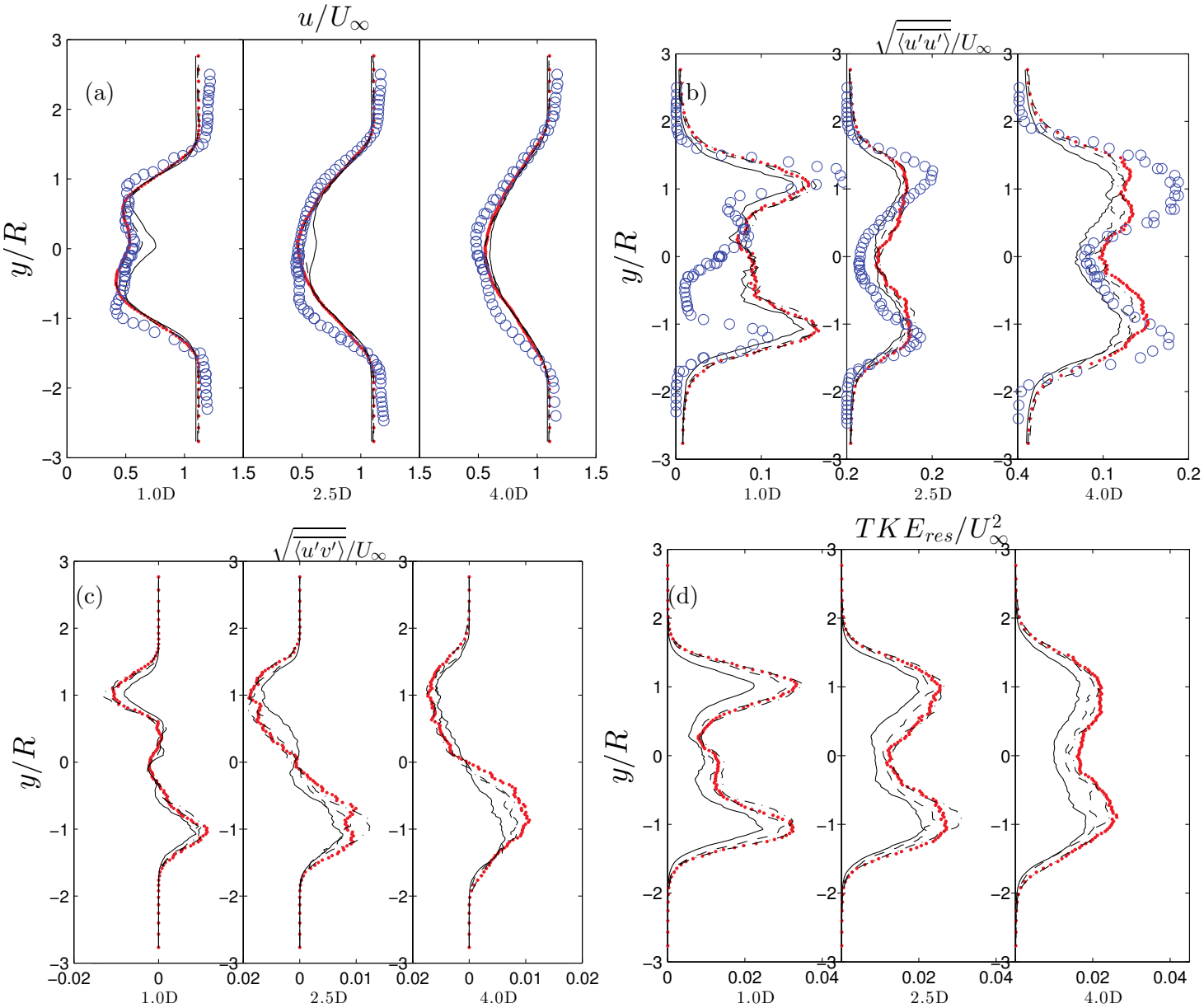

Figure 5.10: Role of smearing parameter ϵ for the Re=50,000 flow. Comparison of (a) mean streamwise velocity, (b) turbulence intensity, (c) turbulent shear stress, and (d) resolved TKE using different values of the force smearing filter width ϵ. [.....] reference case, [——] $\epsilon = 1$, [- - -] $\epsilon = 1.5$, [- . - . -] $\epsilon = 2.2$, [o o o] experimental data. For all cases $j = 35$ and MO model are used.

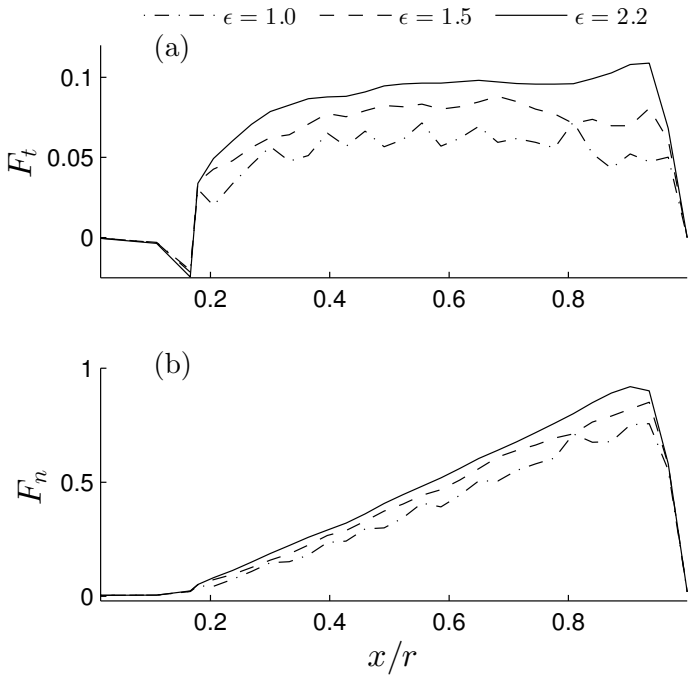

Figure 5.11: (a) Tangential and (b) normal forces acting on the upstream turbine using different force smearing filter widths ϵ.

5.3.4 Role of the SGS modeling and Reynolds number

To evaluate the effectiveness of a SGS models, the portion of the modeled kinetic energy k_{res} to the total TKE, that is, the sum of the resolved and SGS parts $k_{res} + k_{sgs}$,

$$TKE_{ratio} = \frac{k_{modeled}}{k_{total}} = \frac{k_{sgs}}{k_{res} + k_{sgs}} \tag{5.5}$$

are evaluated. The TKE ratio holds a value of 0 in the DNS, where all of the TKE is simulated, and 1 in RANS, where all of the turbulence is modeled. In LES, this ratio can carry a value between 0 and 1 depending on the SGS modeling, filtering, grid size etc. While there is no globally accepted value, a TKE ratio of less than 0.20 is recommended in Pope (2000) and Gant (2010) for different flows.

Figure 5.12 investigates the role of the SGS models and rotor resolutions on the TKE ratio of the in-line simulations. The TKE ratios are obtained based on two methods. The accumulated sum of k_{sgs} divided by the accumulated sum of k_{total} as well as the linear fit to the k_{sgs}/k_{total} ratio for all mesh points. The SGS kinetic energy is obtained using the scale similarity hypothesis by applying the explicit 3D (test) filter presented in equation 2.17 to the velocity components. The resolved TKE is obtained from the components of the r.m.s. of the velocity ($k_{res} = 0.5(u_{rms}^2 + v_{rms}^2 + w_{rms}^2)$). It can be seen from the figure 5.12(a) that for the rotor resolution of $j = 35$, a value

of $\frac{k_{sgs}}{k_{tot}}|_{(best\ fit)} = 2.3\%$, using the linear curve fitting, and $\frac{k_{sgs}}{k_{tot}}|_{(sum)} = 6\%$, using the accumulated values, is obtained. The SGS contribution for the case of the dynamic Smagorinsky (figure 5.12(b)) is 1.6% and 4%, respectively. Prediction of a lower k_{sgs} by the DS model suggests that the model dissipates more SGS kinetic energy than the MO model. For these simulations, it is not clear whether the SGS models are effective, due to the low TKE ratios. For the case with lower resolution ($j = 26$), the TKE ratio grows to $\frac{k_{sgs}}{k_{tot}}|_{(best\ fit)} = 11\%$ and $\frac{k_{sgs}}{k_{tot}}|_{(sum)} = 14\%$, respectively as shown in figure 5.12(c). In other words, the kinetic energy resolved by the grid amounts for 86% or 89% of the total kinetic energy, depending on the method of calculation, which suggests that the TKE is adequately resolved and the SGS models are being functional for this case. From the LES point of view, the computational grid could be even coarser than the case with $j = 26$ to allow LES to take over a larger portion of the kinetic energy. From a physical point of view, however, this would deteriorate the accuracy of the predictions, as was seen in the grid sensitivity study. Therefore, there is a limitation on the use of SGS models depending on the desired mesh resolution in the case of the AL simulations.

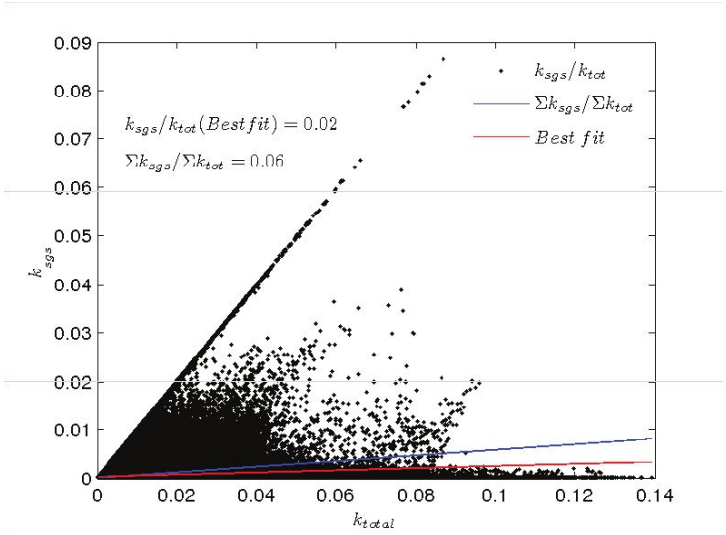

(a)

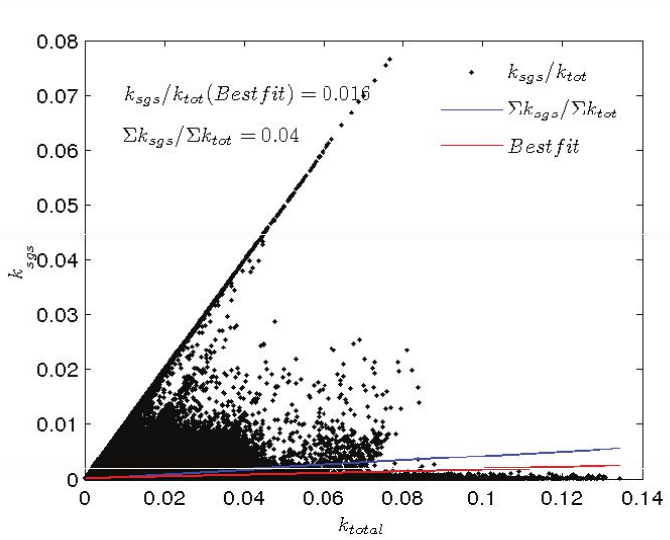

(b)

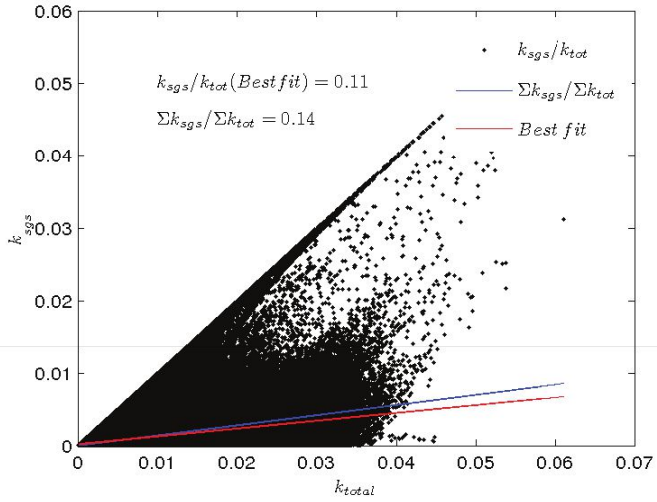

(c)

Figure 5.12:

The ratio of the SGS kinetic energy to the total TKE or the rotors operating at Re = 50, 000. (a) Rotor resolution j = 35 (MO model). (b) Rotor resolution j = 35 (DS model). (c) Rotor resolution j = 26 (MO model). The black dots represent the TKE ratio for each computational node.

Figure 5.13 demonstrates the contours of the SGS, resolved, and the total turbulent kinetic energy plotted at different positions downstream of the first rotor. The MO and the DS models using $j = 35$ are chosen for the comparison. It can be visually acknowledged that the SGS kinetic energy contours are greater for the MO than the DS model, as was also observed in another form in figure 5.12. Nonetheless, the effects of the SGS part on the total TKE is very small and the resolved and total TKE contours are very similar for both cases.

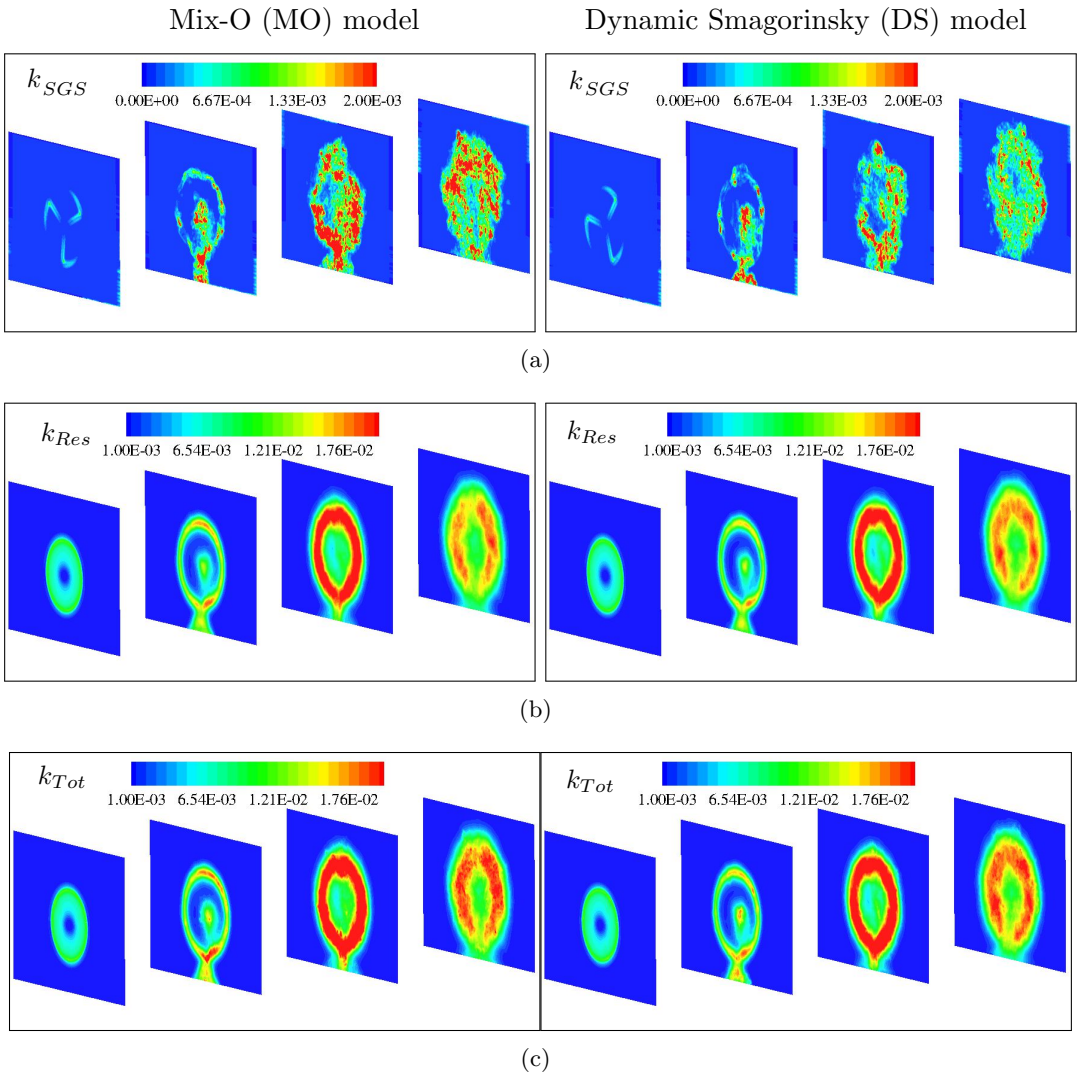

Figure 5.13: Contribution of the SGS model to the total TKE using the MO model (left) and the DS model (right) for the rotors operating at $Re = 50,000$ with rotor resolution of $j = 26$. (a) The SGS kinetic energy. (b) The resolved TKE. (c) The total TKE.

Next, the effects of the various SGS models on the eddy viscosity profiles are compared with respect to the Reynolds number. With increasing the Reynolds number, a higher value for the eddy viscosity is expected due to generation of smaller flow structures and higher dissipation. Here, simulations are performed with two Reynolds numbers of $Re_r = 50,000$ and $Re_r = 500,000$ based on the inflow velocity and the rotor radius. The normalized eddy viscosities calculated with each model can be seen in figure 5.14. The NO model is not presented ($\nu_{sgs} = 0$). As can be seen, the highest eddy viscosity is predicted with the Smagorinsky model (with constant coefficient of $C_s = 0.1$). The dynamic Smagorinsky predicts values that are roughly 2-3 times smaller than the SM model. The MO model predicts even smaller values with peaks smeared out at the tip location. It can also be seen from the low Reynolds number case, that both variants of the dynamic mixed model predict eddy viscosities in the same order of magnitude as the other models, while the values obtained by DMo are closer to the MO predictions and the DMs values are generally the highest among all models, showing that the DMs model is the most dissipative of all cases.

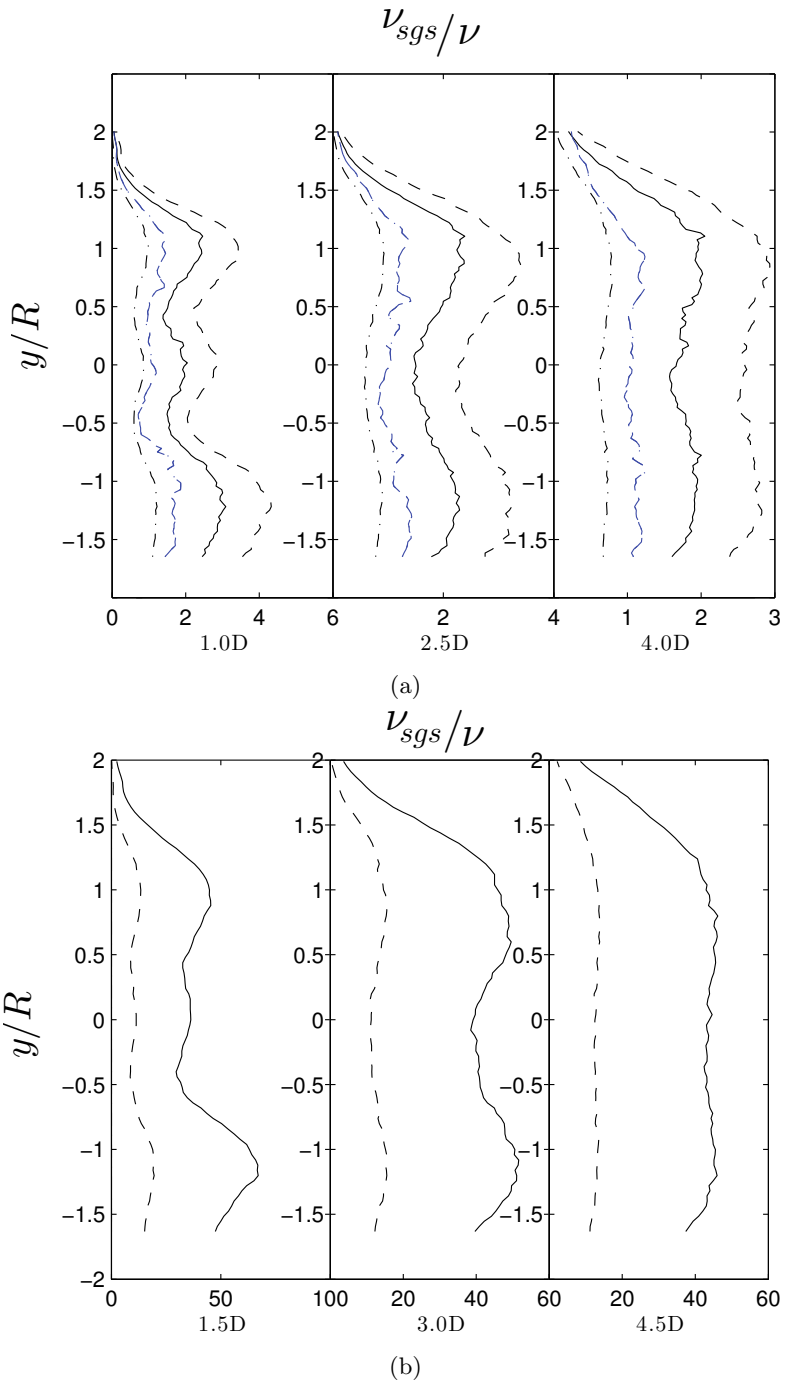

Figure 5.14: (a) Comparison of eddy viscosities (plotted on the abscissa) computed with different SGS models for Re=50,000, [- - -] DMs, [- . - . -] DMo, [——] DS, [- - -] SM. (b) Similar plots for Re=500,000, [- - -] MO, [——] SM.

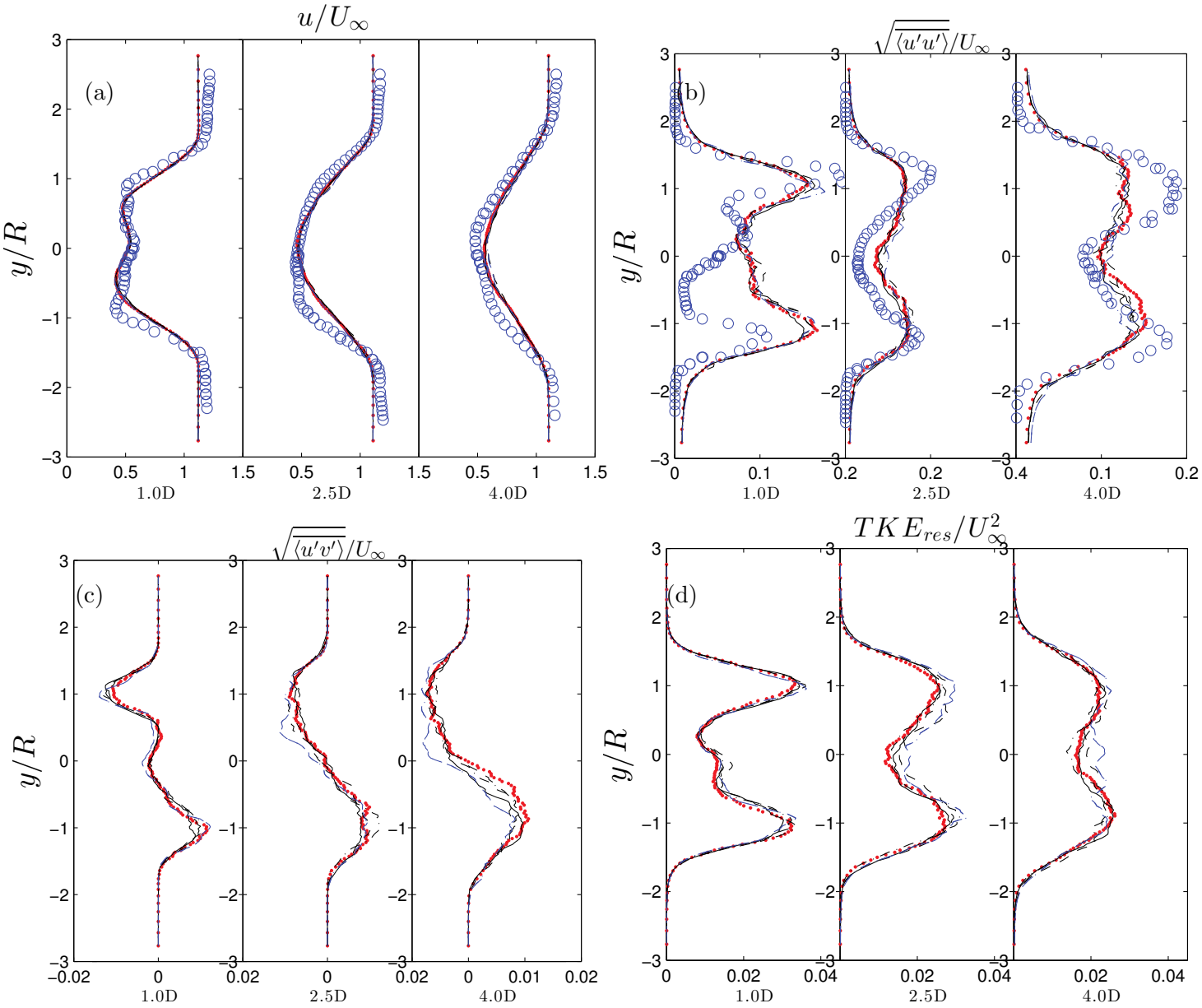

Figure 5.15: Comparison of (a) mean streamwise velocity (b) turbulence intensity (c) turbulent shear stress and (d) resolved TKE using different SGS models at Re=50,000. [——] reference case (NO), [- . - . -] *DMo*, [——] *DS*, [- - -] *SM*, [- . - . -] *MO*, [o o o] experimental data.

Figures 5.15 and 5.16 demonstrate the flow structures obtained by various SGS models for $Re = 50,000$ and $Re = 500,000$. As shown in the figures, the velocity profiles obtained with different SGS models collapse on top of each other although there are significant discrepancies in the predicted eddy viscosities shown in figure 5.14. Because of the direct impact of the eddy viscosity on the generation of vortices, it is valuable to compare the 3D flow structures obtained by different SGS models. Figures 5.17 and 5.18 represent the 3D iso-vorticities and a vertical snapshot of the vorticity through the tower plane for the different SGS models, respectively. Although all of the models predict the transition location for the tip vorticies, it can be seen that the NO model results in excessively small vortical structures whereas DMo for instance dissipates some of the small structures and leaves only the strong vortices. The effects of the SGS model on the wind turbine loading are found to be very small. Figure 5.19 shows the tangential and normal forces for different SGS models at $Re = 50,000$. There is also a case with $Re = 500,000$ on top of the plots to observe the effects of increased Reynolds number. As can be noticed, for $Re = 500,000$, the forces are higher at the tip which is due to the higher aerodynamic coefficients at the high Reynolds numbers, however looking at all cases with Re=50,000, it is clear that SGS modeling does not have a large impact on the loadings.

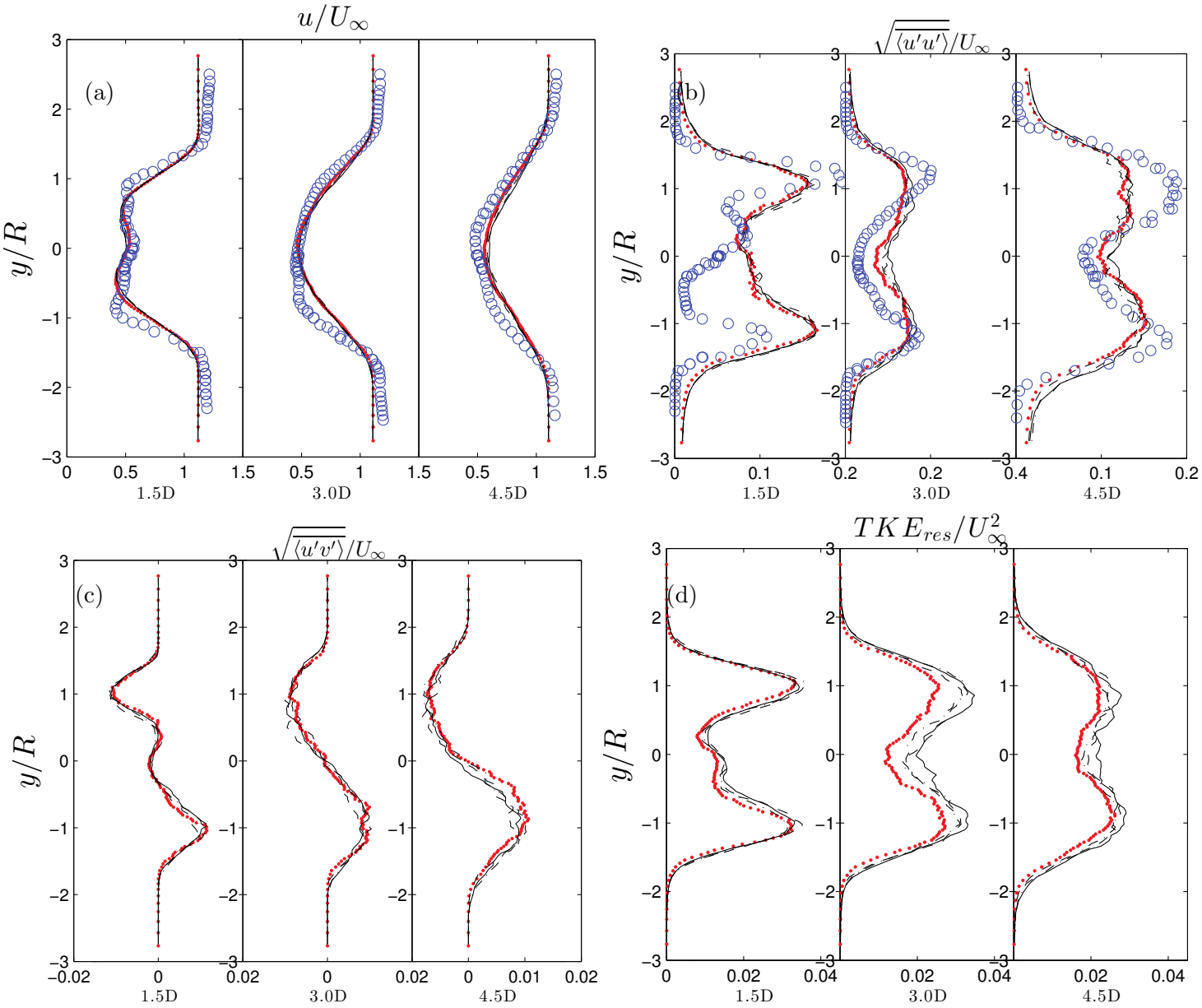

Figure 5.16: Comparison of (a) mean streamwise velocity (b) turbulence intensity (c) turbulent shear stress and (d) resolved TKE using different SGS models at Re=500,000. [——] reference case, [——] *SM*, [- - -] *MO*, [- . - . -] *NO*, [o o o] experimental data.

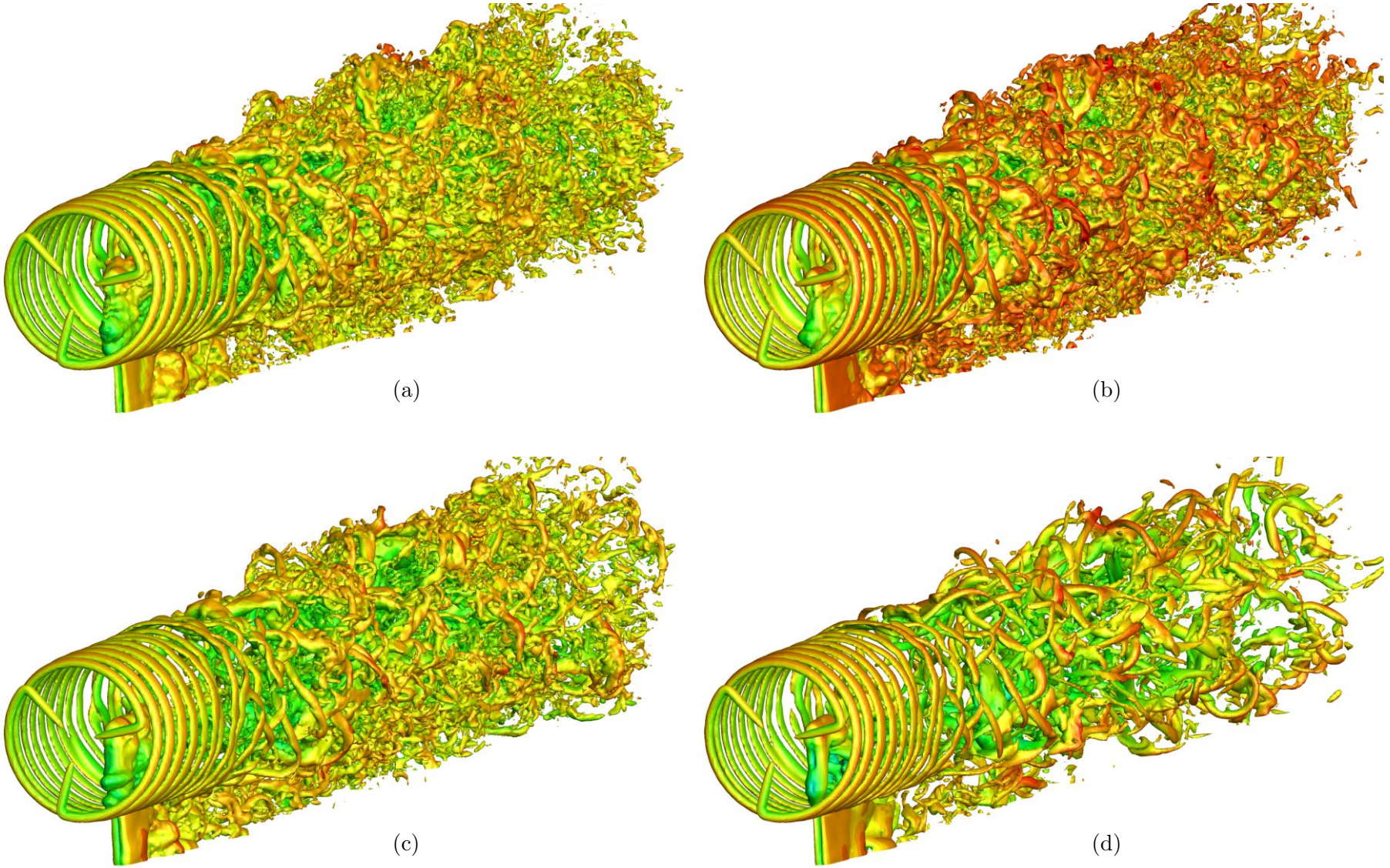

Figure 5.17: Iso-vorticity snapshots for (a) NO, (b) MO, (c) DS, and (d) DMo models at Re=50,000.

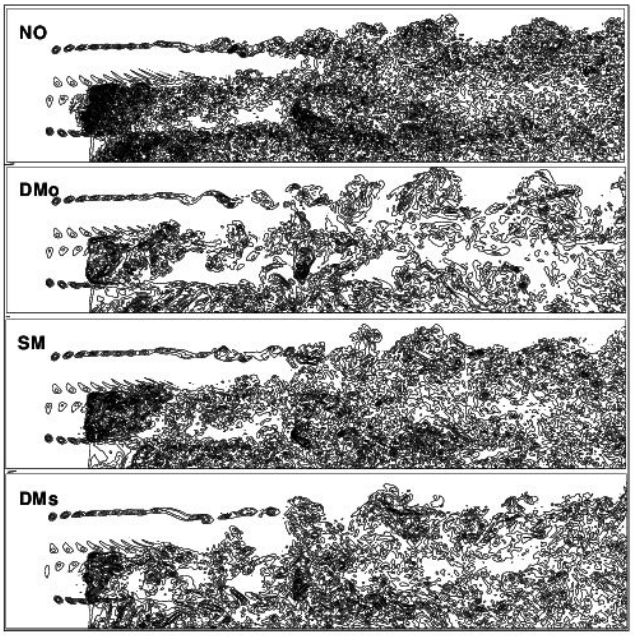

Figure 5.18: 2D snapshots of iso-vorticity for the NO, DMo, SM and DMs models at Re=50,000. Less dissipative models line NO tend to break the vortices down to smaller, more homogeneous structures.

Finally, figure 5.20 compares the performance of the turbines in terms of power and thrust coefficients. Results obtained using different SGS models are compared the measurement values at the tip speed ratios of $\lambda_1 = 6$ and $\lambda_2 = 4$ for the upstream and downstream turbines, respectively. The power and thrust coefficients of the rotors are computed as

$$C_P = \frac{2P}{\pi\rho U_\infty^3 R^2} \quad \text{and} \quad C_T = \frac{2T}{\pi\rho U_\infty^2 R^2}, \tag{5.6}$$

where P and T are the power and thrust forces respectively and velocity at the inlet is used as reference.

As expected from the previous results, the SGS model has almost no effect on these variables. For all of the simulations, the power coefficient obtained for the upstream rotor is captured accurately but for the C_T for the first rotor and C_P and C_T for the second rotor, the numerical results underestimate measurements.

5.4 Simulation of half wake interaction

5.4.1 Investigation of rotor operating conditions

This subsection briefly presents the effects of the tip speed ratio, free stream turbulence, and the rotor configuration on the flow statistics. Different investigated operating

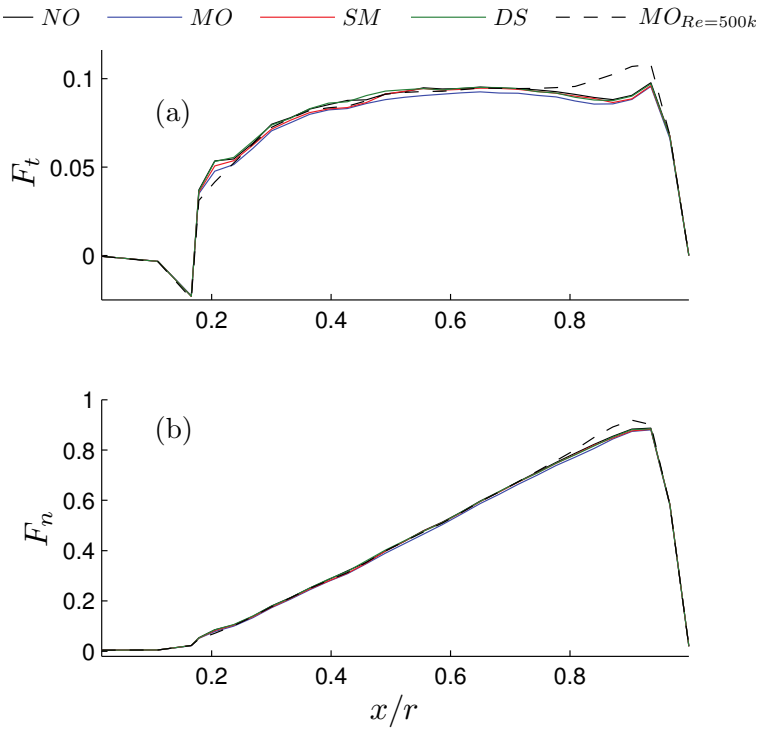

Figure 5.19: Tangential and normal forces acting on the upstream turbine using different SGS models and Reynolds numbers.

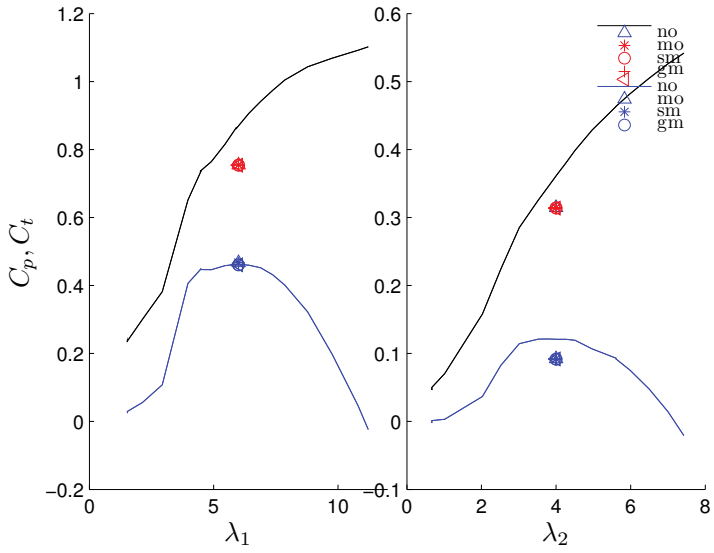

Figure 5.20: Power and thrust coefficients for the upstream (left) and downstream (right) rotors. [——] Experimental C_P curve;[——] Experimental C_T curve at different TSRs.

Case	λ_1	$\lambda_2^{\ddagger}$	rot. config.	I
BT2-A1	6	2.50	*in-line*	0.24%
BT2-A2	6	4.0	*in-line*	0.24%
BT2-A3	6	7.0	*in-line*	0.24%
BT2-B1	6	2.50	*in-line*	10%
BT2-B2	6	4.0	*in-line*	10%
BT2-B3	6	7.0	*in-line*	10%
BT3-A1	6	3.50	*lateral offset*	0.24%
BT3-A2	6	4.75	*lateral offset*	0.24%
BT3-A3	6	8.0	*lateral offset*	0.24%
BT3-B1	6	3.50	*lateral offset*	10%
BT3-B2	6	4.75	*lateral offset*	10%
BT3-B3	6	8.0	*lateral offset*	10%

‡ To obtain C_P and C_T curves, 7 cases of $\lambda_2 \in [1\ \ 9]$ are performed for BT3 cases.

Table 5.2: Different test cases simulated to investigate the effect of the TSR, free-stream turbulence and turbine placement

conditions are summarized in table 5.2.

As can be seen, both in-line and laterally separated cases are considered for the simulations that span a range of tip speed ratios. As discussed earlier, for the third blind test experiments Krogstad and Sætran (2013) refered to as BT3, the turbines are shifted slightly sideways so that the wake from the first turbine partially affects the downstream turbine and imposes a non-symmetrical loading on it. The BT3 set up will be studied numerically in this section.

Numerical settings for the simulations performed in this section are similar to those used in the previous section. Computations are, nevertheless, only performed using the MO model at $Re = 50,000$ and with $\epsilon = 2.2\Delta$. The wind tunnel turbulence is modeled by introducing the synthetic resolved turbulent fluctuations at three rotor radii upstream of the first turbine model following the method described in 1.3.3. The mean velocity and turbulence intensity are then computed at the location of the rotor plane in the empty tunnel. The level of turbulence is extracted and adjusted to match the given turbulent conditions of the experiments. Figure 5.21 shows the computed mean velocity and turbulence intensity profiles obtained for the numerical simulations at three diameters downstream of the inlet section and figure 5.22 represents the decay of turbulence in the numerical tunnel exhibiting a good agreement with the experimental turbulence decay.

The numerical simulations are performed using a range of tip speed ratios. In all cases, the upstream turbine rotates at its design TSR of $\lambda_1 = 6$. For the in-line

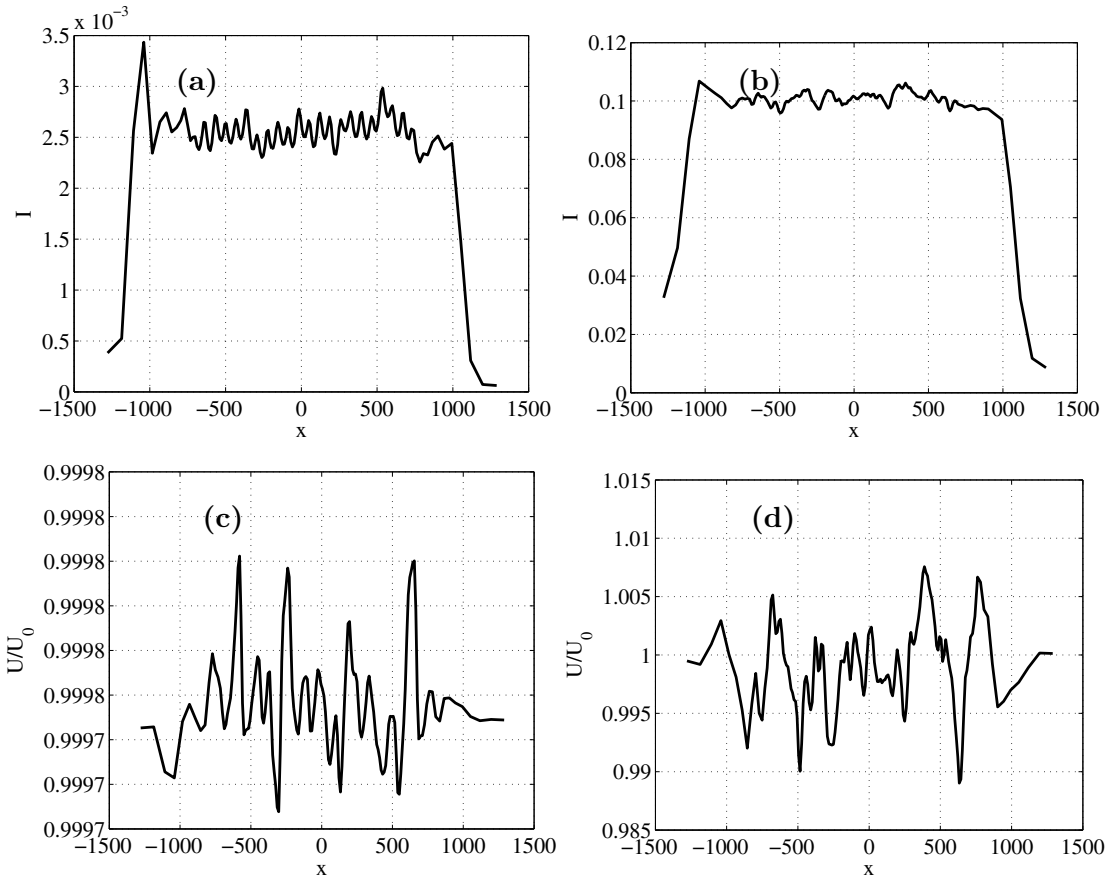

Figure 5.21: Computed time averaged turbulence intensity profile at a horizontal line for (a) low and (b) high turbulence levels. Computed time averaged streamwise velocity profile at a horizontal line for (c) low and (d) high turbulence levels positioned at 2D from the inlet section.

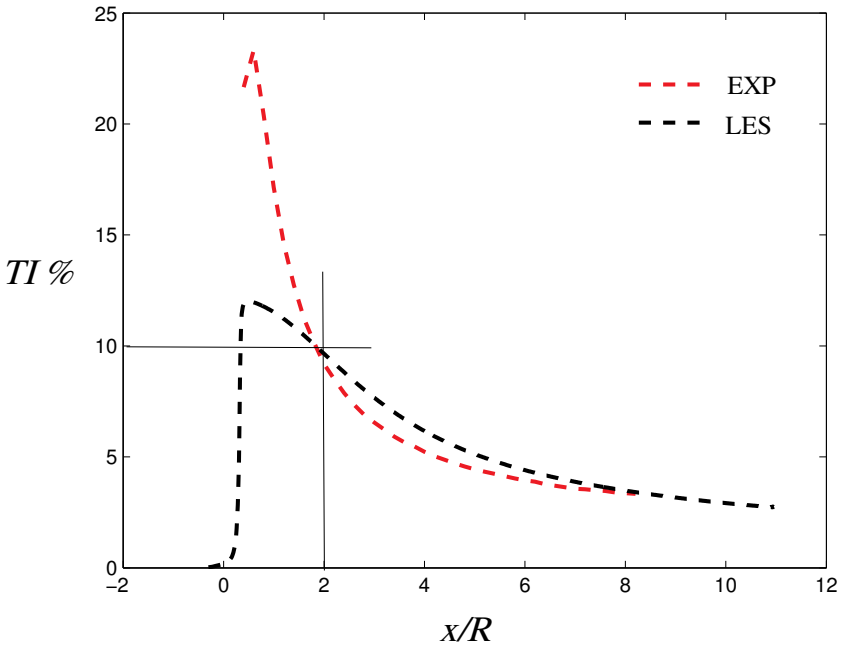

Figure 5.22: The turbulence intensity decay in the wind tunnel versus the numerical simulations.

cases (BT2), the downstream turbine operates under three TSRs of $\lambda_2 = 2.5, 4.0, 7.0$ and for the offset cases (BT3), the downstream turbine operates under three TSRs of $\lambda_2 = 3.5, 4.75, 8.0$, regarded respectively as the at the *partly stalled*, *optimal*, and the *runaway* conditions [1]. Figures 5.23 and 5.24 show the top view of the TKE contour slices through the hub height for the BT2 and the BT3 cases using low and high free stream turbulence and different TSRs for the downstream turbine. As can be seen, for all cases, an increase in the λ_2 results in a significantly higher TKE downstream the rotor. As expected, the BT3 cases do not show a symmetric distribution of the TKE, unlike the BT2 cases.

Quantitatively, figures 5.25 and 5.26 show the time averaged velocity and turbulence intensity profiles at $x/R = 2$ and $x/R = 6$ downstream of the second turbine. It is seen that close to the rotor, the wake is dominated by distinct peaks, due to the root and tip vortices, which break into more homogeneous small-scale turbulent structures further downstream. In general, the wake deficit as well as turbulence intensities are captured very well.

[1] At low TSRs, a high angle of attack is obtained since TSR is proportional to the rotational velocity Ω (see figure 5.2). Therefore, the term *stalled* can be used to characterize the low TSR situation. The optimal values are usually obtained according to the maximum lift-drag ratio in accordance with the TSR. The high TSR values result in very small angles of attack, increased C_T and development of a fully turbulent near wake due to rapid vortex breakdown.

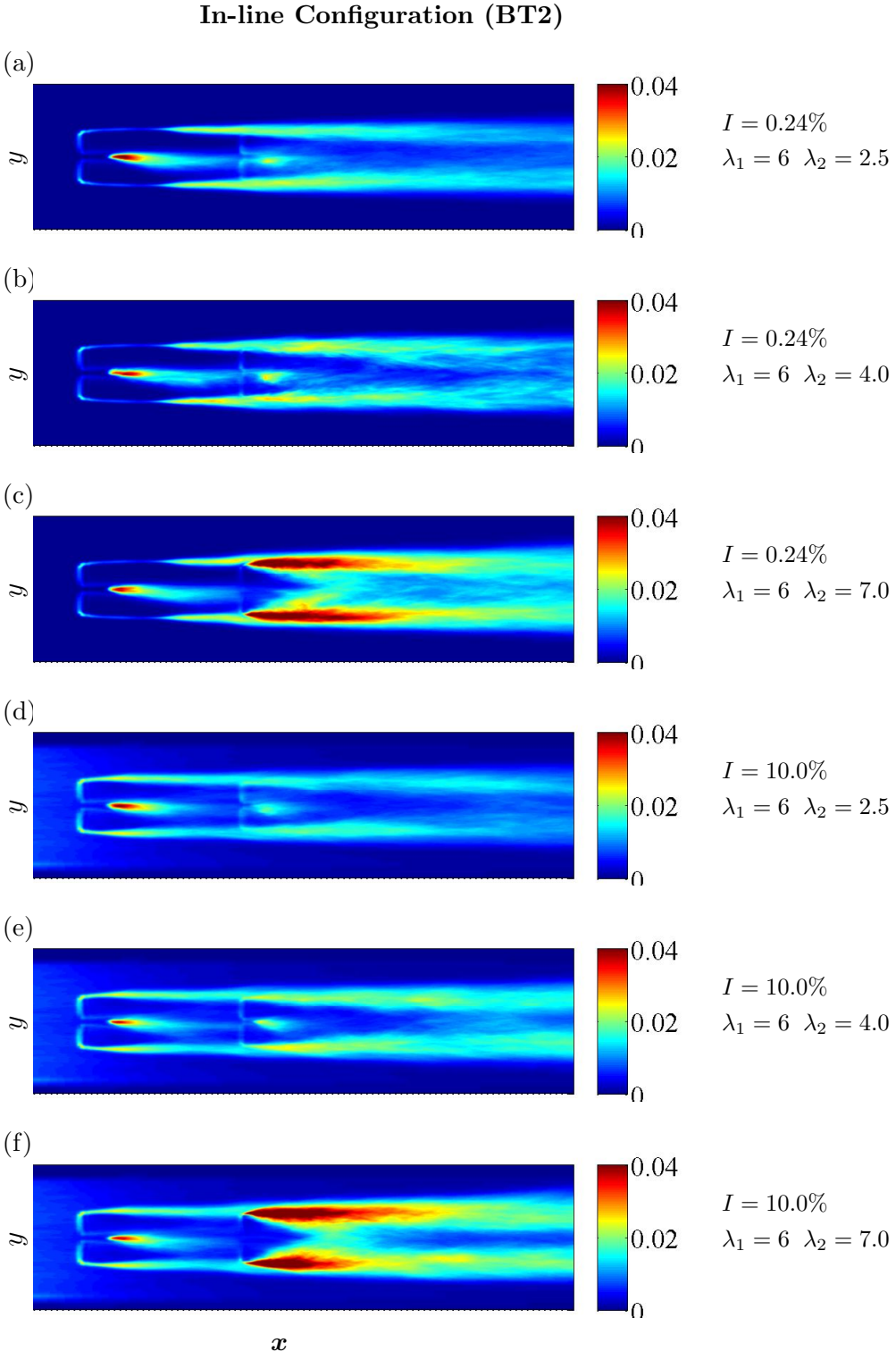

Figure 5.23: Contours of the TKE through the hub height (top view). Low free-stream turbulence using $\lambda_1 = 6.0$ and (a) $\lambda_2 = 2.5$, (b) $\lambda_2 = 4.0$ and (c) $\lambda_2 = 7.0$. High free-stream turbulence with $\lambda_1 = 6.0$ and (d) $\lambda_2 = 2.5$, (e) $\lambda_2 = 4.0$ and (f) $\lambda_2 = 7.0$.

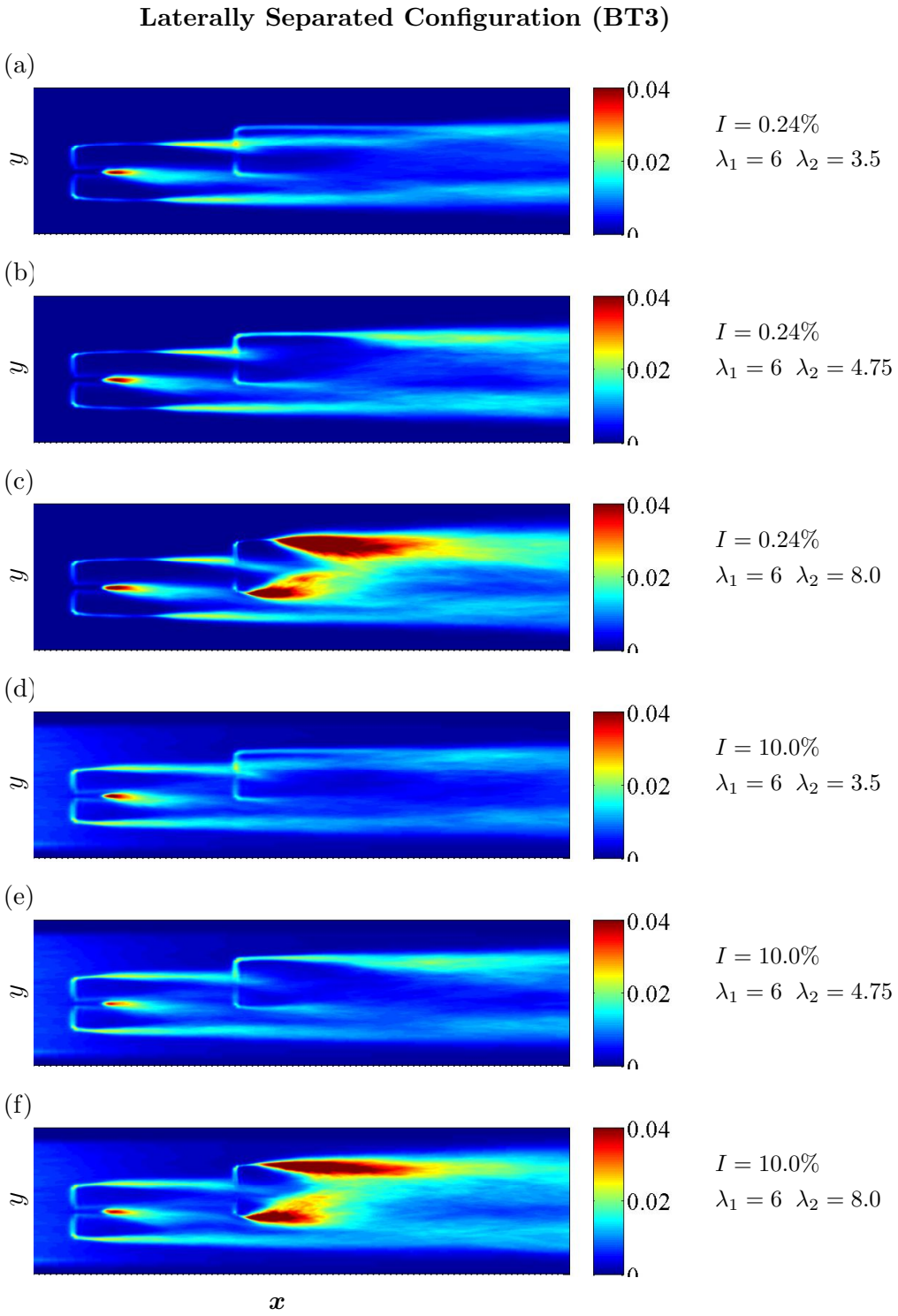

Figure 5.24: Contours of the TKE through the hub height (top view). Low free-stream turbulence using $\lambda_1 = 6.0$ and (a) $\lambda_2 = 3.5$, (b) $\lambda_2 = 4.75$ and (c) $\lambda_2 = 8.0$. High free-stream turbulence using $\lambda_1 = 6.0$ and (d) $\lambda_2 = 3.5$, (e) $\lambda_2 = 4.75$ and (f) $\lambda_2 = 8.0$.

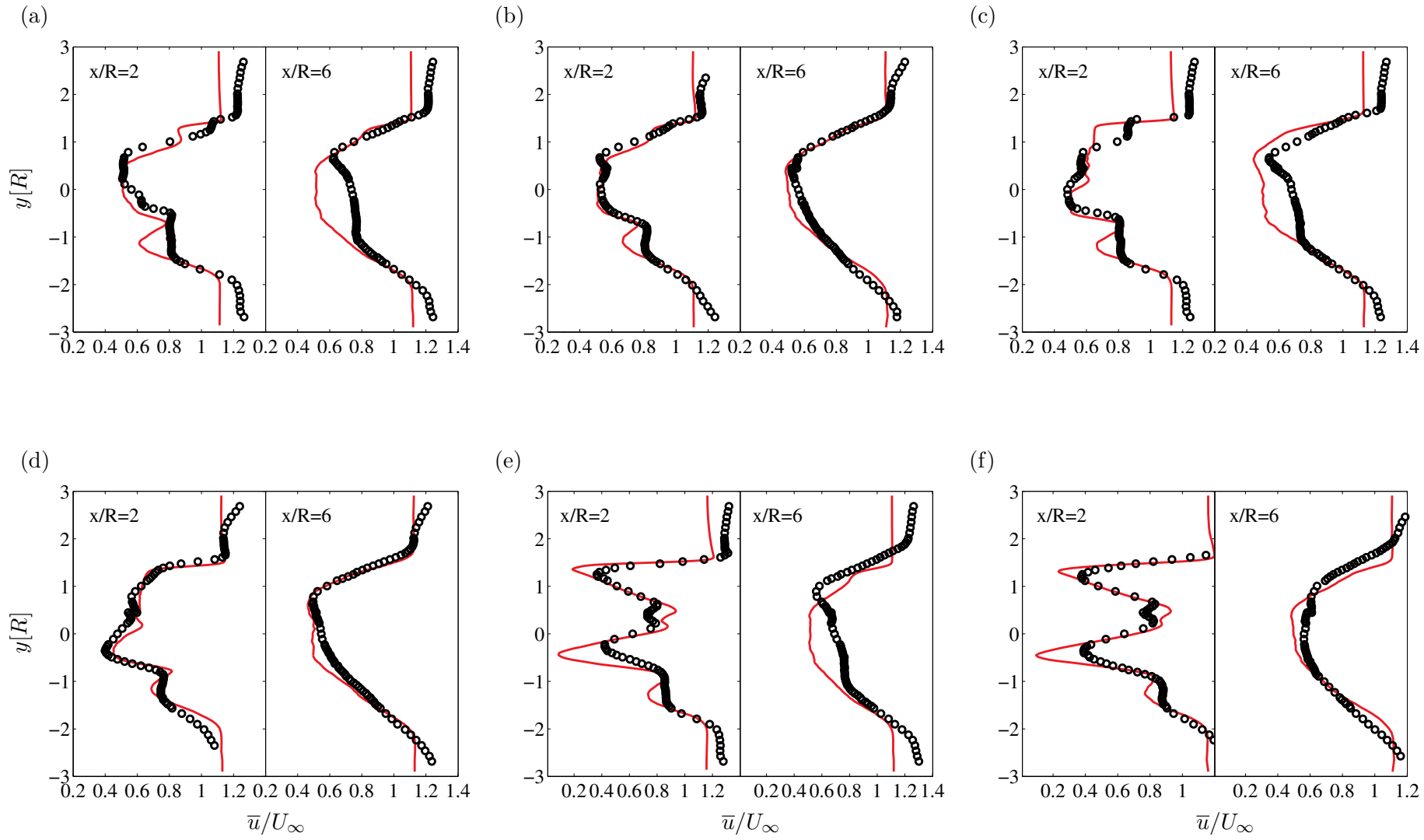

Figure 5.25: Mean velocity profiles $\overline{u}/U_\infty$ obtained along horizontal line through the rotor center. (a,c,e) Low free-stream turbulence. (b,d,f) High free-stream turbulence. (a-b) $\lambda_2 = 3.5$. (c-d) $\lambda_2 = 4.75$. (e-f) $\lambda_2 = 8.0$. [$\circ\ \circ\ \circ$] denotes experimental data and [——] represents LES computations.

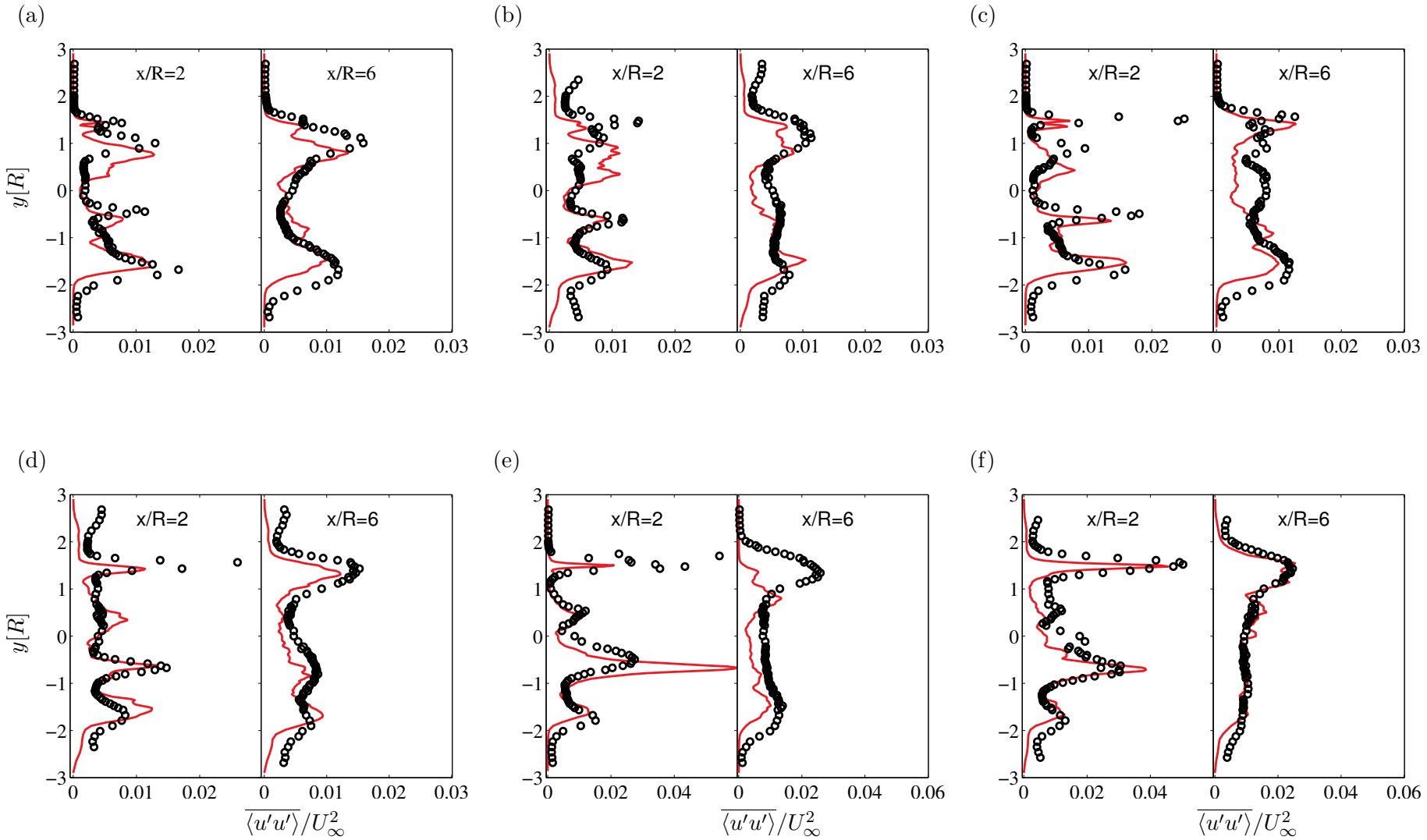

Figure 5.26: Turbulent stress $\overline{\langle u'u' \rangle}/U_\infty^2$ profiles obtained along horizontal line through the rotor center. (a,c,e) Low free-stream turbulence. (b,d,f) High free-stream turbulence. (a-b) $\lambda_2 = 3.5$. (c-d) $\lambda_2 = 4.75$. (e-f) $\lambda_2 = 8.0$. [$\circ\ \circ\ \circ$] denotes experimental data and [——] represents LES computations.

The performance envelope of both wind turbines in presence of low free-stream turbulence is presented in figure 5.27, where 7 different cases with λ_2 varying from deeply stalled case at $\lambda_2 = 1$ to 9 are computed to draw accurate C_P and C_T curves. It can be seen that C_P increases with the tip speed ratio until it reaches its maximum at the design tip speed ratio. Further increase in the TSR, however, decreases the power output. Comparing with the BT2 curves plotted in figure 5.20, it can be seen that higher C_P and C_T values are obtained in the BT3 case, which is due to the partial flow blockage when the rotor models are laterally separated.

The first indication of the stall is observed at $\lambda = 4$ and with further decrease in λ, the blade operates in deep stall over the entire span. At very high tip speed ratios $\lambda > 11$, the near root region operates at negative angle of attack and results in a negative power production. The turbine shows a rapid drop in power production for $\lambda < 4$. This can be directly related to the static stall hysteresis of the blades. The effect of the interacting wake on the downstream turbine is also presented. At the first glance, a general reduction in production level of the downstream turbine is observed. This is due to the fact that the downstream turbine is exposed to relatively lower velocity as compared with the upstream one. The drop in the power performance is removed here. This is because the hysteresis effects are completely removed as the upstream turbine is convecting a turbulent field downstream. The numerical prediction is in excellent agreement with the experiments for the power coefficients. The thrust coefficients are proportional to the TSR. Here it can be observed that the thrust coefficient of the upstream rotor is predicted well by the numerics, while it is generally under-predicted for the downstream rotor.

Figure 5.28 shows the performance curves for the high free-stream turbulence. As can be seen, introduction of the high turbulence decreases the power production at the optimum rotor performance and the removes the hysteresis phenomena. Once again, a good agreement is achieved between LES and the experimental results. The thrust coefficients of the second turbine increases by almost 50% for $\lambda < 4$ and reaches 30% for the runaway condition. LES, however, over-predicts the thrust for the upstream rotor and the under-predicts it for the downstream rotor.

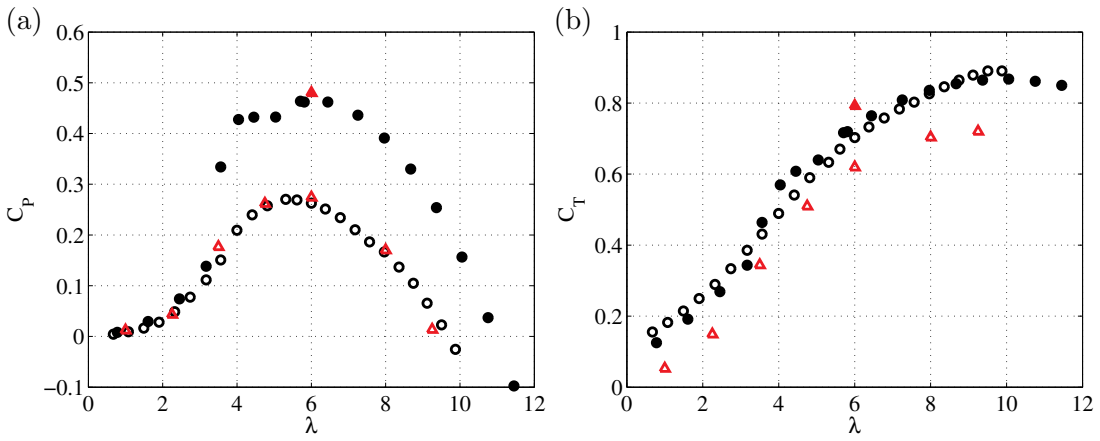

Figure 5.27: (a) Power and (b) thrust coefficients for the upstream and downstream turbines at low free-stream turbulence. [●●●] Experimental data, upstream turbine, [○○○] Experimental data, downstream turbine, [△△△] LES computations, upstream turbine, [▲] LES computations, downstream turbine.

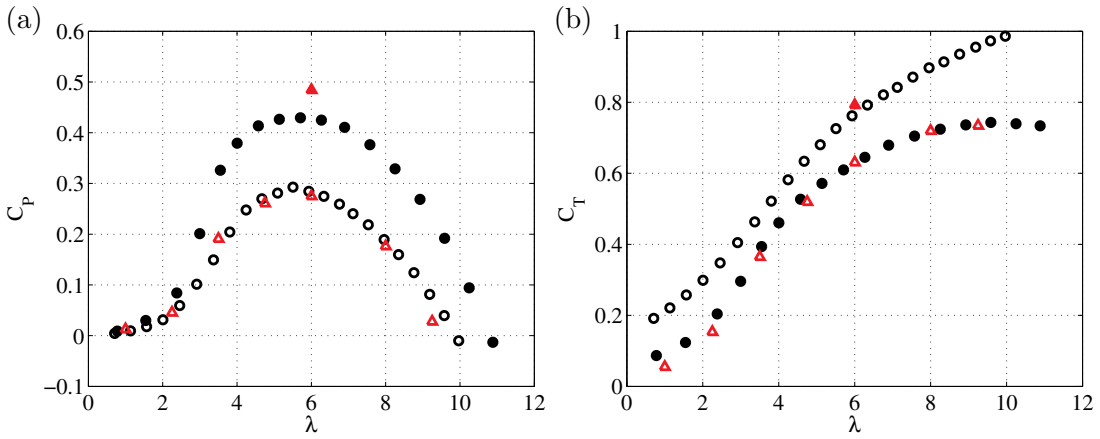

Figure 5.28: (a) Power and (b) thrust coefficients for the upstream and downstream turbines at high free-stream turbulence. [●●●] Experimental data, upstream turbine, [○○○] Experimental data, downstream turbine, [△△△] LES computations, upstream turbine, [▲] LES computations, downstream turbine.

5.5 summary

A detailed investigation of the LES of the wind turbine wakes for the case of a double-rotor arrangement was studied using the actuator line model and the results were compared with the wind tunnel measurements. For all simulations, the first and second order statistical moments (velocity and turbulence intensity) are well captured. The

role of SGS modeling on the predicted flow structures was investigated and it was seen that the dissipative SGS models result in a lower modeled kinetic energy due to the dissipation of the small structures. It was shown that grid coarsening increases the contribution of the SGS model. However, even for the cases in which a proper portion of the kinetic energy was modeled, the impact of the SGS models on the flow statistics was minimal and in the case of the wind turbine loadings and power and thrust coefficients of the turbines, hardly any difference was observed. It was therefore concluded that having a high resolution (more than 30 mesh points per actuator line) can make the SGS modeling ineffective since a very low ratio of the kinetic energy will be modeled in such actuator line simulations (This was opserved to be the case for Reynolds numbers, based on rotor radius, of up to Re=1,000,000). Therefore to save computational power, the flow can be simulated without any SGS modeling.

Simulations with different actuator line force smearing width ϵ parameters were also performed and a choice of $\epsilon \geq 2$ was found necessary in order to predict accurate flow structures and blade loadings. Simulations were also performed using laminar and turbulent inflows and a small amount of free-stream turbulence was found crucial in the simulations in order to trigger instabilities that facilitate breaking-up of the vortices in the tip region.

Finally, studies at different operational conditions were conducted by moving the downstream turbine laterally and running simulations in a range of tip speed ratios for the downstream turbine. It was perceived that increasing the TSR of the downstream turbine results in higher turbulence downstream of the second turbine. It was also shown that moving the downstream turbine laterally to the half-wake of the upstream turbine results in higher power and thrust coefficients as compared to the in-line rotor arrangement due to the lower flow blockage. In general, flow structures and turbine characteristics were captured very well using LES computations.

Chapter 6

Conclusions and future work

Conclusions

In order to provide a better understanding of the role of the sub-grid scale modeling, various flows of relevance for wind energy applications were studied through numerical simulations and wind tunnel measurements. The study began with a general investigation of the LES technique and some of the issues relevant to the finite volume incompressible Navier-Stokes solver, EllipSys3D, were discussed. It was seen that the collocated grid-arrangement (in its standard form) suffers from kinetic energy conservation problems and that the numerical errors can have a large impact on the quality of the LES. Moreover, the use of higher order methods, explicit filtering (on a fine mesh), and the central discretization schemes was recommended for having the highest accuracy. The SGS eddy viscosity and eddy diffusivity models were discussed and new models were presented and examined for different flow applications.

Fully developed boundary layer flows at low Reynolds numbers were investigated using a wall-resolved approach, in which the grid is clustered near the wall and the wall boundary conditions is a Dirichlet type no-slip condition. For the wall-resolved low Reynolds number channel flow, all SGS models resulted in similar statistics. The energy equation was added to the solver and fully developed thermally stratified wall-resolved channel flows were briefly investigated using the implemented SGS eddy diffusivity models and the results were validated against DNS data. Fully developed high Reynolds number BL flows were also investigated. For the high Reynolds number cases, it was not feasible to resolve the walls by clustering the grids. Instead, the walls were represented by Neumann boundary conditions based on a standard shear stress model originated from the resolved velocities in the wall-neighbouring cells. For the high Reynolds number wall-modeled cases, a more advanced SGS model seemed to improve

the simulations. In particular, the dynamic Smagorinsky was found to predict the most accurate surface shear stress compared to other SGS models. The flow structures for low and high Reynolds numbers were compared and it was seen that the low Reynolds number flow case was associated with very long and narrow streaks close to the wall.

An infinite wind farm was simulated in which the turbines were represented by actuator discs and the boundary layer was simulated using both wall-modeled LES and by applying a method in which a prescribed mean shear (PMS) is imposed to the domain. Wall-modeled and PMS simulations were compared and especially in the rotor region, the PMS method was found to be able to predict accurate flow statistics, with a lower computational cost than the WM case.

Furthermore, wind tunnel measurements of the S826 airfoil were investigated for a range of Reynolds numbers from 40,000 to 400,000. This was performed in the low speed wind tunnel at DTU and the measurements included lift and drag polars as well as airfoil pressure measurements. At low Reynolds numbers, the airfoil showed hysteresis behaviour. The hysteresis behaviour was analysed by adding free-stream turbulence and by measuring the wire-generated turbulence (using hot-wire anemometry), it was seen that the unsteady behaviour could be removed and higher lift coefficients achieved with even a low free-stream turbulence. For example, the hysteresis effects were removed for flow at $Re = 40,000$ over the airfoil by introducing 0.65% free-stream turbulence. Parallel to the experiments, LES of the airfoil was performed using a mixed scale SGS model at different angles of attack for Reynolds numbers 40,000 and 100,000 with results validated against wind tunnel measurements. For the LES computations, patterns of the transition due to the growth of the Tollmien-Schlichting (T-S) waves, the Laminar Separation Bubble (LSB) and stall cells (SC) were observed and investigated. By comparing the pressure distribution as well as lift and the drag coefficients, it was found that LES can predict the flows around airfoils accurately provided that the mesh size and discretization are chosen properly.

LES of the wind turbine wakes using the actuator line technique was performed. While the emphasis was on investigation of SGS modeling for the actuator line simulations, several parameters including grid resolution, Reynolds number, and the actuator line force smearing parameter ϵ were also studied, and the results were compared with the wind tunnel experiments of the model turbines. From the simulations, it turned out that even though the SGS modeling had a large impact on the eddy viscosities and the SGS modeling was effectively applied, the flow structures and loadings were rather insensitive to the choice of SGS modeling. It was seen that increasing the mesh resolution results in lower contribution from the SGS modeling and at the same time,

accuracy of the simulations are dependent upon the mesh resolution. Therefore the practicality of SGS modeling is challenged if highly resolved actuator line simulations are desired. Different numerical parameters were seen to have large impact on the statistics. Especially, it was found that an AL force-smearing parameter of $\epsilon = \frac{\epsilon_{AL}}{\Delta} \geq 2$ is necessary to represent realistic blade loadings and flow structures. It was also seen that even having a very small turbulent free stream could give rise to the breakdown of the tip vortices and make the results more accurate.

Future work

In the current research, the parameters affecting the quality of LES were discussed and sources of improvement in EllipSys3D, with respect to the LES, were observed. This opens further investigations of the improved collocated schemes, capable of minimizing the kinetic energy conservation error, and improvement of the spatial and temporal discretizations towards central and higher order schemes.

discretizations towards central and higher order schemes. Thermally stratified channel flows were also investigated briefly. In the future, LES computations will be investigated further and detailed simulations of the stable and convective ABL with advanced wall-modeling techniques will be performed. The effects of the thermal stability on the wind turbine wakes and blade loadings as well as power production will also be considered.

Further investigations of the flow around airfoils will also be performed both numerically and experimentally. Evaluation of the uncertainty of the wind tunnel measurements in greater detail will be a part of the future studies. The studies will be continued with oil flow visualizations to investigate the separation and formation of stall cells experimentally.

The last topic of interest would be further LES investigations regarding actuator line and/or disc modeling of the wind turbines. The simulations can be performed for the Reynolds numbers much higher than those investigated in this research and potentially with other numerical solvers to ensure if the findings of this research, especically on the impact of the SGS models on flow structures and loadings, can be safely generalized.

Appendix: Benchmark results for the wind tunnel measurements

As explained earlier in chapter 4, wind tunnel measurements of the NREL S826 airfoil were performed for Reynolds numbers ranging from 40,000 to 400,000. The measurements were then used for validation of the numerical simulations at selected Reynolds numbers and angles of attack. This appendix presents the measurement data in terms of wake profiles downstream the airfoil and its corresponding drag polars obtained by integration of the wake, lift polars obtained using the force gauge, as well as pressure distributions over the airfoil.

For the Reynolds numbers lower than 100,000, the measurements using turbulence generating trip wires is also presented. See figure 4.8 to find out the level of turbulence produced by each wire at given Reynolds number.

A.1 Tabulated lift and drag coefficients

AOA	No Wire	D=0.05mm	D=0.15mm	D=0.3mm
-9.92	-0.30622	-0.30250	-0.31598	-0.36039
-7.96	-0.45987	-0.45900	-0.45980	-0.47763
-5.97	-0.33099	-0.32419	-0.32701	-0.31023
-4.01	-0.14910	-0.14019	-0.10823	-0.07909
-2.01	-0.15954	-0.15226	-0.13175	0.03245
-1.00	-0.06015	-0.05260	-0.03625	0.19213
-0.00	0.03409	0.04819	0.06231	0.33934
0.98	0.16619	0.17584	0.17232	0.45488
1.99	0.28806	0.29894	0.28016	0.53649
3.02	0.37186	0.38699	0.38473	0.60638
4.00	0.44094	0.43584	0.42178	0.75248
5.00	0.49442	0.50212	0.48245	0.92447
6.01	0.55922	0.55767	0.55077	1.06017
6.99	0.58404	0.58703	0.61503	1.18414
7.99	0.62998	0.63048	0.72001	1.29420
8.99	0.65715	0.65782	1.34316	1.35619
9.95	0.67755	0.67699	1.34856	1.35228
10.95	0.70208	0.70255	1.34108	1.34576
11.96	0.72700	0.72627	1.32509	1.32864
12.96	0.76029	0.75760	1.30658	1.31312
13.98	0.83893	0.82901	1.29006	1.29436
14.95	0.86233	0.88476	0.90703	1.18565
15.96	0.90765	0.91268	0.90947	1.09938
18.00	0.93668	0.95201	0.93947	0.92938
19.98	0.97418	0.98865	0.97220	0.96567
24.94	1.10319	1.10625	1.11445	1.08861

Table A.1: Lift coefficients for the S826 airfoil at Re=40,000 with different free stream turbulence values (Upstroke).

AOA	No Wire	D=0.05mm	D=0.15mm	D=0.3mm
24.94	1.10319	1.10625	1.11445	1.08861
19.98	0.97078	0.97321	0.96199	0.96637
18.01	0.93928	0.95369	0.94180	0.92826
15.97	0.90958	0.90575	0.92123	1.18486
14.97	0.87551	0.89315	0.91322	1.20828
14.03	0.82628	1.02555	1.00632	1.28258
13.02	1.06031	1.01682	1.16193	1.32358
12.03	0.98747	0.94912	1.32906	1.33628
11.04	0.69583	0.69520	1.33999	1.34365
10.04	0.67435	0.67470	1.33835	1.35065
9.06	0.65399	0.65128	1.33917	1.35603
8.05	0.62176	0.62649	0.72691	1.30366
7.05	0.59507	0.59625	0.62578	1.19614
6.06	0.56307	0.56645	0.55630	1.06863
5.04	0.50319	0.50729	0.48332	0.92965
4.06	0.44329	0.44182	0.42828	0.73635
3.04	0.37587	0.38514	0.38671	0.59796
2.04	0.29420	0.29987	0.28040	0.53009
1.02	0.17436	0.17776	0.17419	0.45673
0.06	0.04362	0.05442	0.06708	0.34658
-0.94	-0.05137	-0.04532	-0.03407	0.19831
-1.94	-0.14541	-0.13718	-0.12966	0.04471
-3.93	-0.17049	-0.16590	-0.10856	-0.06632
-5.91	-0.32331	-0.31672	-0.31750	-0.30271
-7.92	-0.46313	-0.46177	-0.46291	-0.47500
-9.92	-0.30928	-0.31131	-0.32228	-0.36526

Table A.2: Lift coefficients for the S826 airfoil at Re=40,000 with different free stream turbulence values (Downstroke).

AOA	No Wire	D=0.05mm	D=0.15mm	D=0.3mm
-9.92	0.14057	0.14553	0.14963	0.16258
-7.96	0.10184	0.10814	0.12204	0.10896
-5.97	0.05280	0.05794	0.06871	0.07017
-4.01	0.03629	0.04269	0.04676	0.05401
-2.01	0.04186	0.04818	0.06096	0.06310
-1.00	0.04325	0.04844	0.06125	0.06282
-0.00	0.04690	0.05704	0.06443	0.06522
0.98	0.05431	0.06259	0.07076	0.06676
1.99	0.05351	0.06321	0.07476	0.07134
3.02	0.06298	0.07231	0.07461	0.07626
4.00	0.07493	0.08431	0.07623	0.07279
5.00	0.07817	0.08558	0.08786	0.06563
6.01	0.07772	0.09026	0.09759	0.06010
6.99	0.09083	0.09945	0.10906	0.06233
7.99	0.10522	0.11605	0.12300	0.06057
8.99	0.11869	0.12904	0.05102	0.05986
9.95	0.14078	0.14789	0.05565	0.06602
10.95	0.16956	0.17537	0.06791	0.07764
11.96	0.19960	0.19725	0.08871	0.09652
12.96	0.22590	0.22176	0.11151	0.12038
13.98	0.25713	0.26256	0.12572	0.14142
14.95	0.25375	0.24447	0.24688	0.22080
15.96	0.26178	0.25231	0.26737	0.23209
18.00	0.32151	0.32303	0.33987	0.34826
19.98	0.36404	0.38556	0.39316	0.39557
24.94	0.45875	0.46171	0.46400	0.46666

Table A.3: Drag coefficients for the S826 airfoil at Re=40,000 with different free stream turbulence values (Upstroke).

AOA	No Wire	D=0.05mm	D=0.15mm	D=0.3mm
24.94	0.45875	0.46171	0.46400	0.46666
19.98	0.37433	0.38380	0.38743	0.39187
18.01	0.32212	0.32473	0.35240	0.34949
15.97	0.26121	0.25553	0.26900	0.23144
14.97	0.25991	0.23232	0.24429	0.21604
14.03	0.25482	0.22012	0.22803	0.14361
13.02	0.10226	0.21614	0.16352	0.11719
12.03	0.10310	0.20768	0.08776	0.09384
11.04	0.17250	0.17680	0.06955	0.07741
10.04	0.14223	0.14843	0.05865	0.06508
9.06	0.12075	0.12778	0.04970	0.05877
8.05	0.10234	0.11306	0.11857	0.06270
7.05	0.09440	0.09975	0.10886	0.06264
6.06	0.08199	0.09064	0.09688	0.06210
5.04	0.07547	0.08272	0.08431	0.06317
4.06	0.07797	0.08201	0.08075	0.07569
3.04	0.06228	0.07098	0.07639	0.07798
2.04	0.05289	0.06242	0.07103	0.07308
1.02	0.05462	0.06126	0.07039	0.06673
0.06	0.04786	0.05660	0.06417	0.06306
-0.94	0.04195	0.04629	0.06128	0.05999
-1.94	0.04228	0.04710	0.06039	0.06185
-3.93	0.03811	0.04495	0.05326	0.05125
-5.91	0.05412	0.05716	0.06596	0.07135
-7.92	0.10117	0.10438	0.11149	0.10840
-9.92	0.14289	0.14433	0.15019	0.15866

Table A.4: Drag coefficients for the S826 airfoil at Re=40,000 with different free stream turbulence values (Downstroke).

AOA	Re=40,000	Re=60,000	Re=80,000	Re=100,000
-9.93	-0.30622	-0.26321	-0.23511	-0.23785
-7.97	-0.45987	-0.45436	-0.44506	-0.44053
-5.98	-0.33099	-0.34059	-0.34712	-0.32471
-4.02	-0.14910	-0.07007	-0.02244	0.04841
-2.02	-0.15954	-0.06385	0.01453	0.25935
-1.01	-0.06015	0.06191	0.18239	0.33485
-0.01	0.03409	0.22376	0.36762	0.53315
0.98	0.16619	0.31481	0.51065	0.61083
1.99	0.28806	0.35822	0.61195	0.71753
3.02	0.37186	0.39873	0.58279	0.84191
4.00	0.44094	0.45132	0.58578	0.94685
5.00	0.49442	0.51023	0.59914	1.05547
6.01	0.55922	0.56258	0.66009	1.17566
6.99	0.58404	0.62408	1.22192	1.26650
7.99	0.62998	1.31178	1.33017	1.32586
8.99	0.65715	1.36348	1.35258	1.33418
9.95	0.67755	1.34450	1.30622	1.27315
10.95	0.70208	1.32079	1.25907	1.22780
11.95	0.72700	1.29851	1.22720	1.19619
12.95	0.76029	1.27306	1.20133	1.17200
13.97	0.83893	1.22101	1.18184	1.15007
14.94	0.86233	0.99962	1.20845	1.12593
15.96	0.90765	0.99820	0.91292	0.90846
17.99	0.93668	0.94394	0.95378	0.95423
19.97	0.97418	0.98053	0.98309	0.98948
24.93	1.10319	1.13021	1.15166	1.16523

Table A.5: Lift coefficients for the S826 airfoil at Re=40,000 up to Re=100,000 (Upstroke).

AOA	Re=40,000	Re=60,000	Re=80,000	Re=100,000
24.93	1.10319	1.13021	1.15166	1.16523
19.97	0.97078	0.98309	0.97020	0.98412
18.00	0.93928	0.94866	0.94507	0.95149
15.96	0.90958	0.97233	0.90779	0.91498
14.95	0.87551	0.99924	1.02865	1.00570
13.97	0.82628	1.01149	1.01900	0.98791
12.96	1.06031	0.98496	1.04104	1.17214
11.96	0.98747	1.30174	1.22971	1.19403
10.95	0.69583	1.32287	1.25773	1.22434
9.96	0.67435	1.34612	1.30699	1.27214
8.99	0.65399	1.36397	1.35281	1.33576
8.00	0.62176	1.30702	1.33062	1.32545
7.00	0.59507	0.63500	1.22032	1.26624
6.01	0.56307	0.56169	1.08809	1.17520
5.01	0.50319	0.51054	0.61028	1.05540
4.01	0.44329	0.45015	0.58253	0.94723
3.03	0.37587	0.39808	0.57780	0.84081
2.00	0.29420	0.35880	0.62256	0.71743
0.98	0.17436	0.31730	0.51800	0.61147
0.00	0.04362	0.21948	0.37006	0.53459
-1.00	-0.05137	0.06500	0.18235	0.35081
-2.01	-0.14541	-0.06511	0.01577	0.25968
-4.01	-0.17049	-0.06899	-0.02343	0.04897
-5.97	-0.32331	-0.34124	-0.34772	-0.32571
-7.97	-0.46313	-0.45818	-0.44211	-0.43883
-9.94	-0.30928	-0.26230	-0.23551	-0.24116

Table A.6: Lift coefficients for the S826 airfoil at Re=40,000 up to Re=100,000 (Downstroke).

AOA	Re=40,000	Re=60,000	Re=80,000	Re=100,000
-9.93	0.14057	0.14007	0.14033	0.14162
-7.97	0.10184	0.12770	0.13031	0.13447
-5.98	0.05280	0.05325	0.05412	0.05193
-4.02	0.03629	0.02940	0.02802	0.03263
-2.02	0.04186	0.04618	0.04723	0.03524
-1.01	0.04325	0.05267	0.04561	0.03363
-0.01	0.04690	0.05296	0.04328	0.02856
0.98	0.05431	0.05521	0.04243	0.02969
1.99	0.05351	0.05784	0.04409	0.02949
3.02	0.06298	0.06434	0.05913	0.03015
4.00	0.07493	0.07047	0.06811	0.03124
5.00	0.07817	0.07755	0.07883	0.03115
6.01	0.07772	0.08758	0.08793	0.03421
6.99	0.09083	0.10762	0.03201	0.02797
7.99	0.10522	0.03511	0.02450	0.02104
8.99	0.11869	0.02947	0.03297	0.03471
9.95	0.14078	0.03967	0.04097	0.04678
10.95	0.16956	0.05132	0.05682	0.07574
11.95	0.19960	0.06937	0.08519	0.11063
12.95	0.22590	0.09291	0.10536	0.13859
13.97	0.25713	0.11774	0.13307	0.16270
14.94	0.25375	0.24889	0.14960	0.19008
15.96	0.26178	0.26799	0.29504	0.29117
17.99	0.32151	0.33029	0.33647	0.34084
19.97	0.36404	0.37238	0.37628	0.37576
24.93	0.45875	0.45884	0.45199	0.45132

Table A.7: Drag coefficients for the S826 airfoil at Re=40,000 up to Re=100,000 (Upstroke).

AOA	Re=40,000	Re=60,000	Re=80,000	Re=100,000
24.93	0.45875	0.45884	0.45199	0.45132
19.97	0.37433	0.38089	0.37437	0.37537
18.00	0.32212	0.33594	0.34008	0.34251
15.96	0.26121	0.27626	0.29248	0.29187
14.95	0.25991	0.25360	0.25741	0.27262
13.97	0.25482	0.21449	0.22933	0.23651
12.96	0.10226	0.20008	0.19529	0.13316
11.96	0.10310	0.06848	0.08500	0.11109
10.95	0.17250	0.04900	0.05845	0.07673
9.96	0.14223	0.03910	0.04036	0.04826
8.99	0.12075	0.02844	0.03253	0.03431
8.00	0.10234	0.03678	0.02502	0.02116
7.00	0.09440	0.10680	0.03228	0.02845
6.01	0.08199	0.08580	0.03998	0.03447
5.01	0.07547	0.07864	0.07945	0.03033
4.01	0.07797	0.07095	0.06911	0.03160
3.03	0.06228	0.06437	0.05713	0.03042
2.00	0.05289	0.05827	0.04285	0.03019
0.98	0.05462	0.05526	0.04195	0.02974
0.00	0.04786	0.05272	0.04321	0.02882
-1.00	0.04195	0.05300	0.04621	0.03365
-2.01	0.04228	0.04386	0.04605	0.03473
-4.01	0.03811	0.03049	0.02749	0.03170
-5.97	0.05412	0.05337	0.05414	0.05153
-7.97	0.10117	0.12829	0.13160	0.13365
-9.94	0.14289	0.13950	0.13937	0.14206

Table A.8: Drag coefficients for the S826 airfoil at Re=40,000 up to Re=100,000 (Downstroke).

AOA	Re=120,000	Re=145,000	Re=200,000	Re=300,000	Re=400,000
-10.04	-0.24283	-0.24445	-0.26796	-0.29518	-0.34907
-8.05	-0.45494	-0.46148	-0.46715	-0.33152	-0.29506
-6.05	-0.29385	-0.27047	-0.16596	-0.08509	-0.09273
-4.09	0.07630	0.11515	0.15769	0.13434	0.11061
-2.09	0.34848	0.35449	0.40129	0.35786	0.32640
-1.08	0.41396	0.48143	0.50439	0.45887	0.42359
-0.08	0.51351	0.53874	0.61355	0.56388	0.52469
0.91	0.60756	0.63538	0.71821	0.65982	0.63068
1.92	0.73197	0.74452	0.83054	0.76904	0.73499
2.95	0.85765	0.84918	0.95200	0.86215	0.84056
3.93	0.95886	0.96538	1.03748	0.94687	0.94030
4.94	1.07504	1.09860	1.10811	1.05565	1.03781
5.95	1.18457	1.20065	1.21108	1.17098	1.13546
6.93	1.27539	1.27802	1.28711	1.25432	1.22482
7.93	1.33128	1.33189	1.32563	1.28616	1.27565
8.93	1.31944	1.30763	1.29827	1.31351	1.30301
9.89	1.25751	1.24977	1.23529	1.31510	1.29752
10.89	1.21511	1.19894	1.18284	1.24210	1.23052
11.90	1.18207	1.16055	1.14343	1.18273	1.16536
12.90	1.15639	1.13711	1.12323	1.13143	1.11384
13.92	1.13559	1.11474	1.10206	1.07800	1.05545
14.89	1.11290	1.09130	1.05770	1.02476	0.98726
15.91	0.99221	1.04256	1.00669	0.97695	0.95648
17.94	0.94976	0.94963	1.06431	1.06794	1.16640
19.92	0.99280	0.99520	1.10667	0.93002	0.94547
24.88	1.17031	1.16774	1.16846	1.01285	0.98515

Table A.9: Lift coefficients for the S826 airfoil at Re=120,000 up to Re=400,000.

AOA	Re=120,000	Re=145,000	Re=200,000	Re=300,000	Re=400,000
-10.04	0.14310	0.14184	0.14761	0.17045	0.17469
-8.05	0.13038	0.13306	0.13045	0.08694	0.08551
-6.05	0.05019	0.04706	0.03779	0.02595	0.02570
-4.09	0.02887	0.02148	0.01925	0.01599	0.01320
-2.09	0.02863	0.02484	0.01950	0.01276	0.01074
-1.08	0.02610	0.02330	0.01733	0.01240	0.01070
-0.08	0.02600	0.02191	0.01740	0.01270	0.01100
0.91	0.02479	0.02175	0.01774	0.01330	0.01149
1.92	0.02504	0.02173	0.01818	0.01400	0.01209
2.95	0.02554	0.02248	0.01886	0.01472	0.01281
3.93	0.02597	0.02370	0.01923	0.01536	0.01353
4.94	0.02706	0.02372	0.02022	0.01585	0.01414
5.95	0.02788	0.02351	0.01717	0.01647	0.01470
6.93	0.02157	0.02025	0.02356	0.01413	0.01284
7.93	0.02689	0.02987	0.02888	0.02023	0.01889
8.93	0.03468	0.03422	0.03434	0.02666	0.02481
9.89	0.05333	0.05608	0.06627	0.03286	0.03159
10.89	0.08837	0.10124	0.11159	0.06231	0.05964
11.90	0.12453	0.13391	0.13870	0.11149	0.11091
12.90	0.14841	0.15477	0.15511	0.14377	0.14275
13.92	0.17326	0.17726	0.18164	0.17948	0.17844
14.89	0.20640	0.20871	0.21887	0.21424	0.22128
15.91	0.27352	0.22472	0.24775	0.24673	0.24226
17.94	0.34180	0.34306	0.29984	0.29136	0.26990
19.92	0.37585	0.37927	0.32586	0.42972	0.40178
24.88	0.45034	0.44620	0.44826	0.37850	0.36851

Table A.10: Drag coefficients for the S826 airfoil at Re=120,000 up to Re=400,000.

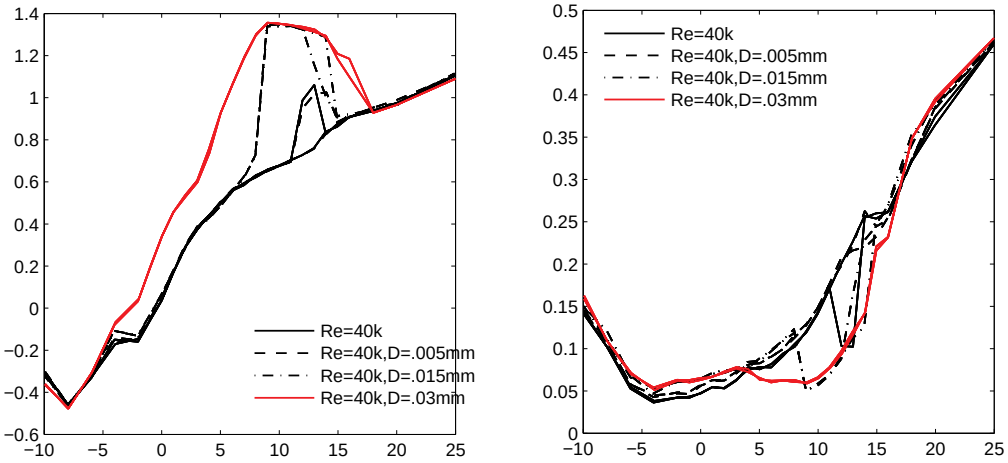

(a) (b)

Figure A.1: Lift (a) and drag (b) coefficients, obtained from the force gauge and wake rake pressure measurements, respectively, for $Re = 40,000$ using different free stream turbulence. The legends show the upstream wire diameters used to trigger the flow instabilities.

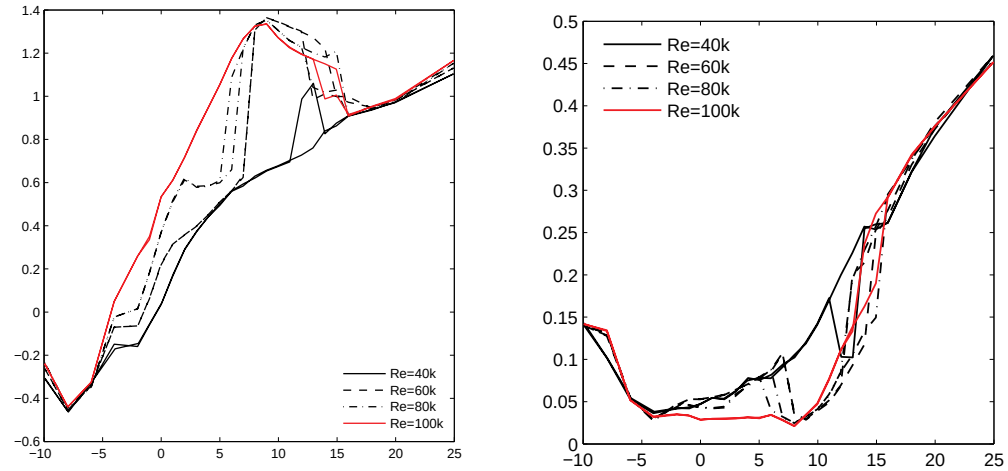

(a) (b)

Figure A.2: Lift (a) and drag (b) coefficients, obtained from the force gauge and wake rake pressure measurements, respectively, for $Re = 40,000$ up to $Re = 100,000$ at empty-tunnel free stream turbulence level.

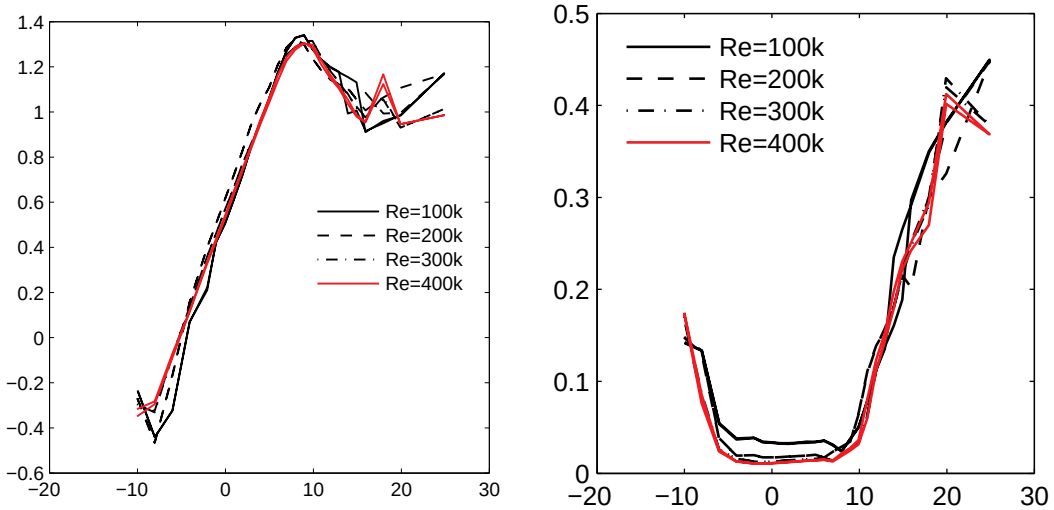

Figure A.3: Lift (a) and drag (b) coefficients, obtained from the force gauge and wake rake pressure measurements, respectively, for $Re = 100,000$ up to $Re = 400,000$ at empty-tunnel free stream turbulence level.

A.2 Pressure distribution over the airfoil

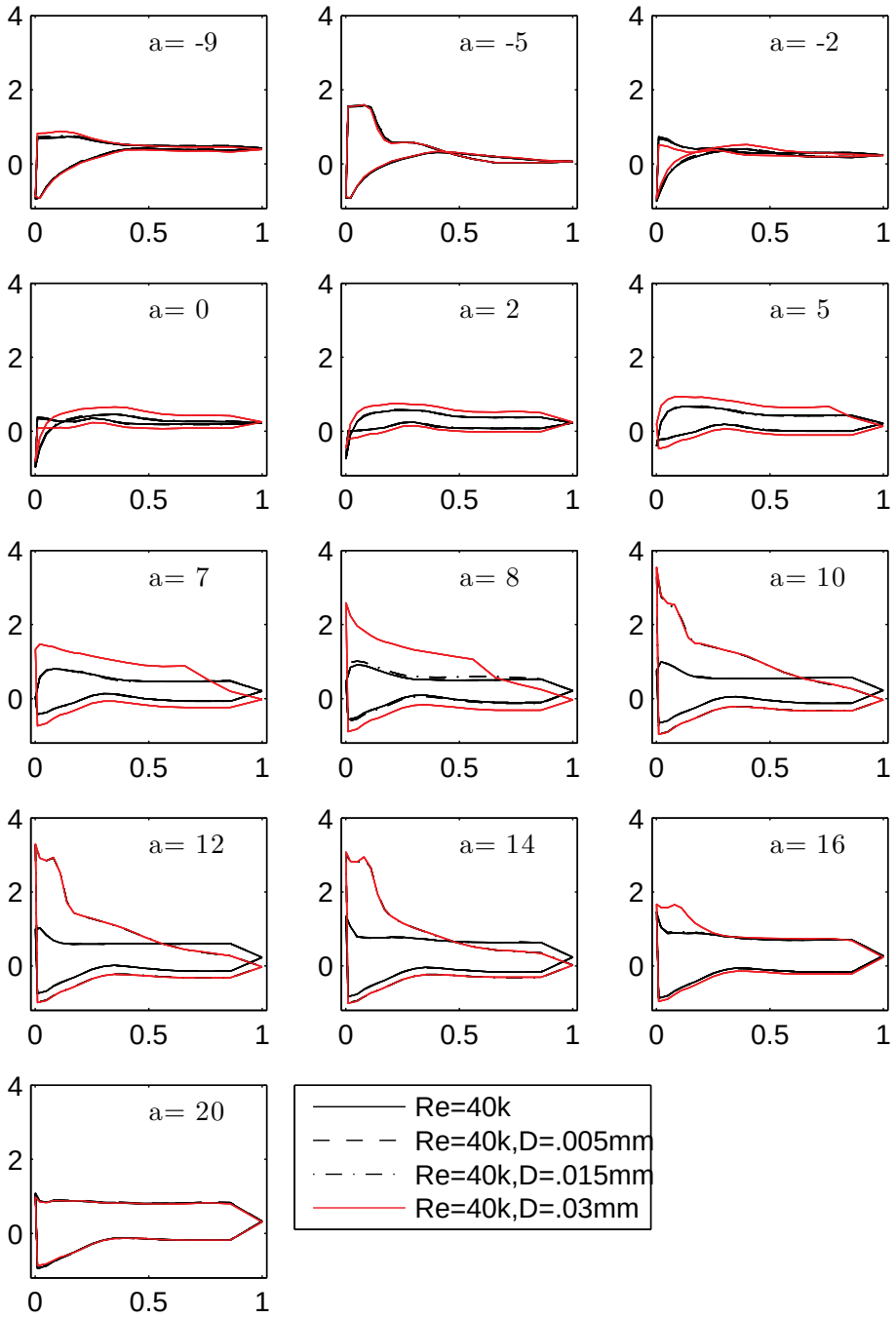

Figure A.4: Pressure distribution on the S826 airfoil for $Re = 40,000$ using different free stream turbulence. The legends show the upstream wire diameters used to trigger the flow instabilities.

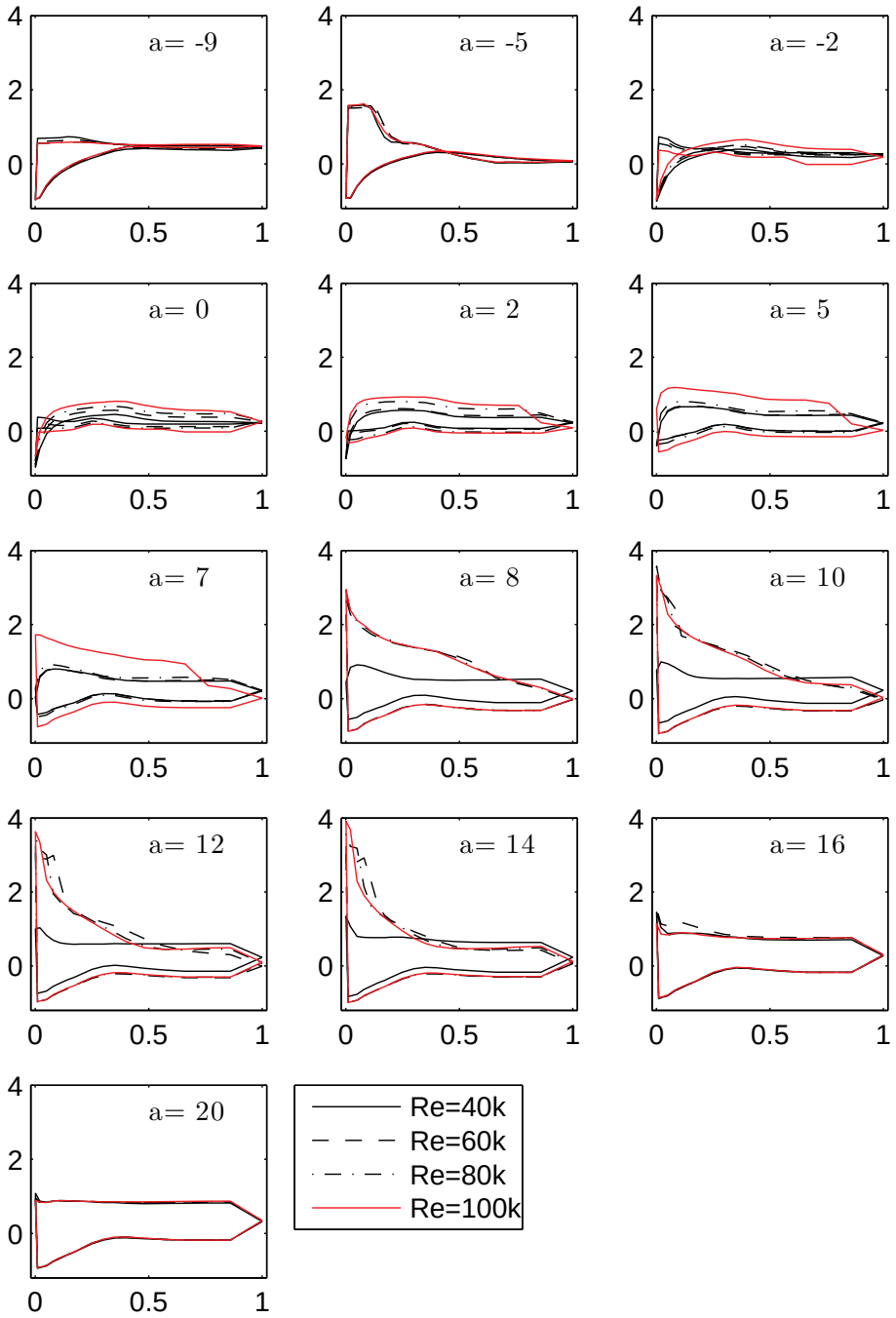

Figure A.5: Pressure distribution on the S826 airfoil for $Re = 40,000$ up to $Re = 100,000$.

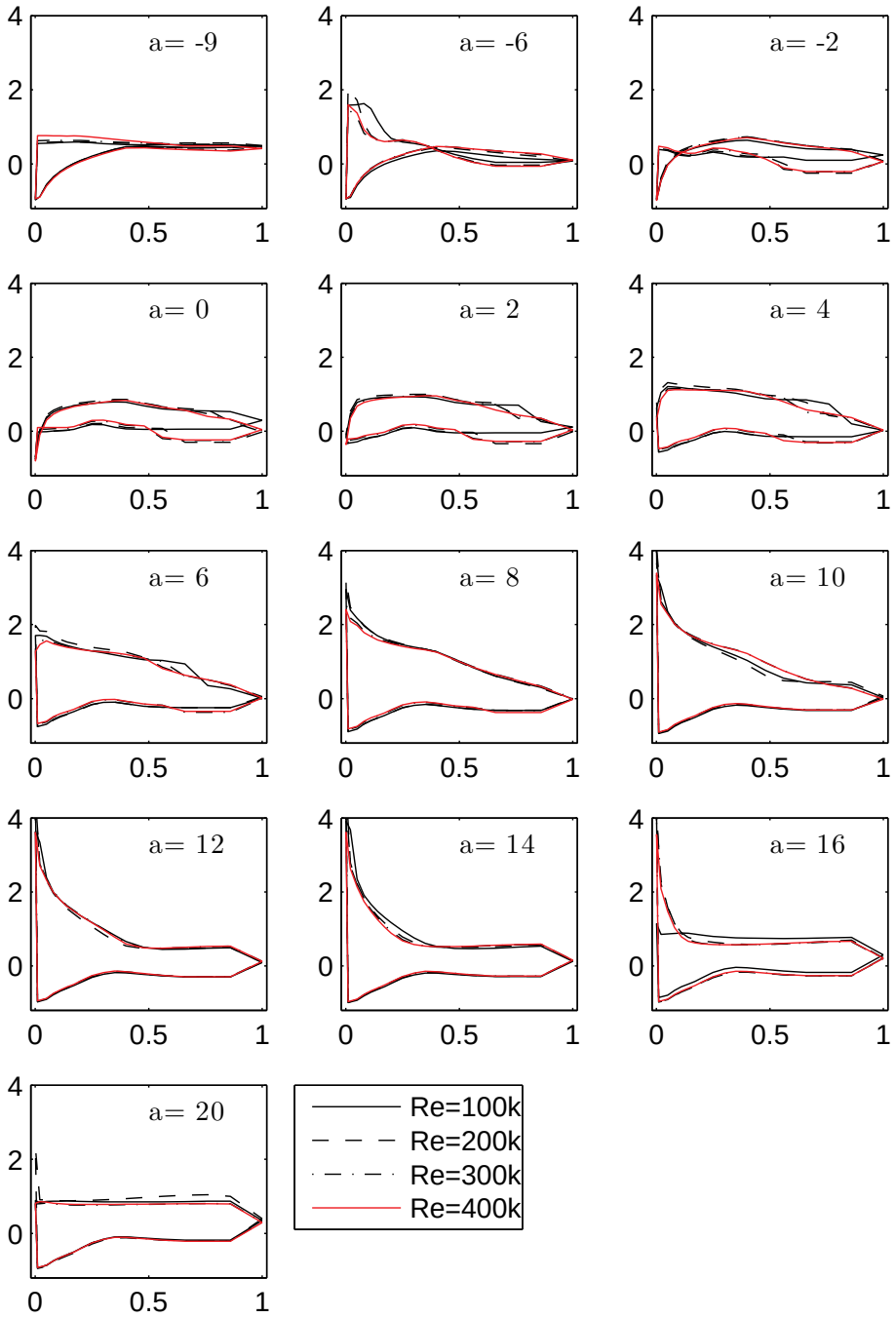

Figure A.6: Pressure distribution on the S826 airfoil for $Re = 100,000$ up to $Re = 400,000$.

A.3 Wake profiles downstream of the airfoil

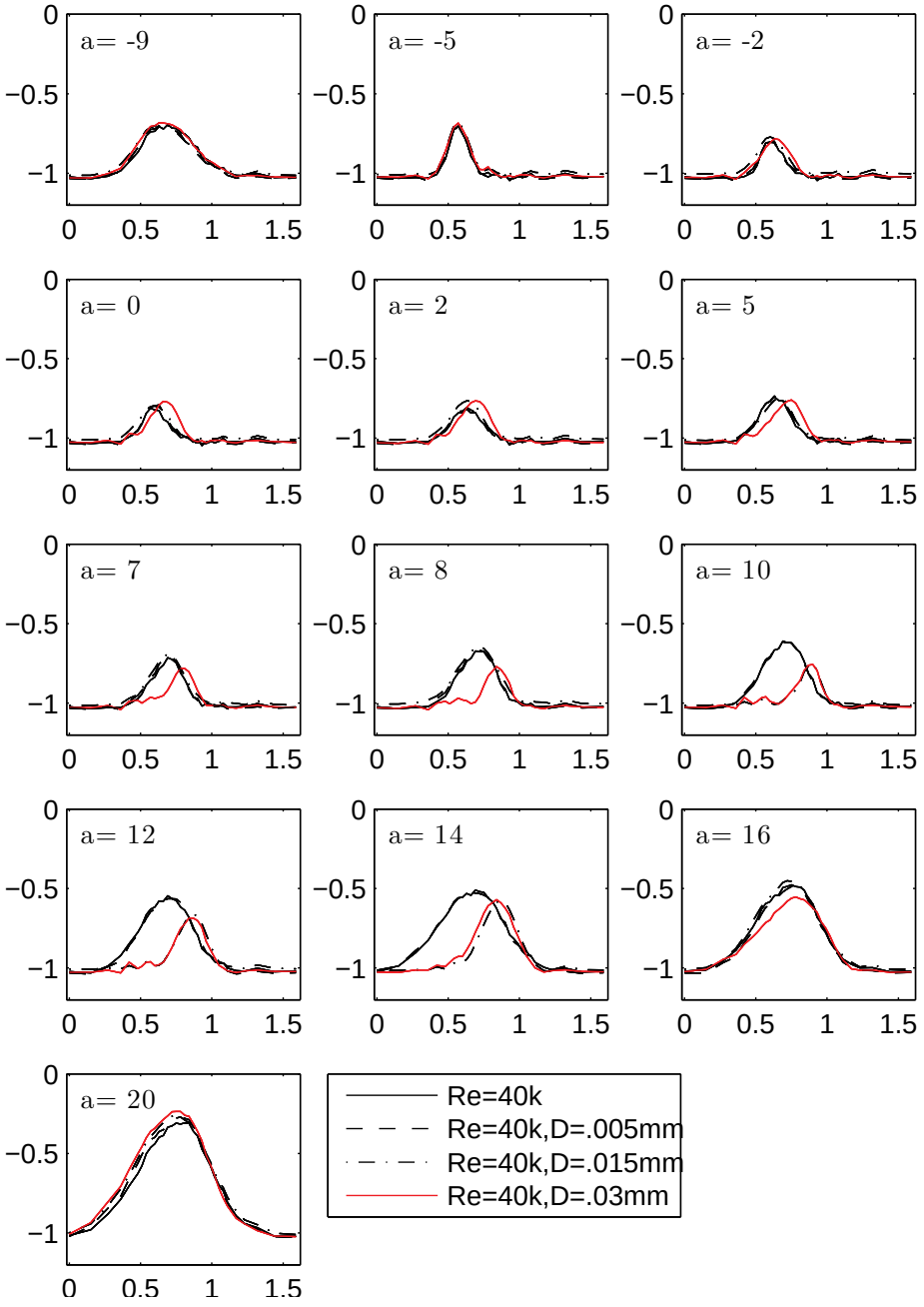

Figure A.7: Wake profiles downstream of the S826 airfoil for $Re = 40,000$ using different free stream turbulence. The legends show the upstream wire diameters used to trigger the flow instabilities.

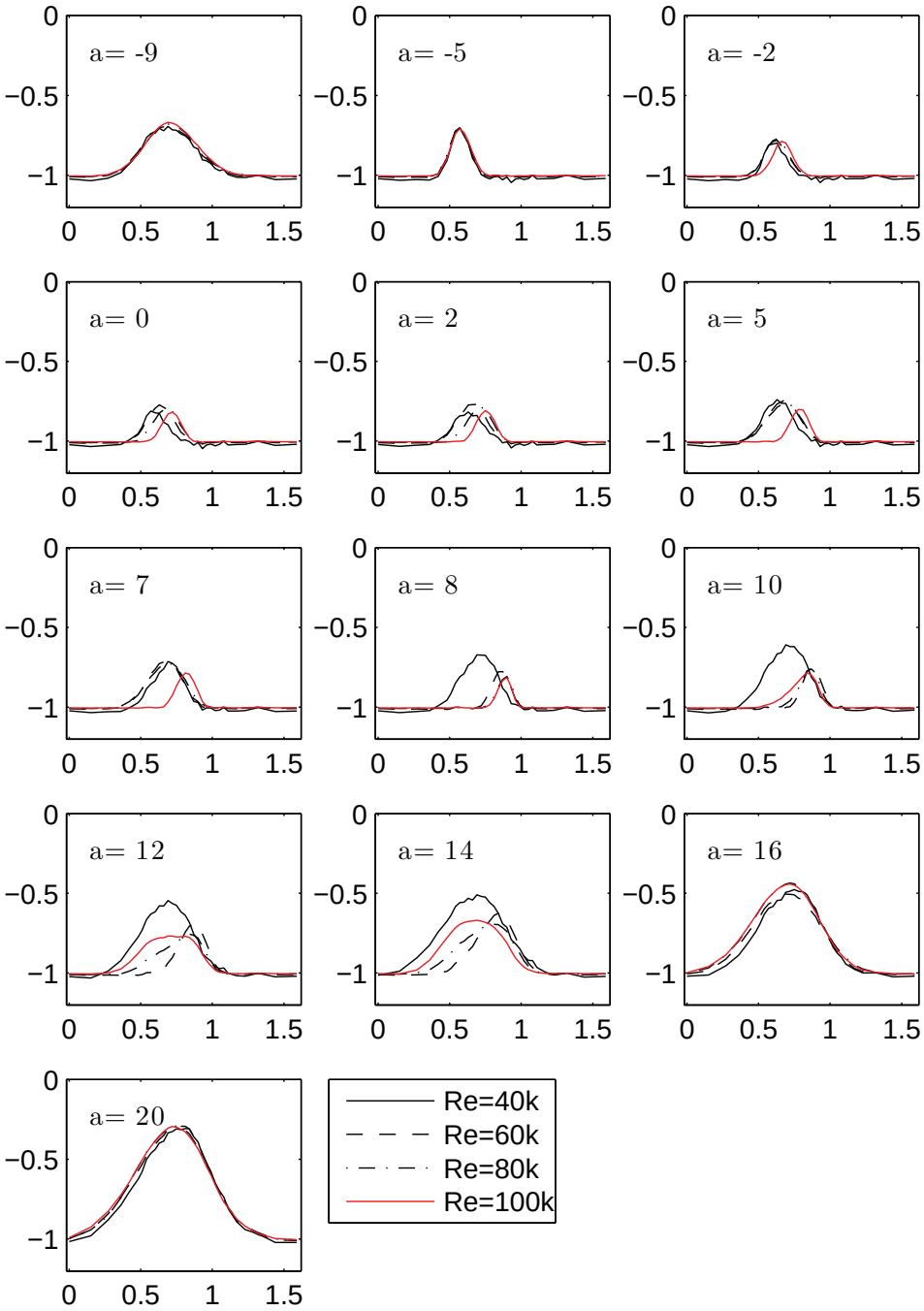

Figure A.8: Wake profiles downstream of the S826 airfoil for $Re = 40,000$ up to $Re = 100,000$.

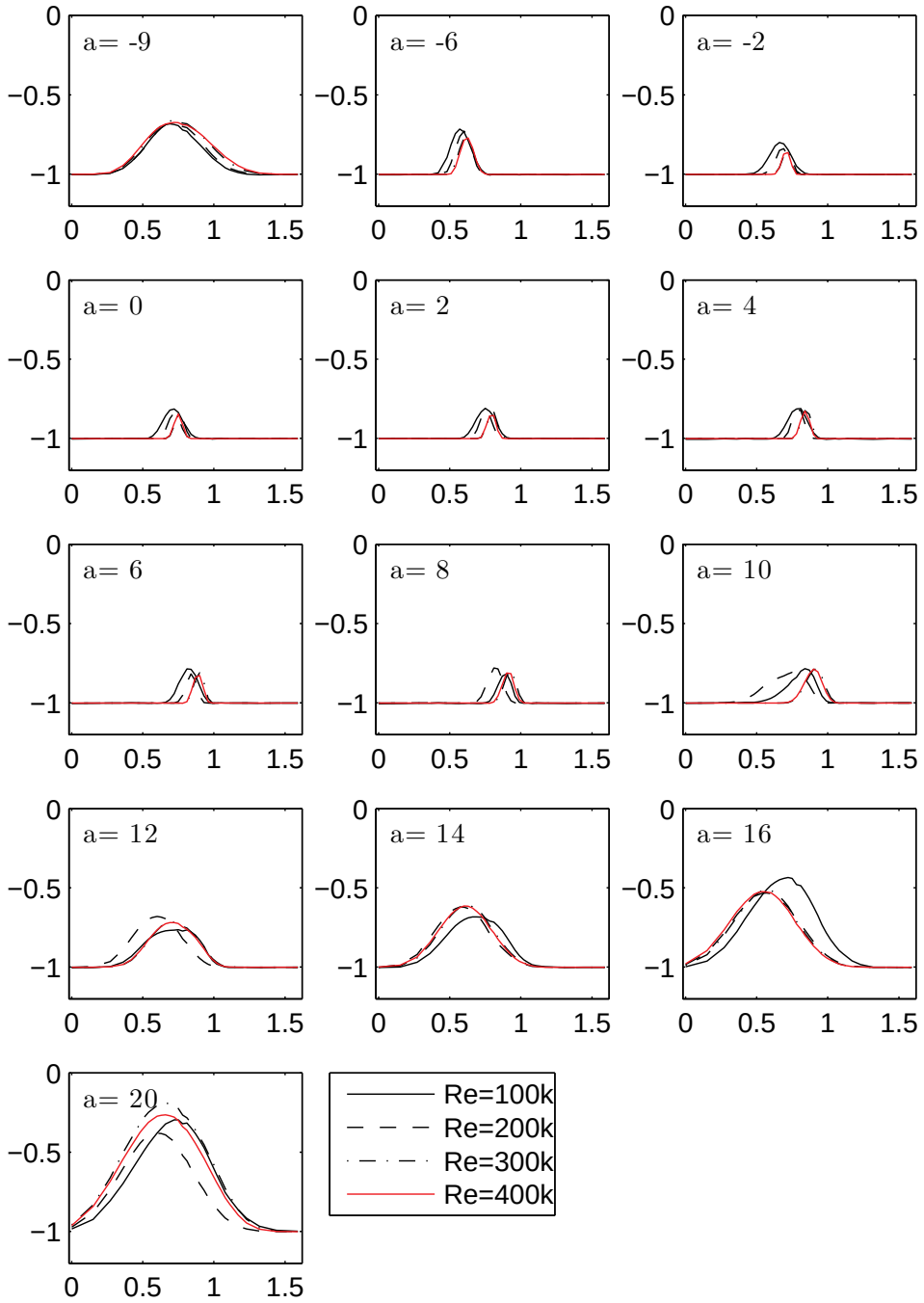

Figure A.9: Wake profiles downstream of the S826 airfoil for $Re = 100,000$ up to $Re = 400,000$.

List of Figures

List of Tables

References

Abbott, I., 1999. Theory of wing sections. Dover Publications, Mineola. 58

Amiri, A., Hannani, S., Mashayek, F., 2005. Evaluation of a Fourth-Order Finite-Volume Compact Scheme for LES with Explicit Filtering. Numerical Heat Transfer, Part B: Fundamentals 48, 147–163. 31

Armenio, V., Sarkar, S., 2002. An investigation of stably stratified turbulent channel flow using large-eddy simulation. Journal of Fluid Mechanics 459, 1–42. 43

Barbato, J., Genta, G., Germak, A., 2013. Measurements for Decision Making. Societ Editrice Esculapio. 81

Bardina, J., Ferziger, J., Reynolds, W., 1980. Improved subgrid-scale models for large-eddy simulation. 23

Barlow, J., Rae, W., Pope, A., 1999. Low-speed wind tunnel testing. Wiley New York. 74

Bartl, J., Pierella, F., Sætran, L., 2012. Wake measurements behind an array of two model wind turbines. Energy Procedia 24, 305–312. 5

Basu, S., 2004. Large-Eddy Simulation of Stably Stratified Atmospheric Boundary Layer Turbulence : A Scale-Dependent Dynamic Modeling Approach. Ph.D. thesis, University of Minnesota. 30

Basu, S., Porté-Agel, F., Foufoula-Georgiou, E., Vinuesa, J., Pahlow, M., 2005. Revisiting the Local Scaling Hypothesis in Stably Stratified Atmospheric Boundary-Layer Turbulence: an Integration of Field and Laboratory Measurements with Large-Eddy Simulations. Boundary-Layer Meteorology 119 (3), 473–500. 29

Benhamadouche, S., 2006. Large Eddy Simulation with the unstructured collocated arrangement. Ph.D. thesis, University of Manchester. 17, 33

Bose, S., Moin, P., You, D., 2010. Grid-independent large-eddy simulation using explicit filtering. Physics of Fluids 22 (10), 105103. 31

Bou-Zeid, E., Meneveau, C., Parlange, M., 2005. A scale-dependent Lagrangian dynamic model for large eddy simulation of complex turbulent flows. Physics of Fluids 17, 025105. 6, 23, 39, 49, 51, 53, 155

Brandt, L., Schlatter, P., Henningson, D., 2004. Transition in boundary layers subject to free-stream turbulence. Journal of Fluid Mechanics 517, 167–198. 31

Brandt, T., 2004. Studies On Numerical Errors In Large Eddy Simulation. Ph.D. thesis, Helsinki University of Technology. 31

Calaf, M., Meneveau, C., Meyers, J., 2010. Large eddy simulation study of fully developed wind-turbine array boundary layers. Physics of Fluids 22 (1), 015110. 6, 10, 34, 59

Cavar, D., 2006. Large Eddy Simulation of Industrially Relevant Flows. Ph.D. thesis, DTU. 24, 26, 37

Chow, F., 2004. Subfilter-Scale Turbulence Modeling For Large-Eddy Simulation Of The Atmospheric Boundary Layer Over Complex Terrain. Ph.D. thesis, University of California, Berkeley. 31

Chow, F., Moin, P., 2003. A further study of numerical errors in large-eddy simulations. Journal of Computational Physics 184 (2), 366–380. 31

Coles, D., 1956. The law of the wake in the turbulent boundary layer. Journal of Fluid Mechanics 1 (02), 191–226. 51

Davidson, L., 2003. LESFOIL: Large Eddy Simulation of Flow Around a High Lift Airfoil: Results of the Project LESFOIL Supported by the European Union 1998-2001. Vol. 83. Springer. 7, 80

Davidson, L., 2009. Large Eddy Simulations: How to evaluate resolution. International Journal of Heat and Fluid Flow 30 (5), 1016–1025. 31

Deardorff, J., 1970. A numerical study of three-dimensional turbulent channel flow at large Reynolds numbers. Journal of Fluid Mechanics 41 (2), 453–480. 4, 21

Deardorff, J., 1972. Numerical investigation of neutral and unstable planetary boundary layers. Journal of the Atmospheric Sciences 29 (1), 91–115. 4

Deardorff, J., 1980. Stratocumulus-capped mixed layers derived from a three-dimensional model. Boundary-Layer Meteorology 18 (4), 495–527. 4

Derbyshire, S., 1990. Nieuwstadt's stable boundary layer revisited. Quarterly Journal of the Royal Meteorological Society 116 (491), 127–158. 5

DeVilliers, E., 2006. The Potential of Large Eddy Simulation for the Modeling of Wall Bounded Flows Eugene de Villiers. Ph.D. thesis, Imperial College London. 36

Dong, Y., Lu, X., 2005. Direct numerical simulation of stably and unstably stratified turbulent open channel flows. Acta mechanica 177 (1-4), 115–136. 43

Drazin, P., Reid, W., 2004. Hydrodynamic stability. Cambridge university press. 36

Eisenbach, S., Friedrich, R., 2008. Large-eddy simulation of flow separation on an airfoil at a high angle of attack and Re= 105 using Cartesian grids. Theoretical and Computational Fluid Dynamics 22 (3-4), 213–225. 7

Fairman, R. S., 2002. Investigation into the discrepancies between computational fluid dynamic lift predictions and experimental results. 7

Felten, F., Lund, T., 2006. Kinetic energy conservation issues associated with the collocated mesh scheme for incompressible flow. Journal of Computational Physics 215 (2), 465–484. 33

Forbes, R., 1964. Studies in ancient technology. Vol. 9. Brill. 1

Frandsen, S., 1992. On the wind speed reduction in the center of large clusters of wind turbines. Journal of Wind Engineering and Industrial Aerodynamics 39 (1-3), 251–265. 59

Frandsen, S., Barthelmie, R., Pryor, S., Rathmann, O., Larsen, S., Højstrup, J., Thøgersen, M., 2006. Analytical modelling of wind speed deficit in large offshore wind farms. Wind Energy 9 (1-2), 39–53. 5, 34

Gant, S., 2010. Reliability issues of LES-related approaches in an industrial context. Flow, turbulence and combustion 84 (2), 325–335. 109

Germano, M., Piomelli, U., Moin, P., Cabot, W., 1991. A dynamic subgrid-scale eddy viscosity model. Physics of Fluids A: Fluid Dynamics 3, 1760. 22, 29

Ghosal, S., Lund, T., Moin, P., Akselvoll, K., 1995. A dynamic localization model for large-eddy simulation of turbulent flows. Journal of Fluid Mechanics 286 (1), 229–255. 30

Gilling, L., 2009. Airfoils in Turbulent Inflow. Ph.D. thesis, Aalborg University. 11, 16, 153

Gullbrand, J., 2002. Grid-independent large-eddy simulation in turbulent channel flow using three-dimensional explicit filtering. CTR Annu. Res. Briefs (1995), 167–179. 31, 37

Ham, F., Iaccarino, G., 2004. Energy conservation in collocated discretization schemes on unstructured meshes. CTR Annu. Res, Briefs. 32, 33

Ivanell, S., Sørensen, J., Mikkelsen, R., Henningson, D., 2009. Analysis of numerically generated wake structures. Wind Energy 12 (1), 63–80. 6

Jimenez, A., Crespo, A., Migoya, E., Garcia, J., 2007. Advances in large-eddy simulation of a wind turbine wake. In: Journal of Physics: Conference Series. Vol. 75. IOP Publishing, p. 012041. 6, 10, 107, 153

JL., H., 1958. Smoothing and Filtering of Time Series and Space Fields. Advances in Geophysics 4, 351–389. 19

Kasagi, N., Iida, O., 1999. Progress in direct numerical simulation of turbulent heat transfer. In: Proceedings of the 5th ASME/JSME Joint Thermal Engineering Conference. pp. 15–19. 44, 155

Kawai, S., Larsson, J., 2012. Wall-modeling in large eddy simulation: Length scales, grid resolution, and accuracy. Physics of Fluids 24, 015105. 46

Kleissl, J., Kumar, V., Meneveau, C., Parlange, M., 2006. Numerical study of dynamic Smagorinsky models in large-eddy simulation of the atmospheric boundary layer: Validation in stable and unstable conditions. Water Resources Research 42 (6), n/a–n/a. 29

Krogstad, P.-Å., Lund, J., 2012. An experimental and numerical study of the performance of a model turbine. Wind Energy 15 (3), 443–457. 66, 93

Krogstad, P.-Å., Sætran, L., 2013. Invitation to the 2013 Blind test 3 Workshop Two in-line wind turbines with spanwise offset. Tech. Rep. December, NTNU. 96, 121

Larsson, J., Iaccarino, G., 2010. A colocated incompressible navier–stokes solver with exact mass, momentum and kinetic energy conservation in the inviscid limit. Journal of Computational Physics 229 (12), 4425–4430. 32, 33

Lenormand, E., Sagaut, P., TaPhuoc, L., Comte, P., 2000. Subgrid-Scale Models for Large-Eddy Simulations of Compressible Wall Bounded Flows. AIAA J. 38 (8), 1340–1350. 7

Lettau, H., 1969. Note on aerodynamic roughness-parameter estimation on the basis of roughness-element description. Journal of Applied Meteorology 8 (5), 828–832. 59

Lilly, D., 1992. A proposed modification of the germano subgrid-scale closure method. Physics of Fluids A: Fluid Dynamics 4, 633. 23

Lu, H., Porté-Agel, F., 2011. Large-eddy simulation of a very large wind farm in a stable atmospheric boundary layer. Physics of Fluids 23, 065101. 10, 29

Lu, H., Rutland, C., Smith, L., 2007. A priori tests of one-equation LES modeling of rotating turbulence. Journal of Turbulence (8). 19, 20, 154

Lund, T., 1997. On the use of discrete filters for large eddy simulation. Center for Turbulence Research Annual Research Briefs 18. 31

Lundquist, K., 2010. Immersed Boundary Methods for High-Resolution Simulation of Atmospheric Boundary-Layer Flow Over Complex Terrain. Ph.D. thesis, University of California, Berkeley. 31

Mahesh, K., Constantinescu, G., Moin, P., 2004. A numerical method for large-eddy simulation in complex geometries. Journal of Computational Physics 197 (1), 215–240. 33

Mann, J., 1998. Wind field simulation. Probabilistic engineering mechanics 13 (4), 269–282. 11, 104

Mary, I., Sagaut, P., 2002. Large eddy simulation of flow around an airfoil near stall. AIAA J. 40 (6), 1139–1145. 7, 80

Mason, P., Thomson, D., 1992. Stochastic backscatter in large-eddy simulations of boundary layers. Journal of Fluid Mechanics 242, 51–78. 49

Melaaen, M., 1992a. Calculation of fluid flows with staggered and nonstaggered curvilinear nonorthogonal grids-a comparison. Numerical Heat Transfer, Part B Fundamentals 21 (1), 21–39. 33

Melaaen, M., 1992b. Calculation of fluid flows with staggered and nonstaggered curvilinear nonorthogonal grids-the theory. Numerical Heat Transfer, Part B Fundamentals 21 (1), 1–19. 33

Mellen, C., J., F., Rodi, W., 2003. Lessons from lesfoil project on large-eddy simulation of flow around an airfoil. AIAA J. 41 (4), 573–581. 7, 80

Mellor, G., Yamada, T., 1974. A hierarchy of turbulence closure models for planetary boundary layers. Journal of the Atmospheric Sciences 31 (7), 1791–1806. 46

Meneveau, C., Katz, J., 2000. Scale-invariance and turbulence models for large-eddy simulation. Annual Review of Fluid Mechanics 32 (1), 1–32. 23

Meneveau, C., Lund, T., Cabot, W., 1996. A Lagrangian dynamic subgrid-scale model of turbulence. Journal of Fluid Mechanics 319, 353–385. 23

Michelsen, J., 1992. Basis3d-a platform for development of multiblock pde solvers. Ph.D. thesis, Technical Note AFM92-05, Technical University of Denmark, Department of Fluid Mechanics. 11

Mikkelsen, R., 2003. Actuator disc methods applied to wind turbines. Ph.D. thesis, Technical University of Denmark. 6, 57, 58, 156

Mikkelsen, R., Sørensen, J., Øye, S., Troldborg, N., 2007. Analysis of Power Enhancement for a Row of Wind Turbines Using the Actuator Line Technique. Journal of Physics: Conference Series 75, 012044. 6, 26

Moeng, C., 1984. A large-eddy-simulation model for the study of planetary boundary-layer turbulence. Journal of the Atmospheric Sciences 41 (13), 2052–2062. 4

Moeng, C., Sullivan, P., 1994. A comparison of shear-and buoyancy-driven planetary boundary layer flows. Journal of the Atmospheric Sciences 51 (7), 999–1022. 4

Moin, P., Squires, K., Cabot, W., Lee, S., 1991. A dynamic subgrid-scale model for compressible turbulence and scalar transport. Physics of Fluids A: Fluid Dynamics 3, 2746. 29

Moser, R., Kim, J., Mansour, N., 1999. Direct numerical simulation of turbulent channel flow up to Re = 590. Physics of Fluids 11, 943. 38, 39, 41, 42, 154

Park, T., 2006. Effects of Time-Integration Method in a Large-Eddy Simulation Using the PISO Algorithm: Part I- Flow Field. Numerical Heat Transfer, Part A: Applications 50 (3), 229–245. 31

Petrila, T., Trif, D., 2005. Basics of fluid mechanics and introduction to computational fluid dynamics. Vol. 3. Springer Verlag. 32

Piomelli, U., 2008. Wall-layer models for large-eddy simulations. Progress in Aerospace Sciences 44 (6), 437–446. 31, 46

Piomelli, U., Balaras, E., 2002. Wall-layer models for large-eddy simulations. Annual review of fluid mechanics 34 (1), 349–374. 80

Piomelli, U., Balaras, E., Pasinato, H., Squires, K., Spalart, P., 2003. The innerouter layer interface in large-eddy simulations with wall-layer models. International Journal of Heat and Fluid Flow 24 (4), 538–550. 14

Pope, S., 2000. Turbulent Flows. Cambridge University Press. 18, 19, 35, 109, 153

Pope, S., 2004. Ten questions concerning the large-eddy simulation of turbulent flows. New Journal of Physics 6, 35–35. 31

Porté-Agel, F., 2000. A scale-dependent dynamic model for large-eddy simulation: application to a neutral atmospheric boundary layer. Journal of Fluid Mechanics 415, 261–284. 23

Porté-Agel, F., Parlange, M., Meneveau, C., Eichinger, W., 2001. A priori field study of the subgrid-scale heat fluxes and dissipation in the atmospheric surface layer. Journal of the atmospheric sciences 58 (18), 2673–2698. 46

Porté-Agel, F., Wu, Y., Lu, H., Conzemius, R., 2011. Large-eddy simulation of atmospheric boundary layer flow through wind turbines and wind farms. Journal of Wind Engineering and Industrial Aerodynamics 99 (4), 154–168. 6

Porté-Agel, F., Wu, Y., Lu, H., Conzemius, R., 2011. Large-eddy simulation of atmospheric boundary layer flow through wind turbines and wind farms. Journal of Wind Engineering and Industrial Aerodynamics 99 (4), 154–168. 7, 29

Ramos-García, N., Sørensen, J., Shen, W., 2013. Development of a three-dimensional viscous-inviscid coupling method for wind turbine computations. Wind Energy. 86

Rethore, P., Sørensen, N., Zahle, F., Johansen, J., 2008. Comparison of an actuator disc model with a full rotor CFD model under uniform and shear inflow condition. 8

Rhie, C., Chow, W., 1983. Numerical study of the turbulent flow past an airfoil with trailing edge separation. AIAA J. 21 (11), 1525–1532. 12

Rodríguez, D., Theofilis, V., 2011. On the birth of stall cells on airfoils. Theoretical and Computational Fluid Dynamics 25 (1-4), 105–117. 67

Ross, I., Altman, A., 2011. Wind tunnel blockage corrections: Review and application to Savonius vertical-axis wind turbines. Journal of Wind Engineering and Industrial Aerodynamics 99 (5), 523–538. 74

Sagaut, P., 1995. Simulations numériques d'écoulements décollés avec des modèles de sous-maille. Ph.D. thesis. 6, 24

Sagaut, P., 2000. Large eddy simulation for incompressible flows. Vol. 3. Springer Berlin. 93

Sanderse, B., 2009. Aerodynamics of wind turbine wakes. Energy Research Center of the Netherlands (ECN), ECN-E–09-016, Petten, The Netherlands, Tech. Rep. 5, 15, 153

Sarlak, H., Meneveau, C., Sørensen, J., Mikkelsen, R., 2014. Quantifying the impact of subgrid scale models in actuator-line based LES of wind turbine wakes in laminar and turbulent inflow. In: Direct and Large Eddy Simulation IX. Springer-Verlag (accepted). 93, 94, 158

Sarlak, H., Sørensen, J., 2013. Large Eddy Simulation of Wind Turbine Wakes in Prescribed Neutral and Non-Neutral Atmospheric Boundary Layers. Journal of Physics: Conference Series (under review). 54

Sarlak, H., Sørensen, J., Mikkelsen, R., 2012. Large eddy simulation of atmospheric boundary layer over wind farms using a prescribed boundary layer approach 121, 121–124. 10

Schewe, G., 1983. On the force fluctuations acting on a circular cylinder in crossflow from subcritical up to transcritical reynolds numbers. Journal of Fluid Mechanics 133 (1), 265–285. 101, 159

Schlichting, H., 1955. Boundary-layer theory. McGraw-Hill. 78

Selig, M., 2003. Low reynolds number airfoil design lecture notes. VKI Lecture Series, November, 24–28. 8

Selig, M., Deters, R., Williamson, G., 2011. Wind tunnel testing airfoils at low reynolds numbers. In: 49th AIAA Aerospace Sciences Meeting. pp. 4–7. 81

Sergent, A., Joubert, P., Le Quéré, P., Tenaud, C., 2000. Extension du modèle d'échelles mixtes à la diffusivité de sous-maille. Comptes Rendus de l'Académie des Sciences - Series IIB - Mechanics 328 (12), 891–897. 30

Sescu, A., Meneveau, C., 2014. Large eddy simulation and single column modeling of thermally-stratified wind-turbine arrays for fully developed, stationary atmospheric conditions. Journal of Atmosheric & Oceanic Technology (submitted). 5

Shepherd, D., 1990. Historical development of the windmill. Vol. 4337. National Aeronautics and Space Administration, Office of Management, Scientific and Technical Information Division. 1

Smagorinsky, J., 1963. General circulation experiments with the primitive equations: I. the basic experiment. Monthly weather review 91 (3), 99–164. 4, 21

Smith, E. P., 2002. Uncertainty analysis. Encyclopedia of environmetrics. 81

Smits, A., McKeon, B., Marusic, I., 2011. High-Reynolds number wall turbulence. Annual Review of Fluid Mechanics 43, 353–375. 46

Sørensen, J., 2011. Aerodynamic aspects of wind energy conversion. Annual Review of Fluid Mechanics 43, 427–448. 1, 6, 93

Sørensen, J., Myken, A., 1992. Unsteady actuator disc model for horizontal axis wind turbines. Journal of Wind Engineering and Industrial Aerodynamics 39 (1), 139–149. 9, 57

Sørensen, J., Shen, W., 2002. Numerical Modeling of Wind Turbine Wakes. Journal of Fluids Engineering 124 (2), 393. 6, 8, 95

Sørensen, N., 1995. General purpose flow solver applied to flow over hills. Ph.D. thesis, Technical University of Denmark, Risø National Laboratory for Sustainable Energy. 11

Sullivan, P., McWilliams, J., Moeng, C., 1994. A subgrid-scale model for large-eddy simulation of planetary boundary-layer flows. Boundary-Layer Meteorology 71 (3), 247–276. 4

Ta Phuoc, L., 1994. Modèles de sous-maille appliqués aux écoulements instationnaires et décollés. Journée Thématique DRET, Paris. 6, 24

Troldborg, N., 2008. Actuator line modeling of wind turbine wakes. Ph.D. thesis, Technical University of Denmark. 58, 59, 107, 156

Troldborg, N., Sørensen, J., Mikkelsen, R., 2007. Actuator line simulation of wake of wind turbine operating in turbulent inflow. In: Journal of Physics: Conference Series. Vol. 75. IOP Publishing, p. 012063. 6, 10, 11, 54

Tuerke, F., Jiménez, J., 2013. Simulations of turbulent channels with prescribed velocity profiles. Journal of Fluid Mechanics 723, 587–603. 59

Uranga, A., Persson, P., Drela, M., Peraire, J., 2009. Implicit large eddy simulation of transitional flows over airfoils and wings. Proceedings of the 19th AIAA Computational Fluid Dynamics, no. AIAA 4131. 7, 67

van Driest, E., 1956. On turbulent flow near a wall. Journal of the Aeronautical Sciences 23 (11). 38

Vasilyev, O., Lund, T., Moin, P., 1998. A General Class of Commutative Filters for LES in Complex Geometries. Journal of Computational Physics 146 (1), 82–104. 17

Venugopal, P., Cheung, L., Jothiprasad, G., Lele, S., 2012. Large eddy simulation of a wind turbine airfoil at high angle of attack. In: Proceedings of the Summer Program (CTR). p. 157. 8

Vermeer, L., Sørensen, J., Crespo, A., 2003. Wind turbine wake aerodynamics. Progress in Aerospace Sciences 39 (6-7), 467–510. 6

Von Karman, T., 1930. Mechanical similarity and turbulence (in German). Message from the Society of Sciences and Göttingen, Mathematics and Physical class 1930, 58–76. 50

Von Karman, T., 1948. Progress in the statistical theory of turbulence. Proceedings of the National Academy of Sciences of the United States of America 34 (11), 530. 11

Wang, L., Lu, X., 2005. Large eddy simulation of stably stratified turbulent open channel flows with low- to high-Prandtl number. International Journal of Heat and Mass Transfer 48, 1883–1897. 43

Windte, J., Radespiel, R., Scholz, S., Eisfeld, B., 2004. RANS simulation of the transitional flow around airfoils at low Reynolds Numbers for steady and unsteady onset conditions. Tech. rep., Univ. Braunschweig. 67, 156

Winkelman, A., Barlow, J., 1980. Flowfield model for a rectangular planform wing beyond stall. AIAA J. 18 (8), 1006–1008. 67

Zang, Y., Street, R., Koseff, J., 1993. A dynamic mixed subgrid-scale model and its application to turbulent recirculating flows. Physics of Fluids A: Fluid Dynamics 5, 3186. 24

Zhou, Y., Wang, Z., 2010. Implicit large eddy simulation of transitional flow over a sd7003 wing using high-order spectral difference method. In: 40th Fluid Dynamics Conference and Exhibit. Vol. 28. 8

The Danish wind energy research environment is internationally recognized as being in the forefront of wind energy technology, and The Technical University of Denmark (DTU) has provided a major part of the wind energy research in Denmark with Risø National Laboratory for Sustainable Energy as a major contributor. As of 1st January 2012, DTU has taken this support to the industry-research collaboration, innovation and public sector consultancy one step further by bringing together all groups with activities within wind energy into a new department of wind energy, DTU Wind Energy, thus strengthening the research capability as well as the education/training activities.

DTU Wind Energy has more than 240 staff members, including 150 academic staff members and approximately 60 PhD students, and the department comprises 8 sections covering wind energy systems, wind turbine technology, and wind energy basics. This thesis has been carried out in the section of Fluid Mechanics. The fundamental research in the section of Fluid Mechanics includes laminar-turbulent transition, flow control, aero-acoustics, rotating flows, turbulence, and convection and heat transfer in boundary layers.

DTU Vindenergi er et institut under Danmarks Tekniske Universitet med en unik integration af forskning, uddannelse, innovation og offentlige/private konsulentopgaver inden for vindenergi. Vores aktiviteter bidrager til nye muligheder og teknologier inden for udnyttelse af vindenergi, både globalt og nationalt. Forskningen har fokus på specifikke tekniske og videnskabelige områder, der er centrale for udvikling, innovation og brug af vindenergi, og som danner grundlaget for højt kvalificerede uddannelser på universitetet.

Vi har mere end 240 ansatte og heraf er ca. 60 ph.d. studerende. Forskningen tager udgangspunkt i ni forskningsprogrammer, der er organiseret i tre hovedgrupper: vindenergisystemer, vindmølleteknologi og grundlagsskabende forskning.

Danmarks Tekniske Universitet
Institut for Vindenergi
Nils Koppels Allé
Bygning 403
2800 Kgs. Lyngby
Phone 46 77 50 85

info@vindenergi.dtu.dk
www.vindenergi.dtu.dk